IN VIVO ANALYTICAL PERFORMANCE ASSESSMENT OF NITRIC OXIDE-RELEASING GLUCOSE BIOSENSORS

Robert Joseph Soto

A dissertation submitted to the faculty at the University of North Carolina at Chapel Hill in partial fulfillment of the requirements for the degree of Doctor of Philosophy in the Department of Chemistry (Analytical Chemistry)

Chapel Hill
2016

Approved by:

Mark H. Schoenfisch

R. Mark Wightman

James W. Jorgenson

Timothy C. Nichols

Zhen Gu

© 2016
Robert Joseph Soto
ALL RIGHTS RESERVED

ABSTRACT

ROBERT JOSEPH SOTO: In Vivo Analytical Performance Assessment of
Nitric Oxide-Releasing Glucose Biosensors
(Under the direction of Mark H. Schoenfisch)

The utility of implantable glucose biosensors as continuous glucose monitoring technologies is limited by poor in vivo accuracy, resulting primarily from the foreign body response (FBR). Polymeric membranes capable of releasing nitric oxide (NO)—an endogenous gas and key mediator of inflammation and angiogenesis—have been shown to mitigate the FBR and thus hold promise for improving in vivo glucose sensor function. Herein, the effect of a reduced FBR on in vivo glucose sensor function was studied using NO-releasing membranes.

To address the low NO storage of silica nanoparticles, a new particle system (mesoporous silica) was synthesized for use in glucose sensor membranes. Briefly, an interfacial ion exchange reaction was developed and used to chemically modify mesoporous silica nanoparticles with NO donors. The resulting materials were capable of large NO storage (0.8–2.4 μmol mg^{-1}) and tunable NO-release kinetics (NO-release durations 2–40 h). The NO-releasing nanoparticles were employed as dopants within polyurethane materials and adapted as coatings for amperometric glucose biosensors.

The in vivo analytical performance of the NO-releasing glucose biosensors was evaluated in a pre-clinical swine model. Two separate NO-releasing sensors were designed to release similar amounts of NO (~3.1 μmol cm^{-2}) for 16.0 h (short) or 3.1 d (extended) durations. Relative to controls, both NO-releasing sensors exhibited improved accuracy during the acute (3

d) implantation period. Sensors capable of ~3 d NO release were also characterized by a shorter response time (<4.2 min) to changing blood glucose levels than burst NO-releasing and control sensors (>5.8 min) at 3, 7, and 10 d.

The NO-releasing sensor membranes were also used to study the FBR in a streptozotocin-induced diabetic swine model. Histopathological evaluation of tissue surrounding control (i.e., non-NO-releasing) materials revealed a more severe inflammatory response, reduced collagen deposition, and inhibited angiogenesis associated with diabetes. Materials capable of ~7–14 d NO release were uniquely capable of mitigating inflammation and increasing blood vessel formation at the implant-tissue interface (relative to 2–3 d NO release). The ~7–14 d NO-releasing membranes also reduced collagen deposition in healthy pigs, but did not produce an effect in the diabetic animal model.

To my parents, Rob and Lorraine, and to my wife, Valerie,

who have selflessly given their love and support

and continue to do so each day

"The road goes ever on and on, down from the door from where it began…

Now far ahead the road has gone, and I must follow it if I can" –J. R. R. T.

ACKNOWLEGEMENTS

Accepting the risk of being unoriginal, I believe the African proverb “it takes a village to raise a child” certainly extends well beyond the normal adolescent age in my case. I am fortunate that, throughout my life, I have been surrounded by scientists with an unconditional passion for their discipline. To Bob Campbell, Del Thorpe, and Vince Dober—thank you for taking an interest in my science education at an early age and for your patience. I can’t bear the thought of having to teach myself at that age. I am grateful to two of my undergraduate mentors, Prof. Craig Aspinwall and Prof. Victor Hruby, for providing a conducive learning environment and encouraging me to pursue graduate research. Finally, I express my endless gratitude to Prof. Mark Schoenfisch for being a teacher, life mentor, and friend. None of this work would have been possible without your ideas and unmatched persistence. You pushed me to reach for the stars.

I am indebted to all of the collaborators and scientists who convened to tackle an important problem in analytical chemistry. I am grateful for the expertise of Dr. Amar Kumbhar and Dr. Wallace Ambrose, the resident electron microscopists at CHANL. Thank you for always going the extra mile and being willing to help with my crazy (and sometimes poorly thought-out…) ideas. I am especially appreciative for your quick responses to e-mails when the focused ion beam needs a restart at 8:30 PM on a Friday night. I also express my gratitude to Dr. Alice Will, Jaime Davis, and Jessica Fuller at Synchrony for your assistance with the initial pre-clinical sensor evaluation and enduring nine months of long testing days. I am humbled by the expertise

of Dr. Elizabeth Merricks, Prof. Timothy Nichols, Prof. Dwight Bellinger, Dr. Lauren Wimsey, Dr. Margaret Whitford, Mark Kloos, and Robin Raymer at the Francis Owen Blood Research Lab. Thank you for all of your work and advice during our studies of the foreign body response and glucose sensor performance in diabetic pigs.

I have had the privilege of working with very talented peers during my time at the University of North Carolina. Many thanks to Dr. Rebecca Hunter, Dr. Ahyeon Koh, and Dr. Danielle Slomberg for giving me a warm welcome to "The Fungeon" during my first year of graduate school. I also express my gratitude to Dr. Chris Backlund, Dr. Katey Reighard, and Dr. Wesley Storm for helping me during my first two years at UNC and, along with Rebecca, contributing to some great memories. An enormous thank you to Dr. Brittany Worley and Dakota Suchyta for being both my close friends and harsh critics of my work. You challenged me to do my very best. I look forward to witnessing your great achievements in the future. Another special thank you to Lei Yang for being an integral contributor to my research, a keen critic of my science, and a good friend. I also thank my fellow classmate and member of the chemistry-themed rock band ("The Monostables") Nathan Rodeberg for a great friendship these past several years. I am grateful for many fun memories. Finally, I acknowledge my friends and co-inhabitants of the Schoenfisch Lab, including Micah Brown, Shaylyn Walter, Mona Ahonen, Jackson Hall, James Talyor, Maggie Malone-Povolny, Kaitlyn Rouillard, Evan Feura, Pedro Cruz, and Haibao Jin. I have had the fortune of publishing with many of you and the pleasure of interacting with all of you. I was particularly lucky to work with two excellent undergraduate students, Blake Schofield and Paige Kinsley. I hope you learned as much from me as I learned from you.

Finally, I have to thank my family for bearing with me through my journey through graduate school. I thank my mother-in-law, Perla Velasquez, for treating me as a son these past seven years. Thank you to Michael and Kim for being a source of support for your (and my) entire lives. To my dogs, Glacia, Kiona, and Jake—I doubt I would have retained any of my sanity through graduate school without you by my side. Your unconditional love and boundless energy kept me positive, brightening up many otherwise difficult days. I express my unimaginable gratitude to my parents, Rob and Lorraine Soto, whose unconditional love, support, and sacrifice has enabled me to achieve my dreams. Undoubtedly, I would not be where I am today without you. Finally, to my wife Valerie, who has forged ahead through graduate school by my side. This dissertation is as much a product of your perseverance as it is my dedication to science. Thank you for supporting me and for all of the sacrifices you made. I could not have done this without you.

TABLE OF CONTENTS

LIST OF TABLES xiv

LIST OF FIGURES xvi

LIST OF ABBREVIATIONS AND SYMBOLS xx

CHAPTER 1. IN VIVO GLUCOSE BIOSENSORS: ROLE OF BIOCOMPATIBILITY ON ANALYTICAL PERFORMANCE 1

1.1. Diabetes and blood glucose management 1

1.2. Analytical technologies for in vivo glucose measurement 3

1.2.1. Electrochemical glucose detection 3

1.2.2. Optical glucose detection 7

1.2.3. Commercial glucose monitoring technologies 8

1.3. Foreign body response 9

1.3.1. Foreign body response and glucose sensor analytical performance 11

1.3.2. Foreign body response deficiencies associated with diabetes 17

1.4. Material strategies to mitigate the foreign body response 20

1.4.1. Zwitterionic polymers 20

1.4.2. Porous and nanopatterned coating materials 22

1.4.3. Release of tyrosine kinase inhibitors 28

1.4.4. Dexamethasone release 29

1.4.5. Nitric oxide release 31

1.4.5A. Nitric oxide-release strategies 33

1.4.5B. Subcutaneous tissue biocompatibility of nitric oxide-releasing materials 37

1.5. Summary of dissertation research 42
1.6. References 44
CHAPTER 2. IN VIVO ANALYTICAL PERFORMANCE OF NITRIC OXIDE RELEASING GLUCOSE BIOSENSORS....66
2.1. Introduction 66
2.2. Experimental section 69
2.2.1. Materials 69
2.2.2. Synthesis of nitric oxide-releasing silica nanoparticles 70
2.2.3. Preparation of nitric oxide-releasing mock sensors 71
2.2.4. Characterization of nitric oxide-releasing substrates 72
2.2.5. Fabrication and in vitro performance of nitric oxide-releasing glucose sensors....73
2.2.6. In vivo protocol for assessing glucose biosensor analytical performance 74
2.2.7. Data analysis 75
2.3. Results and discussion 77
2.3.1. In vitro characterization of nitric oxide-releasing glucose biosensors....77
2.3.2. In vivo biosensor run-in time, glucose sensitivity, and Clarke error grid 83
2.3.3. Biosensor numerical accuracy and adherence to ISO criteria 89
2.3.4. Biosensor lag time....93
2.3.5. Post-explantation analysis....96
2.4. Conclusions 97
2.5. References 99
CHAPTER 3. FUNCTIONALIZED MESOPOROUS SILICA VIA AN AMINOSILANE-SURFACTANT ION EXCHANGE REACTION: CONTROLLED SCAFFOLD DESIGN AND NITRIC OXIDE RELEASE....105
3.1. Introduction 105
3.2. Experimental section 108

3.2.1. Materials 108
3.2.2. Mesoporous silica nanoparticle synthesis 109
3.2.3. Nanoparticle characterization 110
3.2.4. *N*-diazeniumdiolate modification and nitric oxide release measurements 111
3.2.5. Statistical analysis 112
3.3. Results and discussion 113
3.3.1. Nitric oxide release 127
3.3.2. Organosilane modification 132
3.3.3. Aminosilane modification and nitric oxide-release kinetics 137
3.4. Conclusions 141
3.5. References 142
CHAPTER 4. DESIGN CONSIDERATIONS FOR SILICA PARTICLE-DOPED NITRIC OXIDE-RELEASING POLYURETHANE GLUCOSE BIOSENSOR MEMBRANES 149
4.1. Introduction 149
4.2. Experimental section 151
4.2.1. Materials 151
4.2.2. Synthesis of *N*-diazeniumdiolate-modified silica nanoparticles 152
4.2.3. Synthesis of *S*-nitrosothiol-modified silica nanoparticles 156
4.2.4. Preparation and evaluation of nitric oxide-releasing mock sensors 158
4.2.5. Nitric oxide-release measurements 159
4.2.6. Design and analytical performance evaluation of miniaturized nitric oxide-releasing glucose biosensors 162
4.2.7. Membrane and particle characterization 166
4.3. Results and discussion 166
4.3.1. Polyurethane membranes incorporating *N*-diazeniumdiolate-modified silica particles 170

4.3.2. Polyurethane membranes incorporating *S*-nitrosothiol-modified silica particles....176

4.3.3. Nitric oxide release from *S*-nitrosothiol-based polyurethane/silica membranes....179

4.3.4. Analytical performance of nitric oxide-releasing electrochemical glucose biosensors....182

4.4. Conclusions....190

4.5. References....192

CHAPTER 5. FOREIGN BODY RESPONSE TO NITRIC OXIDE-RELEASING SUBCUTANEOUS IMPLANTS IN A STREPTOZOTOCIN-INDUCED SWINE MODEL OF DIABETES....198

5.1. Introduction....198

5.2. Experimental section....200

5.2.1. Materials....200

5.2.2. Synthesis of *N*-diazeniumdiolate-modified mesoporous silica nanoparticles....201

5.2.3. Synthesis of *S*-nitrosothiol-modified mesoporous silica nanoparticles....202

5.2.4. Preparation of nitric oxide-releasing polyurethane-membrane coated implants....203

5.2.5. Membrane characterization....204

5.2.6. In vivo protocol....205

5.2.7. Statistical analysis....207

5.3. Results and discussion....207

5.3.1. Characterization of nitric oxide-releasing polyurethanes....207

5.3.2. Inflammatory response....211

5.3.3. Collagen deposition....217

5.3.4. Angiogenesis....221

5.4. Conclusions....224

5.5. References....226

CHAPTER 6. SUMMARY AND FUTURE DIRECTIONS....232

6.1. Summary of dissertation research 232

6.2. Future directions 234

6.2.1. Hydrophobic surface modification of *N*-diazeniumdiolate-based silica particles 234

6.2.2. Improving the handling and storage stability of *S*-nitrosothiol-based silica particles 236

6.2.3. Molecular and cellular basis for the anti-inflammatory capacities of NO 239

6.2.4. In vivo glucose sensor analytical performance evaluation in diabetic swine 242

6.3. Conclusions 245

6.4. References 247

LIST OF TABLES

Table 2.1. Size and nitric oxide-release characterization for MAP/NO and MPTMS-RSNO silica nanoparticle dopants 78

Table 2.2. Nitric oxide release from polyurethane coatings doped with NO-releasing MPTMS-RSNO and MAP/NO nanoparticles 81

Table 2.3. Glucose sensor analytical performance in phosphate buffered saline (pH 7.41, 37 ^{o}C) 82

Table 2.4. Clinical performance and apparent in vivo sensitivity of glucose biosensors 86

Table 2.5. ISO criteria for NO-releasing and control sensors 91

Table 3.1. Synthesis conditions and nitrogen physisorption data for MSNs of varying size 114

Table 3.2. Characterization of AEAP-modified 1100 nm mesoporous silica particles as a function of reaction aminosilane concentration 117

Table 3.3. Physicochemical characterization of AEAP-functionalized MSNs of varying size 125

Table 3.4. Chemiluminescent NO release measurements in physiological buffer (PBS, pH 7.4, 37 ^{o}C) from AEAP/NO MSNs of varying size 128

Table 3.5. Elemental analysis of 150 nm APTES, BTMS, and MPTMS particles 135

Table 3.6. Physicochemical and nitric oxide-release characterization of 30 nm NO-releasing MSNs as a function of aminosilane modification 138

Table 4.1. Reaction parameters for synthesis of amine-modified mesoporous silica nanoparticles 153

Table 4.2. Reaction parameters for synthesis of thiol-modified silica nanoparticles 157

Table 4.3. Nitric oxide-release properties for selected NO donor-modified silica particles 161

Table 4.4. Analytical performance merits of glucose biosensors coated with different PUs (50 mg mL^{-1} PU solutions) 168

Table 4.5. Analytical performance merits of glucose biosensors coated with different PUs (80 mg mL^{-1} PU solutions) 169

Table 4.6. Particle leaching measurements for membranes doped with RSNO-modified particles of varying MPTMS content 178

Table 4.7. Particle leaching and NO-release measurements for PU membranes doped with 75 mol% MPTMS/TEOS particles 180

Table 5.1. Nitric oxide release from polyurethane membranes doped with different NO donor-modified silica nanoparticles 210

LIST OF FIGURES

Figure 1.1. Schematic design for the needle type glucose biosensor 6

Figure 1.2. Foreign body response to implanted glucose sensors 10

Figure 1.3. Model of macrophage biofouling layer at the surface of implantable glucose sensors 14

Figure 1.4. Pore-size dependence of foreign body response to solid and porous poly(2-hydroxyethyl)methacrylate hydrogels 24

Figure 1.5. Common NO donors and schematic representation of NO donor-doped polymers 34

Figure 1.6. Chemical structures of select NO donor-modified organosilane precursors 36

Figure 1.7. Photomicrographs of Masson's Trichrome or hematoxylin and eosin stained tissue slices adjacent to control or NO-releasing xerogels 38

Figure 1.8. Tissue histology and glucose recovery for control and NO-releasing microdialysis probes 40

Figure 2.1. Amperometric response for NO-releasing needle type glucose sensor after pre-conditioning in PBS 80

Figure 2.2. Representative current trace for glucose biosensor following implantation and distribution of estimated run-in times for NO-releasing and control sensors 84

Figure 2.3. Clarke error grid for MPTMS-RSNO biosensors on day 0 87

Figure 2.4. Comparison of MARD values for NO-releasing and control glucose biosensors 90

Figure 2.5. Estimation of NO-releasing and control sensor lag times via cross-correlation 94

Figure 2.6. Representative post-explantation scanning electron micrographs of glucose biosensor working electrode surfaces 95

Figure 3.1. Nitrogen sorption isotherms for different-sized, unmodified mesoporous silica nanoparticles 115

Figure 3.2. Nitrogen sorption isotherms for 1100 nm AEAP-modified MSNs as a function of AEAP concentration 118

Figure 3.3. Solid-state CP/MAS ^{29}Si NMR spectra of 1100 nm MSNs synthesized at different AEAP concentrations 120

Figure 3.4. Small-angle X-ray scattering profiles for 1100 nm MSNs synthesized at different AEAP reaction concentrations.....121

Figure 3.5. Transmission electron micrographs of different-sized AEAP MSNs 122

Figure 3.6. Scanning electron micrographs of 1100 nm AEAP-modified particles with reactant AEAP concentrations of 11.5 and 14.3 mM.....123

Figure 3.7. Solid-state CP/MAS ^{29}Si NMR spectra of different-sized AEAP-modified particles.....126

Figure 3.8. Small-angle X-ray scattering profiles for different-sized AEAP-modified particles.....131

Figure 3.9. Proposed mechanism for MSN functionalization with aminosilanes.....133

Figure 3.10. Transmission electron micrographs of 150 nm MSNs modified with APTES, BTMS, or MPTMS.....134

Figure 3.11. Real-time NO-release profiles for 30 nm MSNs with different NO donor modifications 139

Figure 4.1. Proposed chemical structures of select silanes modified with either *N*-diazeniumdiolate (MAP, AHAP, DET) or *S*-nitrosothiol (MPTMS) NO donors.....154

Figure 4.2. Inductively coupled plasma optical emission spectrometer instrumental response to sodium silicate standard solutions and silica particle standards prepared in pH 7.4 PBS. 160

Figure 4.3. Scanning electron micrographs of *N*-diazeniumdiolate-modified silica nanoparticles 164

Figure 4.4. Scanning electron micrographs of *S*-nitrosothiol-modified silica nanoparticles.....165

Figure 4.5. Initial NO-release measurements and 1 wk leaching assessment of DET/NO-doped PU membranes.....171

Figure 4.6. Leaching of 800 nm *N*-diazeniumdiolate-modified particles from AL-25-80A PU membranes as a function of aminosilane/NO donor modification 173

Figure 4.7. Leaching of DET/NO particles from AL-25-80A/SG-85A membranes as a function of particle size 174

Figure 4.8. Amperometric glucose response for sensors coated with MPTMS/TEOS-doped HP-93A-100 and PC-3585A topcoat membranes 183

Figure 4.9. Nitric oxide release from HP-93A-100 membranes doped with 75% MPTMS/TEOS particles (33 wt% relative to the PU) and an additional PC-3585A topcoat 184

Figure 4.10. Amperometric signal for sensors coated with MPTMS/HP-93A-100 and PC-3585A topcoat membrane upon immersion in PBS 185

Figure 4.11. Glucose response for sensors coated with MPTMS/TEOS-doped HP-93A-100 and PC-3585A topcoat membranes during 2 wk incubation in PBS.....187

Figure 4.12. Scanning electron micrographs of sensors coated with MPTMS/TEOS-doped HP-93A-100 and PC-3585A topcoat membranes in PBS and in porcine serum 188

Figure 4.13. Glucose response for sensors coated with MPTMS/TEOS-doped HP-93A-100 membranes in PBS and in porcine serum.....189

Figure 5.1. Schematic of NO-releasing subcutaneous implants.....208

Figure 5.2. Initial (1 h) NO release from subcutaneous implants in phosphate buffered saline (37 ^{o}C, pH 7.4).....209

Figure 5.3. Box-and-whisker plot of pigs' post-prandial glucose values before and after streptozotocin administration 212

Figure 5.4. Photomicrographs of hematoxylin and eosin-stained tissues adjacent to implanted control and NO-releasing materials.....214

Figure 5.5. Inflammatory cell densities in the vicinity of control and NO-releasing materials 215

Figure 5.6. Photomicrographs of Masson's Trichrome-stained tissues adjacent to implanted control and NO-releasing materials.....218

Figure 5.7. Collagen density in capsular tissue surrounding control and NO-releasing materials 220

Figure 5.8. Photomicrographs of anti-CD31 and hematoxylin-stained tissues adjacent to implanted DET control and DET/NO materials.....222

Figure 5.9. Blood vessel densities in tissues surrounding DET control and DET/NO materials 223

Figure 6.1. Synthesis of *N*-acetylpenicillamine propyltrimethoxysilane from penicillamine and 3-aminopropyltrimethoxysilane.....238

Figure 6.2. Graph of blood glucose measurements and corresponding CGM trace demonstrating CGM signal attenuation and lag due to slow interstitial glucose transport 244

LIST OF ABBREVIATIONS AND SYMBOLS

~	approximately
^{o}	degree(s)
^{o}C	degree(s) Celsius
>	greater than
$\geq$	greater than or equal to
<	less than
$\leq$	less than or equal to
%	percentage(s)
AP	acetaminophen
APTES	3-aminopropyltriethoxysilane
NH_3	ammonia
NH_4OH	ammonium hydroxide
Å	angstrom(s)
ANOVA	Analysis of Variance
AA	ascorbic acid
Arg-2	arginase enzyme
Ar	argon
HPU	AL-25-80A polyurethane
BET	Brunauer-Emmett-Teller
BG	blood glucose
BJH	Barrett-Joyner-Halenda
BTMS	isobutyltrimethoxysilane
Ca^{2+}	calcium ion (divalent)

cm	centimeter(s)
CTAB	cetyltrimethylammonium bromide
CCL2	Chemokine (C-C motif) ligand 2
CD	cluster of differentiation marker
CGM	continuous glucose monitor
Cu^{+}	copper ion (monovalent)
C	coulombs
CP/MAS	cross-polarization magic angle spinning
d	day(s)
DET	3-(trimethoxysilylpropyl)diethylenetriamine
dia	diameter
DTPA	diethylenetriaminepentaacetic acid
dL	deciliter
DLS	dynamic light scattering
DMF	*N,N'*-dimethylformamide
DX	dexamethasone
L-DOPA	L-3,4-dihydroxyphenylalanine
D_{eff}	effective diffusion coefficient
eNOS	endothelial nitric oxide synthase enzyme
ESEM	environmental scanning electron microscopy
EGA	error grid analysis
et al.	*et alli*; and others
EtOH	ethanol
e.g.	*exempli gratia*; for example
FIR	finite impulse response

FAD	Flavin adenine dinucleotide
FBR	foreign body response
GDH	glucose dehydrogenase
GOx	glucose oxidase
HbA1c	glycated haemoglobin level
g	gravitational acceleration constant
g	gram(s)
Hz	hertz
h	hour(s)
HCl	hydrochloric acid
H_2O_2	hydrogen peroxide
i.e.	*id est*; that is
iNOS	inducible nitric oxide synthase enzyme
ICP-OES	inductively coupled plasma optical emission spectrometry
IC	inflammatory cell(s)
IACUC	institutional animal care and use committee
IL	interleukin(s)
ISO	International Standards Organization
IUPAC	International Union of Pure and Applied Chemistry
IVGTT	intravenous glucose tolerance test
Ir	iridium
kDa	kilodaltons
kg	kilogram(s)
kHz	kilohertz
kV	kilovolt(s)

R^2	linear correlation coefficient
LPS	lipopolysaccharide(s)
MPTMS	(3-mercaptopropyl)trimethoxysilane
MIP-1α	macrophage inflammatory protein 1α
MC	mast cell
$[NO]_{max}$	maximum instantaneous nitric oxide flux
MARD	mean absolute relative deviation
Hg^{2+}	mercury ion (divalent)
MSN	mesoporous silica nanoparticle
MOF	metal-organic framework
MeOH	methanol
MTMOS	methyltrimethoxysilane
MΩ	megaohm(s)
µg	microgram(s)
µL	microliter(s)
µm	micrometer(s)
µM	micromolar
µmol	micromole(s)
m	meter(s)
mg	milligram(s)
mL	milliliter(s)
mm	millimeter(s)
mM	millimolar
mV	millivolt(s)
min	minute(s)

MCM-41	mobil composition of matter
M	molar
mol%	mole percentage(s)
O_2	molecular oxygen
N_2	molecular nitrogen
MCP-1	monocyte chemoattractant protein 1
AEAP	*N*-(2-aminoethyl)-3-aminopropyltrimethoxysilane
AHAP	*N*-(6-aminohexyl)aminopropyltrimethoxysilane
NAPTMS	*N*-acetylpenicillaminepropyltrimethoxysilane
MAP	*N*-methylaminopropyltrimethoxysilane
DBHD	*N,N'*-dibutylhexanediamine
nA	nanoamperes
ng	nanogram(s)
nm	nanometer(s)
nM	nanomolar
nNOS	neuronal nitric oxide synthase enzyme
NO	nitric oxide
NOA	nitric oxide analyzer
NOS	nitric oxide synthase enzyme
NF-κB	nuclear factor kappa-light-chain-enhancer of activated B cells
NMR	nuclear magnetic resonance
ppb	part(s)-per-billon
ppm	part(s)-per-million
PBS	phosphate-buffered saline
Pg	picogram(s)

PDGF	platelet-derived growth factor
Pt	platinum
pHEMA	poly(2-hydroxyethyl)methacrylate
pCBMA	poly(carboxybetaine)methacrylate
PDI	polydispersity index
PEG	poly(ethylene glycol)
PEO	poly(ethylene oxide)
PLLA	poly(L-lactide)/ poly(L-lactic acid)
PLGA	poly(lactic-*co*-glycolic)acid
PTFE	polytetrafluoroethylene
PU	polyurethane
PVA	poly(vinyl alcohol)
pg	picogram(s)
pmol	picomole(s)
RF	radiofrequency
RNS	reactive nitrogen species
ROS	reactive oxygen species
RANTES	regulated on activation, normal T cell expressed and secreted
p/p^0	relative pressure
SNAP	*S*-nitroso-*N*-acetylpenicillamine
RSNO	*S*-nitrosothiol
SEM	scanning electron microscopy
q	scattering vector
s	second(s)
TPU	SG-85A polyurethane

Ag	silver
Ag^+	silver ion, monovalent
AgCl	silver chloride
Ag|AgCl	silver-silver chloride reference electrode
SAXS	small-angle X-ray scattering
NaOMe	sodium methoxide
SCF	stem cell factor
STZ	streptozotocin
SDA	structure-directing agent
TEOS	tetraethylorthosilicate
THF	tetrahydrofuran
$[NO]_T$	total nitric oxide storage
TGF-β	transforming growth factor β
TEM	transmission electron microscopy
TT	TT-2072D-B20 polyurethane
TNF-α	tumor necrosis factor α
FDA	United States Food and Drug Administration
UA	urea
VEGF	vascular endothelial growth factor
vs.	versus
V	volt(s), voltage(s)
v/v	volume/volume
H_2O	water
wk	week(s)
wt%	weight percent

CHAPTER 1. IN VIVO GLUCOSE BIOSENSORS: ROLE OF BIOCOMPATIBILITY ON ANALYTICAL PERFORMANCE[1]

1.1 Diabetes and blood glucose management

Diabetes mellitus is a group of metabolic disorders affecting an estimated 21.9 million people in the United States.[1] Both subclasses of diabetes (e.g., type I/II) result in impaired production of (or resistance to) insulin, a peptide hormone produced by beta cells in the pancreas that aids in distribution of glucose from blood into tissue cells. A common condition associated with diabetes is persistent hyperglycemia (elevated blood glucose, >130 mg dL^{-1})[2] which, if left unmanaged, is responsible for long-term health complications (e.g., retinal failure, kidney disease).[1] Diabetics thus must routinely self-monitor blood glucose (BG) levels and take appropriate therapeutic action (e.g., administer insulin) to avoid hyperglycemia.

Handheld glucometers have proven to be indispensable technologies for personal blood glucose monitoring. Such devices, requiring only ~10 µL blood for accurate glucose determination, provide diabetics with the ability to track trends in blood glucose levels and appropriately adjust insulin, diet, and exercise regimens.[3] Landmark studies have shown that rigorous BG management with glucometer technologies reduce both the morbidity and mortality rates of complications associated with persistent hyperglycemia.[4-6] Despite the obvious benefits

[1]This chapter was adapted in part from articles that have either been submitted for publication or have already been published. The original citations are as follows: (1) Soto, R. J.; Hall, J. R.; Taylor, J. B.; Brown, M. D.; Schoenfisch, M. H. "In vivo chemical sensors: Role of biocompatibility on performance and utility" *submitted.* (2) Soto, R. J.; Schoenfisch, M. H. "Preclinical performance evaluation of percutaneous glucose biosensors: Experimental considerations and recommendations" *Journal of Diabetes Science and Technology* **2015**, *9*, 978–984.

associated with the use of glucometers, BG sampling requires patients to pierce their finger with a lance to obtain blood. The discomfort accompanying blood sampling leads to poor patient compliance and infrequent measurement.[7] Unfortunately, the routine use of glucometers also results in increased propensity for hypoglycemia (i.e., blood glucose <70 mg dL^{-1}), as glucometers provide only static glucose measurements—such devices are incapable of detecting brief, potentially life-threatening hypoglycemic events.[4-6] Although useful for BG monitoring, glucometers alone do not provide the necessary level of diabetes management.

An implantable glucose biosensor that facilitates continuous glucose monitoring (CGM) would be able to achieve meaningful reductions in average blood glucose levels, simultaneously enabling reliable detection of hypoglycemia. To date, the most successful CGM technologies are semi-implantable (i.e., percutaneous) sensors that measure glucose in interstitial fluid, allowing the sensor to be implanted by the user. Several previous studies have shown that intensive glucose monitoring using such devices lowers glycated hemoglobin (HbA1c) levels (an indicator of average BG concentrations) by 0.5–2.0%.[8-10] Importantly, the frequency of hypoglycemia is also reduced compared to patients who self-monitor with portable glucometers.[10-11] Although these studies[8-11] exemplified the capabilities of glucose monitoring systems, poor analytical performance and limited in vivo lifetime (<7 d) due to the foreign body response (FBR) hinder their widespread use. This introductory chapter serves to highlight the current technologies available for in vivo glucose measurement. A mechanistic groundwork relating issues in the analytical performance of glucose sensors to key events in the FBR is also developed.

1.2 Analytical technologies for in vivo glucose measurement

Accurate glucose measurement requires that the employed analytical method distinguishes glucose from other, structurally similar, natural monosaccharides. The most successful strategies rely on glucose-specific recognition elements (e.g., enzymes,[12-14] boronic acid derivatives[15]) that serve as glucose concentration transducers.[16-17] Electrochemical and optical methods are widely utilized for in vivo glucose detection.

1.2.1. Electrochemical glucose detection

Electrochemical glucose sensors represent the most successful technologies to date for glucose measurement.[3] The vast majority of electrochemical assays for glucose (both in vivo and ex vivo) rely on glucose-selective enzyme transducers, such as glucose oxidase (GOx) or glucose dehydrogenase (GDH).[3,16-17] Glucose oxidase is preferred because the enzyme is regenerated by oxygen following reaction with glucose. In contrast, GDH requires low-abundance electron acceptors (e.g., pyrroloquinoline quinone) as co-substrates.[3] In addition, the specificity of GOx (derived from the fungus *Aspergillus Niger*) for glucose is more than three hundred-fold greater than other, structurally similar monosaccharides (e.g., galactose).[13]

$$\mathrm{GOx-FAD+Glucose \rightarrow GOx-FADH_2+Gluconolactone} \quad (1.1)$$

$$\mathrm{GOx-FADH_2+O_2 \rightarrow GOx-FAD+H_2O_2} \quad (1.2)$$

$$\mathrm{H_2O_2 \rightarrow O_2+2H^+ + 2e^-} \quad (1.3)$$

The reaction between GOx and glucose yields the reduced form of the active enzyme center (–$FADH_2$; Equation 1.1). Subsequent reaction with O_2 (the co-substrate for GOx) regenerates the enzyme redox co-factor and produces hydrogen peroxide (Equation 1.2).[7,18] Three general glucose detection schemes have been employed based on these reactions: direct electron transfer from GOx, O_2 reduction, and hydrogen peroxide oxidation (Equation 1.3).

Amperometry is the preferred detection method due to simpler potentiostat hardware, data analysis, and power requirements.[19-31] Of note, low-power instruments for voltammetric glucose measurement were recently described.[32]

Direct electron transfer from GOx to the electrode surface was initially suggested by Heller.[33-34] However, the enzyme redox center (FAD) is significantly removed (tens of Å) from the outer enzyme surface, precluding efficient electron tunneling.[35] Degani et al. proposed that "electrically wiring" the enzyme to the electrode surface would overcome the large energetic barrier to electron tunneling.[33] This concept was realized by using redox mediators (e.g., $[Os(N,N'\text{-dialkylated-}2,2'\text{-biimidazole})_3]^{2+/3+}$) to covalently link GOx to both gold and platinum electrodes.[33] Mao et al. reported another approach for glucose detection based on GOx immobilization in redox hydrogels.[36] Both methods reduced the electrode potential required for electron tunneling (-0.1 V vs silver-silver chloride (Ag|AgCl), 3 M KCl).[36-37] A clear advantage of the lower applied voltage is minimal interference from endogenous electroactive species (e.g., ascorbate). However, the use of heavy metals (e.g., ruthenium, osmium) raises concern regarding toxicity in vivo should such metals leach from the device surface.[38]

Updike and Hicks originally proposed a method for indirect glucose measurement, relying on measurement of O_2 consumed in the reaction with GOx (Equation 1.2).[39] Amperometric oxygen reduction on a GOx-modified platinum electrode (-0.6 V vs. Ag|AgCl) is preferred for glucose detection.[7,12] Unfortunately, fluctuations in tissue oxygen levels can cause sensor drift.[40] A second platinum working electrode is often employed to determine background oxygen levels—in this configuration, the glucose concentration is proportional to the difference in currents measured at the GOx-modified and bare electrodes. Gough and coworkers developed a fully-subcutaneous glucose sensor based on differential oxygen detection at an array of

platinum microdisk electrodes.[19] At least one sensor from an initial pilot study in pigs remained functional for more than a year in vivo. Unfortunately, the accuracy of the device was not assessed in this work. Additionally, the large size of the sensor (3.5 × 1.5 cm) and the need for surgical implantation/removal are shortcomings of this design.

Measurement of hydrogen peroxide production by GOx is the most practical and widely used method for electrochemical glucose measurement in vivo (Equation 1.3). This sensor configuration requires a single working electrode and a combined pseudo-reference/counter electrode. The miniaturized "needle-type" glucose sensor (~1 mm diameter) was first described by Shichiri et al. in 1982 (Figure 1.1).[41] More recently, the size of the sensor was reduced to <300 μm, facilitating self-implantation using similar gauge needles to those used for regular insulin injection.[29] The primary design consideration associated with hydrogen peroxide-detecting sensor designs is limited availability of the GOx co-substrate, oxygen. Tissue oxygen concentrations are ~15-fold lower than analogous glucose levels (4–6 mM).[17,42] As a result, GOx-reaction kinetics (i.e., the rate of hydrogen peroxide production) are oxygen-limited.[43] The oxygen dependence manifests as a non-linear sensor response over physiological glucose concentrations (1–18 mM).[29] This obstacle is generally overcome by application of an outer permselective polymer layer that differentially reduces glucose and oxygen diffusion to the immobilized enzyme.[7,44] Appropriate choice of the polymer identity and membrane thickness ensures that glucose and oxygen concentrations at the enzyme layer are stoichiometrically balanced, thus extending the sensor linear dynamic range. The additional polymer membrane also renders the sensor response reliant on glucose flux rather than GOx reaction kinetics. In turn, dependence of the sensor signal on pH and temperature is reduced.[17]

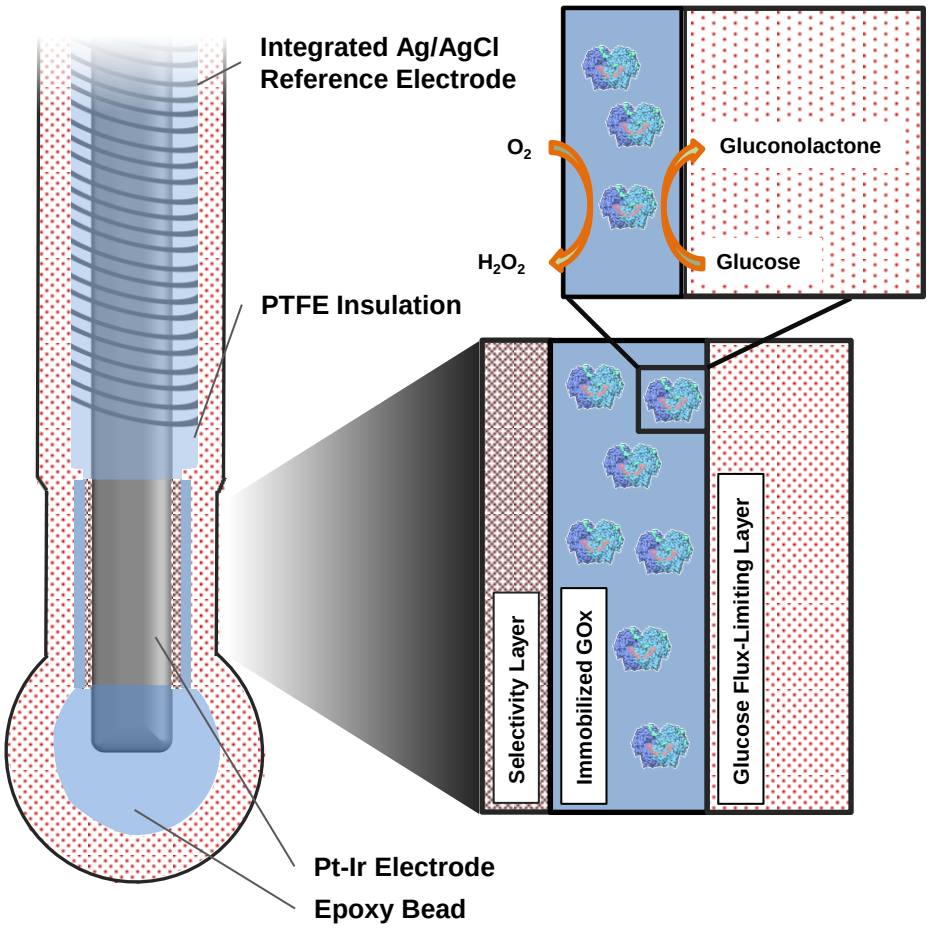

Figure 1.1. Schematic design for the "needle-type" glucose biosensor. The sensor relies on differential glucose and oxygen diffusion through an external flux-limiting layer. The glucose then reacts with immobilized glucose oxidase and, upon regeneration of the enzyme by oxygen, yields hydrogen peroxide. Peroxide is detected at the underlying working electrode (generally a platinum/iridium alloy). The working electrode is electrically isolated from the integrated Ag|AgCl by an insulating layer of polytetrafluoroethylene (PTFE).

The primary disadvantage associated with hydrogen peroxide oxidation is the high required working potentials (+0.6 V vs. Ag|AgCl on platinum) at which other, endogenous redox species (e.g., ascorbate) may also be oxidized.[7] The issue of glucose selectivity has been largely overcome by deposition of additional polymeric layers that obstruct the fluxes of interferents to the sensor surface. For example, cellulose acetate membranes impede ascorbate diffusion via anionic repulsion.[45-46] Electropolymerized films of *m*-phenylenediamine and phenol have been used to impart selectivity for hydrogen peroxide over larger interferents via size-exclusion.[47-50]

1.2.2. Optical glucose detection

Optical approaches to in vivo glucose measurement have also been described, most of which are luminescence-based.[15,51-56] Optical detection schemes display several inherent advantages over electrochemical sensors, including high glucose sensitivity and the possibility of ratiometric detection to offset in vivo signal drift.[51] Several non-luminescence analytical measurement schemes have been reported (e.g., photoacoustic spectroscopy, optical coherence tomography).[38] Glucose detection in subcutaneous tissue can be accomplished directly via visible wavelength fluorescence (excitation 308 nm, emission 340–400 nm).[57] However, this method is nonspecific for glucose. Glucose-specific recognition elements (e.g., proteins, boronic acid derivatives) have been used to improve glucose specificity for fluorescence sensors. Such measurement schemes rely on changes in fluorescence emission or lifetime of a luminescent indicator upon interaction of the recognition element with glucose (typically a binding event). Mansouri et al. immobilized Concanavalin A (a glucose-binding lectin) onto the inner surface of an implantable hollow dialysis fiber.[54] Glucose was measured via a competitive binding strategy using fluorescein isothiocyanate-labeled dextran as the competing ligand. In another approach, Colvin et al. designed a long-term implantable glucose sensor based glucose binding to a

fluorescent boronic acid derivative that was immobilized in a porous polyhydroxyethylmethacrylate hydrogel.[53]

Most glucose binding elements (e.g., Concanavalin A, boronic acid derivatives) do not bind glucose specifically, but are also able to interact with other, structurally similar monosaccharides. For instance, many boronic acid derivatives form strong complexes with galactose and fructose.[58] As a result, luminescence-based glucose sensors are susceptible to interference from other saccharides. A recently reported luminescence glucose sensor made use of GOx as the recognition element to circumvent the issue of poor glucose selectivity.[55-56] The enzyme was co-immobilized in a poly(2-hydroxyethylmethacrylate-*co*-acrylamide) hydrogel with a palladium (II) benzoporphyrin phosphor. This species undergoes luminescence quenching by oxygen. The phosphor is interrogated at 630 nm with changes in local oxygen (via glucose reaction with GOx) altering the phosphorescence lifetime (measured at ~810 nm).[56]

1.2.3. Commercial glucose monitoring technologies

Only two subcutaneous glucose sensors were listed as approved for human use by the U.S. Food and Drug Administration in 2014: Medtronic's Enlite CGM, Dexcom's G5 sensor. Both devices are percutaneous needle-type sensors utilizing hydrogen peroxide oxidation for glucose measurement.[3,59-60] The larger, bulkier electrical components (i.e., potentiostat and radiofrequency data transmitter) are worn externally.[3] A third system (Abbott's Navigator) also resembles the needle-type sensor in physical construction but instead relies on redox mediators to shuttle electrons from GOx to the working electrode.[3,33-34,36-37] The Abbott Navigator CGM is approved for human use in Europe but was discontinued in the U.S. due to issues related to supply and distribution of the CGM components. All three systems (i.e., the Enlite, G5, and Navigator) are associated with error rates of approximately 15% (mean absolute relative

deviation) and are approved for a maximum of 7 d use.[60]

Other, non-invasive CGMs were previously commercialized (i.e., iontophoresis, impedance spectroscopy) but were discontinued due to performance issues.[61-63] For example, a non-implantable sensor based on impedance spectroscopic measurements was approved in Europe in 2003.[7,62] The device interrogated subcutaneous tissue beneath the sensor using 1–200 kHz electromagnetic waves. Glucose levels were measured indirectly by correlation to impedance measurements via principal component analysis.[62-63] However, this method proved unreliable due to the non-specific nature of glucose detection. In addition, changes in skin dielectric properties due to water content and disease state negatively impacted sensor accuracy.[61]

1.3. Foreign body response

A number of miniaturized electrochemical and optical probes meet strict benchtop analytical performance merits required for CGM devices. Unfortunately, sensor function is impeded partially or completely in vivo due to an implant-initiated foreign body response (FBR).[7,44,64-70] This response includes infiltration of the wound (sensor) site by inflammatory cells and the associated wound healing response. Indeed, the FBR may culminate in either persistent inflammation or isolation by a collagenous foreign body capsule, both of which are aberrations in the normal wound healing response (Figure 1.2). A consistent outcome associated with the FBR is poor sensor accuracy and a limited useable lifetime.[7] In the following sections, key inflammatory and tissue reconstruction events during the FBR are considered with respect to their impact on the function of implanted glucose sensors.

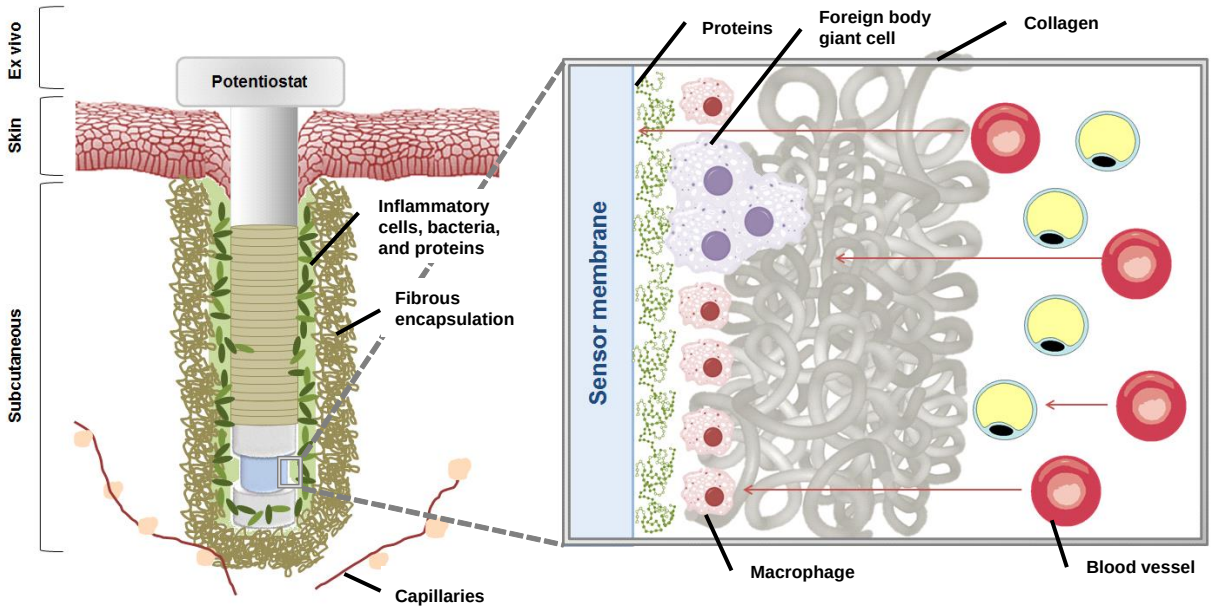

Figure 1.2. Foreign body response to implanted glucose sensors. A classical FBR culminates in the persistence of inflammatory cells (e.g., macrophages, multinucleated giant cells) around the sensor surface for days to weeks. Ultimately, the sensor is sequestered from the surrounding tissue by a dense, avascular collagen capsule. Reprinted with permission from Chemical Reviews, 2013, 113, Nichols, S.P.; Koh, A.; Storm, W. L.; Shin, J. H.; Schoenfisch, M. H. "Biocompatible materials for continuous glucose monitoring devices" pages 2528–2549, Copyright 2013 American Chemical Society.

1.3.1. Foreign body response and glucose sensor analytical performance

The FBR is initiated upon sensor implantation and damaging of vascularized tissue. Rapid accumulation of serum proteins on the sensor surface occurs within seconds of the initial insult—a process termed "protein biofouling." Protein biofouling is believed to be partially irreversible.[71-72] The concentration of surface-bound proteins in the thin adsorption layer may exceed their bulk (solution) concentration, with an adhered protein layer density (typical values of ~1 g protein cm^{-3}) on some classic polymeric surfaces (e.g., polyurethane) approaching that of pure protein (~1.4 g cm^{-3}).[72] A well-known consequence of the accrued protein layer to electrochemical glucose sensors is a loss in analytical sensitivity by up to 40–80%.[73] Mechanistic studies of protein adhesion on biomaterial surfaces indicate that small (<15 kDa) fragments of serum albumin and other large proteins are the primary adsorbed biomolecules.[74] The initial protein biofouling process is heterogeneous. As a result, the specific identities and dynamics of these adherent proteins remain poorly understood. Nevertheless, the composition of the adsorbed protein layer is still considered to at least partially govern the pathology of the implant wound site during subsequent inflammatory phases.[64]

As a result of sensor implantation, platelets aggregate at damaged blood vessel sites to facilitate fibrin clot formation and deter blood loss.[75] Through the release of growth factors (e.g., platelet-derived growth factor, transforming growth factor-β), platelets initiate the accompanying wound healing/inflammatory responses by recruiting circulating cells to the damaged blood vessels.[75] Klueh et al. demonstrated that microhemorrhages, formed via local bleeding at the implant site, resulted in inaccurate glucose biosensor performance.[76] The underlying mechanism of the decreased sensor sensitivity and periods of signal dropout was attributed to glucose and oxygen consumption by erythrocytes around the sensor. Novak and coworkers disputed this

result, clarifying that decreased sensor output is more likely the result of excess glucose metabolism by leukocytes (macrophages). Normal macrophage glucose metabolism (normalized per cell) is >50-fold greater than for erythrocytes.[71] Importantly, Klueh et al.[76] and Novak et al.[71] agreed that microhemorrhages, which may form intermittently as a result of sensor micromotion,[77-78] lead to the observed sensor signal dropout.

Acute inflammation occurs as the initial FBR event during the first several days of implantation, following initial biofouling and provisional matrix formation.[64] Mast cells and neutrophils (phagocytic cells) infiltrate the implant site in an attempt to clear the foreign object.[79] The neutrophilic response is short-lived (24–48 h) but can be quite severe, contingent upon the degree of initial tissue trauma. In one study, Wang and coworkers implanted silicon chips in the subcutaneous tissue of Sprague-Dawley rats using different-sized needles (18, 16, and 14 gauge) and evaluated the FBR at durations between 3 and 30 d using standard tissue histological methods.[80] Implantation of the silicon substrates using a larger needle size (i.e., initial trauma) lead to a more severe 3 d inflammatory response. However, the authors did not observe a significant effect of needle size on the severity of the chronic inflammatory response (>7 d).

If neutrophils are unable to remove the intruding object, the resident mast cells undergo release of cellular vesicles containing histamine and various cytokines/chemokines, including interleukins (IL-4 and IL-13),[64] macrophage inflammatory protein 1α,[81] and monocyte chemoattractant protein 1.[81] Through this degranulation process, mast cells are largely able to orchestrate the recruitment, differentiation, and phenotypes of other inflammatory cells (i.e., monocytes/macrophages), and thus hold considerable sway over the FBR and associated sensor performance. Klueh et al. reported on the performance of glucose sensors implanted for 28 d in mast cell-sufficient and -deficient mouse models.[82] Periods of sensor inaccuracy and signal

dropout were frequently observed in the mast cell-sufficient model, whereas glucose sensors in the mast cell-deficient animals were more consistently able to track physiological glucose fluctuations. Histological analysis of the tissue surrounding the implanted sensors revealed a lessened inflammatory response and minimal collagen encapsulation around the implants in the deficient model at 1–4 wk. A separate report by Egozi and coworkers indicated that the neutrophilic response in a mast cell-deficient mouse model (WBB6F1 Kit^{W}/Kit^{W-V}) was reduced compared to analogous WBB6F1 wild-type mice.[83] Of note, mast cells are also capable of stimulating fibrocyte translocation from blood vessels to the wound site, with potential implications for subsequent collagen deposition and isolation of the sensor from the native tissue.[84] Indeed, Avula et al. showed that collagen deposition was reduced at subcutaneous polyester implants in a mast cell-deficient mouse model (sash model) relative to control mice.[85]

Chronic inflammation and foreign body reactions characterize the host response at $\geq$5 d post-implantation.[64] This period in the FBR strongly correlates with episodes of poor glucose sensor performance due to macrophage infiltration. Until recently, the relationships between macrophage functional polarization (phenotype), glucose metabolism, and in vivo glucose sensor performance were neglected and poorly understood. Macrophages have traditionally been classified as either pro-inflammatory (M1) or anti-inflammatory (M2, with subclasses M2a, M2b, and M2c), although it is now recognized that macrophages retain sufficient phenotypic plasticity to exist in a number of intermediate states between these two extremes.[86-87] Pro-inflammatory macrophages drive the chronic inflammatory response by secretion of pro-inflammatory cytokines and chemokines (e.g., IL-1β, IL-6, IL-12, tumor necrosis factor-α).[88] They also produce a host of reactive oxygen (e.g., hydrogen peroxide, superoxide) and nitrogen (nitric oxide, peroxynitrite, nitrosonium) species (ROS and RNS) via respiratory bursts in the

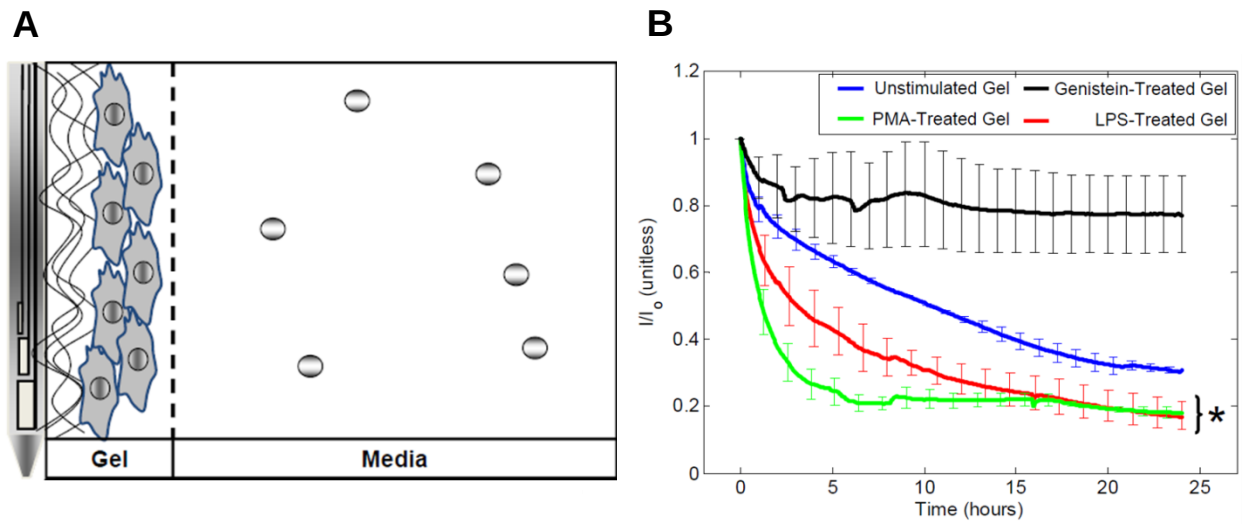

Figure 1.3. (A) Model of macrophage biofouling layer separating the surface of Minimed glucose sensors from the surrounding cell culture solution and (B) decrease in glucose sensor current response (I) normalized to the baseline sensor current (I_0) elicited by macrophages under different stimulating conditions. Macrophages were either unstimulated, induced into a pro-inflammatory state using phorbol myristate or lipopolysaccharide, or polarized to an anti-inflammatory phenotype with genistein. Reprinted from Biomaterials, 2014, 35, Novak, M. T.; Yuan, F.; Reichert, W. M. "Macrophage embedded fibrin gels: An in vitro platform for assessing inflammation effects on implantable glucose sensors" pages 9563–9572, Copyright 2014, with permission from Elsevier.

attempt to destroy the foreign object.[16-17,42,89-91] The local pH can drop to acidic values (~4.0) as a result of macrophage phagocytic activity and exocytosis of acidic phagolysosomes.[42,64] In this respect, GOx activity and associated sensor response are negatively impacted. Excessive macrophage metabolic activity (M1 phenotype) creates glucose and oxygen depletion zones in the direct vicinity of the implant.[71,89,92-93] Klueh et al. reported that large, local macrophage presence at implanted glucose biosensors lead to prolonged (>10 h) periods of signal dropout in mouse implant models.[94] The same authors produced macrophage deficient or depleted mouse models (through selective in-breeding and gene transfection methods, respectively) and demonstrated improved in vivo glucose sensor accuracy and signal stability (i.e., no signal dropout). To more directly examine macrophage metabolism in the context of implantable glucose sensors, Novak and coworkers immobilized RAW 264.7 murine macrophages in a fibrin gel surrounding commercial Medtronic glucose sensors (Figure 1.3A).[93] A pronounced decrease in the sensor signal over the 24 h testing period was attributed to macrophage glucose consumption (Figure 1.3B). The magnitude of this signal decrease was found to be dependent on macrophage phenotypic state; macrophages polarized toward a pro-inflammatory phenotype elicited a larger decrease in the sensor signal (20% of the original glucose signal) than anti-inflammatory macrophages (~80%, similar to gels that did not contain cells). The comparatively large metabolic demands of pro-inflammatory macrophages appear to pose a significant obstacle to accurate in vivo glucose sensing. In addition to creating substantial glucose and oxygen concentration gradients surrounding the sensors, it has been speculated that the analyte levels at the sensor surface do not accurately reflect the true (bulk) analyte concentrations.[95] In contrast, M2 macrophages are characterized by reduced phagocytic capability and glucose/oxygen metabolism,[96] although it is important to note that even macrophages that fall within the M2

designation vary widely in terms of their roles in the FBR.[97] Given that macrophages are primarily responsible for the chronic inflammatory response, macrophage phenotype may be a more reliable indicator of FBR severity than local macrophage densities. Both classically (M1) and alternatively activated (M2/pro-wound healing) macrophages are recognized to stimulate fibroblast activity (i.e., collagen deposition).[98] In particular, expression of transforming growth factor-β by macrophages and FBGCs influences myofibroblast collagen synthesis and deposition.[99] An important distinction between the two traditional subclasses of macrophages is that M1 macrophages are considered anti-angiogenic. In contrast, M2a and M2c macrophages, stimulated via IL-4/IL-13 or IL-10/glucocorticoids/secosteroids respectively, are pro-angiogenic.[100-101]

Macrophages readily adhere to many foreign surfaces through interactions between β1/β2 integrins and surface-bound protein fragments (e.g., Fg fragments) and may remain at the site of an implanted material for months.[102] Failure to initiate or maintain proper adhesion to foreign objects triggers frustrated phagocytosis and fusion into foreign body giant cells, which is likely an attempt to escape apoptosis after surface detachment.[103] These polynuclear cells are characterized with substantial pro-inflammatory character compared to mononuclear macrophages. Giant cell formation further exacerbates local analyte depletion and increases ROS/RNS production with great propensity to damage sensor components and coatings.[104-105] For example, polyetherurethanes—materials that are traditionally used as glucose sensor coatings—are susceptible to stress-cracking and delamination as a result of these intense foreign body reactions,[104-106] both of which are widely accepted mechanisms for in vivo sensor failure.[104]

If unable to digest the implant, macrophages and foreign body giant cells direct the subsequent wound healing/proliferative phases and associated collagen deposition by secreting

growth and angiogenic factors.[75] Collagen deposition, while essential to tissue reconstruction, sequesters the implant from native tissue.[67] It has been recognized since the 1990's that the prototypical foreign body capsule poses a significant diffusion barrier to glucose.[107-109] More recent work using a refined two compartment model for glucose transport dynamics showed that the presence of a dense collagen capsule does not overwhelmingly alter glucose concentrations at the sensor surface (vs. bulk concentrations).[92] Rather, the foreign body capsule increases the tortuosity of the glucose diffusion path from the vasculature to the sensor surface, creating a pronounced lag (on the order of 20–30 minutes) between glucose concentrations at the sensing surface and corresponding plasma levels. Further compounding this issue, the fibrous capsule surrounding the implant is quite avascular,[110] preventing efficient glucose delivery to regions inside the collagen capsule.[111] Kumosa et al. observed that oxygen levels in the tissue surrounding fully subcutaneous O_2 sensors also decrease over the first several weeks of implantation,[20,95] which may further alter glucose sensor response due to limited O_2 (the co-substrate for GOx) availability. Of note, the decreased oxygen levels are more likely due to inflammatory cell metabolism and poor vascularization than obstructed diffusion through the capsule. Notwithstanding, the general consequence of both capsule characteristics (avascularity and collagen density) is that in vivo glucose sensors will ultimately fail for long-term sensing applications (i.e., >7 d) due to inadequate analyte permeability and temporal lag to changing analyte concentrations.[112]

1.3.2. Foreign body response deficiencies associated with diabetes

Although the timeline and specific progression of biochemical events in the FBR have been studied, the impact of diabetes on the FBR remains poorly understood. Qualitatively, external diabetic wounds (e.g., foot ulcers) are characterized by decreased growth factor

production, cellular recruitment, and angiogenesis.[113] Deficient inflammation/wound healing observations are generally extrapolated to include analogous phases in the FBR (i.e., in the presence of a glucose sensor), yet few studies have actually carried out experiments needed to validate these assumptions. This void is partially due to difficulties in producing diabetic animal models that accurately recapitulate FBR in diabetic humans. Animal models of type II diabetes are especially challenging to create, as the disease classification actually encompasses a heterogeneous group of disorders that share the common trait of insulin resistance.[114] Nevertheless, several useful models of type I diabetes have been developed that rely on deficiency/depletion of insulin-producing pancreatic β-cells.[114-115] For example, the non-obese and biobreeding rat models rely on selective inbreeding of diabetic rats. However, larger animal models of diabetes have not been produced through inbreeding. Chemical induction of diabetes has been accomplished by administration of β-cell toxins, such as streptozotocin (STZ), that cause acute β-cell destruction and rapid onset of hyperglycemia. Such methods reliably induce diabetes in both small (e.g., rats, mice) and large animal models (pigs and baboons).[114-116]

Several deficiencies in the FBR have been reported for STZ-induced diabetic animals (relative to wild-type models). For example, Wang and coworkers observed fewer inflammatory cells at subcutaneously-implanted silicon chips in STZ-treated Sprague-Dawley rats (versus healthy controls) over an initial 1 wk implant period.[117] The inflammatory response was similar in both animal models after 14 d, suggesting that diabetes only delayed the inflammatory response. Unfortunately, other key parameters such as collagen deposition and angiogenesis were not evaluated in this work. Soccarrás et al. assessed the FBR to polyetherurethane sponge materials after 10 d implantation in a STZ-treated Wistar rat model.[118] Compared to analogous wild-type rats, tissues in the diabetic rats had fewer inflammatory cells and lower amounts of

collagen. Despite the reduced inflammatory response, tissue concentrations of the pro-inflammatory cytokines MCP-1 and TNF-α were greater in the diabetic rats (~850 and 0.28 pg per gram of wet tissue, respectively) than in controls (~450 and 0.12 pg g^{-1}, respectively). In addition, the authors observed reduced expression of CD-31 (an endothelial cell cluster of differentiation marker), indicating inhibited angiogenesis. In agreement with Wang et al.,[117] Soccarrás et al. also suggested that diabetes delayed the inflammatory response.[118]

The above studies demonstrated the ability to intentionally recreate several diabetes-associated deficiencies (i.e., inflammation and wound healing) in experimental rat models. However, the physiological relevance of the smaller animal models (i.e., rats and mice) to human tissue is still questionable.[119] Indeed, significant differences in subcutaneous tissue physiology exist between humans and mice/rats. Wisniewski et al. quantified the concentrations of glucose, lactate, pyruvate, glycerol, and urea in both human and rat tissue for 8 d using microdialysis and found that absolute analyte concentrations and temporal variations were markedly different between species.[120] In humans, microdialysis glucose recovery increased and eventually stabilized after 4 d, while the glucose recovery for probes implanted in rats steadily decreased for the entire 8 d implantation period. This data indicated a dramatic difference in tissue glucose transport dynamics that the authors attributed in part to the greater proportion of adipose tissue present in human subcutaneous space—more adipose tissue inherently leads to a less severe FBR. The use of larger animal models that more accurately represent human tissue physiology has been proposed in order to obtain translatable sensor performance data. Whereas the rat subcutis is more collagenous, swine in particular possess a tendency to develop significant amounts of adipose tissue.[121] The cutaneous blood supply, dermal thickness, and timeline of wound healing biochemical events in pigs are also more comparable to humans, suggesting

excellent utility as a FBR model.[121]

1.4. Material strategies to mitigate the foreign body response

Strategies to improve the function of implantable glucose sensors are largely directed at mitigating or avoiding key events in the FBR.[122-123] Classically, the FBR has been studied as a function of implant surface chemistry.[64,69,102-105,124-127] A simple but useful biocompatibility principle that was established early on is that hydrophobic surfaces, such as polystyrene, generally promote a more severe FBR (i.e., greater degrees of macrophage adhesion and frustrated phagocytosis) than hydrophilic surfaces (e.g., polyacrylamide).[69,103] However, increased production of pro-inflammatory cytokines was routinely observed on hydrophilic surfaces and was speculated to offset the benefits of any reduced cellular response. As such, proper choice of implant materials/composition alone has not mitigated the FBR to an extent that would benefit the analytical performance of in vivo glucose sensors. The most successful recent tissue biocompatibility strategies, discussed below, aim to simultaneously reduce inflammation and guide appropriate wound healing around the implanted sensor.

1.4.1. Zwitterionic polymers

The initial event experienced by an in vivo glucose sensor is the adhesion of serum proteins to the sensor surface. In addition to reducing glucose sensor sensitivity,[73] proteins and protein fragments that accumulate on the sensor serve as anchors for cell attachment during the ensuing inflammatory phases.[64] Strategies that prevent, or at least mitigate, protein adsorption have thus been postulated to improve the overall host response by reducing cellular adhesion. Certain neutral hydrophilic polymers, namely poly(ethylene glycol) (PEG), poly(ethylene oxide) (PEO), and polyamides, have long been recognized for their resistance protein adsorption relative to other polymeric materials.[128-130] Among these materials, PEG has been the most

frequently investigated due to ease of synthesis and low-fouling characteristics—however, in vivo degradation/oxidation has limited its usefulness for in vivo glucose sensing.[131]

The use of zwitterionic polymers (notably those prepared from monomer units of carboxybetaine, sulfobetaine, and phosphobetaine) has received greater attention recently, as these polymers have been shown to both adsorb only trace quantities of protein (<10 ng cm^{-2} in blood plasma).[128-130,132] Zwitterionic polymer surfaces are characterized with a strongly-associated water layer, stabilized by ionic and hydrogen-bonding interactions between the electrically charged polymer head groups and water molecules in solution.[96,133-135] In turn, the surface hydration layer presents an energetic barrier to biomolecule adhesion. Recent evidence suggests that zwitterionic polymeric biomaterials reduce the FBR by mitigating the extent of initial protein biofouling. In an initial study, Zhang and co-workers implanted cross-linked poly(carboxy betaine)methacrylate (pCBMA) and poly(hydroxyl-2-ethyl)methacrylate (pHEMA) hydrogels in mice.[136] The zwitterionic pCBMA materials elicited reduced collagen encapsulation and greater blood vessel densities at 4 and 12 wk post-implantation relative to the neutrally-charged pHEMA hydrogels. Macrophages surrounding the implants at 4 wk were characterized using immunofluorescence to assess phenotypic state. In general, the macrophages surrounding the pHEMA hydrogels expressed greater levels of classical markers of inflammatory activity (iNOS, tumor necrosis factor-α, IL-12), whereas the cells surrounding the pCBMA implants expressed greater levels of pro-wound healing and anti-inflammatory markers (arginase and IL-10). Of note, the favorable FBR observed for these materials appeared to be sensitive to the CBMA content of the hydrogels. Previous studies by the same group indicated that hydrogels formed from copolymers of CBMA and HEMA (~80 mol% CBMA) elicited a similar FBR relative to pHEMA hydrogels in terms of collagen and inflammatory cell densities.[137] Despite

reduced FBR via pCBMA materials, no reports to date have studied the utility of such biomaterials for improving in vivo glucose sensor performance.

1.4.2. Porous and nanopatterned coating materials

As most surface chemical approaches do not appreciably influence the FBR, researchers have investigated the influence of porosity and surface topography on cellular behavior.[138] The most successful illustrations of this approach are porous coatings that have been known to reduce the FBR to implants for more than two decades. Brauker et al. published a seminal report describing the FBR to several commercial polymers (cellulose, polytetrafluoroethylene, and acrylic copolymer) with pore sizes in the range of 0.02–15 μm.[139] Vascular structures were consistently observed at large-pore (>0.8 μm) materials that enabled cellular infiltration, irrespective of the chemical composition of the membranes. Neovascularity was enhanced by a factor of 80–100 for polytetrafluoroethylene membranes with a nominal pore size of ~5 μm versus membranes with sub-cellular pore sizes (0.02 μm). Subsequent investigations by Sharkawy and coworkers began to elucidate the mechanisms through which porosity and improved FBR outcomes could impact the performance of in vivo glucose sensors.[107-109] In the first of these studies, stainless steel cage implants were coated with either nonporous or porous (60 and 350 μm pores) poly(vinyl alcohol) (PVA) and implanted in rat subcutaneous tissue for tissue histology assessment after 3 and 12 wk.[107] Whereas a thick, dense, avascular collagen capsule was observed immediately proximal to the nonporous PVA implants, both porous PVA coatings increased angiogenesis and decreased collagen density. Carefully removed tissue samples adjacent to the implants were used to study fluorescein diffusion through the collagen capsule (as a surrogate for glucose). The measured effective diffusion coefficient (D_{eff}) for fluorescein through the capsule surrounding nonporous PVA implants was lower (1.11×10^{-6} cm^2

s^{-1}) than in subcutaneous tissue alone (2.35×10^{-6} cm^2 s^{-1}). In contrast, tissues surrounding the 60 and 350 μm porous PVA implants had diffusion coefficients that were more in line with native tissue (2.19×10^{-6} and 1.87×10^{-6} cm^2 s^{-1}, respectively) because of the reduced collagen density. In a follow-up study, tissue response times to changing plasma concentrations of a fluorescent tracer analyte (lissamine-rhodamine) were examined in capsular tissue surrounding the PVA-coated implants.[108] As expected, the tissue surrounding 60 μm porous PVA-coated implants responded more quickly to changes in tracer concentrations than in capsules surrounding nonporous PVA materials (~12 and 34 minutes, respectively), implicating neovascularization as an additional key parameter in tissue analyte transport.

Koschwanez and coworkers examined the effects of porosity on the FBR using commercial (Medtronic) glucose sensors.[140-141] Sensors were modified with porous poly(L-lactide) (PLLA) coatings (~30 μm average pore sizes) produced via a salt-leaching method. Histological evaluation of the tissue surrounding the porous implants after 2 wk implantation in rats revealed increased blood vessel formation in the vicinity of the implant relative to the tissue adjacent to nonporous control materials (221 and 152 vessels mm^{-2}, respectively).[141] Greater total collagen was measured at the porous coatings versus controls (53 and 25%, respectively) as well, although the collagen inside the pores was less dense. The authors initiated in vivo sensor analytical performance evaluation studies as a function of coating porosity but did not observe significant differences between porous versus nonporous PLLA-coated sensors. They hypothesized that micromotion of the percutaneous sensors may have been a convoluting variable responsible for this result. Alternatively, the increased total amounts of collagen at the porous PLLA-coated sensors may have offset the beneficial effects of increased angiogenesis.

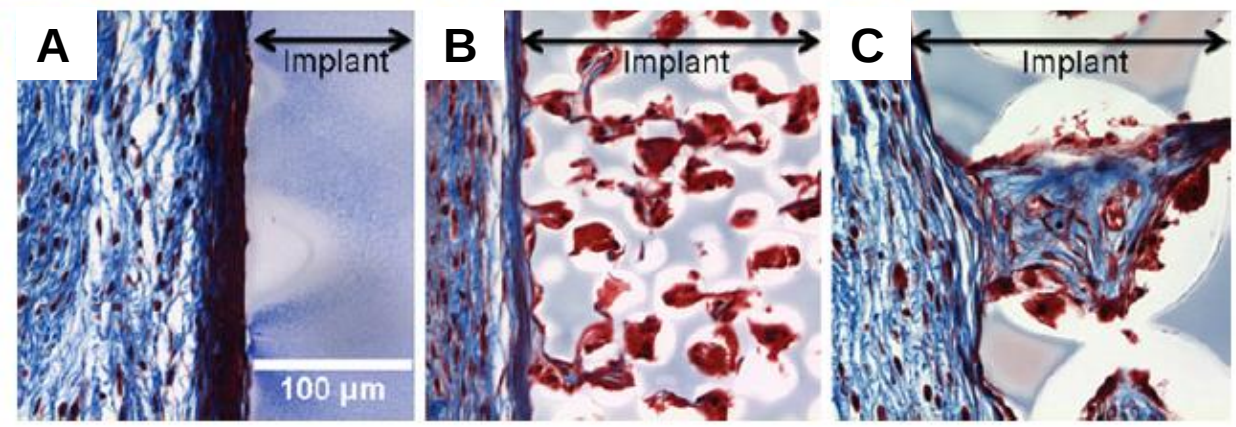

Figure 1.4. The cellular and collagen composition of the foreign body reaction to solid and porous implants is pore-size dependent. Representative Masson's Trichrome photomicrographs show histological responses based on pore size. Collagen is shown in blue, cellular cytoplasm in red, and cell nuclei in black. (A) non-porous implants have a dense FBC at the implant edge, (B) 34 µm porous scaffolds have highly cellular infiltrate, and (C) 160 µm porous scaffolds have a cellular infiltrate that is much richer in collagen than 34 µm scaffolds. Reprinted from *Annals of Biomedical Engineering*, "Porous implants modulate healing and induce shifts in local macrophage polarization in the foreign body reaction," 42, 1508–1516 by Sussman, E. M.; Halpin, M. C.; Muster, J.; Moon, R. T.; Ratner, B. D. Copyright Annals of Biomedical Engineering 2013, with permission of Springer.

The underlying biological mechanisms and optimal porosity levels were not systematically studied by Koschwanez et al.[140-141] due to pore size heterogeneity resulting from the salt-leaching process. Materials with spherical, uniform pore sizes—produced by sphere templating methods—have since been used to study the FBR.[142-144] Sussman and coworkers used monodisperse ~34 and 160 μm diameter poly(methyl methacrylate) beads as templates for pHEMA hydrogel fabrication.[144] After bead removal in a subsequent Soxhlet extraction step, the resulting porous pHEMA hydrogels were used to examine a potential relationship between pore size and FBR severity in mice. As shown in Figure 1.4, the inability of cells to migrate into the nonporous pHEMA coatings resulted in dense collagen deposition immediately adjacent to the material-tissue interface (Figure 1.4A). In contrast, minimal collagen encapsulation and angiogenesis were hallmarks of the tissue reactions at pHEMA implants with pore sizes on the order of cellular dimensions (~34 μm; Figure 1.4B). Large-pore materials (~160 μm) invoked a more classical FBR, with heavy collagen deposition inside the pores (Figure 1.4C). Other studies by Ratner and coworkers have established favorable FBR outcomes for porous materials with pore sizes on the order of cellular dimensions (~10–20 μm for most leukocytes) irrespective of the identity of the polymer.[145] The prevailing hypothesis is that the inability of phagocytic cells (i.e., macrophages) to spread on the material directs them to a more reconstructive M2 phenotype.[145-146] Of note, FBR-mitigating pore sizes reported by Brauker et al.,[139] Sharkawy et al.,[107-109] and Koschwanez et al.[140-141] are similar to the optimal pore sizes reported by Ratner's group.

Although the porous materials described above unequivocally influence the FBR, work to develop porous sensor membranes for implantable chemical sensors has been scarce, likely due to difficulties associated with thin coating deposition on the sensors and/or potential sensor-

material incompatibilities (e.g., high temperatures associated with Soxhlet extraction and GOx instability). Electrospinning of polymer solutions represents an alternative approach to fabricating porous sensor membranes. The process of forming nanofibrous polymer mats by electrospinning is straightforward, requiring readily available experimental components (i.e., a syringe pump, high voltage power supply, and metal object to serve as a grounded collector).[147] The electrospinning process is typically carried out by applying a high voltage (>5 kV) to a polymer solution droplet at the tip of a metal needle. Repulsive electrostatic forces within the droplet exceed attractive surface tension forces, resulting in the formation of a Taylor cone. The polymer solution stream accelerates toward electrical ground and, upon solvent loss during flight, solidifies into nanofibers that accumulate on the grounded metal collector.[147-148] Although the polymer fibers formed by this method are generally polydisperse with respect to fiber diameter, both the fiber size (0.01–10 μm) and porosity of the resulting fiber mats (30–95%) can be controlled by appropriate selection of solution composition (e.g., polymer concentration, polymer identity, conductivity, viscosity) and electrospinning parameters (e.g., voltage, tip-to-collector distance, collector geometry, humidity).[147-148]

Analogous to the porous materials produced by salt-leaching and sphere-templating methods, electrospun fiber mats are also associated with a reduced FBR.[149] Optimal tissue responses have proven to be dependent on a number of material parameters of the fibers, including polymer identity and fiber/pore size. Garg and coworkers recently studied how the pore size of electrospun polydioxanone fibers impacted the phenotypes of primary mouse macrophages.[150] Macrophages cultured on electrospun fiber mats with ~15 μm pores expressed 2–3 fold greater levels of the M2 (anti-inflammatory) marker arginase relative to the macrophages on fibers with smaller pores (~1 μm). In contrast, expression of iNOS, a classic

pro-inflammatory marker, was elevated for macrophages seeded on the 1 μm pore size fiber mats versus macrophages on the larger pore size material. The authors also examined the ability of the polydioxanone fiber mats to influence the phenotypes of macrophages that were pre-polarized to either M1 or M2 states by stimulation with interferon-γ or a cocktail of IL-4/IL-13, respectively. Although the initial macrophage phenotype did impact arginase/iNOS expression, fibers with 15 μm pores consistently yielded macrophages with reduced pro-inflammatory character (i.e., greater arginase/iNOS ratios).[150] Based on these results, pore sizes on the order of cellular dimensions (2–20 μm) appear to mitigate the FBR by forcing macrophages and other inflammatory cells to adopt more reconstructive phenotypes.[151]

Initial work indicates that the orientation of electrospun fibers also appears to be a strong determinant of the FBR. Cao et al. reported that aligned electrospun poly(caprolactone) fibers (~300–500 nm diameter) facilitated greater in vivo cell migration into the fibers compared to randomly oriented fibers in a rat subcutaneous FBR model. Tissue surrounding the aligned fibers consistently exhibited lower grades of inflammation at 1–4 wk post-implantation compared to the tissue at random nanofiber scaffolds. Irrespective of fiber alignment, both types of fibers elicited a 75–90% decrease in collagen capsule thickness (compared to polymeric films) after 4 wk implantation.[152]

The electrospinning process is amenable to modifying electrochemical glucose biosensors.[22,153] Wang et al. coated epoxy polyurethane fiber mats onto miniaturized glucose sensors using a modified electrospinning setup in which the sensor was fixed onto a rotating mandrel that served as the grounded electrospinning collector.[153] The sensors retained suitable glucose sensitivity and linear dynamic range (2–30 mM) at coating thicknesses of ~40–50 μm. Although the authors demonstrated the ability to successfully modify glucose sensors with

electrospun fibers, potential benefits to in vivo glucose sensor analytical performance have not been reported.

1.4.3. Release of tyrosine kinase inhibitors

Tyrosine kinases are a class of enzymes involved in phosphorylation and signal transduction for many biochemical cascades. For instance, the tyrosine kinase KIT (also identified as CD117) serves as a binding receptor for stem cell factor (SCF), an important mast cell growth factor and activator.[154] Inhibition of the SCF-KIT pathway limits production of histamine and the pro-inflammatory cytokine IL-4 by mast cells, suggesting suppressed degranulation.[155] As outlined in Section 3, mast cells play a crucial role in determining the chronic inflammatory response to implanted sensors.[156] Of note, Klueh et al. examined the roles mast cells in the FBR using a mast cell-deficient mouse model (WBB6F1 KIT^{W}/KIT^{W-V}) produced by selective mutation to the gene encoding KIT.[82] The mast cell-deficient mice consequently produced a milder FBR relative to wild-type mice.

As mast-cell deficiency has been shown to improve the accuracy of in vivo glucose sensors,[156] the release of mast cell inhibitors from the surface of glucose sensors may represent a promising approach for improving in vivo sensor analytical performance. Grainger and coworkers have begun to study the impact of the KIT inhibitor masitinib on tissue biocompatibility.[85,157-158] Avula et al. synthesized masitinib-releasing poly(lactic-*co*-glycolic acid) (PLGA) microspheres using an oil-in-water/solvent evaporation method.[158] The PLGA microspheres were doped into poly(ethylene glycol)/poly(ethylene oxide) membranes and shown to release ~11.2 μg masitinib at near-constant rates for up to 30 d.[85,157-158] Such polymers reduced collagen deposition at the subcutaneous implants by 75–90% in wild-type mice. Of note, the masitinib release did not reduce collagen encapsulation in mast cell-deficient mice,

demonstrating masitinib selectivity toward mast cells.[85,158] In a separate study, Avula et al. fabricated electrochemical glucose sensors using the masitinib-releasing coatings. [157] The signal stability of the masitinib-releasing glucose sensors was enhanced versus controls over a 21 d implantation period in mice. Although these results are initially encouraging, the authors did not assess the accuracy of the sensors. In addition, optimal rates and amounts of masitinib (in relation to sensor performance) remain unclear.

1.4.4. Dexamethasone release

Dexamethasone (DX), a synthetic anti-inflammatory glucocorticoid hormone, was one of the initial release agents used to potentially improve the performance of implantable glucose sensors.[7] Dexamethasone is a potent agonist for the cytosol-localized glucorticoid receptor that, upon DX binding, translocates to the cell nucleus and achieves its anti-inflammatory effects in part through transactivation/transrepression of key chemokines and cytokines (e.g., IL-1, nuclear factor κB, activating protein-1).[159-160] Although the mechanisms of DX's anti-inflammatory action have not been fully elucidated, DX is also known to subdue production of other pro-inflammatory mediators (e.g., tumor necrosis factor-α, IL-6) through other, indirect pathways.[161]

A significant concern associated with DX release is systemic immune suppression. Hori et al. implanted DX-loaded sponges in the subcutaneous tissue of rats and observed indicators of a compromised immune system (i.e., thymus and spleen weight loss) at daily doses of 5–50 μg DX per implant, even though the DX was administered locally.[161] Of note, DX doses lower than 0.5 μg per day did not elicit noticeable immunosuppression. Several years following this report, Ward and coworkers investigated the required DX release amounts and rates for achieving localized anti-inflammatory action without causing immune suppression in Yucatan-minipigs.[162] Mock sensors were coupled to an osmotic pump that delivered DX/saline to the subcutaneously-

implanted sensor at pre-determined doses (0.7, 0.28, 0.168, 0.1, or 0.05 mg kg^{-1} over 28 d). Doses <0.1 mg kg^{-1} did not incite systemic immune suppression, as illustrated by serum cortisol levels that were similar to those before DX administration. In contrast, DX doses exceeding 0.1 mg kg^{-1} produced a noticeable decrease in cortisol concentrations. Based on histological analysis of tissues surrounding the implants, it was concluded that the lower DX doses were still sufficient to reduce granulocyte densities at 28 d post-implantation, although the macrophage response was only lessened at DX doses greater than 0.1 mg kg^{-1}.

It is clear from the investigation by Ward et al. that achieving localized anti-inflammatory effects without causing systemic immune suppression requires slow, precisely-controlled DX release.[162] Patil et al. developed DX-loaded PLGA microspheres capable of slow hydrolysis in physiological buffer, enabling DX release.[163] The PLGA microspheres were immobilized in poly(vinyl alcohol) hydrogels that were shown to release ~4 μg DX per implant over 28 d. These hydrogels were then implanted into the subcutaneous space of rats for histopathological FBR evaluation. Regardless of the implant time (1–28 d), the authors reported reduced inflammatory cell densities at the DX-releasing hydrogels relative to control gels.

An additional concern that is routinely observed in tissue studies of DX-releasing materials involves inhibited angiogenesis.[164-166] Proposed strategies for overcoming DX-induced ischemia have revolved around the concurrent release of endogenous angiogenic stimulators, including vascular endothelial growth factor (VEGF)[164,167-168] and platelet-derived growth factor (PDGF).[168] However, growth factor release strategies are not straightforward due to issues with stability and controlled delivery.[169] Price and coworkers suggested the use of L-3,4-dihydroxyphenylalanine (L-DOPA) as a more reliable alternative to either VEGF or PDGF.[169] Using a chlorioallantoic membrane model, the authors demonstrated that DX that was released

from a hydrogel inhibited angiogenesis, but simultaneous delivery of DX and L-DOPA increased the formation of blood vessel sprouts relative to controls (i.e., hydrogels that did not contain DX or L-DOPA). While initial results appear promising, achieving optimal delivery rates of both species from sensor coatings remains an arduous task.

Despite the promising histological and immunohistochemical data involving DX-release strategies, few reports have demonstrated improvements to glucose sensor analytical performance. Klueh et al. implanted electrochemical glucose sensors into the subcutis of mice and evaluated the influence of daily intraperitoneal DX injections (1, 6, or 10 mg kg^{-1}) on sensor performance.[170] The glucose sensitivity of control sensors degraded rapidly almost immediately after implantation (<1 nA mM^{-1}), with total loss of the glucose response of the sensor within ~24 h. DX treatment helped maintain glucose sensitivity for up to 7 d (3–20 nA mM^{-1}). Histological analysis of tissue samples from the implant site confirmed that a reduced inflammatory response was at least partially responsible for the improved sensor function. The promising sensor performance data notwithstanding, systemic DX administration in this manner is not a viable approach for improving device function outside of the research setting.

1.4.5. Nitric oxide release

Nitric oxide (NO), an endogenously-produced, reactive diatomic gas, is involved in hemostasis,[171] angiogenesis,[172] inflammation,[90,173-174] neurotransmission,[175] and wound healing.[176-177] The biosynthesis of NO occurs through the metabolism of L-arginine to L-citrulline via one of three isoforms of nitric oxide synthase (NOS): endothelial NOS (eNOS), inducible NOS (iNOS), and neuronal NOS (nNOS).[178] The eNOS and nNOS isoforms are generally categorized as lower NO production enzymes (compared to iNOS), requiring elevated concentrations of Ca^{2+} (>70–100 nM) that facilitate binding of the enzymatic co-factor

calmodulin.[179] As such, both eNOS and nNOS transiently produce ~nM concentrations of NO (bursts of several minutes in duration) for homeostatic processes such as blood pressure regulation and neurotransmission.[178] The endothial NOS isoform is expressed by endothelial cells and platelets, whereas nNOS is expressed in the brain and skeletal muscle.[180] The third isoform, iNOS, is not constitutively expressed in tissue but rather produced by immune cells (e.g., macrophages, mast cells) in response to various stimulating factors, including lipopolysaccharides, interferon-γ, and nuclear factor κB.[181-182] Calmodulin binding for iNOS is less sensitive to intracellular Ca^{2+} levels and occurs at normal resting cell Ca^{2+} levels (70–100 nM).[179,181] Thus, iNOS activity is largely independent of intracellular calcium and is capable of continuous, high-output (~μM) NO production, primarily as a defense against foreign pathogens.[181]

Although NO has traditionally been viewed as an antimicrobial molecule with respect to its function in the FBR,[90] evidence suggests that NO may also regulate the recruitment of cells to the implant site during the acute inflammatory response.[176] The mechanisms for NO's involvement in chemotaxis are not fully understood. However, NO is known to alter expression of key inflammatory cell mediators and growth factors, including tumor necrosis factor-α,[183-184] chemokine (C-C motif) ligand 2,[183] RANTES,[185] IL-1β,[183,186] and IL-6.[184] On the other hand, the involvement of NO as an angiogenic agent during tissue reconstruction has been well-studied. Angiogenesis during the reconstructive end-stages of the FBR requires NO derived from eNOS.[172] Angiogenic factors, such as VEGF and transforming growth factor β, stimulate NO production.[187-188] Nitric oxide may also upregulate VEGF via a positive feedback loop.[189]

1.4.5A. Nitric oxide-release strategies

The anti-inflammatory and pro-angiogenic capacities of NO indicate that NO-releasing materials may prove useful for mitigating the FBR and improving the analytical performance of tissue-implanted glucose sensors. However, localized NO delivery from in vivo sensors is not straightforward due to NO's reactive nature and short lifetime in vivo. The most successful NO-release strategies have relied on the use of NO donors (e.g., *N*-diazeniumdiolates or *S*-nitrosothiols) as dopant molecules within polymeric sensor coatings (Figure 1.5). The NO donors are purposefully selected for their ability to undergo chemical breakdown reactions via specific physiochemical triggers with ensuing NO release. *N*-diazeniumdiolates, formed by the base-catalyzed reaction of secondary amines with gaseous NO, degrade upon protonation of the amine coordinating the NO donor to yield two moles of NO and the regenerated parent amine. The rates of NO production in physiological buffer are predictable and dependent on solution pH, temperature, and the chemical structure of the precursor amine.[190] The tunable decomposition rates render *N*-diazeniumdiolates the most frequently investigated class of NO donors for applications in NO release. *S*-nitrosothiols (RSNOs), an alternative NO donor, are readily synthesized by reaction of thiols with nitrosating reagents (e.g., acidified sodium nitrite). A number of endogenous RSNOs (e.g., *S*-nitrosoglutathione) serve as NO transporters that augment NO's in vivo lifetime.[191-192] Light (330–350 and 550–600 nm for primary RSNOs) and thermal irradiation both serve as RSNO decomposition triggers, causing homolytic cleavage of the S–N bond to yield NO and thiyl radicals.[192] Several transition metal ions (Cu^{+}, Ag^{+}, and Hg^{2+}) undergo irreversible catalytic redox reactions with RSNOs to generate NO.[193] *S*-nitrosothiol decomposition and concomitant NO release in vivo occurs primarily through thermal methods.

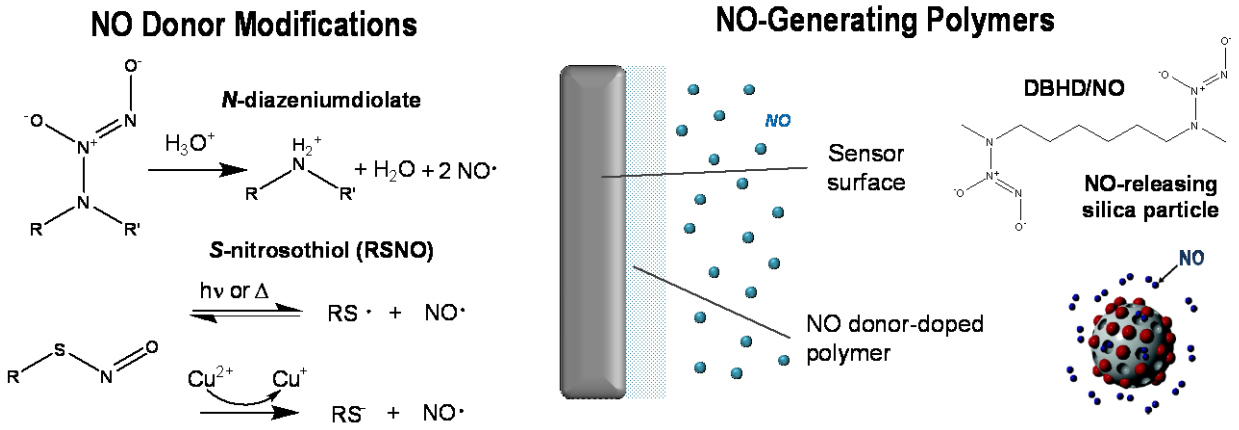

Figure 1.5. Common NO donors and schematic representation of NO-doped polymer membranes that have been utilized for in vivo glucose sensors.

Small molecule NO donors have been extensively utilized as dopants in sensor membranes for improving the in vivo analytical performance of ion, oxygen, glucose, and lactate sensors.[194-198] Early work relied on small molecule *N*-diazeniumdiolates (e.g., (*Z*)-1-[*N*-methyl-*N*-[6-(*N*-methylammoniohexyl)amino]]diazen-1-ium-1,2-diolate)[196] to prevent platelet adhesion and thrombus formation on intravascular sensors. The success of these initial biocompatibility reports notwithstanding, NO donor leaching from the sensor membranes was identified as a concern for reasons including undesirable formation of toxic *N*-nitrosamine species on the parent amines.[199] In recent reports by the Meyerhoff research group, a more lipophilic NO donor (*N*-diazeniumdiolate-modified *N,N'*-dibutylhexanediamine) has been utilized to limit NO donor leaching from NO-releasing polymer membranes.[197,200] A number of macromolecular NO-release scaffolds have also been developed to avoid concerns over *N*-nitrosamine mutagenicity, including silica xerogels,[201-202] gold[203-204] and silica nanoparticles,[192,205-206] organic dendrimers,[207-208] and liposomes.[209] In particular, silica materials (i.e., xerogels and nanoparticles) have proven useful because they are functionalized through straightforward silane chemistries to store and release NO.[192,205,210-211] A diverse selection of secondary amine- and thiol-containing organosilanes are available, allowing for tunable NO-release kinetics based on the chemical structure of the silane reagent (Figure 1.6). For example, the *N*-diazeniumdiolate form of *N*-(6-aminohexyl)aminomethyltrimethoxysilane (Figure 1.6A) decomposes rapidly (NO-release half-life ~3 min) in phosphate buffered saline (PBS; pH 7.4, 37 ^{o}C).[212] In contrast, the *N*-diazeniumdiolate modification on *N*-(2-aminoethyl)-3-aminopropyltrimethoxysilane (Figure 1.6C) is stabilized by the peripheral primary ammonium ion, leading to more extended NO release (NO-release half-life ~120 min in PBS).[201,212]

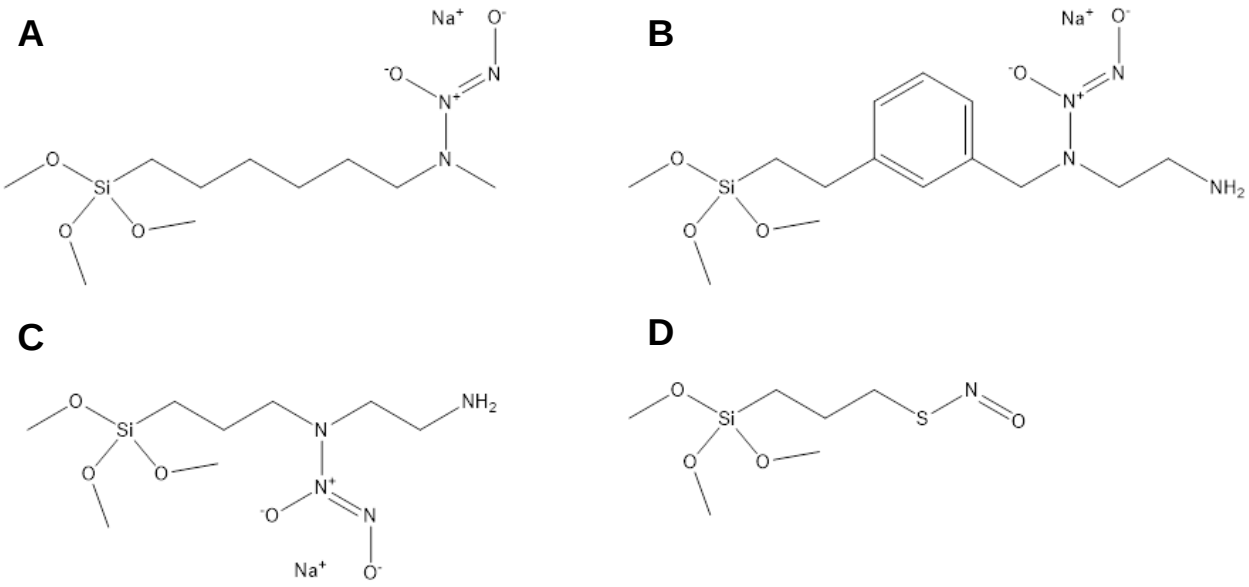

Figure 1.6. Chemical structures of select NO-donor modified organosilane precursors. The sodium-stabilized salts of *N*-diazeniumdiolate-modified silanes are shown for (A) *N*-(6-aminohexyl)aminomethyltrimethoxysilane, (B) *N*-[4-[2-(trimethoxysilyl)ethyl]benzyl] ethylenediamine, and (C) *N*-(2-aminoethyl)aminopropyltrimethoxysilane. (D) is the *S*-nitrosothiol-modified form of 3-mercaptopropyltrimethoxysilane.

Shin et al. initially developed NO-releasing silica xerogels for use as glucose biosensor coatings.[23] However, the *N*-diazeniumdiolate formation reaction necessitated exposure of the underlying glucose oxidase layer to high pressures of NO, resulting in enzyme deactivation. To avoid compromising the stability of the enzyme, Koh et al. synthesized smaller NO-releasing silica nanoparticles (with diameters in the range of 100 nm–1 μm) for use as polyurethane (PU) sensor membrane dopants.[21-23] The authors demonstrated control over membrane NO-release kinetics based on either the type of NO-releasing silica particle or the identity of the polyurethane. Glucose sensor analytical performance (i.e., sensitivity and linear dynamic range) was also dependent on polyurethane identity (i.e., water uptake) and membrane thickness. Despite promising initial results, later research indicated that the particles were prone to leaching from the sensor membranes[205,213] with the potential to aggravate the FBR.[206,214-215]

1.4.5B. Subcutaneous tissue biocompatibility of nitric oxide-releasing materials

Hetrick and coworkers were the first to establish the viability of NO release as a strategy for mitigating the FBR using NO-releasing silica xerogels.[216] A co-condensation reaction was initially carried out between isobutyltrimethoxysilane and *N*-(6-aminohexyl)aminopropyltrimethoxysilane to form the silica xerogel. The secondary amines within the xerogel were subsequently reacted with NO to form *N*-diazeniumdiolate NO donors. The tissue biocompatibility of these coatings was then evaluated in the subcutaneous space of a rodent model. After 3 and 6 wk implantation periods, tissue histology indicated that the NO-releasing xerogels, which released 1.35 μmol NO cm^{-2} over 72 h, decreased inflammatory cell density and collagen capsule thickness/density immediately adjacent to the implants (Figure 1.7). Quantitative immunohistochemistry for CD-31 (an endothelial cell adhesion molecule) revealed greater vascularization (angiogenesis) at both 1 and 3 wk for the NO-releasing substrates relative

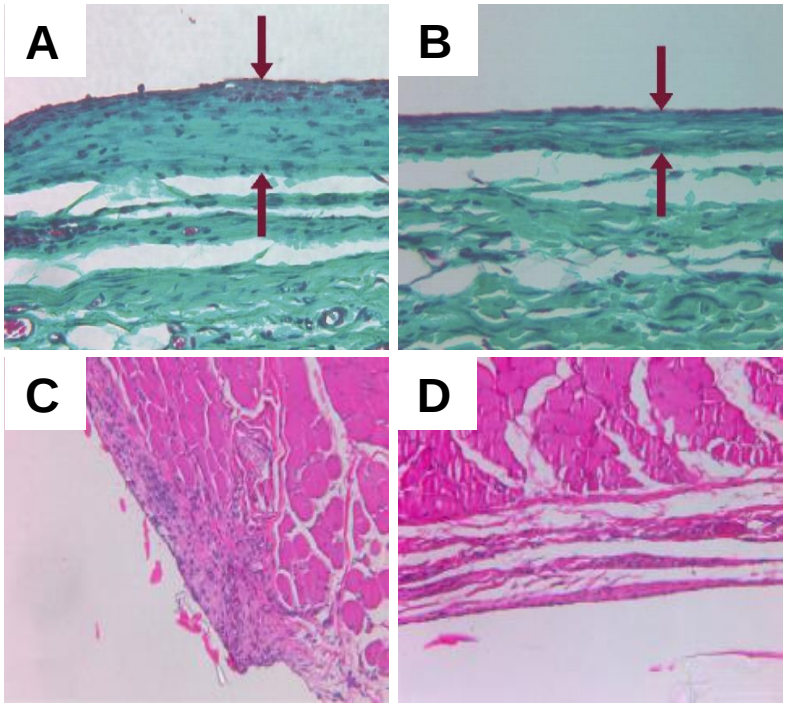

Figure 1.7. Photomicrographs of tissue slices stained with (A, B) Masson's Trichrome or (C, D) hematoxylin and eosin at (A, C) control and (B, D) NO-releasing xerogels. The tissue samples stained with Masson's Trichrome (A, B) show reduced collagen deposition (blue-stained fibers) at NO-releasing implants after 6 wk. Nitric oxide release also reduced inflammation after 3 wk, as evidenced by the reduced number of purple-colored inflammatory cell nuclei in the hematoxylin and eosin stained tissue sections (C, D). Reprinted with permission from Biomaterials, 2007, 28, Hetrick, E. M.; Prichard, H. L.; Klitzman, B.; Schoenfisch, M. H. "Reduced foreign body response at nitric oxide-releasing subcutaneous implants," pages 4571–4580. Copyright 2007 Elsevier.

to controls. However, this work did not identify optimal NO-release payloads or kinetics.

In subsequent work, Nichols et al. evaluated the severity of the FBR in a swine model as a function of NO-release kinetics.[217] Silica particles modified with either *N*-diazeniumdiolate or *S*-nitrosothiol NO donors[218] were employed as polyurethane dopant molecules to fabricate NO-releasing polymer coatings. The resulting polyurethane/silica composites were diverse with respect to their NO-release kinetics, releasing 2.7–9.3 μmol NO cm^{-2} for 1–14 d durations depending on the type of silica nanoparticle dopant. Materials capable of releasing NO for at least 2 d both decreased inflammation over the first wk post-implantation and lead to reduced collagen capsule thickness at 3 and 6 wk. In contrast, more rapid NO-releasing materials (~24 h NO-release durations) did not decrease inflammation and were observed to increase collagen density relative to control materials. Although the anti-inflammatory effects of NO were localized to the tissue immediately surrounding the implants, these results indicate the need for precise control of NO-release kinetics for achieving the optimal tissue response.

A critical, yet frequently overlooked aspect of biocompatibility is whether reductions in the FBR actually translate to improved sensor performance. With knowledge that NO mitigates the FBR, Nichols et al. evaluated the glucose recovery of NO-releasing microdialysis probes in a rat model as a measure of subcutaneous tissue mass transfer resistance.[219] An NO-saturated buffer solution (1.9 mM NO) was used as the probe perfusate to achieve approximately constant NO release (~162 pmol cm^{-2} s^{-1} for 8 h daily) from the microdialysis probes via retrodialysis over a 2 wk implantation period. Although the glucose recovery of NO-releasing and control probes remained constant during the first 6 d of implantation (~15–25% glucose recovery), only the NO-releasing probes maintained adequate recovery values over the entire 14 d implantation

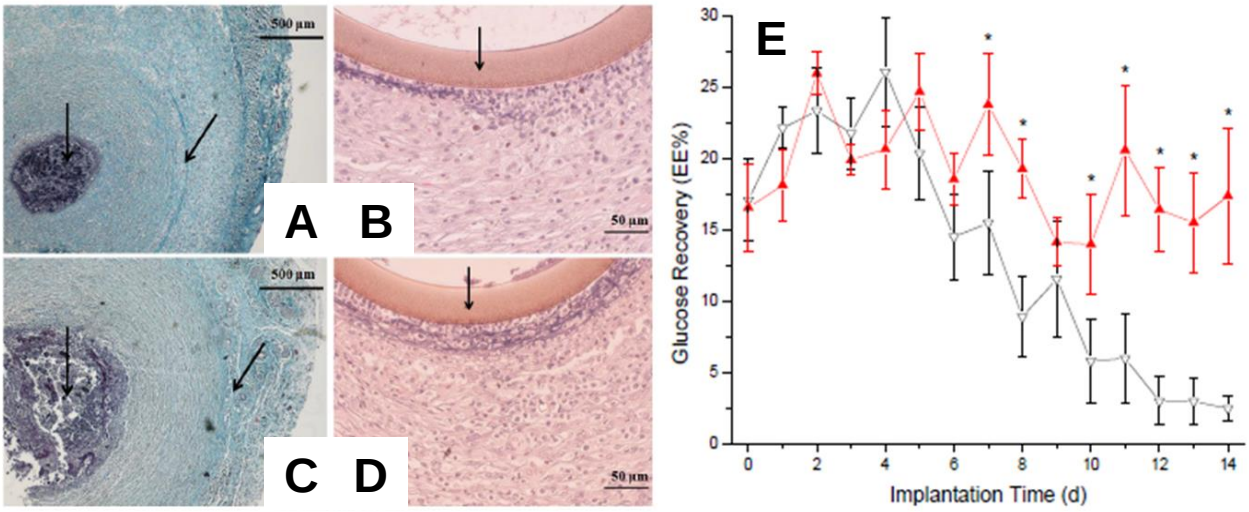

Figure 1.8. Photomicrographs of (A, C) Masson's trichrome or (B, D) hematoxylin & eosin stained tissues surrounding (A, B) NO-releasing and (C, D) control microdialysis probes after 14 d implantation in Sprague-Dawley rats. The photomicrographs in (A,C) stain blue for collagen fibers and those in (B, D) stain cell nuclei purple. The graph in (E) presents the glucose recovery of (red, triangle) NO-releasing and (black, inverted triangle) control microdialysis probes as a function of implantation time. Reprinted with permission from Analytical Chemistry, 2011, 83, Nichols, S. P.; Le, N. N.; Klitzman, B.; Schoenfisch, M. H. "Increased in vivo glucose recovery via nitric oxide release," pages 1180–1184. Copyright 2011 American Chemical Society.

period (Figure 1.8E). After 8 d, control probe glucose recovery was approximately half that of the NO-releasing probes and further diminished to $\leq$5% after 10 d. Tissue histology analysis revealed that the NO-releasing probes induced lower degrees of inflammation and collagen encapsulation than the control probes (Figures 1.8A–D), indicating that the superior glucose recovery for the NO-releasing probes was due in part to a reduced FBR. Based on the favorable improvements to subcutaneous glucose transport, the authors suggested potential benefits of NO release to subcutaneous glucose sensor performance.

Only one prior investigation has examined the potential benefits of NO release to the analytical performance of in vivo glucose biosensors.[198] Gifford et al. functionalized percutaneous, needle-type electrochemical glucose biosensors to release NO by doping *N*-diazeniumdiolate-modified *N,N'*-dibutylhexanediamine into polyurethane/polydimethylsiloxane glucose sensor membranes.[198] The NO-releasing sensors and analogous controls were implanted in the subcutis of rats for performance evaluations up to 48 h in duration. The NO-releasing sensors better maintained glucose sensitivity throughout implantation (~12% sensitivity decrease over 48 h) than did control sensors (32% decrease). On the day of implantation, 99.7% of blood glucose determinations made by the NO-releasing sensors were reported to be clinically acceptable by Clarke Error Grid analysis of the sensor data in comparison to paired reference measurements (i.e., a handheld glucometer). In contrast, fewer measurements by control sensors met the criteria for a clinically acceptable measurement (96.3%). However, the clinical accuracy of NO-releasing sensors after 48 h was similar to controls. Histological analysis of tissues surrounding the sensors indicated reduced inflammatory response for the NO-releasing sensors at 24 h but not at 48 h, highlighting a potential source for decreased NO-releasing sensor performance. The authors hypothesized that the NO release, limited to only 18 h in duration, was

insufficient to improve sensor performance beyond 24 h. Based on the tissue histology studies by Hetrick[216] and Nichols,[217] more extended NO release is likely required to improve in vivo glucose sensor analytical performance for longer durations.

1.5. Summary of dissertation research

The focus of this dissertation research was to develop an understanding of the relationships between the foreign body response and the in vivo analytical performance of NO-releasing electrochemical glucose biosensors. Specifically, I sought to translate the NO-releasing silica-based polyurethane sensor membranes to an implantable sensor design for an evaluation of in vivo sensor function. Sensor performance was evaluated as a function of NO-release kinetics using a porcine FBR model. At the same time, the tissue responses to subcutaneously-implanted polyurethanes were assessed in both healthy and diabetic swine models to generate new information on how diabetes and NO impact the FBR. My research aims were to:

(1) evaluate the role of a reduced FBR to NO-releasing glucose sensors on in vivo sensor analytical performance in a pre-clinical swine model;

(2) develop silica nanoparticles with large NO storage and tunable NO-release kinetics for use as dopants in glucose sensor membranes;

(3) systematically develop NO-releasing polyurethanes, adapting the resulting membranes to serve as coatings for electrochemical glucose biosensors;

(4) assess the FBR to subcutaneous implants as a function of disease state (i.e., healthy versus diabetic) and NO-release kinetics.

This introductory chapter established a theoretical framework relating key events in the FBR to in vivo glucose sensor analytical performance. Additional impetus for studying the FBR in a diabetic animal model was also provided. This introduction served to highlight design flaws

associated with the NO-releasing polymers (e.g., silica particle leaching) that may counteract the benefits of NO release directed at reducing the FBR. In Chapter 2, the in vivo analytical performance of electrochemical glucose biosensors in a pre-clinical swine model is described as a function of NO-release kinetics. In Chapter 3, the synthesis of *N*-diazeniumdiolate-modified mesoporous silica particles via an interfacial ion exchange reaction is shown to enable superior NO storage and tunable NO-release kinetics. A systematic evaluation of NO-releasing polyurethane/silica membranes is described in Chapter 4 in pursuit of a high-performance, NO-releasing glucose sensor with non-leaching constituent silica. The NO-releasing silica nanoparticles that were developed in Chapter 3 were then utilized to study the FBR to NO-releasing glucose biosensors side-by-side in healthy and diabetic swine. This work is described in Chapter 5. An overall summary of this research is provided in Chapter 6, along with suggestions for future work to aid in translation of this technology to future use in humans.

REFERENCES

(1) Centers for Disease Control and Prevention "National diabetes statistics report: Estimates of diabetes and its burden in the United States"; Atlanta, GA: U.S. Department of Health and Human Services; **2014**.

(2) National Diabetes Data Group "Classification and diagnosis of diabetes mellitus and other categories of glucose intolerance" *Diabetes* **1979**; 1039-1057.

(3) Heller, A.; Feldman, B. "Electrochemical glucose sensors and their applications in diabetes management." *Chemical Reviews* **2008,** *108*, 2482-2505.

(4) The Diabetes Control and Complications Trial Group "The effect of intensive treatment of diabetes on the development and progression of long-term complications in insulin-dependent diabetes mellitus" *New England Journal of Medicine* **1993**; 977-986.

(5) UK Prospective Diabetes Study Group "Intensive blood-glucose control with sulphonylureas or insulin compared with conventional treatment and risk of complications in patients with type 2 diabetes" *Lancet* **1998**; 837-53.

(6) UK Prospective Diabetes Study Group "Effect of intensive blood-glucose control with metformin on complications in overweight patients with type 2 diabetes"; *Lancet* **1998**; 854-65.

(7) Nichols, S. P.; Koh, A.; Storm, W. L.; Shin, J. H.; Schoenfisch, M. H. "Biocompatible materials for continuous glucose monitoring devices." *Chemical Reviews* **2013,** *113*, 2528-2549.

(8) The Juvenile Diabetes Research Foundation Continuous Glucose Monitoring Study Group "Continuous glucose monitoring and intensive treatment of type 1 diabetes." *New England Journal of Medicine* **2008,** *359*, 1464-1476.

(9) Deiss, D.; Bolinder, J.; Riveline, J.-P.; Battelino, T.; Bosi, E.; Tubiana-Rufi, N.; Kerr, D.; Phillip, M. "Improved glycemic control in poorly controlled patients with type 1 diabetes using real-time continuous glucose monitoring." *Diabetes Care* **2006,** *29*, 2730-2732.

(10) Benhamou, P. Y.; Catargi, B.; Delenne, B.; Guerci, B.; Hanaire, H.; Jeandidier, N.; Leroy, R.; Meyer, L.; Penfornis, A.; Radermecker, R. P.; Renard, E.; Baillot-Rudoni, S.; Riveline, J. P.; Schaepelynck, P.; Sola-Gazagnes, A.; Sulmont, V.; Tubiana-Rufi, N.; Durain, D.; Mantovani, I.; Sola-Gazagnes, A.; Riveline, J. P. "Real-time continuous glucose monitoring (CGM) integrated into the treatment of type 1 diabetes: Consensus of experts from SFD, EVADIAC and SFE." *Diabetes & Metabolism* **2012,** *38*, S67-S83.

(11) Radermecker, R. P.; Saint Remy, A.; Scheen, A. J.; Bringer, J.; Renard, E. "Continuous glucose monitoring reduces both hypoglycaemia and HbA1c in hypoglycaemia-prone type 1 diabetic patients treated with a portable pump." *Diabetes & Metabolism* **2010,** *36*, 409-413.

(12) Matsumoto, N.; Chen, X.; Wilson, G. S. "Fundamental studies of glucose oxidase deposition on a Pt electrode." *Analytical Chemistry* **2002,** *74*, 362-367.

(13) Adams, E. C.; Mast, R. L.; Free, A. H. "Specificity of glucose oxidase." *Archives of Biochemistry and Biophysics* **1960,** *91*, 230-234.

(14) Kleppe, K. "The effect of hydrogen peroxide on glucose oxidase from *Aspergillus Niger*." *Biochemistry* **1966,** *5*, 139-143.

(15) Sun, X.; James, T. D. "Glucose sensing in supramolecular chemistry." *Chemical Reviews* **2015,** *115*, 8001-8037.

(16) Wilson, G. S.; Gifford, R. "Biosensors for real-time in vivo measurements." *Biosensors and Bioelectronics* **2005,** *20*, 2388-2403.

(17) Wilson, G. S.; Ammam, M. "In vivo biosensors." *The FEBS Journal* **2007,** *274*, 5452-61.

(18) Kotanen, C. N.; Moussy, F. G.; Carrara, S.; Guiseppi-Elie, A. "Implantable enzyme amperometric biosensors." *Biosensors and Bioelectronics* **2012,** *35*, 14-26.

(19) Gough, D. A.; Kumosa, L. S.; Routh, T. L.; Lin, J. T.; Lucisano, J. Y. "Function of an implanted tissue glucose sensor for more than 1 year in animals." *Science Translational Medicine* **2010,** *2*, 42ra53.

(20) Kumosa, L. S.; Routh, T. L.; Lin, J. T.; Lucisano, J. Y.; Gough, D. A. "Permeability of subcutaneous tissues surrounding long-term implants to oxygen." *Biomaterials* **2014,** *35*, 8287-96.

(21) Koh, A.; Riccio, D. A.; Sun, B.; Carpenter, A. W.; Nichols, S. P.; Schoenfisch, M. H. "Fabrication of nitric oxide-releasing polyurethane glucose sensor membranes." *Biosensors and Bioelectronics* **2011,** *28*, 17-24.

(22) Koh, A.; Lu, Y.; Schoenfisch, M. H. "Fabrication of nitric oxide-releasing porous

polyurethane membranes-coated needle-type implantable glucose biosensors." *Analytical Chemistry* **2013,** *85*, 10488-10494.

(23) Shin, J. H.; Marxer, S. M.; Schoenfisch, M. H. "Nitric oxide-releasing sol-gel particle/polyurethane glucose biosensors." *Analytical Chemistry* **2004,** *76*, 4543-9.

(24) Vaddiraju, S.; Wang, Y.; Qiang, L.; Burgess, D. J.; Papadimitrakopoulos, F. "Microsphere erosion in outer hydrogel membranes creating macroscopic porosity to counter biofouling-induced sensor degradation." *Analytical Chemistry* **2012,** *84*, 8837-45.

(25) Armour, J. C.; Lucisano, J. Y.; McKean, B. D.; Gough, D. A. "Application of chronic intravascular blood glucose sensor in dogs." *Diabetes* **1990,** *39*, 1519-26.

(26) Updike, S. J.; Shults, M. C.; Gilligan, B. J.; Rhodes, R. K. "A subcutaneous glucose sensor with improved longevity, dynamic range, and stability of calibration." *Diabetes Care* **2000,** *23*, 208-14.

(27) Johnson, K. W.; Mastrototaro, J. J.; Howey, D. C.; Brunelle, R. L.; Burden-Brady, P. L.; Bryan, N. A.; Andrew, C. C.; Rowe, H. M.; Allen, D. J.; Noffke, B. W.; McMahan, W. C.; Morff, R. J.; Lipson, D.; Nevin, R. S. "In vivo evaluation of an electroenzymatic glucose sensor implanted in subcutaneous tissue." *Biosensors and Bioelectronics* **1992,** *7*, 709-14.

(28) Kvist, P. H.; Iburg, T.; Aalbaek, B.; Gerstenberg, M.; Schoier, C.; Kaastrup, P.; Buch-Rasmussen, T.; Hasselager, E.; Jensen, H. E. "Biocompatibility of an enzyme-based, electrochemical glucose sensor for short-term implantation in the subcutis." *Diabetes Technology and Therapeutics* **2006,** *8*, 546-59.

(29) Bindra, D. S.; Zhang, Y.; Wilson, G. S.; Sternberg, R.; Thevenot, D. R.; Moatti, D.; Reach, G. "Design and in vitro studies of a needle-type glucose sensor for subcutaneous monitoring." *Analytical Chemistry* **1991,** *63*, 1692-1696.

(30) Vaddiraju, S.; Burgess, D. J.; Jain, F. C.; Papadimitrakopoulos, F. "The role of H_2O_2 outer diffusion on the performance of implantable glucose sensors." *Biosensors and Bioelectronics* **2009,** *24*, 1557-62.

(31) Croce, R. A., Jr.; Vaddiraju, S.; Kondo, J.; Wang, Y.; Zuo, L.; Zhu, K.; Islam, S. K.; Burgess, D. J.; Papadimitrakopoulos, F.; Jain, F. C. "A miniaturized transcutaneous system for continuous glucose monitoring." *Biomedical Microdevices* **2013,** *15*, 151-60.

(32) Nazari, M. H.; Mujeeb-U-Rahman, M.; Scherer, A. "An implantable continuous glucose monitoring microsystem in 0.18 µm CMOS." *2014 Symposium on VLSI Circuits Digest of Technical Papers* **2014**.

(33) Degani, Y.; Heller, A. "Direct electrical communication between chemically modified enzymes and metal electrodes. I. Electron transfer from glucose oxidase to metal electrodes via electron relays, bound covalently to the enzyme." *The Journal of Physical Chemistry* **1987,** *91*, 1285-1289.

(34) Heller, A. "Electrical wiring of redox enzymes." *Accounts of Chemical Research* **1990,** *23*, 128-134.

(35) Hecht, H. J.; Kalisz, H. M.; Hendle, J.; Schmid, R. D.; Schomburg, D. "Crystal structure of glucose oxidase from *Aspergillus Niger* refined at 2.3 Å resolution." *Journal of Molecular Biology* **1993,** *229*, 153-72.

(36) Mao, F.; Mano, N.; Heller, A. "Long tethers binding redox centers to polymer backbones enhance electron transport in enzyme "wiring" hydrogels." *Journal of the American Chemical Society* **2003,** *125*, 4951-4957.

(37) Heller, A. "Electron-conducting redox hydrogels: Design, characteristics and synthesis." *Current Opinion in Chemical Biology* **2006,** *10*, 664-672.

(38) Vaddiraju, S.; Burgess, D. J.; Tomazos, I.; Jain, F. C.; Papadimitrakopoulos, F. "Technologies for continuous glucose monitoring: Current problems and future promises." *Journal of Diabetes Science and Technology* **2010,** *4*, 1540-1562.

(39) Updike, S. J.; Hicks, G. P. "The enzyme electrode." *Nature* **1967,** *214*, 986-988.

(40) Clark, L. "Monitor and control of blood and tissue oxygen tension." *Transactions–American Society for Artificial Internal Organs* **1956**, *2*, 41–48.

(41) Shichiri, M.; Yamasaki, Y.; Kawamori, R.; Hakui, N.; Abe, H. "Wearable artificial endocrine pancreas with needle-type glucose sensor." *The Lancet* **1982,** *320*, 1129-1131.

(42) Wilson, G. S.; Hu, Y. "Enzyme-based biosensors for in vivo measurements." *Chemical Reviews* **2000,** *100*, 2693-704.

(43) Michaelis, L.; Menten, M. L. "Die kinetik der invertinwirkung." *Biochemische Zeitschrift* **1913,** *49*, 352.

(44) Koh, A.; Nichols, S. P.; Schoenfisch, M. H. "Glucose sensor membranes for mitigating the foreign body response." *Journal of Diabetes Science and Technology* **2011,** *5*, 1052-9.

(45) Sternberg, R.; Bindra, D. S.; Wilson, G. S.; Thevenot, D. R. "Covalent enzyme coupling on cellulose acetate membranes for glucose sensor development." *Analytical Chemistry* **1988,** *60*, 2781-2786.

(46) Sittampalam, G.; Wilson, G. S. "Surface-modified electrochemical detector for liquid chromatography." *Analytical Chemistry* **1983,** *55*, 1608-1610.

(47) Chen, X.; Hu, Y.; Wilson, G. S. "Glucose microbiosensor based on alumina sol–gel matrix/electropolymerized composite membrane." *Biosensors and Bioelectronics* **2002,** *17*, 1005-1013.

(48) Chen, X.; Matsumoto, N.; Hu, Y.; Wilson, G. S. "Electrochemically mediated electrodeposition/electropolymerization to yield a glucose microbiosensor with improved characteristics." *Analytical Chemistry* **2002,** *74*, 368-372.

(49) Malitesta, C.; Palmisano, F.; Torsi, L.; Zambonin, P. G. "Glucose fast-response amperometric sensor based on glucose oxidase immobilized in an electropolymerized poly(*o*-phenylenediamine) film." *Analytical Chemistry* **1990,** *62*, 2735-2740.

(50) Moussy, F.; Harrison, D. J.; O'Brien, D. W.; Rajotte, R. V. "Performance of subcutaneously implanted needle-type glucose sensors employing a novel trilayer coating." *Analytical Chemistry* **1993,** *65*, 2072-2077.

(51) Pickup, J. C.; Hussain, F.; Evans, N. D.; Rolinski, O. J.; Birch, D. J. S. "Fluorescence-based glucose sensors." *Biosensors and Bioelectronics* **2005,** *20*, 2555-2565.

(52) Ballerstadt, R.; Schultz, J. S. "A fluorescence affinity hollow fiber sensor for continuous transdermal glucose monitoring." *Analytical Chemistry* **2000,** *72*, 4185-4192.

(53) Colvin, A. E.; Jiang, H. "Increased in vivo stability and functional lifetime of an implantable glucose sensor through platinum catalysis." *Journal of Biomedical Materials Research Part A* **2013,** *101*, 1274-1282.

(54) Mansouri, S.; Schultz, J. S. "A miniature optical glucose sensor based on affinity binding." *Nature Biotechnology* **1984,** *2*, 885-890.

(55) Roberts, J. R.; Park, J.; Helton, K.; Wisniewski, N.; McShane, M. J. "Biofouling of polymer hydrogel materials and its effect on diffusion and enzyme-based luminescent glucose sensor functional characteristics." *Journal of Diabetes Science and Technology* **2012,** *6*, 1267-75.

(56) Unruh, R. M.; Roberts, J. R.; Nichols, S. P.; Gamsey, S.; Wisniewski, N. A.; McShane, M. J. "Preclinical evaluation of poly(HEMA-*co*-acrylamide) hydrogels encapsulating glucose oxidase and palladium benzoporphyrin as fully implantable glucose sensors." *Journal of Diabetes Science and Technology* **2015,** *9*, 985-92.

(57) Khalil, O. S. "Non-invasive glucose measurement technologies: An update from 1999 to the dawn of the new millennium." *Diabetes Technology and Therapeutics* **2004,** *6*, 660-97.

(58) Alexeev, V. L.; Sharma, A. C.; Goponenko, A. V.; Das, S.; Lednev, I. K.; Wilcox, C. S.; Finegold, D. N.; Asher, S. A. "High ionic strength glucose-sensing photonic crystal." *Analytical Chemistry* **2003,** *75*, 2316-2323.

(59) Damiano, E. R.; El-Khatib, F. H.; Zheng, H.; Nathan, D. M.; Russell, S. J. "A comparative effectiveness analysis of three continuous glucose monitors." *Diabetes Care* **2013,** *36*, 251-9.

(60) Gifford, R. "Continuous glucose monitoring: 40 years, what we've learned and what's next." *Chemphyschem* **2013,** *14*, 2032-44.

(61) Vashist, S. K. "Non-invasive glucose monitoring technology in diabetes management: A review." *Analytica Chimica Acta* **2012,** *750*, 16-27.

(62) Caduff, A.; Hirt, E.; Feldman, Y.; Ali, Z.; Heinemann, L. "First human experiments with a novel non-invasive, non-optical continuous glucose monitoring system." *Biosensors and Bioelectronics* **2003,** *19*, 209-217.

(63) Mueller, M.; Talary, M. S.; Falco, L.; De Feo, O.; Stahel, W. A.; Caduff, A. "Data processing for noninvasive continuous glucose monitoring with a multisensor device." *Journal of Diabetes Science and Technology* **2011,** *5*, 694-702.

(64) Anderson, J. M.; Rodriguez, A.; Chang, D. T. "Foreign body reaction to biomaterials." *Seminars in Immunology* **2008,** *20*, 86-100.

(65) Schutte, R. J.; Xie, L.; Klitzman, B.; Reichert, W. M. "In vivo cytokine-associated responses to biomaterials." *Biomaterials* **2009,** *30,* 160-8.

(66) Anderson, J. M. "Biological responses to materials." *Annual Review of Materials Research* **2001,** *31,* 81-110.

(67) Ward, K. W. "A review of the foreign-body response to subcutaneously-implanted devices: The role of macrophages and cytokines in biofouling and fibrosis." *Journal of Diabetes Science and Technology* **2008,** *2,* 768-77.

(68) Klueh, U. "Analysis: On the path to overcoming glucose-sensor-induced foreign body reactions." *Journal of Diabetes Science and Technology* **2013,** *7,* 452-4.

(69) Anderson, J. M.; Jones, J. A. "Phenotypic dichotomies in the foreign body reaction." *Biomaterials* **2007,** *28,* 5114-5120.

(70) Sides, C. R.; Stenken, J. A. "Microdialysis sampling techniques applied to studies of the foreign body reaction." *European Journal of Pharmaceutical Sciences* **2014,** *57,* 74-86.

(71) Novak, M. T.; Yuan, F.; Reichert, W. M. "Predicting glucose sensor behavior in blood using transport modeling: Relative impacts of protein biofouling and cellular metabolic effects." *Journal of Diabetes Science and Technology* **2013,** *7,* 1547-1560.

(72) Horbett, T. A., Proteins: Structure, properties, and adsorption to surfaces. In *Biomaterials science: An introduction to materials in medicine*, Ratner, B. D.; Hoffman, A. S.; Schoen, F. J.; Lemons, J. E., Eds. Academic Press Inc.: **1996**; 133–141.

(73) Thomé-Duret, V.; Gangnerau, M. N.; Zhang, Y.; Wilson, G. S.; Reach, G. "Modification of the sensitivity of glucose sensor implanted into subcutaneous tissue." *Diabetes & Metabolism* **1996,** *22,* 174-178.

(74) Gifford, R.; Kehoe, J. J.; Barnes, S. L.; Kornilayev, B. A.; Alterman, M. A.; Wilson, G. S. "Protein interactions with subcutaneously implanted biosensors." *Biomaterials* **2006,** *27,* 2587-98.

(75) Martin, P.; Leibovich, S. J. "Inflammatory cells during wound repair: The good, the bad and the ugly." *Trends in Cell Biology* **2005,** *15,* 599-607.

(76) Klueh, U.; Liu, Z.; Feldman, B.; Henning, T. P.; Cho, B.; Ouyang, T.; Kreutzer, D. "Metabolic biofouling of glucose sensors in vivo: Role of tissue microhemorrhages." *Journal of Diabetes Science and Technology* **2011,** *5*, 583-95.

(77) Helton, K. L.; Ratner, B. D.; Wisniewski, N. A. "Biomechanics of the sensor-tissue interface-effects of motion, pressure, and design on sensor performance and the foreign body response-Part I: Theoretical framework." *Journal of Diabetes Science and Technology* **2011,** *5*, 632-46.

(78) Helton, K. L.; Ratner, B. D.; Wisniewski, N. A. "Biomechanics of the sensor-tissue interface-effects of motion, pressure, and design on sensor performance and foreign body response-Part II: Examples and application." *Journal of Diabetes Science and Technology* **2011,** *5*, 647-56.

(79) Wu, Y.; Meyerhoff, M. E. "Nitric oxide-releasing/generating polymers for the development of implantable chemical sensors with enhanced biocompatibility." *Talanta* **2008,** *75*, 642-650.

(80) Wang, Y.; Vaddiraju, S.; Gu, B.; Papadimitrakopoulos, F.; Burgess, D. J. "Foreign body reaction to implantable biosensors: Effects of tissue trauma and implant size." *Journal of Diabetes Science and Technology* **2015,** *9*, 966-77.

(81) Tang, L.; Jennings, T. A.; Eaton, J. W. "Mast cells mediate acute inflammatory responses to implanted biomaterials." *Proceedings of the National Academy of Sciences of the United States of America* **1998,** *95*, 8841-8846.

(82) Klueh, U.; Kaur, M.; Qiao, Y.; Kreutzer, D. L. "Critical role of tissue mast cells in controlling long-term glucose sensor function in vivo." *Biomaterials* **2010,** *31*, 4540-4551.

(83) Egozi, E. I.; Ferreira, A. M.; Burns, A. L.; Gamelli, R. L.; Dipietro, L. A. "Mast cells modulate the inflammatory but not the proliferative response in healing wounds." *Wound Repair and Regeneration* **2003,** *11*, 46-54.

(84) Thevenot, P. T.; Baker, D. W.; Weng, H.; Sun, M.-W.; Tang, L. "The pivotal role of fibrocytes and mast cells in mediating fibrotic reactions to biomaterials." *Biomaterials* **2011,** *32*, 8394-8403.

(85) Avula, M. N.; Rao, A. N.; McGill, L. D.; Grainger, D. W.; Solzbacher, F. "Foreign body response to subcutaneous biomaterial implants in a mast cell-deficient KIT(W-SH) murine model." *Acta Biomaterialiaialia* **2014,** *10*, 1856-63.

(86) Mosser, D. M.; Edwards, J. P. "Exploring the full spectrum of macrophage activation." *Nature Reviews Immunology* **2008,** *8*, 958-969.

(87) Mantovani, A.; Biswas, S. K.; Galdiero, M. R.; Sica, A.; Locati, M. "Macrophage plasticity and polarization in tissue repair and remodelling." *Journal of Pathology* **2013,** *229*, 176-85.

(88) Martinez, F. O. "Regulators of macrophage activation." *European Journal of Immunology* **2011,** *41*, 1531-1534.

(89) Shin, J. H.; Schoenfisch, M. H. "Improving the biocompatibility of in vivo sensors via nitric oxide release." *Analyst* **2006,** *131*, 609-615.

(90) MacMicking, J.; Xie, Q. W.; Nathan, C. "Nitric oxide and macrophage function." *Annual Review of Immunology* **1997,** *15*, 323-50.

(91) Liu, W. F.; Ma, M.; Bratlie, K. M.; Dang, T. T.; Langer, R.; Anderson, D. G. "Real-time in vivo detection of biomaterial-induced reactive oxygen species." *Biomaterials* **2011,** *32*, 1796-801.

(92) Novak, M. T.; Yuan, F.; Reichert, W. M. "Modeling the relative impact of capsular tissue effects on implanted glucose sensor time lag and signal attenuation." *Analytical and Bioanalytical Chemistry* **2010,** *398*, 1695-705.

(93) Novak, M. T.; Yuan, F.; Reichert, W. M. "Macrophage embedded fibrin gels: An in vitro platform for assessing inflammation effects on implantable glucose sensors." *Biomaterials* **2014,** *35*, 9563-72.

(94) Klueh, U.; Frailey, J.; Qiao, Y.; Antar, O.; Kreutzer, D. L. "Cell based metabolic barriers to glucose diffusion: Macrophages and continuous glucose monitoring." *Biomaterials* **2014,** *35*, 3145-3153.

(95) Novak, M. T.; Reichert, W. M. "Modeling the physiological factors affecting glucose sensor function in vivo." *Journal of Diabetes Science and Technology* **2015,** *9*, 993-8.

(96) Zhu, L.; Zhao, Q.; Yang, T.; Ding, W.; Zhao, Y. "Cellular metabolism and macrophage functional polarization." *International Reviews of Immunology* **2015,** *34*, 82-100.

(97) Murray, Peter J.; Allen, Judith E.; Biswas, Subhra K.; Fisher, Edward A.; Gilroy, Derek W.; Goerdt, S.; Gordon, S.; Hamilton, John A.; Ivashkiv, Lionel B.; Lawrence, T.; Locati, M.; Mantovani, A.; Martinez, Fernando O.; Mege, J.-L.; Mosser, David M.; Natoli, G.; Saeij, Jeroen P.; Schultze, Joachim L.; Shirey, Kari A.; Sica, A.; Suttles, J.; Udalova, I.; van Ginderachter, Jo A.; Vogel, Stefanie N.; Wynn, Thomas A. "Macrophage activation and polarization: Nomenclature and experimental guidelines." *Immunity* **2014,** *41*, 14-20.

(98) Gratchev, A.; Guillot, P.; Hakiy, N.; Politz, O.; Orfanos, C. E.; Schledzewski, K.; Goerdt, S. "Alternatively activated macrophages differentially express fibronectin and its splice variants and the extracellular matrix protein betaIG-H3." *Scandinavian Journal of Immunology* **2001,** *53*, 386-92.

(99) Li, A. G.; Quinn, M. J.; Siddiqui, Y.; Wood, M. D.; Federiuk, I. F.; Duman, H. M.; Ward, W. K. "Elevation of transforming growth factor beta and its downstream mediators in subcutaneous foreign body capsule tissue." *Journal of Biomedical Materials Research Part A* **2007,** *82*, 498-508.

(100) Spiller, K. L.; Anfang, R. R.; Spiller, K. J.; Ng, J.; Nakazawa, K. R.; Daulton, J. W.; Vunjak-Novakovic, G. "The role of macrophage phenotype in vascularization of tissue engineering scaffolds." *Biomaterials* **2014,** *35*, 4477-4488.

(101) Keeler, G. D.; Durdik, J. M.; Stenken, J. A. "Effects of delayed delivery of dexamethasone-21-phosphate via subcutaneous microdialysis implants on macrophage activation in rats." *Acta Biomaterialiaialia* **2015,** *23*, 27-37.

(102) McNally, A. K.; Anderson, J. M. " β1 and β2 integrins mediate adhesion during macrophage fusion and multinucleated foreign body giant cell formation." *The American Journal of Pathology* **2002,** *160*, 621-630.

(103) Brodbeck, W. G.; Shive, M. S.; Colton, E.; Nakayama, Y.; Matsuda, T.; Anderson, J. M. "Influence of biomaterial surface chemistry on the apoptosis of adherent cells." *Journal of Biomedical Materials Research* **2001,** *55*, 661-8.

(104) Zhao, Q.; Topham, N.; Anderson, J. M.; Hiltner, A.; Lodoen, G.; Payet, C. R. "Foreign-body giant cells and polyurethane biostability: In vivo correlation of cell adhesion and surface cracking." *Journal of Biomedical Materials Research* **1991,** *25*, 177-183.

(105) Zhao, Q. H.; McNally, A. K.; Rubin, K. R.; Renier, M.; Wu, Y.; Rose-Caprara, V.; Anderson, J. M.; Hiltner, A.; Urbanski, P.; Stokes, K. "Human plasma alpha 2-macroglobulin promotes in vitro oxidative stress cracking of Pellethane 2363-80a: In vivo and in vitro correlations." *Journal of Biomedical Materials Research* **1993,** *27*, 379-88.

(106) Zdrahala, R. J.; Zdrahala, I. J. "Biomedical applications of polyurethanes: A review of past promises, present realities, and a vibrant future." *Journal of Biomaterials Applications* **1999,** *14*, 67-90.

(107) Sharkawy, A. A.; Klitzman, B.; Truskey, G. A.; Reichert, W. M. "Engineering the tissue which encapsulates subcutaneous implants. I. Diffusion properties." *Journal of Biomedical Materials Research* **1997,** *37*, 401-12.

(108) Sharkawy, A. A.; Klitzman, B.; Truskey, G. A.; Reichert, W. M. "Engineering the tissue which encapsulates subcutaneous implants. III. Effective tissue response times." *Journal of Biomedical Materials Research* **1998,** *40*, 598-605.

(109) Sharkawy, A. A.; Klitzman, B.; Truskey, G. A.; Reichert, W. M. "Engineering the tissue which encapsulates subcutaneous implants. II. Plasma-tissue exchange properties." *Journal of Biomedical Materials Research* **1998,** *40*, 586-97.

(110) Sieminski, A. L.; Gooch, K. J. "Biomaterial-microvasculature interactions." *Biomaterials* **2000,** *21*, 2232-41.

(111) Worthington, K. S.; Wiley, L. A.; Mullins, R. F.; Tucker, B. A.; Nuxoll, E. "Prevascularized silicon membranes for the enhancement of transport to implanted medical devices." *Journal of Biomedical Materials Research Part B* **2015**.

(112) Klueh, U.; Dorsky, D. I.; Kreutzer, D. L. "Enhancement of implantable glucose sensor function in vivo using gene transfer-induced neovascularization." *Biomaterials* **2005,** *26*, 1155-63.

(113) Brem, H.; Tomic-Canic, M. "Cellular and molecular basis of wound healing in diabetes." *Journal of Clinical Investigation* **2007,** *117*, 1219-22.

(114) Le, N. N.; Rose, M. B.; Levinson, H.; Klitzman, B. "Implant healing in experimental animal models of diabetes." *Journal of Diabetes Science and Technology* **2011,** *5*, 605-18.

(115) Bellinger, D. A.; Merricks, E. P.; Nichols, T. C. "Swine models of type 2 diabetes mellitus: Insulin resistance, glucose tolerance, and cardiovascular complications." *ILAR Journal* **2006,** *47*, 243-58.

(116) Thomson, S. E.; McLennan, S. V.; Hennessy, A.; Boughton, P.; Bonner, J.; Zoellner, H.;

Yue, D. K.; Twigg, S. M. "A novel primate model of delayed wound healing in diabetes: Dysregulation of connective tissue growth factor." *Diabetologia* **2010,** *53*, 572-83.

(117) Wang, Y.; Papadimitrakopoulos, F.; Burgess, D. J. "Polymeric “smart” coatings to prevent foreign body response to implantable biosensors." *Journal of Controlled Release* **2013,** *169*, 341-347.

(118) Socarras, T. O.; Vasconcelos, A. C.; Campos, P. P.; Pereira, N. B.; Souza, J. P.; Andrade, S. P. "Foreign body response to subcutaneous implants in diabetic rats." *PLoS One* **2014,** *9*, e110945.

(119) Roy, S.; Biswas, S.; Khanna, S.; Gordillo, G.; Bergdall, V.; Green, J.; Marsh, C. B.; Gould, L. J.; Sen, C. K. "Characterization of a preclinical model of chronic ischemic wound." *Physiological Genomics* **2009,** *37*, 211-24.

(120) Wisniewski, N.; Rajamand, N.; Adamsson, U.; Lins, P. E.; Reichert, W. M.; Klitzman, B.; Ungerstedt, U. "Analyte flux through chronically implanted subcutaneous polyamide membranes differs in humans and rats." *American Journal of Physiology. Endocrinology and Metabolism* **2002,** *282*, E1316-23.

(121) Swindle, M. M.; Makin, A.; Herron, A. J.; Clubb, F. J.; Frazier, K. S. "Swine as models in biomedical research and toxicology testing." *Veterinary Pathology Online* **2012,** *49*, 344-356.

(122) Williams, D. F. "28th annual scientific meeting clinical applications of biomechanics-A model for biocompatibility and its evaluation." *Journal of Biomedical Engineering* **1989,** *11*, 185-191.

(123) Williams, D. F. "On the mechanisms of biocompatibility." *Biomaterials* **2008,** *29*, 2941-2953.

(124) Brodbeck, W. G.; Voskerician, G.; Ziats, N. P.; Nakayama, Y.; Matsuda, T.; Anderson, J. M. "In vivo leukocyte cytokine mrna responses to biomaterials are dependent on surface chemistry." *Journal of Biomedical Materials Research Part A* **2003,** *64*, 320-9.

(125) Anderson, J. M.; Defife, K.; Mcnally, A.; Collier, T.; Jenney, C. "Monocyte, macrophage and foreign body giant cell interactions with molecularly engineered surfaces." *Journal of Materials Science: Materials in Medicine* **1999**, *10*, 579-588.

(126) Jones, J. A.; Chang, D. T.; Meyerson, H.; Colton, E.; Kwon, I. K.; Matsuda, T.; Anderson,

J. M. "Proteomic analysis and quantification of cytokines and chemokines from biomaterial surface-adherent macrophages and foreign body giant cells." *Journal of Biomedical Materials Research Part A* **2007,** *83*, 585-596.

(127) MacEwan, M. R.; Brodbeck, W. G.; Matsuda, T.; Anderson, J. M. "Monocyte/lymphocyte interactions and the foreign body response: In vitro effects of biomaterial surface chemistry." *Journal of Biomedical Materials Research Part A* **2005,** *74*, 285-293.

(128) Gombotz, W. R.; Guanghui, W.; Horbett, T. A.; Hoffman, A. S. "Protein adsorption to poly(ethylene oxide) surfaces." *Journal of Biomedical Materials Research* **1991,** *25*, 1547-1562.

(129) Deible, C. R.; Petrosko, P.; Johnson, P. C.; Beckman, E. J.; Russell, A. J.; Wagner, W. R. "Molecular barriers to biomaterial thrombosis by modification of surface proteins with polyethylene glycol." *Biomaterials* **1999,** *20*, 101-109.

(130) Chen, S.; Li, L.; Zhao, C.; Zheng, J. "Surface hydration: Principles and applications toward low-fouling/nonfouling biomaterials." *Polymer* **2010,** *51*, 5283-5293.

(131) Browning, M. B.; Cereceres, S. N.; Luong, P. T.; Cosgriff-Hernandez, E. M. "Determination of the in vivo degradation mechanism of PEGDA hydrogels." *Journal of Biomedical Materials Research Part A* **2014,** *102*, 4244-51.

(132) Venault, A.; Zheng, Y.-S.; Chinnathambi, A.; Alharbi, S. A.; Ho, H.-T.; Chang, Y.; Chang, Y. "Stimuli-responsive and hemocompatible pseudozwitterionic interfaces." *Langmuir* **2015,** *31*, 2861-2869.

(133) Leng, C.; Hung, H. C.; Sun, S.; Wang, D.; Li, Y.; Jiang, S.; Chen, Z. "Probing the surface hydration of nonfouling zwitterionic and peg materials in contact with proteins." *ACS Applied Materials and Interfaces* **2015,** *7*, 16881-8.

(134) Tanaka, M.; Mochizuki, A.; Ishii, N.; Motomura, T.; Hatakeyama, T. "Study of blood compatibility with poly(2-methoxyethyl acrylate). Relationship between water structure and platelet compatibility in poly(2-methoxyethylacrylate-co-2-hydroxyethylmethacrylate)." *Biomacromolecules* **2002,** *3*, 36-41.

(135) Tanaka, M.; Mochizuki, A.; Shiroya, T.; Motomura, T.; Shimura, K.; Onishi, M.; Okahata, Y. "Study on kinetics of early stage protein adsorption on poly(2-methoxyethylacrylate) (PMEA) surface." *Colloids and Surfaces A: Physicochemical and Engineering Aspects* **2002,** *203*, 195-204.

(136) Zhang, L.; Cao, Z.; Bai, T.; Carr, L.; Ella-Menye, J.-R.; Irvin, C.; Ratner, B. D.; Jiang, S. "Zwitterionic hydrogels implanted in mice resist the foreign-body reaction." *Nature Biotechnology* **2013,** *31*, 553-556.

(137) Zhang, Z.; Chao, T.; Liu, L.; Cheng, G.; Ratner, B. D.; Jiang, S. "Zwitterionic hydrogels: An in vivo implantation study." *Journal of Biomaterials Science, Polymer Edition* **2009,** *20*, 1845-1859.

(138) Chen, S.; Jones, J. A.; Xu, Y.; Low, H. Y.; Anderson, J. M.; Leong, K. W. "Characterization of topographical effects on macrophage behavior in a foreign body response model." *Biomaterials* **2010,** *31*, 3479-91.

(139) Brauker, J. H.; Carr-Brendel, V. E.; Martinson, L. A.; Crudele, J.; Johnston, W. D.; Johnson, R. C. "Neovascularization of synthetic membranes directed by membrane microarchitecture." *Journal of Biomedical Materials Research* **1995,** *29*, 1517-24.

(140) Koschwanez, H. E.; Reichert, W. M.; Klitzman, B. "Intravital microscopy evaluation of angiogenesis and its effects on glucose sensor performance." *Journal of Biomedical Materials Research Part A* **2010,** *93*, 1348-57.

(141) Koschwanez, H. E.; Yap, F. Y.; Klitzman, B.; Reichert, W. M. "In vitro and in vivo characterization of porous poly-l-lactic acid coatings for subcutaneously implanted glucose sensors." *Journal of Biomedical Materials Research Part A* **2008,** *87*, 792-807.

(142) Bota, P. C.; Collie, A. M.; Puolakkainen, P.; Vernon, R. B.; Sage, E. H.; Ratner, B. D.; Stayton, P. S. "Biomaterial topography alters healing in vivo and monocyte/macrophage activation in vitro." *Journal of Biomedical Materials Research Part A* **2010,** *95*, 649-57.

(143) Bryant, S. J.; Cuy, J. L.; Hauch, K. D.; Ratner, B. D. "Photo-patterning of porous hydrogels for tissue engineering." *Biomaterials* **2007,** *28*, 2978-2986.

(144) Sussman, E. M.; Halpin, M. C.; Muster, J.; Moon, R. T.; Ratner, B. D. "Porous implants modulate healing and induce shifts in local macrophage polarization in the foreign body reaction." *Annals of Biomedical Engineering* **2014,** *42*, 1508-16.

(145) Bryers, J. D.; Giachelli, C. M.; Ratner, B. D. "Engineering biomaterials to integrate and heal: The biocompatibility paradigm shifts." *Biotechnology and Bioengineering* **2012,** *109*, 1898-1911.

(146) Brown, B. N.; Ratner, B. D.; Goodman, S. B.; Amar, S.; Badylak, S. F. "Macrophage polarization: An opportunity for improved outcomes in biomaterials and regenerative medicine." *Biomaterials* **2012,** *33*, 3792-3802.

(147) Teo, W. E.; Ramakrishna, S. "A review on electrospinning design and nanofibre assemblies." *Nanotechnology* **2006,** *17*, R89.

(148) Li, D.; Xia, Y. "Electrospinning of nanofibers: Reinventing the wheel?" *Advanced Materials* **2004,** *16*, 1151-1170.

(149) Vacanti, N. M.; Cheng, H.; Hill, P. S.; Guerreiro, J. D. T.; Dang, T. T.; Ma, M.; Watson, S.; Hwang, N. S.; Langer, R.; Anderson, D. G. "Localized delivery of dexamethasone from electrospun fibers reduces the foreign body response." *Biomacromolecules* **2012,** *13*, 3031-3038.

(150) Garg, K.; Pullen, N. A.; Oskeritzian, C. A.; Ryan, J. J.; Bowlin, G. L. "Macrophage functional polarization (M1/M2) in response to varying fiber and pore dimensions of electrospun scaffolds." *Biomaterials* **2013,** *34*, 4439-51.

(151) Agarwal, S.; Wendorff, J. H.; Greiner, A. "Use of electrospinning technique for biomedical applications." *Polymer* **2008,** *49*, 5603-5621.

(152) Cao, H.; McHugh, K.; Chew, S. Y.; Anderson, J. M. "The topographical effect of electrospun nanofibrous scaffolds on the in vivo and in vitro foreign body reaction." *Journal of Biomedical Materials Research Part A* **2010,** *93*, 1151-9.

(153) Wang, N.; Burugapalli, K.; Song, W.; Halls, J.; Moussy, F.; Ray, A.; Zheng, Y. "Electrospun fibro-porous polyurethane coatings for implantable glucose biosensors." *Biomaterials* **2013,** *34*, 888-901.

(154) Dubreuil, P.; Letard, S.; Ciufolini, M.; Gros, L.; Humbert, M.; Casteran, N.; Borge, L.; Hajem, B.; Lermet, A.; Sippl, W.; Voisset, E.; Arock, M.; Auclair, C.; Leventhal, P. S.; Mansfield, C. D.; Moussy, A.; Hermine, O. "Masitinib (AB1010), a potent and selective tyrosine kinase inhibitor targeting KIT." *PLoS One* **2009,** *4*, e7258.

(155) Reber, L.; Da Silva, C. A.; Frossard, N. "Stem cell factor and its receptor c-KIT as targets for inflammatory diseases." *European Journal of Pharmacology* **2006,** *533*, 327-340.

(156) Zdolsek, J.; Eaton, J. W.; Tang, L. "Histamine release and fibrinogen adsorption mediate

acute inflammatory responses to biomaterial implants in humans." *Journal of Translational Medicine* **2007,** *5*, 31.

(157) Avula, M.; Jones, D.; Rao, A. N.; McClain, D.; McGill, L. D.; Grainger, D. W.; Solzbacher, F. "Local release of masitinib alters in vivo implantable continuous glucose sensor performance." *Biosensors and Bioelectronics* **2016,** *77*, 149-156.

(158) Avula, M. N.; Rao, A. N.; McGill, L. D.; Grainger, D. W.; Solzbacher, F. "Modulation of the foreign body response to implanted sensor models through device-based delivery of the tyrosine kinase inhibitor, masitinib." *Biomaterials* **2013,** *34*, 9737-46.

(159) Re, F.; Muzio, M.; De Rossi, M.; Polentarutti, N.; Giri, J. G.; Mantovani, A.; Colotta, F. "The type II "receptor" as a decoy target for interleukin 1 in polymorphonuclear leukocytes: Characterization of induction by dexamethasone and ligand binding properties of the released decoy receptor." *The Journal of Experimental Medicine* **1994,** *179*, 739-743.

(160) Auphan, N.; DiDonato, J. A.; Rosette, C.; Helmberg, A.; Karin, M. "Immunosuppression by glucocorticoids: Inhibition of NF-κb activity through induction of iκb synthesis." *Science* **1995,** *270*, 286-290.

(161) Hori, Y.; Hu, D.-E.; Yasui, K.; Smither, R. L.; Gresham, G. A.; Fan, T.-P. D. "Differential effects of angiostatic steroids and dexamethasone on angiogenesis and cytokine levels in rat sponge implants." *British Journal of Pharmacology* **1996,** *118*, 1584-1591.

(162) Ward, W. K.; Hansen, J. C.; Massoud, R. G.; Engle, J. M.; Takeno, M. M.; Hauch, K. D. "Controlled release of dexamethasone from subcutaneously-implanted biosensors in pigs: Localized anti-inflammatory benefit without systemic effects." *Journal of Biomedical Materials Research Part A* **2010,** *94*, 280-7.

(163) Patil, S. D.; Papadimitrakopoulos, F.; Burgess, D. J. "Dexamethasone-loaded poly(lactic-co-glycolic) acid microspheres/poly(vinyl alcohol) hydrogel composite coatings for inflammation control." *Diabetes Technology and Therapeutics* **2004,** *6*, 887-97.

(164) Norton, L. W.; Koschwanez, H. E.; Wisniewski, N. A.; Klitzman, B.; Reichert, W. M. "Vascular endothelial growth factor and dexamethasone release from nonfouling sensor coatings affect the foreign body response." *Journal of Biomedical Materials Research Part A* **2007,** *81*, 858-69.

(165) Moura, S. A. L.; Lima, L. D. C.; Andrade, S. P.; Silva-Cunha Junior, A. D.; Órefice, R. L.; Ayres, E.; Da Silva, G. R. "Local drug delivery system: Inhibition of inflammatory angiogenesis

in a murine sponge model by dexamethasone-loaded polyurethane implants." *Journal of Pharmaceutical Sciences 100*, 2886-2895.

(166) Nakao, S.; Hata, Y.; Miura, M.; Noda, K.; Kimura, Y. N.; Kawahara, S.; Kita, T.; Hisatomi, T.; Nakazawa, T.; Jin, Y.; Dana, M. R.; Kuwano, M.; Ono, M.; Ishibashi, T.; Hafezi-Moghadam, A. "Dexamethasone inhibits interleukin-1β-induced corneal neovascularization: Role of nuclear factor-κB-activated stromal cells in inflammatory angiogenesis." *The American Journal of Pathology* **2007** *171*, 1058-1065.

(167) Patil, S. D.; Papadmitrakopoulos, F.; Burgess, D. J. "Concurrent delivery of dexamethasone and VEGF for localized inflammation control and angiogenesis." *Journal of Controlled Release* **2007,** *117*, 68-79.

(168) Kastellorizios, M.; Papadimitrakopoulos, F.; Burgess, D. J. "Multiple tissue response modifiers to promote angiogenesis and prevent the foreign body reaction around subcutaneous implants." *Journal of Controlled Release* **2015,** *214*, 103-11.

(169) Price, C. F.; Burgess, D. J.; Kastellorizios, M. "L-DOPA as a small molecule surrogate to promote angiogenesis and prevent dexamethasone-induced ischemia." *Journal of Controlled Release* **2016,** *235*, 176-181.

(170) Klueh, U.; Kaur, M.; Montrose, D. C.; Kreutzer, D. L. "Inflammation and glucose sensors: Use of dexamethasone to extend glucose sensor function and life span in vivo." *Journal of Diabetes Science and Technology* **2007,** *1*, 496-504.

(171) Radomski, M. W.; Palmer, R. M. J.; Moncada, S. "Endogenous nitric oxide inhibits human platelet adhesion to vascular endothelium." *The Lancet* **1987,** *330*, 1057-1058.

(172) Cooke, J. P.; Losordo, D. W. "Nitric oxide and angiogenesis." *Circulation* **2002,** *105*, 2133-2135.

(173) Coleman, J. W. "Nitric oxide in immunity and inflammation." *International Immunopharmacology* **2001,** *1*, 1397-406.

(174) Korhonen, R.; Lahti, A.; Kankaanranta, H.; Moilanen, E. "Nitric oxide production and signaling in inflammation." *Current Drug Targets. Inflammation and Allergy* **2005,** *4*, 471-479.

(175) Bult, H.; Boeckxstaens, G. E.; Pelckmans, P. A.; Jordaens, F. H.; Maercke, Y. M. V.; Herman, A. G. "Nitric oxide as an inhibitory non-adrenergic non-cholinergic neurotransmitter."

Nature **1990,** *345*, 346-347.

(176) Schwentker, A.; Vodovotz, Y.; Weller, R.; Billiar, T. R. "Nitric oxide and wound repair: Role of cytokines?" *Nitric Oxide* **2002,** *7*, 1-10.

(177) Carpenter, A. W.; Schoenfisch, M. H. "Nitric oxide release part II. Therapeutic applications." *Chemical Society reviews* **2012,** *41*, 3742-3752.

(178) Nathan, C.; Xie, Q.W. "Nitric oxide synthases: Roles, tolls, and controls." *Cell* **1994,** *78*, 915-918.

(179) Nathan, C. "Nitric oxide as a secretory product of mammalian cells." *FASEB Journal* **1992,** *6*, 3051-64.

(180) Griffith, O. W.; Stuehr, D. J. "Nitric oxide synthases: Properties and catalytic mechanism." *Annual Review of Physiology* **1995,** *57*, 707-734.

(181) Bogdan, C. "Nitric oxide and the immune response." *Nature Immunology* **2001,** *2*, 907-16.

(182) Aktan, F. "iNOS-mediated nitric oxide production and its regulation." *Life Sciences* **2004,** *75*, 639-653.

(183) Wetzler, C.; Kampfer, H.; Pfeilschifter, J.; Frank, S. "Keratinocyte-derived chemotactic cytokines: Expressional modulation by nitric oxide in vitro and during cutaneous wound repair in vivo." *Biochemical and Biophysical Research Communications* **2000,** *274*, 689-96.

(184) Deakin, A. M.; Payne, A. N.; Whittle, B. J.; Moncada, S. "The modulation of IL-6 and TNF-α release by nitric oxide following stimulation of J774 cells with LPS and IFN-γ." *Cytokine* **1995,** *7*, 408-16.

(185) Frank, S.; Kämpfer, H.; Wetzler, C.; Stallmeyer, B.; Pfeilschifter, J. "Large induction of the chemotactic cytokine rantes during cutaneous wound repair: A regulatory role for nitric oxide in keratinocyte-derived RANTES expression." *Biochemical Journal* **2000,** *347*, 265-273.

(186) Hill, J. R.; Corbett, J. A.; Kwon, G.; Marshall, C. A.; McDaniel, M. L. "Nitric oxide regulates interleukin-1 bioactivity released from murine macrophages." *Journal of Biological Chemistry* **1996,** *271*, 22672-8.

(187) Inoue, N.; Venema, R. C.; Sayegh, H. S.; Ohara, Y.; Murphy, T. J.; Harrison, D. G. "Molecular regulation of the bovine endothelial cell nitric oxide synthase by transforming growth factor-β 1." *Arteriosclerosis, Thrombosis, and Vascular Biology* **1995,** *15*, 1255-61.

(188) van der Zee, R.; Murohara, T.; Luo, Z.; Zollmann, F.; Passeri, J.; Lekutat, C.; Isner, J. M. "Vascular endothelial growth factor/vascular permeability factor augments nitric oxide release from quiescent rabbit and human vascular endothelium." *Circulation* **1997,** *95*, 1030-7.

(189) Dulak, J.; Jozkowicz, A.; Dembinska-Kiec, A.; Guevara, I.; Zdzienicka, A.; Zmudzinska-Grochot, D.; Florek, I.; Wojtowicz, A.; Szuba, A.; Cooke, J. P. "Nitric oxide induces the synthesis of vascular endothelial growth factor by rat vascular smooth muscle cells." *Arteriosclerosis, Thrombosis, and Vascular Biology* **2000,** *20*, 659-66.

(190) Keefer, L. K. "Fifty years of diazeniumdiolate research. From laboratory curiosity to broad-spectrum biomedical advances." *ACS Chemical Biology* **2011,** *6*, 1147-1155.

(191) Broniowska, K. A.; Diers, A. R.; Hogg, N. "*S*-nitrosoglutathione." *Biochimica et Biophysica Acta* **2013,** *1830*, 3173-3181.

(192) Riccio, D. A.; Nugent, J. L.; Schoenfisch, M. H. "Stöber synthesis of nitric oxide-releasing *S*-nitrosothiol-modified silica particles." *Chemistry of Materials* **2011,** *23*, 1727-1735.

(193) McCarthy, C. W.; Guillory Ii, R. J.; Goldman, J.; Frost, M. C. "Transition metal mediated release of nitric oxide (NO) from *S*-nitroso-*N*-acetylpenicillamine (SNAP): Potential applications for endogenous release of NO on the surface of stents via corrosion products." *ACS Applied Materials and Interfaces* **2016,** *8*, 10128–10135.

(194) Batchelor, M. M.; Reoma, S. L.; Fleser, P. S.; Nuthakki, V. K.; Callahan, R. E.; Shanley, C. J.; Politis, J. K.; Elmore, J.; Merz, S. I.; Meyerhoff, M. E. "More lipophilic dialkyldiamine-based diazeniumdiolates: Synthesis, characterization, and application in preparing thromboresistant nitric oxide release polymeric coatings." *Journal of Medicinal Chemistry* **2003,** *46*, 5153-5161.

(195) Espadas-Torre, C.; Oklejas, V.; Mowery, K.; Meyerhoff, M. E. "Thromboresistant chemical sensors using combined nitric oxide release/ion sensing polymeric films." *Journal of the American Chemical Society* **1997,** *119*, 2321-2322.

(196) Schoenfisch, M. H.; Mowery, K. A.; Rader, M. V.; Baliga, N.; Wahr, J. A.; Meyerhoff, M. E. "Improving the thromboresistivity of chemical sensors via nitric oxide release: Fabrication and in vivo evaluation of nitric oxide-releasing oxygen-sensing catheters." *Analytical Chemistry*

2000, *72*, 1119-1126.

(197) Yan, Q.; Major, T. C.; Bartlett, R. H.; Meyerhoff, M. E. "Intravascular glucose/lactate sensors prepared with nitric oxide releasing poly(lactide-*co*-glycolide)-based coatings for enhanced biocompatibility." *Biosens Bioelectron* **2011,** *26*, 4276-82.

(198) Gifford, R.; Batchelor, M. M.; Lee, Y.; Gokulrangan, G.; Meyerhoff, M. E.; Wilson, G. S. "Mediation of in vivo glucose sensor inflammatory response via nitric oxide release." *Journal of Biomedical Materials Research Part A* **2005,** *75*, 755-66.

(199) Coneski, P. N.; Schoenfisch, M. H. "Competitive formation of *N*-diazeniumdiolates and *N*-nitrosamines via anaerobic reactions of polyamines with nitric oxide." *Organic Letters* **2009,** *11*, 5462-5465.

(200) Wolf, A. K.; Qin, Y.; Major, T. C.; Meyerhoff, M. E. "Improved thromboresistance and analytical performance of intravascular amperometric glucose sensors using optimized nitric oxide release coatings." *Chinese Chemical Letters* **2015,** *26*, 464-468.

(201) Storm, W. L.; Schoenfisch, M. H. "Nitric oxide-releasing xerogels synthesized from *N*-diazeniumdiolate-modified silane precursors." *ACS Applied Materials and Interfaces* **2013,** *5*, 4904-4912.

(202) Riccio, D. A.; Coneski, P. N.; Nichols, S. P.; Broadnax, A. D.; Schoenfisch, M. H. "Photoinitiated nitric oxide-releasing tertiary *S*-nitrosothiol-modified xerogels." *ACS Applied Materials and Interfaces* **2012,** *4*, 796-804.

(203) Polizzi, M. A.; Stasko, N. A.; Schoenfisch, M. H. "Water-soluble nitric oxide-releasing gold nanoparticles." *Langmuir* **2007,** *23*, 4938-4943.

(204) Rothrock, A. R.; Donkers, R. L.; Schoenfisch, M. H. "Synthesis of nitric oxide-releasing gold nanoparticles." *Journal of the American Chemical Society* **2005,** *127*, 9362-9363.

(205) Carpenter, A. W.; Johnson, J. A.; Schoenfisch, M. H. "Nitric oxide-releasing silica nanoparticles with varied surface hydrophobicity." *Colloids and Surfaces A: Physicochemical and Engineering Aspects* **2014,** *454*, 144-151.

(206) Backlund, C. J.; Worley, B. V.; Sergesketter, A. R.; Schoenfisch, M. H. "Kinetic-dependent killing of oral pathogens with nitric oxide." *Journal of Dental Research* **2015,** *94*, 1092-1098.

(207) Stasko, N. A.; Fischer, T. H.; Schoenfisch, M. H. "*S*-nitrosothiol-modified dendrimers as nitric oxide delivery vehicles." *Biomacromolecules* **2008,** *9*, 834-841.

(208) Worley, B. V.; Soto, R. J.; Kinsley, P. C.; Schoenfisch, M. H. "Active release of nitric oxide-releasing dendrimers from electrospun polyurethane fibers." *ACS Biomaterials Science and Engineering* **2016,** *2*, 426-437.

(209) Suchyta, D. J.; Schoenfisch, M. H. "Encapsulation of n-diazeniumdiolates within liposomes for enhanced nitric oxide donor stability and delivery." *Molecular Pharmaceutics* **2015,** *12*, 3569-74.

(210) Backlund, C. J.; Worley, B. V.; Schoenfisch, M. H. "Anti-biofilm action of nitric oxide-releasing alkyl-modified poly(amidoamine) dendrimers against streptococcus mutans." *Acta Biomaterialiaialia* **2016,** *29*, 198-205.

(211) Worley, B. V.; Schilly, K. M.; Schoenfisch, M. H. "Anti-biofilm efficacy of dual-action nitric oxide-releasing alkyl chain modified poly(amidoamine) dendrimers." *Molecular Pharmaceutics* **2015,** *12*, 1573-83.

(212) Shin, J. H.; Schoenfisch, M. H. "Inorganic/organic hybrid silica nanoparticles as a nitric oxide delivery scaffold." *Chemistry of Materials* **2008,** *20*, 239-249.

(213) Koh, A.; Carpenter, A. W.; Slomberg, D. L.; Schoenfisch, M. H. "Nitric oxide-releasing silica nanoparticle-doped polyurethane electrospun fibers." *ACS Applied Materials and Interfaces* **2013,** *5*, 7956-7964.

(214) Kusaka, T.; Nakayama, M.; Nakamura, K.; Ishimiya, M.; Furusawa, E.; Ogasawara, K. "Effect of silica particle size on macrophage inflammatory responses." *PLoS One* **2014,** *9*, e92634.

(215) Waters, K. M.; Masiello, L. M.; Zangar, R. C.; Tarasevich, B. J.; Karin, N. J.; Quesenberry, R. D.; Bandyopadhyay, S.; Teeguarden, J. G.; Pounds, J. G.; Thrall, B. D. "Macrophage responses to silica nanoparticles are highly conserved across particle sizes." *Toxicological Sciences* **2009,** *107*, 553-569.

(216) Hetrick, E. M.; Prichard, H. L.; Klitzman, B.; Schoenfisch, M. H. "Reduced foreign body response at nitric oxide-releasing subcutaneous implants." *Biomaterials* **2007,** *28*, 4571-4580.

(217) Nichols, S. P.; Koh, A.; Brown, N. L.; Rose, M. B.; Sun, B.; Slomberg, D. L.; Riccio, D. A.; Klitzman, B.; Schoenfisch, M. H. "The effect of nitric oxide surface flux on the foreign body response to subcutaneous implants." *Biomaterials* **2012,** *33*, 6305-12.

(218) Soto, R. J.; Yang, L.; Schoenfisch, M. H. "Functionalized mesoporous silica via an aminosilane surfactant ion exchange reaction: Controlled scaffold design and nitric oxide release." *ACS Applied Materials & Interfaces* **2016,** *8*, 2220-2231.

(219) Nichols, S. P.; Le, N. N.; Klitzman, B.; Schoenfisch, M. H. "Increased in vivo glucose recovery via nitric oxide release." *Analytical Chemistry* **2011,** *83*, 1180-1184.

CHAPTER 2. IN VIVO ANALYTICAL PERFORMANCE OF NITRIC OXIDE-RELEASING GLUCOSE BIOSENSORS[2]

2.1. Introduction

Despite the obvious benefits of continuous glucose monitoring (CGM) for the management of diabetes, the utility of in vivo amperometric glucose biosensors is limited to <1 week due to poor analytical performance, resulting primarily from the foreign body response (FBR).[1-2] Insertion of the sensor damages vascularized tissue and results in a cascade of inflammatory events, many of which negatively impact glucose measurements.[3] For example, the resulting passive adsorption of biomolecules (mainly <15 kDa protein fragments) to the sensor surface initiates an inflammatory response and is responsible for a dramatic decrease in sensor sensitivity (~50%) following sensor implantation.[3-6] Increased metabolic activity of inflammatory cells (i.e., macrophages and foreign body giant cells) at the sensor-tissue interface results in inordinate consumption of glucose and oxygen, decreasing their local concentrations and attenuating sensor performance.[7] The hallmark of the FBR is the formation of a thick, avascular collagen capsule surrounding the sensor, isolating it from the surrounding tissue and obstructing mass transport of interstitial glucose to the sensor.[3] Indeed, the FBR increases sensor response time, decreases sensitivity, and often results in device failure.

Efforts to improve the analytical performance of in vivo biosensors have largely focused on chemical or physical modifications to the outermost, tissue-contacting membrane to mitigate

[2]This chapter was adapted from an article that previously appeared in *Analytical Chemistry*. The original citation is as follows: Soto, R. J.; Privett, B. J.; Schoenfisch, M. H. "In vivo analytical performance of nitric oxide-releasing glucose biosensors" *Analytical Chemistry* **2014**, *86*, 7141–7149.

the FBR.[8] Examples of such strategies include biomimicry (e.g., the attachment of phospholipids to coating surfaces),[9] employing naturally-derived materials as coatings,[10] utilizing membranes that reduce cell adhesion,[11] encouraging tissue ingrowth into porous coatings,[12-13] and modulating cell behavior through coating topography.[14] The active release of anti-inflammatory or pro-angiogenic bioactive agents such as dexamethasone (DX) and vascular endothelial growth factor (VEGF) has also been proposed as a viable option for improving glucose sensor function.[15-16] However, in addition to the immune suppression associated with DX[17] and pro-inflammatory roles of VEGF,[18] controlled release of these molecules from sensor coatings remains a major hurdle.

The release of nitric oxide (NO)—an endogenous molecule with multiple roles in inflammation, wound healing, and angiogenesis—from polymeric coatings has shown ability to minimize the FBR.[1,19-21] Hetrick et al. examined the FBR to subcutaneously implanted NO-releasing xerogels coated on silicone elastomers in a murine model.[22] Nitric oxide-releasing implants, which generated ~1.35 μmol cm^{-2} NO over 72 h at fluxes >1 pmol cm^{-2} s^{-1}, elicited only a mild FBR with reduced fibrous encapsulation (>25%) after 3 and 6 wk compared to tissue near control implants. Concomitant with a reduced FBR, blood vessel density in the tissue surrounding the NO-releasing implants was greater (~50%) than that observed surrounding control implants. Nichols et al. assessed glucose recovery as a function of NO release percutaneously implanted microdialysis probes.[23] A constant NO flux (162 pmol cm^{-2} s^{-1}, 4.6 μmol cm^{-2} NO daily) was achieved from microdialysis probes by using a saturated NO solution as the perfusate. While glucose recovery from control probes was severely diminished beyond 7 d, NO-releasing microdialysis probes exhibited near constant glucose recovery throughout the study. These results were correlated to tissue histology observations. Indeed, histological

analysis of the tissue surrounding NO-releasing probes at 14 d revealed lower inflammatory cell counts and a thinner collagen capsule versus probes that did not release NO. The lessened FBR and increased glucose recovery suggest that NO release lowered tissue impedance to glucose transport. In a separate study, Nichols and coworkers investigated the effects of NO-release kinetics on the FBR to subcutaneous NO-releasing wire implants (i.e., mock glucose sensors) in a porcine model.[24] Decreased collagen capsule thickness (>50%) was observed for substrates that released NO for extended durations (i.e., >3 d) versus implants that did not release NO. In contrast, substrates with shorter NO-release durations (12–24 h) were characterized by greater collagen density at the implant-tissue interface compared to the materials which released NO for extended durations. Collectively, this body of work highlights the dramatic effect of NO-release kinetics on the FBR and the potential to impact the analytical performance of in vivo glucose biosensors.

Despite extensive characterization of the host response to NO-releasing implants, the interplay between reduced FBR and actual sensor performance remains a critical void. To date, only one study has evaluated the in vivo performance of a NO-releasing glucose sensor. Gifford et al. reported improved clinical accuracy for NO-releasing needle-type glucose biosensors implanted in rats for 3 d.[25] However, the NO release from the sensors was limited to 16 h and deterioration of sensor performance by day 3 was observed.[26] Histological analysis of the surrounding tissues revealed suppressed inflammation at NO-releasing sensors on day 1 versus controls, but no benefits following depletion of the NO reservoir. Clearly, the role of NO release on sensor analytical performance should be studied in greater detail.

As the severity of the FBR to NO-releasing implants is dependent on release properties, we sought to investigate these effects on the performance of percutaneously implanted glucose

biosensors. Given previous findings, it is hypothesized that by extending NO-release duration, sensor merits (i.e., accuracy, sensitivity, response time) may be maintained for longer implantation periods (>7 d). Herein, we report on the analytical performance of NO-releasing needle-type glucose biosensors in swine as a function of NO-release duration.

2.2. Experimental section

2.2.1. Materials

Glucose oxidase (GOx; type VII from *Aspergillus niger*, >100,000 units g^{-1}), D-(+)-glucose anhydrous, acetaminophen (AP), L-ascorbic acid (AA), urea (UA), phenol, and sodium methoxide (5.4 M in methanol) were purchased from Sigma (St. Louis, MO.). Tetrahydrofuran (THF), ethanol (EtOH), aqueous ammonium hydroxide (30 wt%), and all salts were purchased from Fisher Scientific (St. Louis, MO.). Tetraethyl orthosilicate (TEOS), (3-mercaptopropyl)trimethoxysilane (MPTMS), and (3-methylaminopropyl)trimethoxysilane (MAP) were purchased from Gelest (Tullytown, PA). Methyltrimethoxysilane (MTMOS) and diethylenetriaminepentaacetic acid (DTPA) was purchased from Fluka (Buchs, Switzerland). Cetyltrimethylammonium bromide (CTAB) was purchased from Acros Organics (Geel, Belgium). Hydrothane (AL-25-80A) polyurethane (HPU) was a gift from AdvanSource Biomaterials (Wilmington, MA). Tecoflex (SG-85A) polyurethane (TPU) was a gift from Lubrizol (Cleveland, OH). Steel wire (356 μm dia.) was purchased from McMaster-Carr (Atlanta, GA). Argon, nitrogen, oxygen, and nitric oxide calibration gas (25.87 ppm in nitrogen) were purchased from Airgas National Welders (Raleigh, NC). Nitric oxide gas was purchased from Praxair (Danbury, CT). Water was purified to a resistivity of 18.2 MΩ·cm and a total organic content of ≤6 ppb using a Millipore Milli-Q UV gradient A10 system (Bedford, MA). All other chemicals were reagent grade and used as received.

2.2.2. Synthesis of nitric oxide-releasing silica nanoparticles

Synthesis of the NO-releasing silica nanoparticles was carried out as described previously.[27] The MPTMS particles were synthesized via a co-condensation approach by adding a pre-mixed solution of MPTMS (2.27 mmol) and TEOS (0.76 mmol) at 0.5 mL min^{-1} to a stirred solution of EtOH (16.3 mL), H_2O (1.4 mL), and 29 wt% aqueous NH_3 (11.0 mL). The resulting solution was stirred for 2 h at room temperature. The MPTMS particles were collected by centrifugation (4500×*g*, 10 min), washed twice with EtOH to remove ammonia and unreacted silane precursors, and dried under reduced pressure. *S*-nitrosation of the thiol-containing nanoparticles was accomplished by reaction with acidified sodium nitrite. The particles (~120 mg) were suspended in a stirred mixture of MeOH (4 mL), 5 M HCl (2 mL), and 2.3 M aqueous sodium nitrite (2 mL) with DTPA (500 μM) added to chelate trace copper ions. The reaction was carried out on ice and in the dark for 2 h. The NO-releasing particles were collected by centrifugation (4500×*g*, 4 ^{o}C, 10 min) and washed with cold 500 μM aqueous DTPA (1×) followed by cold MeOH (2×). The particles were dried under reduced pressure for 1 h and used immediately thereafter.

The MAP particles were prepared by grafting the aminosilane (MAP) to the surface of mesoporous silica nanoparticles (MSNs). The MSNs were first synthesized using CTAB as a surfactant template. Tetraethylorthosilicate (6.25 mmol) was added as a bolus to a stirred solution of EtOH (175 mL), H_2O (162 mL), 29 wt% aqueous NH_3 (11.8 mL), and the surfactant CTAB (0.77 mmol). The resulting solution was stirred for 2 h. The mesoporous silica particles were collected by centrifugation (4500×*g*, 10 min) and washed once with EtOH. The surfactant was removed by agitating the particles in 35 mL 10 vol% ethanolic HCl in an ultrasonicator bath. After repeating this wash procedure three times, the particles were again purified with EtOH and

dried under vacuum. Secondary amines were introduced into the silica scaffold by reacting 50 mg particles with MAP (0.50 mmol) and pyridine (0.60 mmol) in toluene (20 mL) at 90 ^{o}C for 18 h. The particles were again collected by centrifugation, washed twice with EtOH, and dried under vacuum. Subsequently, *N*-diazeniumdiolate NO donors were formed on the secondary amines. The MAP-modified MSNs (~15 mg) were suspended in 9:1 DMF:MeOH at 5 mg mL^{-1} in a glass vial and dispersed by ultrasonication for 20 min. A base catalyst for the *N*-diazeniumdiolate formation reaction (NaOMe, 5.4 M in MeOH; 9.0 μmol per mg MSN) was added to the solution. The MSN-containing vials were equipped with stir bars, placed in a stainless steel reaction bottle (Parr Instrument Co.; Moline, IL), and connected to an in-house NO reactor. The Parr bottle was flushed six times (three rapid, three 10 min) with 8 bar Ar gas to remove atmospheric oxygen and minimize the formation of NO byproducts. The vessel was subsequently pressurized with 10 bar NO gas and allowed to react for 72 h. Of note, the NO gas used for *N*-diazeniumdiolate formation was purified over solid potassium hydroxide for at least 4 h prior to reaction. The Parr bottle was vented after 72 h and the vessel flushed with Ar six more times to remove unreacted NO. The particles were collected by centrifugation (4500×*g*, 4 ^{o}C, 15 min), washed three times with EtOH, and dried under reduced pressure for 1–2 h. The resulting *N*-diazeniumdiolate-modified particles were stored in a vacuum-sealed Mylar bag at -20 ^{o}C until further use.

2.2.3. Preparation of nitric oxide-releasing mock sensors

Steel wire was cut in 7 cm pieces and cleaned by sonication in EtOH for 10 min. Polymer solutions containing the macromolecular NO-release scaffolds were prepared by dispersing MAP or MPTMS particles (72 and 48 mg mL^{-1}, respectively) in an 80 mg mL^{-1} solution of 1:1 (by mass) HPU/TPU in 1:1 (v/v) EtOH:THF. Wire substrates were modified by dip coating (5 mm s^{-}

[1] with a 5-s hold time) four times into the particle-containing PU solution using a DipMaster™ 50 dip coater (Chemat Technology, Inc.; Northridge, CA) with 30 min drying periods under ambient conditions between dips. A final TPU topcoat was applied by dip coating into a 40 mg mL^{-1} TPU solution in THF.

2.2.4. Characterization of nitric oxide-releasing substrates

Nitric oxide release from the steel wire substrates was measured in real time using a Sievers 280i chemiluminescence NO analyzer (NOA; Boulder, CO). Generation of NO from PU films was detected indirectly by the formation of a chemiluminescent product (NO_2^*) upon reaction of NO with ozone. The NOA was calibrated using an atmospheric gas sample passed through a Sievers NO zero filter (0 ppb) and 25.9 ppm NO in N_2. Substrates were immersed in deoxygenated phosphate buffered saline (PBS; 0.01 M, pH 7.4) at 37 ^oC. The liberated NO from PU films was carried to the NOA by a stream of nitrogen gas, bubbled into solution at a volumetric flow rate of 75 mL min^{-1}. For films containing *S*-nitrosothiol NO donors (i.e., MPTMS particles), the sample flask was shielded from light and 500 μM DTPA was added to the PBS buffer to chelate trace copper. Data output from the NOA was collected every 1 s, allowing for near real-time monitoring of NO generated from the films.

The stability of silica particles in PU films was assessed using inductively coupled plasma optical emission spectrometry (ICP-OES). Modified wire substrates were immersed in PBS buffer and incubated at 37 ^oC for 10 d. The degree of particle leaching into soak solutions was determined by monitoring the silicon emission intensity at 251.611 nm using a Prodigy high dispersion ICP-OES instrument (Teledyne Leeman Labs; Hudson, NH).

2.2.5. Fabrication and in vitro performance of nitric oxide-releasing glucose sensors

Bare needle-type glucose sensors (Pinnacle Technology, Inc., Lawrence, KS), composed of an integrated silver/silver chloride (Ag|AgCl) pseudo-reference electrode wound around a 90:10 platinum:iridium (Pt/Ir) working electrode (176 μm dia., ~1 mm length), were functionalized by the successive deposition of a polyphenol selectivity layer, a GOx enzyme layer, a NO-releasing flux-limiting membrane, and a polyurethane topcoat, as described previously.[28-30] Bare sensors were first cleaned by sonication in EtOH. Electropolymerization of phenol onto the working electrode was carried out via chronocoulometry (+900 mV vs. Ag|AgCl, 15 min) in a stirred solution of deoxygenated PBS buffer containing 40 mM phenol. The total charge passed was measured to be $-1.64\pm0.18\times10^{-3}$ C cm^{-2}. Following electrodeposition of the inner-most polyphenol layer, sensors were sterilized in CIDEX PLUS® 28 Day Solution per the manufacturer's instructions and rinsed with sterile water. All subsequent fabrication steps were carried out in a sterile laminar flow hood. Glucose oxidase was immobilized on the sensing surface by encapsulating the GOx in a MTMOS xerogel membrane. A GOx-containing sol was prepared by mixing 50 μL 120 mg mL^{-1} GOx in H_2O with 125 μL 20% v/v MTMOS in EtOH. The addition of water to the alcohol/silane mixture initiates the condensation of the silane monomers to form a polymerized silica xerogel that entraps GOx. Sensors were dip-coated 15 times (5-s still time with 10-s drying periods) into the resulting sol and allowed to dry for 30 min. Following deposition of the selectivity and enzyme layers, sensors were coated with a PU diffusion-limiting/NO-releasing layer by dip-coating into a particle-containing PU solution. A TPU topcoat was then applied as an additional layer. Control sensors were coated using PU solutions containing MAP or MPTMS nanoparticles (72 and 48 mg mL^{-1}, respectively) that were not functionalized with *N*-diazeniumdiolate or *S*-nitrosothiol

NO donors.

2.2.6. In vivo protocol for assessing glucose biosensor analytical performance

The animal protocol used in this study was IACUC approved. The in vivo performance of glucose biosensors was evaluated in ten Yorkshire-type piglets weighing approximately 7–15 kg. Pigs were initially anesthetized using Telazol (2–6 mg kg^{-1} intramuscular) and anesthesia was maintained using isoflurane (2–3% v/v balance oxygen gas) during sensor implantation. Six sensors (three NO-releasing, three control) were implanted in pairs (one NO-releasing, one control, spaced 3 cm apart) by cannulation (22-gauge needle) into the subcutaneous space using aseptic technique. Sensors were positioned approximately 4 cm lateral and perpendicular to the spine and 12–30 cm caudal to the scapulae. Dermabond™ was used to secure the sensor at the entry wound. The sensors were further secured using Prolene 3-0 sutures, gauze, and Opsite®. Sensor pairs were connected to battery-operated wireless bipotentiostats (model 8100 K-5, Pinnacle Technology, Inc.; Lawrence, KS) to allow free motion of the animal while applying a constant +600 mV (vs. Ag|AgCl) to the working electrode. The bipotentiostats transmitted current measurements wirelessly via an integrated RF transmitter to a nearby receiver. Data was collected in real time using Sirenia acquisition software (Pinnacle Technology, Inc.; Lawrence, KS).

Biosensor performance was evaluated at 0, 1, 3, 7, and 10 d post-implantation. A peripherally-inserted central catheter was placed in an external jugular vein for blood draws. Reference blood glucose (BG) concentrations were measured every 10 min for 6–8 h using a One Touch® Ultra glucometer (LifeScan, Inc.; Milpitas, CA) for comparison to sensor data. During glucose sensor evaluation, pigs were fasted and sedated with propofol (2 mg kg^{-1} h^{-1}) administered through a catheter in a peripheral ear vein. Once on the day of implantation and

three times daily thereafter, the swine were challenged with an intravenous glucose tolerance test (IVGTT; 0.7 g kg^{-1}, 50 wt% dextrose, 1–1.5 h duration), administered over 30 s through the peripheral catheter, to assess the ability of glucose sensors to track changing blood glucose concentrations. On day 10, pigs were euthanized and the sensors removed from the surrounding tissue. Post-explantation, sensors were imaged using environmental scanning electron microscopy (ESEM; FEI Quanta 200 Field Emission Gun; Hillsboro, OR).

2.2.7. Data analysis

Sensor current traces were filtered and analyzed using custom MATLAB scripts (Mathworks, Inc.; Natick, MA). A finite impulse response (FIR) filter was used to attenuate large noise spikes caused by pig motion and potentiostat RF transmitter dropout.[31] A one-minute median filter was used to further smooth the data before pairing sensor current traces with reference measurements. Glucose sensors were calibrated with respect to reference BG measurements once per day using a two-point retrospective calibration.[32-33] One point for calibration was taken at a stable glucose baseline (i.e., prior to the first IVGTT), while the second point was taken at a stable point after the first dextrose administration with at least a 15 mg dL^{-1} difference between BG concentrations. The slope of a linear trend line connecting these two points was taken as the apparent in vivo biosensor sensitivity on each day, expressed as mean values ± standard deviation. The method of Poincaré was used to approximate the time delay at which the correlation between the reference and calibrated sensor signals was greatest, using R^2 as the agreement criterion.[34-35] This delay was determined at ~5 min and used to correct sensor data on each day for the physiological time lag characteristic of glucose mass transfer from blood to tissue.[36] After sensor implantation, the "run-in" time (i.e., the time required for sensors to achieve a stable background current) was estimated by determining the period over which two

consecutive sensor measurements agreed with their respective reference measurements within 20%.

Sensor performance was determined using numerical and clinical accuracy metrics. The mean absolute relative deviation (MARD) for a data set collected by a single sensor (~25–35 measurements) was used to characterize sensor numerical accuracy at each time point.[37] Sensor MARD was calculated using Equation 1, where CGM and BG are the blood glucose values determined by the sensor and reference glucometer, respectively.

$$\text{MARD} = \text{Mean}\left(\frac{|\text{CGM}-\text{BG}|}{\text{BG}} * 100\right) \quad (1)$$

Additionally, the International Standards Organization (ISO) criteria for glucose monitor performance was used to assess sensor numerical accuracy by separately calculating the percentage of glucose measurements determined by sensors that were within (1) ±15 mg dL^{-1} of the paired reference determination when BG was $\leq$70 mg dL^{-1} and (2) ±20% of the paired reference determination when BG was >70 mg dL^{-1}.[37] Sensor clinical accuracy was determined using Clarke error grid analysis (EGA) by quantifying the percentage of blood glucose determinations falling in zones A and B of the error grid.[38] Cross-correlation of the reference signals and raw sensor current traces was used to estimate sensor lag time, with possible lag times restricted to >100 s.[39-40] Values for MARD and lag time are expressed as mean values ± standard error of the mean. Differences in median values for sensor MARD, lag time, and sensitivity between NO-releasing and control sensors were analyzed using a two-tailed non-parametric Mann-Whitney U test.[41]

2.3. Results and discussion

Nitric oxide-releasing polyurethanes were selected as sensor coatings for evaluating the effect of NO-release duration on in vivo glucose biosensor performance. Total NO payloads

sufficient for minimizing inflammation (i.e., >1 μmol cm^{-2})[22] with varied NO-release durations (<1 h to >14 d) were achieved by tuning the PU properties (i.e., water uptake) and NO donor type.[29] We have shown previously that sensor response is not negatively affected by NO release from PU coatings at a working electrode potential of +600 mV vs. Ag|AgCl.[29] The versatile NO-release kinetics and compatibility with amperometric glucose sensing make NO-releasing polyurethanes an ideal platform for assessing the effects of NO release on in vivo glucose biosensor performance.

2.3.1. In vitro characterization of nitric oxide-releasing glucose biosensors

Wire substrates, selected to mimic the geometry and size of a needle-type glucose sensor, were modified with NO-releasing PU coatings via a dip-coating procedure. A hydrophobic TPU topcoat was employed to both minimize any leaching of the macromolecular NO donors and eliminate the surface roughness introduced by nanoparticle dopants. Undoubtedly, the physical properties (i.e., roughness) of an implant surface will affect the FBR.[14,42] The stability of the nanoparticle-doped PU coatings in PBS was investigated over 10 d by analyzing the silicon content of soak solutions using ICP-OES. While silica is considered non-toxic,[22,43] the resulting changes in coating structure or potential tissue inflammation may affect the performance of glucose sensors in vivo. For coatings doped with NO-releasing MPTMS-RSNO particles as well as controls, leaching of silica particles from the PU matrix was undetectable (<2%). Slight leaching (10.8±2.9% of the total incorporated silica) was observed from coatings containing NO-releasing MAP/NO particles. Interestingly, the majority of the observed leaching occurred during the first 4 h, suggesting some instability associated with encapsulating the charged *N*-diazeniumdiolate NO donor moieties within the polyurethane coating (data not shown).

Table 2.1. Size and nitric oxide-release characterization for MAP/NO and MPTMS-RSNO silica nanoparticle dopants.

Nanoparticle NO Donor	$[NO]_T$ (μmol mg^{-1})[a]	Particle Diameter (nm)[b]
MAP	2.03±0.20	820±80
MPTMS	3.36±0.62	620±80

[a]Total NO storage [b]Nanoparticle diameter estimated via scanning electron microscopy

The effect of NO-release duration on in vivo sensor performance was studied using two different macromolecular NO release systems: *N*-diazeniumdiolate NO donors and *S*-nitrosothiol modified silica nanoparticles (MAP/NO and MPTMS-RSNO, respectively). Briefly, *N*-diazeniumdiolate NO donors undergo proton-initiated decomposition in aqueous environments to generate NO.[44] Conversely, NO release from *S*-nitrosothiols may be triggered using light or Cu(I), but also decompose sluggishly through thermal mechanisms in vivo.[27,45] To simulate in vivo conditions, NO release from PU films was measured in PBS at 37 ^{o}C. For MPTMS-RSNO coatings, thermal decomposition of the *S*-nitrosothiol moieties was achieved using a light-shielded sample flask and the addition of DTPA to chelate trace copper. Particle characterization is presented in Table 2.1. By appropriate selection of the nanoparticle dopant concentration (72 and 48 mg mL^{-1} for MAP/NO and MPTMS-RSNO particles, respectively) we attained similar total NO payloads (~3.1 μmol cm^{-2}) for both coating formulations (Table 2.2). Of note, NO payloads from these coatings were more than two times greater than the xerogel coatings utilized by Hetrick et al. (~1.35 μmol cm^{-2}) and similar in magnitude to those employed by Nichols et al. (2.7–9.3 μmol cm^{-2})—both of which proved effective at reducing the FBR to subcutaneous implants.[22,24]

Upon immersion in PBS, MAP/NO films exhibited a large initial NO flux ($[NO]_{max}$=685.8 pmol cm^{-2} s^{-1}) and released 99% of their total NO payload within ~16 h, with no additional NO release measurable beyond 24 h (Table 2.2). The NO-release duration (16 h) was similar to that reported to improve glucose sensor accuracy by Gifford and coworkers (12–18 h).[25] Similarly, MPTMS-RSNO films showed a large initial NO flux ($[NO]_{max}$=551.4 pmol cm^{-2} s^{-1}), with a rapid decrease to ~14.0 pmol cm^{-2} s^{-1} at 14 h. In contrast to the MAP/NO films, MPTMS-RSNO coatings required ~3.1 d to release 99% of their total NO payload, with NO

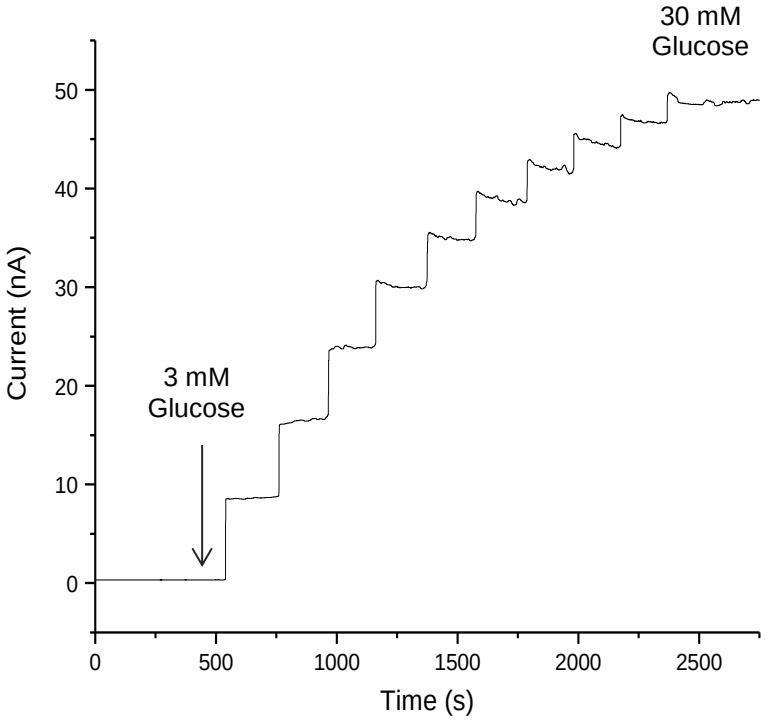

Figure 2.1. Amperometric glucose response for NO-releasing PU-coated (MPTMS-RSNO) needle type sensor after pre-conditioning in PBS.

Table 2.2. Nitric oxide release from polyurethane coatings doped with NO-releasing MPTMS-RSNO and MAP/NO nanoparticles.

NO-Release Merits	MPTMS-RSNO	MAP/NO
$[NO]_{max}$ (pmol cm^{-2} s^{-1})[a]	551.4±130.0	685.8±11.4
t_{max} (min)[b]	1.68±0.20	23.80±7.17
$t_{1/2}$ (h)[c]	6.29±2.07	0.93±0.17
$[NO]_{8h}$ (pmol cm^{-2} s^{-1})	14.0±3.9	13.0±3.2
$[NO]_{12h}$ (pmol cm^{-2} s^{-1})	9.8±3.8	3.7±1.5
$[NO]_{24h}$ (pmol cm^{-2} s^{-1})	3.3±0.2	0[d]
$[NO]_{48h}$ (pmol cm^{-2} s^{-1})	1.0 ±0.1	0[d]
$[NO]_{72h}$ (pmol cm^{-2} s^{-1})	0.5±0.0	0[d]
$[NO]_{168h}$ (pmol cm^{-2} s^{-1})	0.5±0.0	0[d]
$[NO]_T$ (μmol cm^{-2})[e]	3.14±0.26[f]	3.11±0.27
t_d (h)[g]	74.6±16.6	16.0±4.4

[a]Maximum instantaneous NO concentration. [b]Time required to reach maximum NO flux. [d]Half-life for NO-release from PU films. [d]Nitric oxide release was below the limit of detection of the NOA. [e]Total amount of NO released. [f]Measured by irradiation of the sample flask with 200 W light. [g]Determined at the time at which 99% of the total NO was released.

Table 2.3. Glucose sensor analytical performance in phosphate buffered saline at 37 ^{o}C.

Performance Merit	**Day[a]**	**MAP Control**	**MAP/NO**	**MPTMS Control**	**MPTMS-RSNO**
Sensitivity (nA mM^{-1})	0	2.3±0.2	2.3±0.1	2.1±0.4	2.2±0.7
	1	2.2±1.0	2.4±1.8	2.7±0.1	2.1±0.9
	3	1.3±0.3	1.5±1.3	2.2±1.0	2.0±1.4
	7	1.6±0.1	1.8±1.1	2.0±0.5	1.8±0.3
	10	1.4±1.0	1.9±1.5	1.3±0.3	1.4±0.8
Response Time (s)	0	28±18	13±9	36±12	40±27

[a]Time elapsed after immersing the sensors in PBS.

release (0.5 pmol cm^{-2} s^{-1}) still measurable at ~7 d. Even such low levels of NO are physiologically relevant, as vascular endothelial cells release NO at 1–7 pmol cm^{-2} s^{-1} to prevent platelet activation.[26,46] Additionally, similar NO fluxes (1.5–30 pmol cm^{-2} s^{-1}) inhibit in vitro bacterial adhesion to surfaces.[47-48] As expected, NO release from the outer glucose sensor membrane did not impact biosensor response. After an initial hydration period of 3–4 h, the glucose sensitivities of NO-releasing and control sensors were comparable and remained constant (1.3–2.3 nA mM^{-1}) over 10 d in PBS at 37 ^{o}C for all membrane formulations (Table 2.3). In the absence of pre-conditioning, sensors exhibited poorer dynamic range and longer response times to changes in glucose concentration during the first several hours of testing (data not shown). Both NO-releasing and control sensors exhibited acceptable response times (<40 s) to an increase in glucose concentration of 5.6 mM. All sensors responded linearly to glucose between 1–12 mM after pre-conditioning in PBS (Figure 2.1). Furthermore, the amperometric selectivity coefficients for glucose over acetaminophen, ascorbic acid, and urea were 0.82, 0.49, and 0.03, respectively for blank sensors (i.e., sensors that were coated solely with polyurethane). As expected, selectivity for glucose was sufficient.

2.3.2. In vivo biosensor run-in time, glucose sensitivity, and Clarke error grid

Following implantation, both NO-releasing and control biosensors displayed a run-in period during which the sensor response converged to a steady baseline signal (Figure 2.2A). While Gifford et al. reported a reduced run-in time for NO-releasing sensors versus control sensors in rodents,[25] we did not observe differences in run-in time between NO-releasing sensors and controls—all four sensor configurations required ~3–6 h to achieve a steady background current. The source of this discrepancy is unclear, but a number of variables (e.g., different animal model, implant method, and extended sensor hydration time) may have contributed to this

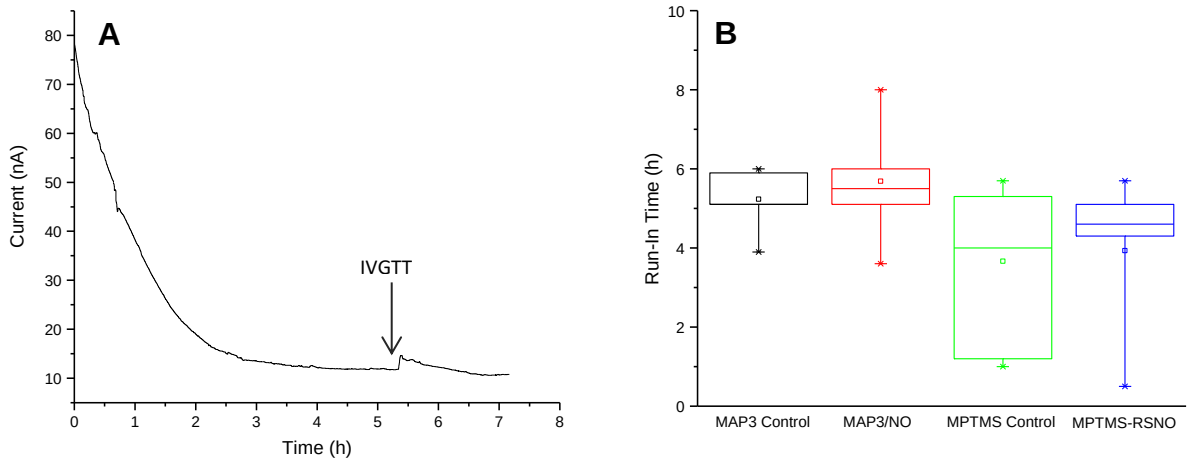

Figure 2.2. Representative current trace for glucose biosensor following implantation (A) and distribution of estimated run-in times for NO-releasing and control sensors (B). Error bars indicate the total spread of data and boxes represent data points that lie in the center quartiles (25–75%).

result. The potential analytical performance benefits of NO-releasing amperometric glucose biosensors were evaluated in a healthy swine model. The use of digital noise filters was required to achieve stable current traces due to swine motion and intermittent potentiostat RF transmitter dropout. The filtering algorithms were restricted to those compatible with real-time continuous glucose monitoring.[31] As expected, the FIR and median filters sufficiently improved signal quality without introducing an undesirable artificial time delay (>20%) between sensor and reference signals. Subsequently, sensors were calibrated by comparison to corresponding reference blood glucose measurements using a two-point retrospective calibration. A one-point calibration (which assumes a negligible background current) has been suggested to be superior to a two-point calibration.[32] However, the in vivo background in our study was substantial (6–10 nA) compared to the in vitro baseline (1–3 nA), necessitating the use of a two-point calibration. Other researchers have also reported disparities between in vitro and in vivo sensor baseline currents.[49] Despite minimizing the artificial delay caused by filtering, a physiological lag between the sensor signal and reference BG measurements was still observed. This delay arises from the slow mass transfer of glucose from the vasculature to the tissue and ultimately the sensor.[34-36] An analysis of sensor performance on day 0 via the method of Poincaré[35] indicated a ~5-min lag between the reference signal and calibrated sensor signal. This lag time was thus accounted for in all remaining data sets (days 1, 3, 7, and 10) by shifting the reference signal in time relative to the sensor signal.

The clinical accuracies of NO-releasing and control in vivo glucose biosensors were first assessed via the Clarke error grid.[38] The percentage of BG measurements falling in zones A and

Table 2.4. Clinical performance and apparent in vivo sensitivity of glucose biosensors.

Day		MAP Control	MAP/NO	MPTMS Control	MPTMS-RSNO
	% Points in Zones A/B	89.6	87.6	91.0	94.7
0	N[a]	183	105	311	321
	Sensitivity (nA mM^{-1})	0.90±0.87	0.72±0.40	0.74±0.47	0.60±0.30
	% Points in Zones A/B	78.6	86.2	90.6	89.1
1	N[a]	168	174	224	347
	Sensitivity (nA mM^{-1})	0.14±0.09	0.59±0.54[b]	0.29±0.18	0.39±0.17
	% Points in Zones A/B	84.8	92.0	81.7	83.9
3	N[a]	169	173	180	124
	Sensitivity (nA mM^{-1})	0.18±0.04	0.59±0.40[b]	0.24±0.16	0.49±0.18
	% Points in Zones A/B	93.2	94.2	88.3	88.1
7	N[a]	115	87	157	69
	Sensitivity (nA mM^{-1})	0.23±0.15	0.39±0.26	0.20±0.07	0.45±0.19
	% Points in Zones A/B	84.8	81.4	91.8	84.9
10	N[a]	138	97	135	66
	Sensitivity (nA mM^{-1})	0.16±0.06	0.20±0.13	0.09±0.02	1.3±1.1

[a]Total number of measurements.
[b]Significantly different at $p<0.05$.

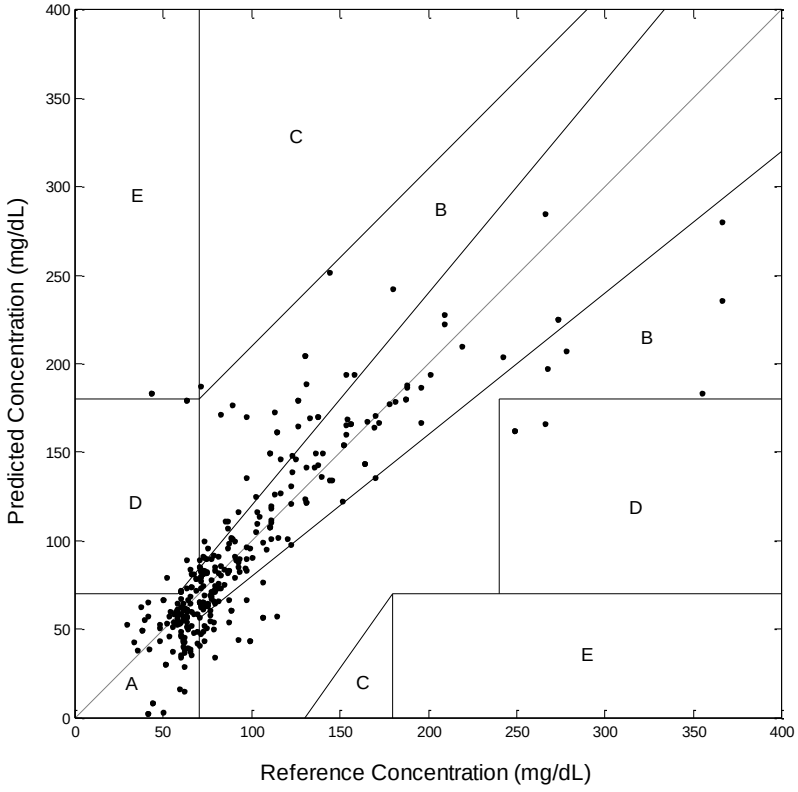

Figure 2.3. Clarke error grid for MPTMS-RSNO biosensors on day 0. While daily IVGTT provided excursions into the hyperglycemic range, the majority of glucose determinations (~70%) were made in the 50–100 mg dL^{-1} range. Zones labeled A and B represent clinically acceptable blood glucose measurements, while zones C, D, and E represent erroneous and progressively worse determinations.

B (clinically accurate and clinically benign determinations, respectively) of the error grid are shown in Table 2.4. On the day of implantation (day 0), the MAP/NO-based sensors performed slightly worse than control sensors, with a 2% difference in the percentage of determinations in zones A and B. However, the performance of MAP/NO sensors on days 1 and 3 was superior to controls, with >7% difference in the percentage of clinically accurate and acceptable determinations. Concomitant with improved clinical performance, sensors that rapidly released NO were characterized as having greater glucose sensitivity on days 1 and 3 (0.59 nA mM^{-1} on both days) versus controls (0.14 and 0.18 nA mM^{-1}, respectively). However, the MAP/NO sensors exhibited similar clinical accuracy and glucose sensitivity to control sensors at implant periods beyond three days (i.e., days 7 and 10), suggesting that sensor performance is only improved during periods of active NO release. The trends in sensor clinical performance and glucose sensitivity correlate well with the NO-release kinetics from the sensors, with clear benefits to sensor performance early during in vivo use (i.e., days 1 and 3) but no improvements after the NO supply was exhausted. Nichols et al. showed that the FBR $\geq$1 wk post-implantation was unaffected for implants that released NO for <24 h. As such, inflammation may be the primary culprit for decreased sensor performance beyond 3 d.[24] The MPTMS-RSNO based sensors exhibited similar clinical accuracy to MPTMS control sensors throughout the 10 d in vivo study. The sensitivity of the MPTMS-RSNO sensors to glucose appeared greater than controls at 1–3 d post-implantation, but these differences were not significant ($p>0.05$). This result may be due to the low, sustained NO fluxes released from sensors when compared to the MAP/NO-based sensors (Table 2.2).

Of importance, the majority (~70%) of BG determinations were obtained in the 50–100 mg dL^{-1} range, as shown in the representative Clarke error grid analysis in Figure 2.3. In addition

to the similarities between swine and humans (e.g., skin, vasculature, subcutaneous tissue composition) which render the pig an appropriate model for evaluating in vivo biosensors, baseline blood glucose concentrations obtained in this study were comparable to human euglycemic levels.[25,49-51] As maintenance of euglycemia increases the propensity of diabetic individuals to enter the hypoglycemic BG range,[52] the Clarke error grid presents austere requirements for sensor accuracy in this region. Thus, the error grid analysis presented herein is at BG levels clinically and physiologically pertinent to humans.

2.3.3. Biosensor numerical accuracy and adherence to ISO criteria

To evaluate in vivo biosensor performance in more detail, the sensor numerical accuracy was represented using the MARD of each sensor from corresponding reference values.[37] While the Clarke error grid measures sensor accuracy based on the clinical implications of a given BG measurement, the MARD represents a statistical entity that exemplifies the average percent deviation of the sensor from a reference. Additionally, ISO criteria for in vivo glucose biosensor performance was considered as a metric for numerical accuracy because it can be used to assess sensor accuracy in both hypoglycemic ($\leq$70 mg dL^{-1}) and euglycemic/hyperglycemic (>70 mg dL^{-1}) BG ranges separately.[37] A comparison of the numerical accuracies for control and NO-releasing sensors is shown in Figure 2.4. As anticipated, the analytical performance of MAP/NO-based sensors on days 1 and 3 was superior to control (MAP) sensors. The improvements in numerical accuracy agree with the increased clinical accuracy and greater glucose sensitivity for the more rapid NO-releasing sensors. Furthermore, the performance of the MAP/NO-based sensors worsened beyond 3 d implantation. The desirably lower MARD for rapid NO-releasing glucose sensors is attributed to the improved accuracy in both the hypoglycemic and euglycemic/hyperglycemic ranges, as shown in Table 2.5. Indeed, >55% of the total BG

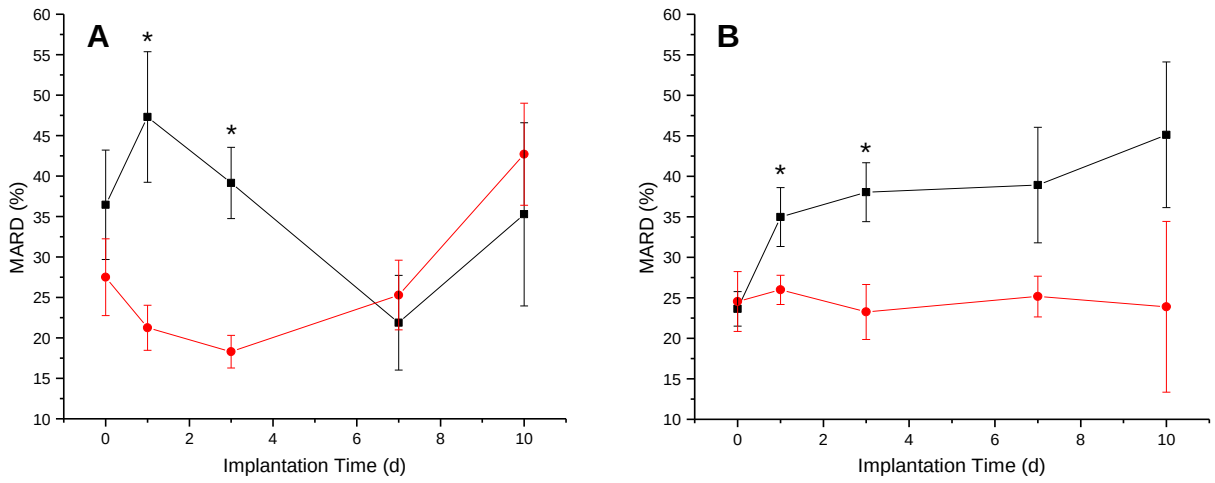

Figure 2.4. Comparison of MARD for (A) MAP/NO (red circle) and control (MAP) sensors (black, square) and (B) MPTMS-RSNO (red circle) and control (MPTMS) (black, square) sensors. Significant differences ($p<0.05$) in the median value for the MARD are indicated with an asterisk.

Table 2.5. ISO criteria for NO-releasing and control sensors.

Day	MAP Control (%)	MAP/NO (%)	MPTMS Control (%)	MPTMS-RSNO (%)
0	58.0[a]/50.0[b]	51.9/61.5	55.7/60.0	60.2/67.0
1	37.9/39.2	55.6/56.7	45.9/59.7	55.5/59.4
3	52.9/47.7	65.6/57.3	39.5/57.3	58.5/74.7
7	62.5/62.7	42.1/57.8	35.5/45.2	42.1/52.0
10	55.6/54.9	30.6/45.9	15.0/34.8	63.6/45.5

[a]Calculated as the percentage of determinations within 15 mg dL^{-1} of the reference measurement when BG$\leq$70 mg dL^{-1}. [b]Calculated as the percentage of determinations within 20% of the reference measurement when BG>70 mg dL^{-1}.

determinations obtained by MAP/NO-based sensors agreed well with corresponding reference measurements in both BG ranges on days 1 and 3. Unexpectedly, the MARD for control (MAP) sensors was lowest at 7 d implantation (21.9 ± 13.1%). Despite the inconsistent numerical accuracy for control sensors, the analytical performance was comparable to NO-releasing sensors at both 7 and 10 d.

Although the clinical accuracy of the MPTMS-RSNO based sensors was comparable to controls, the numerical accuracy of NO-releasing sensors remained constant (MARD range 22.2–26.0 %) throughout the experiment. Furthermore, the sensors that released NO for extended durations exhibited a significantly lower MARD on days 1 and 3 (26.0 and 23.9%, respectively) versus controls (34.3 and 38.8%, respectively). We attribute the good agreement between MPTMS-RSNO sensors and reference measurements to the increased accuracy of the NO-releasing biosensors in both the hypoglycemic and euglycemic/hyperglycemic BG ranges. The percentage of determinations for MPTMS-RSNO based sensors that adhered to ISO criteria was typically >50% throughout implantation, while control sensor performance worsened with implant duration, particularly in the hypoglycemic range. The stable biosensor response provided by the sustained NO-releasing sensor membranes highlights the utility of having more extended NO release for continuous glucose monitoring.

Of importance, the NO-release kinetics also correlated with the magnitude of the improvement in numerical accuracy for NO-releasing sensors versus controls. For example, MAP/NO-based sensors showed vastly decreased MARD versus control (MAP) sensors on day 1 (22.0 and 47.3%, respectively), whereas sensors with longer NO-release durations (MPTMS-RSNO) exhibited more modest improvements relative to controls (28.4 and 34.3%, respectively). However, the differences in the MARD between MAP/NO and MPTMS-RSNO sensors on days

1 and 3 were not statistically significant ($p>0.05$). The enhanced numerical accuracy afforded by rapid NO-release from sensor membranes indicates a possible advantage to greater NO fluxes, as MAP/NO-based sensors delivered ~3.1 μmol cm^{-2} NO in <24 h. Although MPTMS-RSNO sensors had a near constant MARD throughout the experiment duration, the improvements in numerical accuracy provided by lower, more sustained NO release may not have been large enough to result in improved clinical performance. Collectively, these results suggest that sensor performance benefits to a greater extent with prolonged NO release and that these gains are dependent on the fluxes at which NO is liberated.

2.3.4. Biosensor lag time

While poor glucose sensitivity often contributes to undesirable sensor performance in vivo, diminished accuracy also results from sluggish response of the sensor to changes in BG levels.[53] In addition to an inherent blood-tissue glucose lag, progression of the FBR increases the difficulty of glucose diffusion to the sensor. Distinct properties of the collagen capsule (i.e., thickness, density, and avascularity) produced upon resolution of the foreign body response have been shown to affect the transport properties of small molecules from the vasculature to the tissue.[12-13,54] Even in the absence of a mature fibrotic capsule, biofouling and inflammation at the sensor-tissue interface may create a diffusion barrier to glucose.[55] As amperometric glucose biosensors are diffusion-limited with respect to glucose, a longer response time may hinder the competence of the sensor to track rapid changes in BG levels, resulting in decreased accuracy. Since tissue surrounding NO-releasing implants exhibits less inflammation,[22-24] reduced collagen encapsulation,[22,24] and low impedance to glucose transport,[23] NO-releasing sensors may show more rapid response to changes in BG. While time-shifting methods (i.e., Poincaré dynamical analysis) have been used to correct CGM data for time-lag effects,[34-35] calibration of the sensor

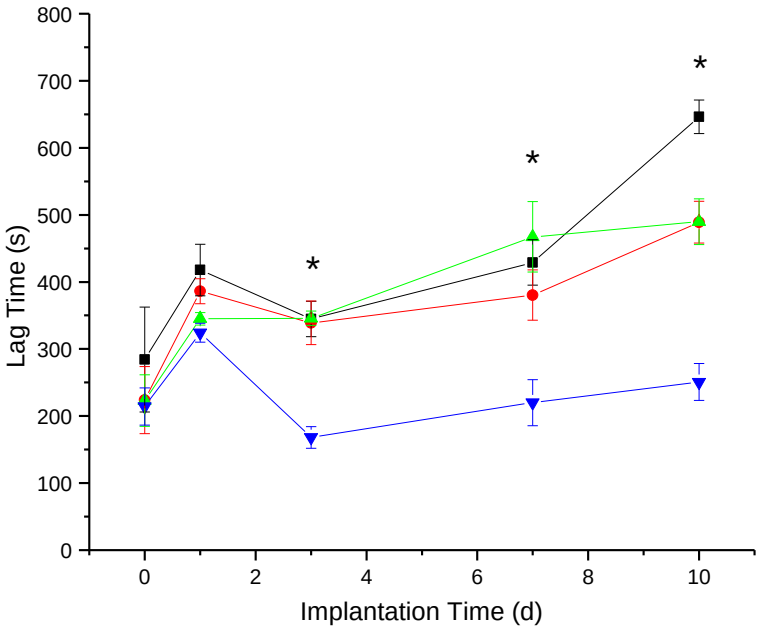

Figure 2.5. Estimation of sensor lag time via cross-correlation. MPTMS-RSNO biosensors (blue inverted triangle) exhibited significantly reduced lag times on days 3, 7, and 10 versus MAP/NO sensors (red circle), and MAP and MPTMS controls (black square and green triangle, respectively). Asterisks denote significant differences ($p<0.05$) in the median values for lag time between the MPTMS-RSNO sensors and all other sensor types.

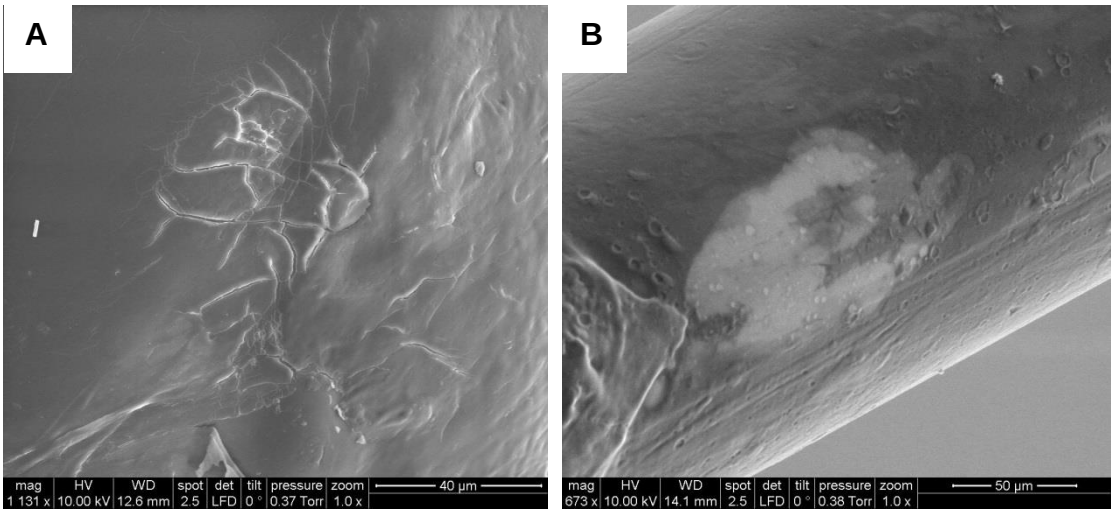

Figure 2.6. Representative post-explantation scanning electron micrographs of glucose biosensor working electrode surfaces exhibiting (A) membrane cracking and (B) partial coating delamination.

signal may corrupt a comparison of sensor lag times. Cross-correlation of the raw sensor signals and paired reference signals were thus used to estimate sensor delay, avoiding the requirement for sensor calibration.[39-40]

Initially (i.e., 0–1 d implant period), NO release had little effect on sensor lag times (Figure 2.5). However, NO release did impact sensor lag times on days 3, 7, and 10. The MPTMS-RSNO based sensors resulted in significantly faster response to changing glucose concentrations during the IVGTT (<4.2 min) compared with both control (MPTMS) and MAP/NO-based sensors (>5.8 min). As well, the response time of the MAP/NO-based sensors worsened with implantation time analogous to control sensors, suggesting that the benefit of reduced response time is only attained when sensors are still releasing NO. Despite similar NO payloads, the difference in lag time between the two types of NO-releasing sensors was somewhat expected. Nichols et al. demonstrated a reduced FBR to materials capable of >2 d NO release at both 3 and 7 d post-implantation.[24] In contrast, shorter NO-release durations (<24 h) did not produce an observable effect. In a separate study, sustained NO release from percutaneously implanted microdialysis probes reduced tissue impedance to glucose transport,[23] which may explain the reduced sensor lag time observed in the present study.

2.3.5. Post-explantation analysis

Approximately 40% of implanted NO-releasing and control sensors functioned beyond 3 d, indicating a limitation in this study. Following sensor explantation, the sensors were imaged via environmental scanning electron microscopy to investigate the implant surfaces and perhaps understand the potential sources of sensor failure. Representative scanning electron micrographs (SEMs) of the surface of the sensors are shown in Figure 2.6. Electrical failure and membrane delamination/cracking were identified as causes of in vivo sensor failure, with contributions from

both the FBR and mechanical stresses to the percutaneous sensor.[49] Koschwanez et al. previously reported that micromotion and the associated stress for percutaneous implants yielded unanticipated results for studies evaluating glucose sensor coatings.[56] Indeed, the significant mechanical stress to percutaneous implants convolutes the interpretation of sensor failure. Nonetheless, percutaneous glucose sensors remain the most realistic method for implementing continuous glucose monitoring due to their low cost and facile implantation, and serve as a suitable model for evaluating candidate biomaterials.[49,57] Furthermore, NO has been shown to provide benefits to percutaneous implants even in the presence of such physical factors.[23]

2.4. Conclusions

Nitric oxide was shown to clearly enhance the analytical performance of in vivo glucose biosensors, with the associated benefits being dependent on the NO-release kinetics from the outer sensor membranes. Both rapid and extended NO-releasing sensors exhibited improved numerical accuracy versus controls. Rapid NO release from sensors resulted in positive differences in both clinical accuracy and glucose sensitivity, while sustained NO-release from MPTMS-RSNO biosensors provided constant numerical accuracy over the entire 10 d implant period. The MPTMS-RSNO sensors were characterized by a quicker response to the IVGTT than both the MPTMS control and MAP-based sensors, which we attribute to the generation of NO. It is hypothesized that shorter lag times for the MPTMS-RSNO sensors are the result of improved glucose transport from the tissue surrounding the implants. The predictable performance of MPTMS-RSNO glucose biosensors suggests that materials that are capable of releasing large NO payloads for even longer durations (i.e., several weeks) represent the ultimate NO-release strategy for long-term glucose sensing technologies (i.e., months), rather than the short term (i.e., ~10 d) period that was the focus of this study. However, the effects of NO on diabetic tissue may

be dissimilar. Indeed, diabetic tissue is characterized by numerous deficiencies including altered wound repair,[58-59] lessened inflammation and pro-inflammatory cytokine production at wound sites,[59] disrupted blood flow,[60] and susceptibility to infection.[61] Work characterizing the response of diabetic tissue to implantation has been limited thus far. The disparities between diabetic and healthy tissue motivate the need for understanding the diabetic response to sensor implantation and warrant a careful investigation of the role of NO on the diabetic FBR.

REFERENCES

(1) Koh, A.; Nichols, S. P.; Schoenfisch, M. H. "Glucose sensor membranes for mitigating the foreign body response." *Journal of Diabetes Science and Technology* **2011,** *5*, 1052–1059.

(2) Wilson, G. S.; Zhang, Y. In *In vivo glucose sensing* Cunningham, D. D.; Stenken, J. A., Eds. John Wiley & Sons: Hoboken, **2009**; 1–27.

(3) Anderson, J. M.; Rodriguez, A.; Chang, D. T. "Foreign body reaction to biomaterials." *Seminars in Immunology* **2008,** *20*, 86–100.

(4) Gifford, R.; Kehoe, J. J.; Barnes, S. L.; Kornilayev, B. A.; Alterman, M. A.; Wilson, G. S. "Protein interactions with subcutaneously implanted biosensors." *Biomaterials* **2006,** *27*, 2587–2598.

(5) Vroman, L.; Adams, A. L.; Fischer, G. C.; Munoz, P. C. "Interaction of high molecular weight kininogen, factor XII, and fibrinogen in plasma at interfaces." *Blood* **1980,** *55*, 156–159.

(6) Thomé-Duret, V.; Gangnerau, M. N.; Zhang, Y.; Wilson, G. S.; Reach, G. "Modification of the sensitivity of glucose sensor implanted into subcutaneous tissue." *Diabetes and Metabolism* **1996,** *22*, 174–178.

(7) Wilson, G. S.; Ammam, M. "In vivo biosensors." *FEBS Journal* **2007,** *274*, 5452–5461.

(8) Nichols, S. P.; Koh, A.; Storm, W. L.; Shin, J. H.; Schoenfisch, M. H. "Biocompatible materials for continuous glucose monitoring devices " *Chemical Reviews* **2013,** *113*, 2528–2549.

(9) Ishihara, K.; Nomura, H.; Mihara, T.; Kurita, K.; Iwasaki, Y.; Nakabayashi, N. "Why do phospholipid polymers reduce protein adsorption?" *Journal of Biomedical Materials Research Part A* **1998,** *39*, 323–330.

(10) Ju, Y. M.; Yu, B. Z.; West, L.; Moussy, Y.; Moussy, F. "A novel porous collagen scaffold around an implantable biosensor for improving biocompatibility. Ii. Long-term in vitro/in vivo sensitivity characteristics of sensors with ndga- or ga-crosslinked collagen scaffolds." *Journal of Biomedical Materials Research Part A* **2010,** *92*, 650–658.

(11) Massia, S. P.; Stark, J.; Letbetter, D. S. "Surface-immobilized dextran limits cell adhesion and spreading." *Biomaterials* **2000,** *21*, 2253–2261.

(12) Sharkawy, A. A.; Klitzman, B.; Truskey, G. A.; Reichert, W. M. "Engineering the tissue which encapsulates subcutaneous implants. I. Diffusion properties." *Journal of Biomedical Materials Research Part A* **1997,** *37*, 401–412.

(13) Sharkawy, A. A.; Klitzman, B.; Truskey, G. A.; Reichert, W. M. "Engineering the tissue which encapsulates subcutaneous implants. II. Plasma-tissue exchange properties." *Journal of Biomedical Materials Research Part A* **1998,** *40*, 586–597.

(14) Cao, H.; McHugh, K.; Chew, S. Y.; Anderson, J. M. "The topographical effect of electrospun nanofibrous scaffolds on the in vivo and in vitro foreign body reaction." *Journal of Biomedical Materials Research Part A* **2010,** *93*, 1151-9.

(15) Norton, L. W.; Tegnell, E.; Toporek, S. S.; Reichert, W. M. "In vitro characterization of vascular endothelial growth factor and dexamethasone releasing hydrogels for implantable probe coatings." *Biomaterials* **2005,** *26*, 3285–3297.

(16) Ward, W. K.; Hansen, J. C.; Massoud, R. J.; Engle, J. M.; Takeno, M. M.; Hauch, K. D. "Controlled release of dexamethasone from subcutaneously-implanted biosensors in pigs: Localized anti-inflammatory benefit without systemic effects." *Journal of Biomedical Materials Research Part A* **2010,** *94*, 280–287.

(17) Ziesche, E.; Scheiermann, P.; Bachmann, M.; Sadik, C. D.; Hofstetter, C.; Zwissler, B.; Pfeilschifter, J.; Muhl, H. "Dexamethasone suppresses interleukin-22 associated with bacterial infection in vitro and in vivo." *Clinical and Experimental Immunology* **2009,** *157*, 370–376.

(18) Klueh, U.; Dorsky, D. I.; Kreutzer, D. L. "Enhancement of implantable glucose sensor function in vivo using gene-transfer induced neovascularization " *Biomaterials* **2005,** *26*, 1155–1163.

(19) Cooke, J. P. "Nitric oxide and angiogenesis." *Atherosclerosis Supplements* **2003,** *4*, 53–60.

(20) Schwentker, A.; Vodovotz, Y.; Weller, R.; Billiar, T. R. "Nitric oxide and wound repair: Role of cytokines?" *Nitric Oxide* **2002,** *7*, 1-10.

(21) Riccio, D. A.; Schoenfisch, M. H. "Nitric oxide release part I. Macromolecular scaffolds." *Chemical Society Reviews* **2012,** *41*, 3731–3741.

(22) Hetrick, E. M.; Prichard, H. L.; Klitzman, B.; Schoenfisch, M. H. "Reduced foreign body response at nitric oxide-releasing subcutaneous implants." *Biomaterials* **2007,** *28*, 4571–4580.

(23) Nichols, S. P.; Le, N. N.; Klitzman, B.; Schoenfisch, M. H. "Increased in vivo glucose recovery via nitric oxide release." *Analytical Chemistry* **2011,** *83*, 1180–1184.

(24) Nichols, S. P.; Koh, A.; Brown, N. L.; Rose, M. B.; Sun, B.; Slomberg, D. L.; Riccio, D. A.; Klitzman, B.; Schoenfisch, M. H. "The effect of nitric oxide surface flux on the foreign body response to subcutaneous implants." *Biomaterials* **2012,** *33*, 6305–6312.

(25) Gifford, R.; Batchelor, M. M.; Lee, Y.; Gokulrangan, G.; Meyerhoff, M. E.; Wilson, G. S. "Mediation of in vivo glucose sensor inflammatory response via nitric oxide release." *Journal of Biomedical Materials Research Part A* **2005,** *75*, 755-66.

(26) Frost, M. C.; Batchelor, M. M.; Lee, Y.; Zhang, H.; Kang, Y.; Oh, B.; Wilson, G. S.; Gifford, R.; Rudich, S. M.; Meyerhoff, M. E. "Preparation and characterization of implantable sensors with nitric oxide release coatings." *Microchemical Journal* **2003,** *74*, 277–288.

(27) Riccio, D. A.; Nugent, J.; Schoenfisch, M. H. "Stöber synthesis of nitric oxide-releasing *S*-nitrosothiol-modified silica particles." *Chemistry of Materials* **2011,** *23*, 1727–1735.

(28) Koh, A.; Lu, Y.; Schoenfisch, M. H. "Fabrication of nitric oxide-releasing porous polyurethane membranes-coated needle-type implantable glucose biosensors." *Analytical Chemistry* **2013,** *85*, 10488–10494.

(29) Koh, A.; Riccio, D. A.; Sun, B.; Carpenter, A. W.; Nichols, S. P.; Schoenfisch, M. H. "Fabrication of nitric oxide-releasing polyurethane glucose sensor membranes." *Biosensors and Bioelectronics* **2011,** *28*, 17–24.

(30) Shin, J. H.; Marxer, S. M.; Schoenfisch, M. H. "Nitric oxide-releasing sol-gel particle/polyurethane glucose biosensors." *Analytical Chemistry* **2004,** *76*, 4543-9.

(31) Bequette, B. W. "Continuous glucose monitoring: Real-time algorithms for calibration, filtering, and alarms." *Journal of Diabetes Science and Technology* **2010,** *4*, 404–418.

(32) Choleau, C.; Klein, J. C.; Reach, G.; Aussedat, B.; Demaria-Pesce, V.; Wilson, G. S.; Gifford, R.; Ward, W. K. "Calibration of a subcutaneous amperometric glucose sensor: Part 1. Effect of measurement uncertainties on the determination of sensor sensitivity and background current." *Biosensors and Bioelectronics* **2002,** *17*, 641–646.

(33) Choleau, C.; Klein, J. C.; Reach, G.; Aussedat, B.; Demaria-Pesce, V.; Wilson, G. S.;

Gifford, R.; Ward, W. K. “Calibration of a subcutaneous amperometric glucose sensor implanted for 7 d in a diabetic patient: Part 2. Superiority of the one-point calibration method.” *Biosensors and Bioelectronics* **2002,** *17*, 647–654.

(34) Garg, S. K.; Voelmle, M.; Gottlieb, P. A. "Time lag characterization of two continuous glucose monitoring systems." *Diabetes Research and Clinical Practice* **2010,** *87*, 348–353.

(35) Kovatchev, B. P.; Shields, D. S.; Breton, M. "Graphical and numerical evaluation of continuous glucose sensing time lag." *Diabetes Technology and Therapeutics* **2009,** *11*, 139–143.

(36) Keenan, D. B.; Mastrototaro, J. J.; Weinzimer, S. A.; Steil, G. M. "Interstitial fluid glucose time-lag correction for real-time continuous glucose monitoring." *Biomedical Signal Processing and Control* **2013,** *8*, 81–89.

(37) Clarke, W. L.; Kovatchev, B. P. "Continuous glucose sensors: Continuing questions about clinical accuracy." *Journal of Diabetes Science and Technology* **2007,** *1*, 669–675.

(38) Clarke, W. L. "The original clarke error grid analysis (EGA)." *Diabetes Technology and Therapeutics* **2005,** *7*, 776–779.

(39) Venton, B. J.; Michael, D. J.; Wightman, R. M. "Correlation of local changes in extracellular oxygen and ph that accompany dopaminergic terminal activity in the rat caudate-putamen." *Journal of Neurochemistry* **2003,** *84*, 373–381.

(40) Jacovitti, G.; Scarano, G. "Discrete time techniques for time delay estimation." *IEEE Transactions on Signal Processing* **1993,** *41*, 525–533.

(41) McDonald, J. H. “Handbook of biological statistics” 2nd Edition.; Sparky House Publishing: Baltimore, Maryland, U.S.A., **2009**.

(42) Chen, S.; Jones, J. A.; Xu, Y.; Low, H. Y.; Anderson, J. M.; Leong, K. W. "Characterization of topographical effects on macrophage behavior in a foreign body response model." *Biomaterials* **2010,** *31*, 3479-91.

(43) Barbe, C.; Bartlett, J.; Kong, L. G.; Finnie, K.; Lin, H. Q.; Larkin, M.; Calleja, S.; Bush, A.; Calleja, G. "Silica particles: A novel drug-delivery system." *Advanced Materials* **2004,** *16*, 1959–1966.

(44) Shin, J. H.; Metzger, S. K.; Schoenfisch, M. H. "Synthesis of nitric oxide-releasing silica nanoparticles." *Journal of the American Chemical Society* **2007,** *129*, 4612–4619.

(45) Al-Sádoni, H. H.; Ferro, A. "*S*-nitrosothiols as nitric oxide donors: Chemistry, biology, and possible future therapeutic applications." *Current Medicinal Chemistry* **2004,** *11*, 2679–2690.

(46) Vaughn, M. W.; Kuo, L.; Liao, J. C. "Estimation of nitric oxide production and reaction rates in tissue by use of a mathematical model." *American Journal of Physiology* **1998,** *274*, 2163–2176.

(47) Hetrick, E. M.; Schoenfisch, M. H. "Antibacterial nitric oxide-releasing xerogels: Cell viability and parallel plate flow cell adhesion studies." *Biomaterials* **2007,** *28*, 1948–1956.

(48) Storm, W. L.; Schoenfisch, M. H. "Nitric oxide-releasing xerogels synthesized from *N*-diazeniumdiolate-modified silane precursors." *ACS Applied Materials and Interfaces* **2013,** *5*, 4904–4912.

(49) Koschwanez, H. E.; Reichert, W. M. "In vitro, in vivo, and post-explantation testing of glucose-detecting biosensors: Current methods and recommendations." *Biomaterials* **2007,** *28*, 3687–3703.

(50) Larsen, M. O.; Rolin, B. "Use of the göttingen minipig as a model of diabetes, with special focus on type 1 diabetes research." *ILAR Journal* **2004,** *45*, 303–313.

(51) Swindle, M. M.; Makin, A.; Herron, A. J.; Clubb, F. J.; Frazier, K. S. "Swine as models in biomedical research and toxicology testing." *Veterinary Pathology* **2012,** *49*, 344–356.

(52) The Diabetes Control and Complications Trial Group "The effect of intensive treatment of diabetes on the development and progression of long-term complications in insulin-dependent diabetes mellitus." *New England Journal of Medicine* **1993,** *329*, 977–986.

(53) Wilson, G. S.; Gifford, R. "Biosensors for real-time in vivo measurements." *Biosensors and Bioelectronics* **2005,** *20*, 2388–2403.

(54) Sharkawy, A. A.; Klitzman, B.; Truskey, G. A.; Reichert, W. M. *Journal of Biomedical Materials Research Part A* **1998,** *40*, 598–605.

(55) Rebrin, K.; Fischer, U.; Hahn von Dorsche, H.; von Woetke, T.; Abel, P.; Brunstein, E. "Subcutaneous glucose monitoring by means of electrochemical sensors: Fiction or reality." *Journal of Biomedical Engineering* **1992,** *14*, 33–40.

(56) Koschwanez, H. E.; Yap, F. Y.; Klitzman, B.; Reichert, W. M. "In vitro and in vivo characterization of porous poly-l-lactic acid coatings for subcutaneously implanted glucose biosensors." *Journal of Biomedical Materials Research Part A* **2008,** *87*, 792–807.

(57) Henry, C. "Gettin under the skin: Implantable glucose sensors." *Analytical Chemistry* **1998,** *70*, 594A–598A.

(58) Schaper, N. C.; Havekes, B. "Reducing lower leg amputations in diabetes: A challenge for patients, healthcare providers and the healthcare system." *Diabetalogia* **2012,** *55*, 18–20.

(59) Fahey, T. J.; Sadaty, A.; Jones, W. G.; Barber, A.; Smoller, B.; Shires, G. T. "Diabetes impairs the late inflammatory response to wound healing." *Journal of Surgical Research* **1991,** *50*, 308–313.

(60) Vinik, A. I.; Maser, R. E.; Mitchell, B. D.; Freeman, R. "Diabetic autonomic neuropathy." *Diabetes Care* **2003,** *26*, 1553–1579.

(61) Wheat, L. J. "Infection and diabetes mellitus." *Diabetes Care* **1980,** *3*, 187–197.

CHAPTER 3. FUNCTIONALIZED MESOPOROUS SILICA VIA AN AMINOSILANE-SURFACTANT ION EXCHANGE REACTION: CONTROLLED SCAFFOLD DESIGN AND NITRIC OXIDE RELEASE[3]

3.1. Introduction

Nitric oxide (NO), an endogenous diatomic free radical, mediates multiple physiological processes including angiogenesis,[1] blood pressure regulation,[2] wound healing,[3-4] and the immune response.[5-6] In vivo, nitric oxide synthase (NOS) enzymes generate NO at concentrations (nM–μM) and kinetics dependent on the enzyme location and purpose.[3] For example, low concentrations of NO generated via calcium-dependent endothelial and neuronal NOS regulate neovascularization[1] and serve roles in neurotransmission.[7] Activation of the inducible NOS isoform by immunological stimuli (e.g., lipopolysaccharide, interferon-γ) causes sustained NO release at high concentrations to eradicate foreign pathogens as part of the innate immune response.[5-6] The multifaceted roles of endogenous NO are attributable to precise spatiotemporal NO release by cells expressing the NOS enzymes. In addition, NO's short biological lifetime (seconds) restricts its action to <0.5 mm from the point of generation.[8]

Due to NO's overwhelming presence in physiology, the administration of exogenous NO gas represents a potential therapy for many diseases.[9] A significant body of research has focused on the development of donors that store and release NO under specific chemical conditions in order to address the concentration-dependent behavior of NO and avoid challenges associated

[3]This chapter was adapted from an article that previously appeared in *ACS Applied Materials and Interfaces*. The original citation is as follows: Soto, R. J.; Yang, L.; Schoenfisch, M. H. "Functionalized mesoporous silica via an aminosilane surfactant ion exchange reaction: Controlled scaffold design and nitric oxide release," *ACS Applied Materials and. Interfaces* **2016**, *8*, 2220–2231.

with the administration of NO directly, such as the need for a pressurized gas cylinder and NO's rapid reaction in biological media.[9] In particular, *N*-diazeniumdiolate NO donors, formed by the reaction of gaseous NO with secondary amines, spontaneously release NO in physiological buffer upon reaction with hydronium ions. This class of molecules has accordingly received attention for biological applications because the breakdown of the NO donor and concomitant NO release occurs at rates dependent on pH, temperature, and the chemical structure of the precursor molecule used for *N*-diazeniumdiolate formation.

The potential utility of the *N*-diazeniumdiolate functional group originally inspired research on low molecular weight NO donors.[10-11] Unfortunately, limited NO capacity and duration generally preclude the use of these small molecule NO donors for therapeutic applications. To enhance NO storage and exert additional control over NO release, much work has focused on the synthesis of *N*-diazeniumdiolate-modified macromolecular NO-delivery scaffolds, including chitosan oligosaccharides,[12] dendrimers,[13-15] gold clusters,[16-17] and silica nanoparticles.[18-25] With respect to silica, surface grafting,[21,26] co-condensation,[20,27] and water-in-oil microemulsion[19] methods have been used to prepare *N*-diazeniumdiolate-functionalized particles. Silica is attractive as an NO-release scaffold as it is well tolerated (non-toxic) and readily implemented as a drug delivery vehicle.[11,19,26] For example, NO donor-modified silica particles have served as reinforcing fillers for NO-releasing polymeric coatings (i.e., for in vivo sensors) to promote angiogenesis and wound healing.[28-29] Such materials have also proven effective as antimicrobial abrasives that may be integrated with oral hygiene technologies.[18,27]

Despite their value as potential therapeutics, current strategies for synthesizing NO-releasing silica nanoparticles remain limited by challenges associated with altering the physical properties of the particles and the NO release independent of one another. The use of

mesoporous silica represents an attractive macromolecular scaffold for enhancing NO storage and release because of the inherently greater and modifiable surface area (500–1,200 m^2 g^{-1}) relative to previous nonporous silica systems.[19-21,23,25-27] Control over pore formation and the silica mesophase is achieved via the synthesis of the nanoparticles around an ordered surfactant aggregate, generally an alkyltrimethylammonium salt, that serves as the structure-directing agent (SDA).[30-31] Covalent attachment of secondary-amine containing silanes (i.e., NO donor precursors) to mesoporous silica is carried out by direct incorporation of the aminosilane into the particle backbone via co-condensation[32-34] or post-synthetically through surface grafting.[35-37] In the co-condensation approach, coulombic repulsion between the cationic surfactant molecules and the protonated backbone amines destabilizes the template, resulting in materials with irregular morphology, even at low aminosilane concentrations.[32,38] Post-synthetic surface grafting (after extracting the SDA) is generally the preferred method for functionalizing mesoporous silica, albeit at the cost of a multi-step workflow and loss of control over the amount of aminosilane incorporated. Moreover, the grafting process requires a nonpolar aprotic solvent to avoid irreversible water-induced particle agglomeration,[25] often resulting in heterogeneous amine distribution and batch-to-batch irreproducibility.[37]

Ion exchange between cationic organosilanes and common alkyltrimethylammonium SDAs represents a new MSN functionalization approach. To date, this strategy has been limited to post-synthetic modification in organic solvents, raising concerns regarding synthesis irreproducibility similar to surface grafting. Herein, we report aminosilane ion exchange with cetyltrimethylammonium bromide (CTAB) in the aqueous particle sol. Initially, we prepare a diverse selection of monodisperse amine-functionalized mesoporous silica nanoparticles (MSNs). The surface- and pore-bound secondary amines are then converted to *N*-

diazeniumdiolate moieties to yield the NO-releasing MSNs. Using the aqueous ion exchange approach, we demonstrate autonomous control over particle size and NO-release capabilities (i.e., NO-release rates and total NO storage), representing a significant advantage over conventional co-condensation and grafting methods. The relationship between NO-release kinetics and particle mesophase ordering is also elucidated via detailed physicochemical analysis of the MSNs.

3.2. Experimental section

3.2.1. Materials

Tetraethylorthosilicate (TEOS), 3-aminopropyltriethoxysilane (APTES), 3-mercaptopropyltrimethoxysilane (MPTMS), 3-(trimethoxysilylpropyl)diethylenetriamine (DET), *N*-methylaminopropyltrimethoxysilane (MAP), *N*-(6-aminohexyl)aminopropyltrimethoxysilane (AHAP), and *N*-(2-aminoethyl)-3-aminopropyltrimethoxysilane (AEAP), and isobutyltrimethoxysilane (BTMS) were purchased from Gelest (Morrisville, PA) and stored under nitrogen atmosphere. Sodium methoxide (NaOMe; 5.4 M in methanol), anhydrous *N*,*N*-dimethylformamide (DMF), anhydrous methanol (MeOH), ethanol (EtOH), aqueous ammonium hydroxide (30 wt%; NH_4OH), concentrated hydrochloric acid (HCl) and all salts were purchased from Fisher Scientific (Fair Lawn, NJ). Cetyltrimethylammonium bromide was purchased from Sigma (St. Louis, MO). Nitrogen (N_2), argon (Ar), and nitric oxide (NO) calibration (25.87 ppm in nitrogen) gases were purchased from Airgas National Welders (Raleigh, NC). Pure NO gas was purchased from Praxair (Danbury, CT). Water was purified to a resistivity of 18.2 MΩ·cm and a total organic content of $\leq$10 ppb using a Millipore Milli-Q UV Gradient A10 system (Bedford, MA). Unless specified, all chemicals were used as received without further purification.

3.2.2. Mesoporous silica nanoparticle synthesis

Particle synthesis was achieved by addition of tetraethylorthosilicate as a bolus to a stirred solution of water, EtOH, NH_4OH, and CTAB, allowing the reaction to proceed for 2 h. For synthesis of the 30, 150, and 450 nm diameter particles, 2.500 mL TEOS in EtOH (0.88, 1.06, and 1.33 M, respectively) was added to the reaction mixture, whereas 1.395 mL concentrated TEOS was used for the synthesis of the larger 1100 nm particles. Synthesis conditions for the MSNs are provided in Table 3.1. In all cases, reaction solutions appeared turbid within 15 min of silane introduction. Following particle formation, additional organosilane (AEAP, AHAP, APTES, BTMS, MAP, MPTMS, or DET) was introduced directly to the colloidal sol dropwise for 5 min using a Kent Scientific Genie Plus syringe pump (Torrington, CT). The reaction was then aged overnight (~18 h) with stirring. Unless specified, an optimized TEOS:organosilane molar ratio of 1.56:1.00 was used. Following functionalization, particles were collected by centrifugation (6540*g*, 4 ^{o}C, 15 min), washed three times with EtOH, and dried under vacuum. For both the 30 and 150 nm particles, EtOH (one volume per two volumes of the reaction mixture) was added to the sol to induce particle flocculation during the collection procedure and improve the overall yield. Bare MSNs were synthesized and collected similarly but without the organosilane functionalization step.

Following MSN synthesis, residual CTAB was removed by ion exchange with hydrochloric acid (HCl). Particles (~200 mg) were suspended in 30 mL 10 vol% HCl in EtOH, agitated in an ultrasonicator bath for 30 min, and collected by centrifugation (6540*g*, 4 ^{o}C, 15 min). This process was repeated three times to ensure complete CTAB removal, followed by two additional EtOH washes. The particles were dried under vacuum to yield the surfactant-free nanoparticles. Typical yields for the amine-modified 30, 150, 450, and 1100 nm MSNs were

150, 175, 275, and 650 mg, respectively.

3.2.3. Nanoparticle characterization

Particle morphology was characterized using an FEI Helios 600 Nanolab scanning electron microscope (SEM; Hillsboro, OR) and a JEOL 2010F transmission electron microscope (TEM; Peabody, MA). Particles were suspended in MeOH at 1 mg mL^{-1} via brief agitation with an ultrasonicator. Subsequently, 5 µL of the resulting dispersion was cast onto a Formvar-coated copper grid (Ted Pella, Inc.; Redding, CA) and analyzed using TEM. For SEM analysis, samples were dispersed instead on one-sided copper adhesive substrates and coated with a ~3 nm gold layer to improve sample conductivity. The geometric size distribution of the particles was estimated from the electron micrographs using ImageJ software (Bethesda, MD). The solution-phase behavior of the nanoparticles in water was investigated using dynamic light scattering (Malvern Zetasizer Nano-ZS; Westborough, MA) to determine MSN hydrodynamic diameter (Z-average size) and polydispersity index. Aqueous colloidal nanoparticle suspensions were prepared by dispersing particles at a concentration of 0.5 mg mL^{-1} via probe sonication at 7 W for 45 s using a Misonix S-4000 ultrasonicator (Farmingdale, NY). Nitrogen sorption isotherms were collected on a Micromeritics Tristar II 3020 surface area and porosity analyzer (Norcross, GA). Samples were dried under a stream of N_2 gas at 110 ^oC overnight and then degassed for 2 h prior to analysis. Brunauer-Emmett-Teller (BET) analysis of physisorption data was used to calculate MSN specific surface area for p/p^0 values of 0.05–0.20. Pore size analysis using the adsorption branch of the sorption isotherm ($0.05<p/p^0<0.60$) was accomplished using the Barrett-Joyner-Halenda (BJH) method. Data obtained at relative pressures >0.60 p/p^0 were not considered for pore size determination as nitrogen capillary condensation occurred in the inter-particle volumes for the 30 nm and 150 nm particles, inflating the calculated pore width. Pore

structure/ordering information was obtained by small-angle X-ray scattering analysis of the dry MSN powder. The Cu Kα line (1.54 Å) was used as the source radiation and scattering profiles were collected on a SAXSLab Ganesha point collimated pinhole system equipped with a moveable Dectris Pilatus 300K 2-dimensional single-photon-counting detector (Northampton, MA). Scattering vector (q) calibration was accomplished using the 1st-order ring for silver behenate, and data was collected for q-values of 0.005–0.724 Å^{-1}. Covalent incorporation of aminosilanes into the MSN backbone was confirmed *via* solid-state cross-polarization/magic angle spinning (CP/MAS) ^{29}Si nuclear magnetic resonance spectroscopy using a Bruker DMX 360 wide-bore spectrometer at a resonance frequency of 71.548 Hz. Samples were carefully ground in a mortar and pestle, packed into a 4 mm ZrO_2 rotor, and spun at 10 kHz. All chemical shifts were determined relative to an external tetramethylsilane standard. Elemental analysis was used to quantify the nitrogen weight percent of particles before and after functionalization with secondary amine-containing silanes using a Perkin Elmer 2400 CHNS/O analyzer (Waltham, MA) operated in CHN mode.

3.2.4. N-diazeniumdiolate modification and nitric oxide release measurements

The aminosilane-modified MSNs (~15 mg) were suspended in 9:1 DMF:MeOH at 5 mg mL^{-1} in a glass vial and dispersed by ultrasonication for 20 min. After forming a homogeneous particle dispersion, NaOMe (5.4 M in MeOH; 9.0 μmol per mg MSN) was added to the solution and mixed. The MSN-containing vials were equipped with stir bars, placed in a stainless steel reaction bottle (Parr Instrument Co.; Moline, IL), and connected to an in-house NO reactor. The Parr bottle was flushed six times (three rapid, three 10 min) with 8 bar Ar gas to remove atmospheric oxygen and minimize the formation of NO byproducts. The vessel was subsequently pressurized with 10 bar NO gas and the reaction proceeded for 72 h. Of note, the NO gas used

for *N*-diazeniumdiolate formation was purified over solid potassium hydroxide for at least 4 h prior to reaction. After 72 h, the Parr bottle was vented and the vessel was flushed six more times (three short, three 10 min) to remove unreacted NO. The particles were again collected by centrifugation (6540*g*, 4 ^{o}C, 15 min), washed three times with EtOH, and dried under vacuum for 1–2 h. The resulting *N*-diazeniumdiolate-modified particles were stored in a vacuum-sealed Mylar bag at -20 ^{o}C until further use.

Nitric oxide release measurements were carried out using a Sievers 280i NO analyzer (Boulder, CO). Generation of NO from the proton-labile *N*-diazeniumdiolate NO donors was detected indirectly via chemiluminescence from excited state nitrogen dioxide formed upon the reaction of NO with ozone. The NOA was calibrated using a two-point linear calibration; air passed through a Sievers NO zero filter served as the blank value and 25.87 ppm NO in N_2 was used as the second calibration point. Particles (~1 mg) were added to the NOA sample flask containing 30 mL deoxygenated phosphate buffered saline (PBS, 0.010 M, pH 7.41) at 37 ^{o}C. A stream of N_2 gas (80 mL min^{-1}) was continuously bubbled through solution to carry liberated NO to the analyzer. Supplemental nitrogen flow was provided to the flask to match the instrument collection rate of 200 mL min^{-1}. Instantaneous NO concentrations were determined at a sampling frequency of 1 Hz, providing near real-time NO release measurements. The NO measurements were terminated when NO release from the particles was below 10 ppb mg^{-1}.

3.2.5. Statistical analysis

One-way Analysis of Variance was used for multiple comparisons of MSN physicochemical properties (e.g., surface area, pore size, NO-release total amounts and kinetics) with provided p-values. Individual comparisons were carried out using a two-tailed Student's t-test with α=0.05 considered as the threshold for statistical significance. All results presented

represent data from three or more separate synthesis experiments.

3.3. Results and discussion

The synthesis of NO-releasing nanoparticles has been previously reported,[18-27] but without autonomous control over particle size, NO-release kinetics, and NO storage. Generally, total NO storage for silica-based materials is limited to <0.40 μmol mg^{-1} due to low aminosilane incorporation. Limited NO storage often is further compounded by a lack of morphological control and poor synthesis yields. Mesoporous silica was thus selected as a new scaffold in an attempt to exert greater control over particle NO-release properties. Mesoporous silica nanoparticles were prepared via a supramolecular liquid-crystal templating approach. Cationic, amphiphilic CTAB aggregates were used as the structure-directing agent for particle synthesis.[31] The synthesis of four different sized MSNs was achieved using TEOS as the backbone silane by altering the reaction temperature and reactant concentrations (Table 3.1). Surfactant was removed by ion exchange in ethanolic HCl to yield the bare mesoporous scaffold. While other methods (e.g., calcination) have been used for CTAB removal, irreversible particle agglomeration often results.[39-40] Surfactant removal from the MSNs after agitation in HCl was evaluated using elemental analysis. The measured nitrogen wt% for the bare particles was <0.2% in all cases (indicating complete CTAB removal), with the exception of the 150 nm system (~1.11%). The significant nitrogen content was attributed to trapped ammonia, since the low carbon content (5.48±1.00%) did not reflect the presence of CTAB (~80.3% carbon by mass). Indeed, the 150 nm particles had a propensity to aggregate and did not disperse into solution during the washing and CTAB removal processes, whereas all three remaining particle systems

Table 3.1. Synthesis conditions and nitrogen physisorption data for MSNs of varying size.[a]

Particle Size (nm)	[H_2O] (M)	[NH_3] (M)	[CTAB] (mM)	Reaction Volume (mL)	Temperature (^oC)	Specific Surface Area ($m^2\ g^{-1}$)[b]	Average Pore Width (Å)[c]	Nitrogen wt%[d]
30	54.5	0.267	5.30	150	68±1	1290±90	23.6±2.3	$\leq$0.01
150	39.4	0.267	5.30	150	38±1	1170±80	21.9±0.6	1.11±0.12
450	35.0	0.267	5.30	150	23±1	1280±120	20.4±0.2	0.13±0.06
1100	25.5	0.521	2.20	350	23±1	1170±70	19.5±0.3	$\leq$0.01

[a]Error bars represent standard deviation for n$\geq$3 separate syntheses. [b]Determined by BET analysis of the nitrogen sorption isotherms ($0.05 \leq p/p^0 \leq 0.20$). [c]Calculated via BJH analysis of the nitrogen adsorption isotherm ($p/p^0 \leq 0.60$). [d]Nitrogen wt% measured by elemental analysis.

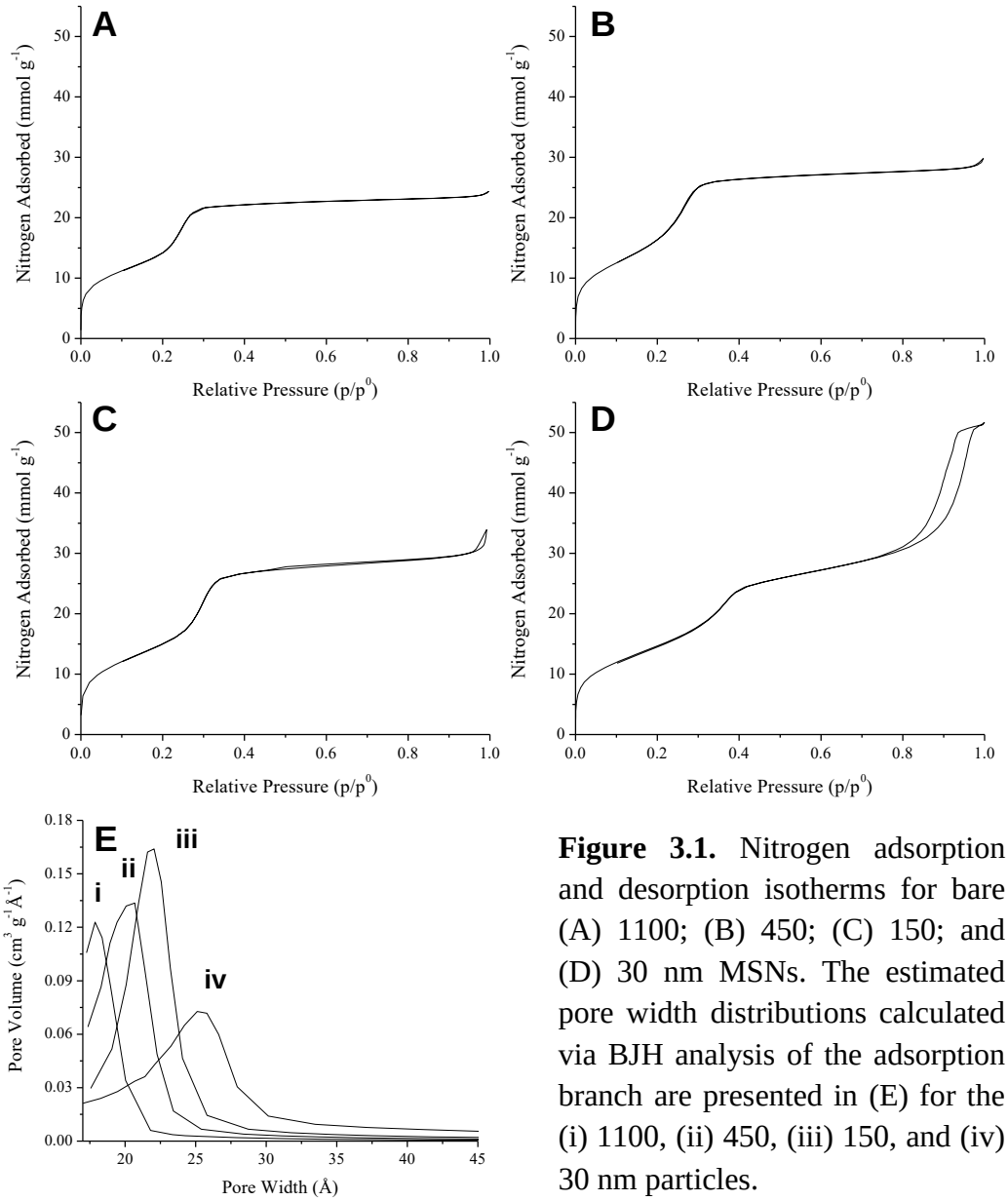

Figure 3.1. Nitrogen adsorption and desorption isotherms for bare (A) 1100; (B) 450; (C) 150; and (D) 30 nm MSNs. The estimated pore width distributions calculated via BJH analysis of the adsorption branch are presented in (E) for the (i) 1100, (ii) 450, (iii) 150, and (iv) 30 nm particles.

(e.g., 30, 450, and 1100 nm) readily suspended with sonication. The heterogeneity of these wash steps is likely at fault for residual nitrogen content in the 150 nm MSNs.

The surface areas and pore sizes of the unmodified MSNs were calculated from the affiliated nitrogen sorption isotherms (Figure 3.1). Each of the physisorption isotherms exhibited steep inflections at ~0.2–0.4 p/p^0 and >0.8 p/p^0 corresponding to capillary condensation of nitrogen in the particle mesopores and inter-particle volumes, respectively.[41] All isotherms were classified as Type IV isotherms without hysteresis according to the conventions adopted by the International Union of Pure and Applied Chemistry (IUPAC).[42] Nitrogen gas adsorption/desorption on CTAB-templated mesoporous silica has consistently yielded similar results.[43] Importantly, MSN surface areas calculated using the Brunauer-Emmett-Teller (BET) method exceeded 1000 $m^2\ g^{-1}$ in all cases (Table 3.1) regardless of particle size. Average pore sizes were evaluated using Barrett-Joyner-Halenda (BJH) analysis of a portion of the nitrogen adsorption branch (Figure 3.1E) and yielded calculated pore widths in the range of 19.5–23.6 Å, which are comparable to those reported in the literature.[32,44-45]

The particles were modified with secondary amines by direct organosilane addition to the reaction solution following completion of the particle synthesis reaction ($\leq$2 h as determined by dynamic light scattering). Residual surfactant SDA was removed in a subsequent step, similar to unmodified particles. The aminosilane *N*-(2-aminoethyl)-3-aminopropyltrimethoxysilane (AEAP) was selected to optimize this process, initially using the largest (1100 nm) particles. As expected, lower specific surface areas were observed due to increased particle aminosilane content (Table 3.2). Pore size analysis of the nitrogen adsorption isotherms indicated a clear decrease in mesopore volume with increasing AEAP concentration, while the pore width remained invariable ($p>0.50$). The gas sorption isotherm abruptly transitioned from a type IV to

Table 3.2. Characterization of AEAP-modified 1100 nm mesoporous silica particles as a function of reaction aminosilane concentration.[a]

[AEAP] (mM)	Specific Surface Area (m^2 g^{-1})[b]	Cumulative Pore Volume (cm^3 g^{-1})[c]	Average Pore Width (Å)[c]	Nitrogen wt%[d]
0	1200±70	0.47±0.09	19.5±0.3	$\leq$0.01
1.4	790±60	0.13±0.02	19.4±0.7	2.41±0.25
2.9	520±130	0.05±0.01	20.0±0.7	3.38±0.41
5.7	5±1	0.01±0.00	20.7±2.0	4.38±0.33
11.5	3±1	0.00±0.00	N.D.[e]	4.87±0.04

[a]Error bars represent standard deviation for $n\geq3$ separate syntheses. [b]Determined by BET analysis of the nitrogen sorption isotherms ($0.05\leq p/p^0\leq0.20$). [c]Calculated via BJH analysis of the nitrogen adsorption isotherm ($p/p^0\leq0.60$). [d]Nitrogen wt% measured by elemental analysis. [e]Pore width could not be calculated from the adsorption isotherm.

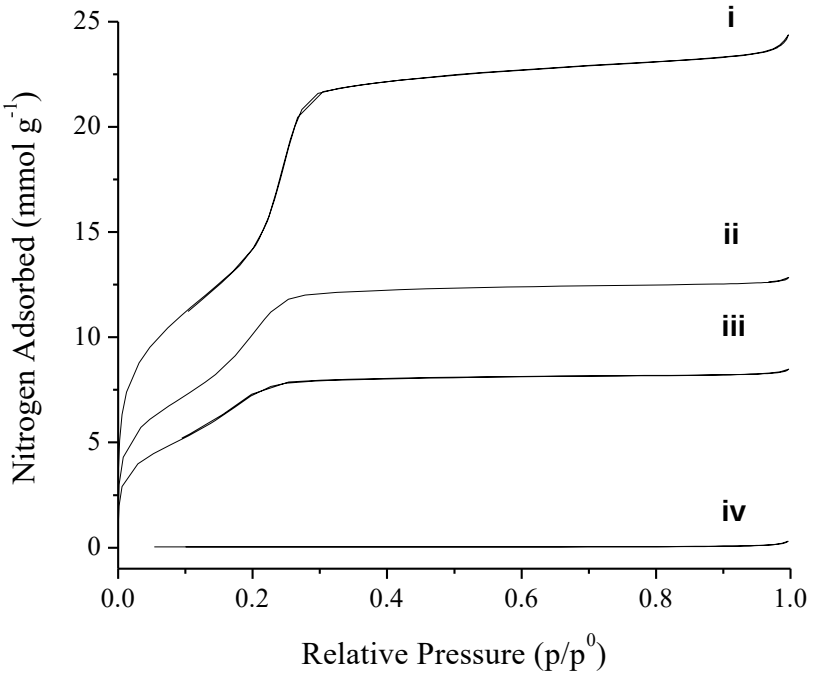

Figure 3.2. Nitrogen sorption isotherms for 1100 nm AEAP-modified MSNs at reaction AEAP concentrations of (i) 0, (ii) 1.4, (iii) 2.9, and (iv) 11.5 mM. Data for the 5.7 mM AEAP-based synthesis was omitted for clarity because the isotherm overlapped with that for the 11.5 mM synthesis.

a type I isotherm at AEAP concentrations at or exceeding 5.7 mM, consistent with bound organic groups on the silica network (Figure 3.2).[46]

Solid-state cross-polarization ($^{1}H/^{29}Si$)/magic angle spinning (CP/MAS) nuclear magnetic resonance spectroscopy (NMR) confirmed covalent incorporation of AEAP into the inorganic TEOS backbone (Figure 3.3).[47] The Q-band peaks at -94, -103, and -112 ppm were assigned to backbone Si atoms present as geminal silanol (Q_2), lone silanol (Q_3), and siloxane (Q_4) species, respectively. The T-band, indicative of the bound organosilane (AEAP), consisted of peaks at -60 and -69 ppm that were assigned to T_2 and cross-linked T_3 species, respectively. The intensity of the T-band increased with aminosilane concentration, corresponding to progressively greater amine incorporation in the final product. However, quantitative CP/MAS NMR analysis was not pursued due to signal intensity dependence on the location of ^{1}H atoms relative to ^{29}Si. Interestingly, we noted a considerable amount of cross-linked (T_3) surface-bound aminosilanes that was attributed to the large water concentration (>20 M) in the reaction mixture, driving condensation between aminosilanes.[47] For comparison, MCM-41 materials produced through post-synthetic surface grafting in anhydrous solvents are primarily bidentate T_2 species and exhibit limited cross-linking (T_3).[48]

While CP/MAS ^{29}Si NMR confirmed covalent aminosilane incorporation, elemental analysis was used as an adjunct experiment to quantitatively assess amine incorporation. As expected, nitrogen content increased with the overall reaction aminosilane concentration. At the highest AEAP concentration tested (11.5 mM; Table 3.2), a maximum nitrogen content of 4.87 wt%, was measured. Taken together, the nitrogen sorption, NMR, and elemental analysis experiments indicated covalent incorporation of AEAP and suggested mesopore infiltration at aminosilane concentrations $\leq$11.5 mM. Powder small-angle X-ray scattering (SAXS) was used to

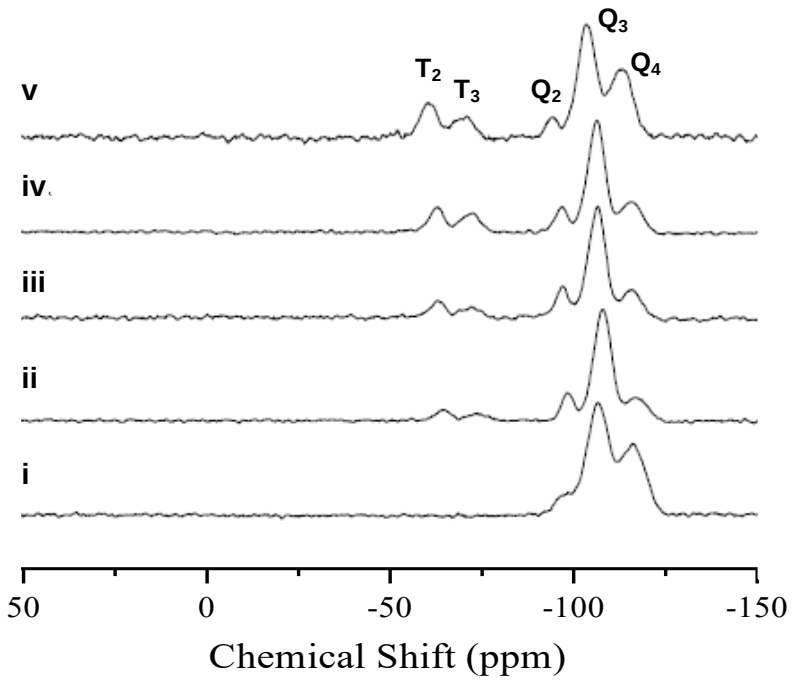

Figure 3.3. Solid-state CP/MAS ^{29}Si NMR spectra of 1100 nm MSNs at AEAP reaction concentrations of (i) 0.0; (ii) 1.4; (iii) 2.9; (iv) 5.7; and (v) 11.5 mM.

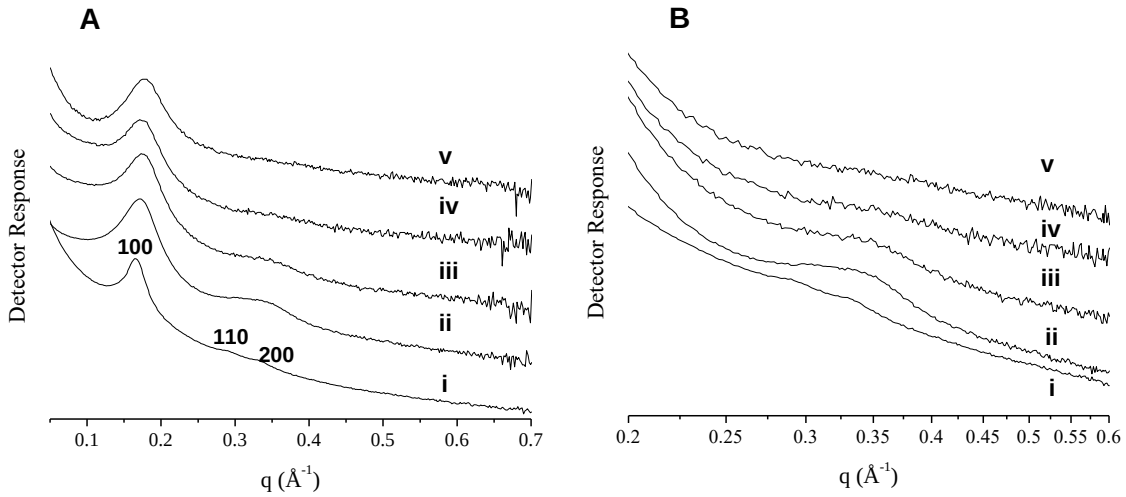

Figure 3.4. Small-angle X-ray scattering profiles for 1100 nm MSNs at AEAP reaction concentrations of (i) 0, (ii) 1.4, (iii) 2.9, (iv) 5.7, and (v) 11.5 mM. The scattering profile is presented in (A) and an enlarged view of the 110/200 scattering lines is displayed in (B).

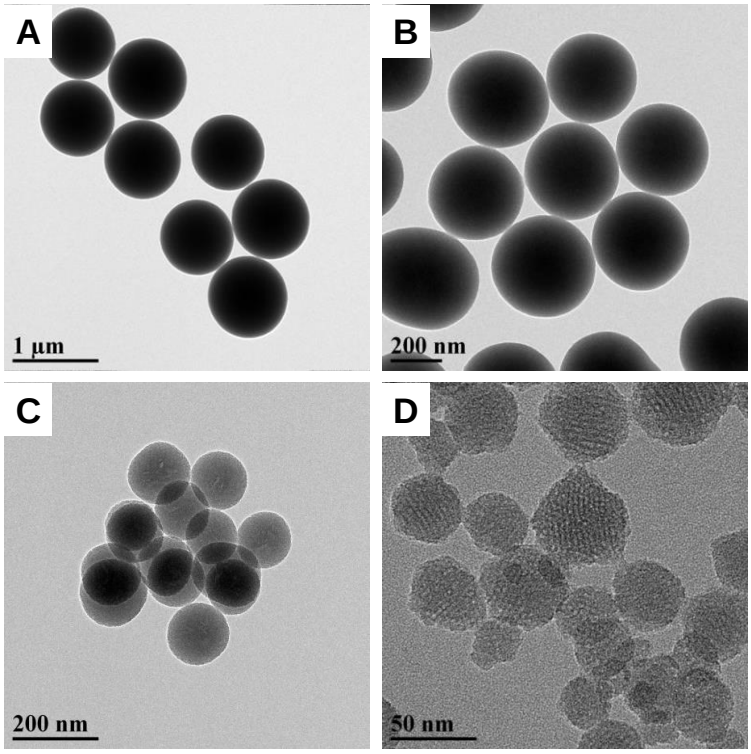

Figure 3.5. Transmission electron micrographs of (A) 1100; (B) 450; (C) 150; and (D) 30 nm AEAP-modified mesoporous silica nanoparticles.

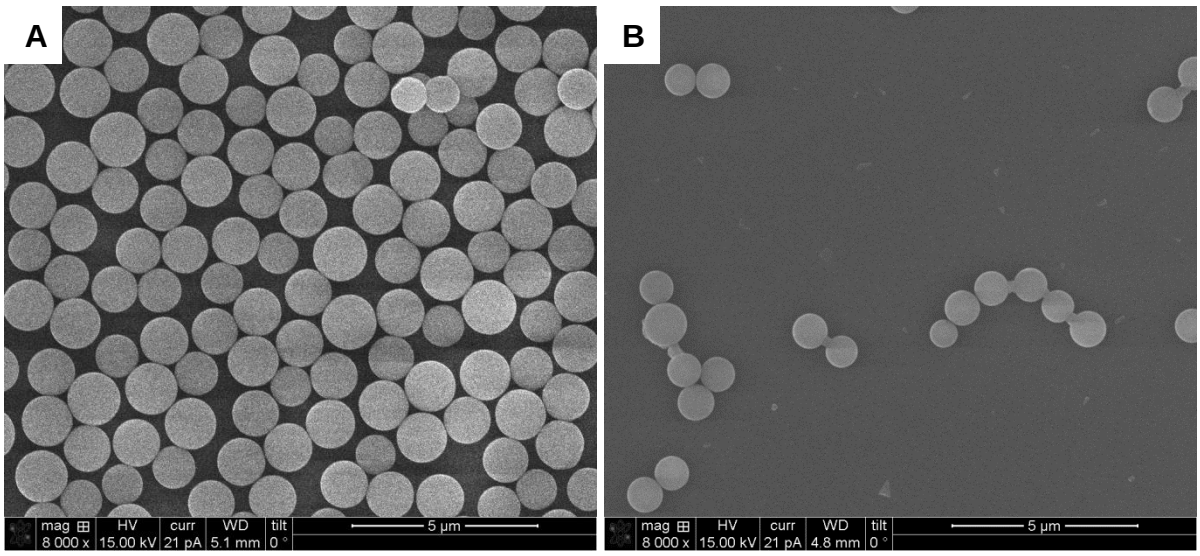

Figure 3.6. Scanning electron micrographs of 1100 nm AEAP-modified particles with reactant AEAP concentrations of (A) 11.5 mM and (B) 14.3 mM. Although the particles in (A) exhibited smooth morphology, undesirable particle agglomeration occurred at higher AEAP concentrations (B).

gain insight into potential alterations to MSN pore structure as a function of reaction AEAP concentration (Figure 3.4).[49] The SAXS profile for the bare 1100 nm MSNs (Figure 3.4A(i)) exhibited an intense scattering peak at 0.170 $Å^{-1}$ (2θ=2.41 ^{o}; *hkl* 100) and two weaker, larger-angle peaks in the scattering profile were assigned to the 110 (0.292 $Å^{-1}$) and 210 (0.339 $Å^{-1}$) reflections indexed on a hexagonal lattice (lattice constant a=43.1±1.5 Å). While the absence of higher-order peaks indicated only modest mesoscopic ordering, the scattering profile consisted of the prominent structural lines for MCM-41-type (hexagonal) silica.[31,50-52] Broadening of the 100 reflection (Figure 3.4A) and the gradual disappearance of the 110/200 scattering peaks (Figure 3.4B) was observed for the amine-modified MSNs (relative to the bare particles), representing a loss of long-range ordering with increasing AEAP concentration. These results further verify aminosilane localization within the pores. Importantly, the particles retained excellent sphericity and monodispersity (Figure 3.5A) upon amine modification as indicated by transmission electron microscopy (TEM), even at the highest AEAP concentration presented in Table 3.2 (11.5 mM). Undesirable particle agglomeration was routinely noted at greater AEAP concentrations ($\geq$14.3 mM). Inter-particle bridging was occurring at these higher concentrations, revealing a practical maximum in the attainable aminosilane incorporation (Figure 3.6).

Based on the results for the 1100 nm particles, the optimal TEOS:aminosilane molar ratio of 1.56:1.00 (corresponding to 11.5 mM AEAP in Table 2) was used to synthesize smaller AEAP particles. Regardless of the intended size, this approach resulted in well-defined nanomaterials (Figure 3.5B–D). Dynamic light scattering (DLS) analysis of aqueous MSN dispersions (Table 3.3) supported TEM observations. The low observed polydispersity indices (PDIs; 0.12, 0.02, and 0.04 for the 30, 150, and 450 nm particles, respectively) affirmed narrow particle size distributions. The DLS/TEM data also verified covalent bonding of aminosilanes to the particle

Table 3.3. Physicochemical characterization of AEAP-functionalized MSNs of varying size.[a]

Geometric Diameter (nm)[b]	Z-average Size (nm)[c]	PDI[c]	Nitrogen wt%[d]	Specific Surface Area (m^2 g^{-1})[e]	Pore Width (Å)[f]
36±8	74±6	0.12±0.06	4.65±0.19	210±40	25.1±1.1
149±13	223±17	0.02±0.01	5.91±0.13	69±13	24.8±0.6
450±50	564±66	0.04±0.02	5.07±0.10	68±20	21.5±0.8
1110±210	n/a[g]	n/a[g]	4.87±0.04	3±1	n/a[h]

[a]Error bars represent standard deviation for $n \geq 3$ separate syntheses. [b]Estimated using electron micrographs. [c]Measured via dynamic light scattering. [d]Nitrogen wt% measured by elemental analysis. [e]Determined by BET analysis of the nitrogen sorption isotherms ($0.05 \leq p/p^0 \leq 0.20$). [f]Calculated via BJH analysis of the nitrogen adsorption isotherm ($p/p^0 \leq 0.60$). [g]Particle sedimentation interfered with DLS measurement. [h]Pore width could not be calculated from the adsorption isotherm.

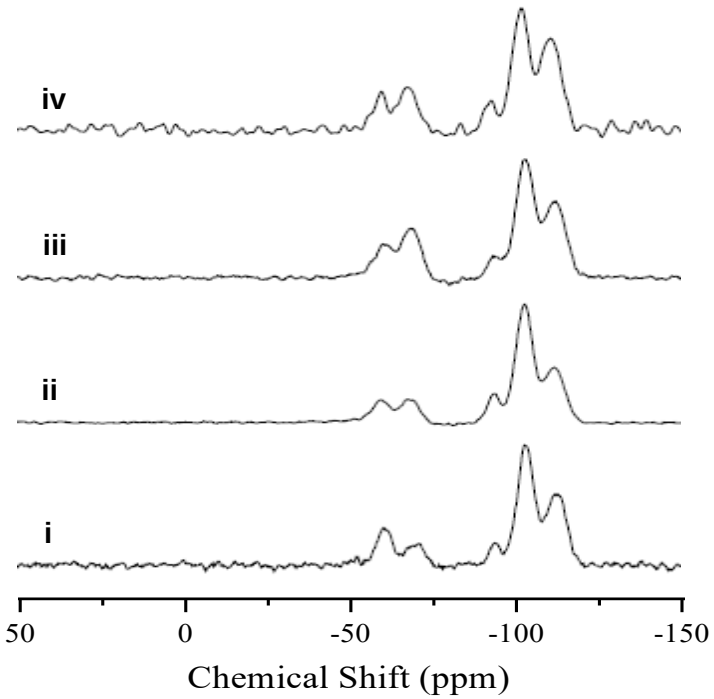

Figure 3.7. Solid-state CP/MAS ^{29}Si NMR spectra of (i) 1100; (ii) 450; (iii) 150; and (iv) 30 nm AEAP-modified particles.

surface, rather than the formation of discrete entities and likely large agglomerates. Elemental analysis (Table 3.3) and CP/MAS NMR (Figure 3.7) confirmed aminosilane incorporation, with significant measured nitrogen content (>4.50 %N) for each particle system.

3.3.1. Nitric oxide release

Different sized AEAP-modified particles were functionalized with *N*-diazeniumdiolate moieties by reaction with NO gas at high pressure in the presence of sodium methoxide. Nitric oxide release was evaluated in real-time via chemiluminescent analysis of the NO-releasing particles in physiological buffer (PBS, pH 7.4) at 37 ^{o}C (Table 3.4). Upon immersion into aqueous solution the AEAP/NO MSNs released large instantaneous NO fluxes corresponding to reaction of the proton-labile *N*-diazeniumdiolate with water to generate NO.[53-54] Despite large total NO storage (>0.8 μmol mg^{-1}) for all four particle systems, total NO storage ($p<0.01$), NO-release half-lives ($p<0.01$), and release durations ($p=0.02$) were unexpectedly diverse. The 1100 nm particles exhibited large NO storage (1.41 μmol mg^{-1}) and rapid release ($t_{1/2}$=25.6 min). Similarly, the 30 nm AEAP/NO particles released their total NO payload rapidly ($t_{1/2}$=27.4 min) but stored only a fraction of the NO measured for the 1100 nm particles ($[NO]_t$=0.88 μmol mg^{-1}).

While the 450 nm MSNs were characterized with low NO storage (0.82 μmol mg^{-1}), they were associated with the longest NO-release half-life (88.2 min). Relative to the 1100 nm AEAP/NO particles, the 150 nm MSNs exhibited comparable NO storage (1.30 μmol mg^{-1}) and intermediate NO-release rates ($t_{1/2}$=41.9 min). The difference in NO-release kinetics between particle systems was not anticipated, as all particles were functionalized with the same *N*-diazeniumdiolate precursor (AEAP). To shed further light on these effects, total NO release from the AEAP/NO particles were compared to the degree of nitrogen incorporation measured by

Table 3.4. Chemiluminescent NO release measurements in physiological buffer (PBS, pH 7.4, 37 ^{o}C) from AEAP/NO MSNs of varying size.[a]

Particle Size (nm)	$[NO]_{max}$ (ppm mg^{-1})[b]	$t_{1/2}$ (min)[c]	t_d (h)	$[NO]_t$ (μmol mg^{-1})	NO Donor Formation Efficiency (%)
30	18.7±2.2	27.4±8.9	12.2±3.0	0.88±0.05	26.6±1.8
150	22.6±4.4	40.7±11.0	16.7±1.4	1.30±0.11	30.9±2.7
450	6.6±1.8	88.2±10.5	14.0±0.3	0.82±0.08	22.8±2.3
1100	32.8±9.8	25.6±5.0	11.1±0.7	1.41±0.19	40.7±5.2

[a]Error bars represent standard deviation for $n \geq 3$ separate syntheses. [b]Maximum instantaneous NO concentration. [c]Half-life of NO release. [d]NO-release duration; time required for NO concentrations to reach $\leq$ 10 ppb mg^{-1}. [e]Total NO release. [f]Calculated using total NO release and nitrogen wt% determined by elemental analysis (Table 3.3).

elemental analysis (Table 3.3) to determine *N*-diazeniumdiolate formation efficiencies. As expected based on the NO release data, the 1100 nm MSNs exhibited the greatest NO donor formation efficiency (40.7%), far greater than that reported by Carpenter et al. (<27%).[19] The NO donor formation efficiencies for the other three particle sizes were calculated at 23–31%.

The wide range of NO-release kinetics (half-lives 27–88 min) and NO donor formation efficiencies (23–41%) suggested additional factors were controlling the NO release. One possible influence to NO-release kinetics is particle size and the position of the *N*-diazeniumdiolates within the pore network, which may affect NO donor accessibility by water and thus impact NO-release kinetics. However, aminosilane (*N*-diazeniumdiolate) location alone does not alone account for the differences in NO-release kinetics. For example, the largest particles, which could have NO donors buried as far as 0.5 μm from their external surface, also had the shortest NO-release half-life ($t_{1/2}$=25.6 min) and duration (t_d=11.1 h). We hypothesized that the structure and ordering of the particle pore network may also affect NO-release kinetics and partially account for these variations, particularly since a link between mesoscopic ordering and diffusion-based drug release has been demonstrated previously.[55] For example, decreased organization may impede sodium methoxide access to pore-bound secondary amines, hindering *N*-diazeniumdiolate formation. As an extension of the same logic, altered water diffusion into the pores would give rise to differences in NO-release kinetics between AEAP/NO MSNs of different size.

Small-angle X-ray scattering was used to assess pore ordering of the bare and amine-modified MSNs (Figure 3.8). As determined previously, the SAXS profile for the 1100 nm MSNs corresponded to a hexagonal lattice with modest ordering. In contrast to the observed MCM-41 structure for the largest particles, the scattering profile for the 30 nm MSNs alluded to

an alternative mixed pore structure. Analysis of the smallest particles revealed three scattering peaks at 0.155 $Å^{-1}$, 0.301 $Å^{-1}$, and 0.552 $Å^{-1}$, which represented an intermediate to typical hexagonal and lamellar (layered) pore ordering.[51-52] The appearance of the high angle reflection (0.552 $Å^{-1}$) was evidence for a significant degree of pore ordering; this peak is seldom observed for intermediate products. The electron micrographs for the 30 nm MSNs (Figure 4D) were in good agreement with the scattering data and provided further confirmation of a mixed pore structure. X-ray scattering patterns obtained for the 150 and 450 nm particles were representative of a greater degree of pore disorder. Only a broad peak centered at ~0.32 $Å^{-1}$ was observed in both scattering profiles (in addition to the 100 line at ~0.17–0.19 $Å^{-1}$). The absence of an additional reflection confirmed mesophase irregularity for these particles. In fact, the scattering profiles for the 150 and 450 nm particles were characteristic of mesopore arrangements between hexagonal and lamellar structures.[31] While pore disorder was not as extensive for the 150 nm particles, the skewed peak at ~0.18 $Å^{-1}$ for 450 nm MSNs suggested a more heterogeneous pore structure. In fact, the irregular peak shape was likely the superimposition of two separate low order reflections. Of note, the X-ray scattering data for the amine-functionalized particles 1100 nm particles pointed to a slight loss in long-range ordering (Figure 5A) due to pore filling by AEAP.[56-57] Only broad reflections were evident in the scattering profiles for the 30, 150, and 450 nm AEAP-modified MSNs, indicating that aminosilane modification impacted the pore structures of these particle systems. Potential interference to pore structure determination by scattering contributions from the particles themselves (i.e., as monodisperse spheres) was unlikely, since the raw scattering profile did not display typical interference fringes in the 0.01–0.1 $Å^{-1}$ region.

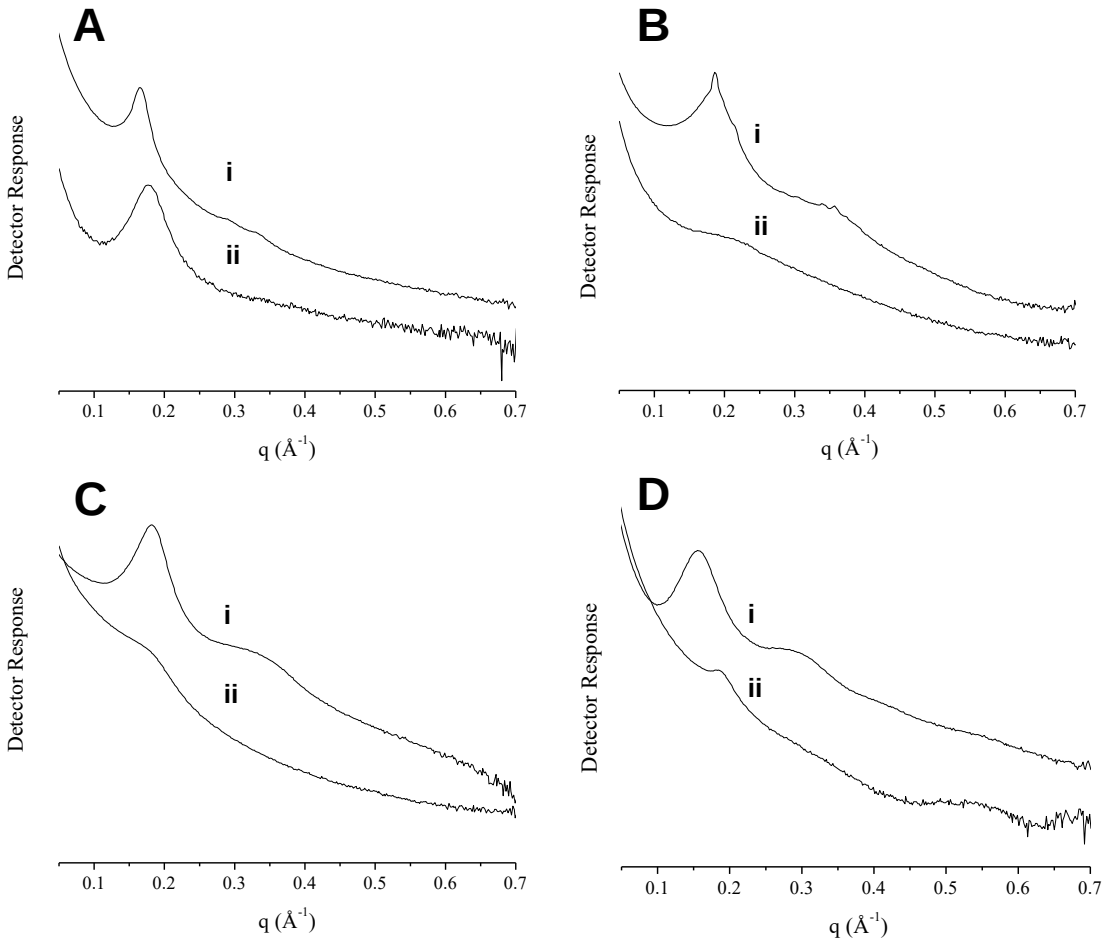

Figure 3.8. Small-angle X-ray scattering profiles for (A) 1100; (B) 450; (C) 150; and (D) 30 nm (i) bare and (ii) AEAP-modified MSNs.

Particle X-ray scattering data provided insight into the relationship between MSN pore structure and NO-release kinetics. The more ordered pore system (i.e., amine-modified 1100 nm particles) enables unrestricted pore access of sodium methoxide and water, resulting in large NO storage and rapid NO release, respectively. The 150 and 450 nm particles were capable of more sustained NO release, likely due to mesophase disruption with aminosilane addition. In contrast, the smallest 30 nm MSNs exhibited rapid NO release and lower NO storage (0.88 μmol mg^{-1}) despite collapse of the pore system. In this case, location of the *N*-diazeniumdiolates within the pore network and water access to the NO donors may more significantly affect NO release than particle mesoporosity.

3.3.2. Organosilane modification

While aminosilanes are highly reactive with the silanol groups that populate the surface of silica nanoparticles, they also readily undergo hydrolysis and auto-condensation in aqueous conditions to form new, discrete entities. For this reason, addition of organosilane directly to the colloidal sol (i.e., particle reaction mixture) generally yields amorphous materials with heterogeneous functional group distribution. Post-synthetic grafting approaches thus require active steps for water removal from the reaction mixture to avoid undesirable particle agglomeration.[38] In addition to anhydrous conditions, efficient particle modification is contingent upon successful removal of the pore-resident surfactant prior to reaction with aminosilanes, as the positively charged template molecule stabilizes the anionic surface silanols and may impede diffusion of external species into the pores.[58-59] De Juan and co-workers previously exploited the stability of the surfactant CTAB template for selective derivatization of the outer and inner mesoporous silica surfaces using a step-by-step functionalization approach.[60] In our study, the large degree of particle functionalization suggested that the aminosilanes likely displaced CTAB

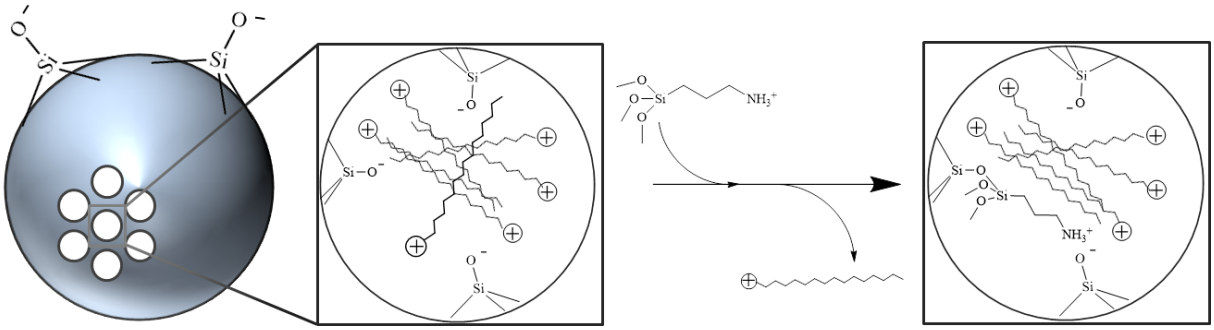

Figure 3.9. Proposed mechanism for MSN functionalization with aminosilanes. Positively charged aminosilanes undergo ion exchange with the template surfactant to stabilize anionic silanol species anchored to the mesopore walls.

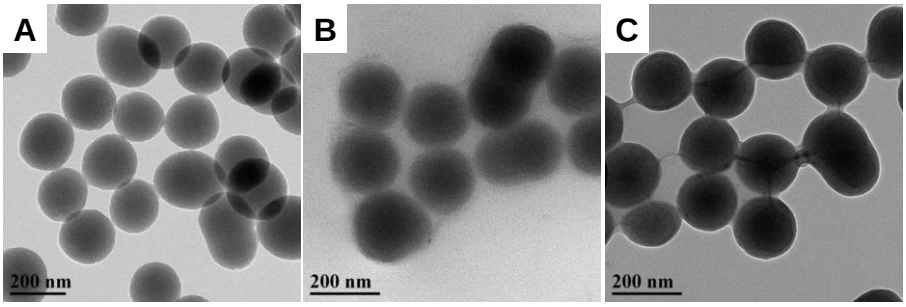

Figure 3.10. Transmission electron micrographs of 150 nm MSNs modified with (A) APTES; (B) BTMS; and (C) MPTMS. Particles in (A) exhibit smooth morphology, while agglomeration is observed in (B) and (C).

Table 3.5. Elemental analysis of 150 nm APTES, BTMS, and MPTMS particles.

Silane Modification	Carbon wt%	Hydrogen wt%	Nitrogen wt%
APTES	13.21	4.08	4.49
BTMS	23.16	4.79	0.16
MPTMS	25.58	4.84	0.88

before undergoing auto-condensation. We rationalized that this phenomenon might be due to an ion-exchange process between the surfactant and protonated aminosilanes (Figure 3.9). Both Dai et al.[61] and Bourlinos et al.[62] have described ion exchange between cationic species (metal ions and aminosilanes, respectively) and the CTAB template as a method for particle modification. In both cases the uncalcined (i.e., CTAB-containing) silica was modified in a separate reaction rather than a one-step procedure.

We sought to verify that only MSN modification with cationic species would retain particle morphology. Using the 150 nm particle system, the MSNs were functionalized with either isobutyl(trimethoxy)silane (BTMS) or (3-mercaptopropyl)trimethoxysilane (MPTMS) at concentrations equal to those employed for the 150 nm AEAP particles. As the colloidal sol is formed under basic conditions, the BTMS alkyl groups remain neutral whereas a significant fraction of the MPTMS side chains would exist as the anionic thiolate species (pK_a~10),[63-64] in both cases preventing ion exchange. 3-aminopropyltriethoxysilane (APTES) was used as a positive control, as APTES is similar in size to BTMS and MPTMS but should undergo efficient ion exchange with CTAB due to the presence of a basic primary amine.

The morphology of the 150 nm APTES, BTMS, and MPTMS particles was examined using transmission electron microscopy (Figure 3.10). As expected, 150 nm particles functionalized with APTES exhibited uniform morphology and excellent sphericity, consistent with the 150 nm AEAP MSNs. Evaluation of aqueous APTES particle suspensions by DLS indicated that the monodispersity of the particles (PDI=0.03±0.02) was preserved upon aminosilane modification. In contrast, undesirable silane bridging and particle agglomeration were evident in electron micrographs of the MPTMS- and BTMS-modified particles. A significant increase in the carbon wt% (measured by elemental analysis; Table 3.5) for all

particle systems indicated that the silanes were incorporated into the final product. The morphological differences between particles observed using TEM were due to reaction with organosilanes. While this data does not exclude the possibility of alternative reaction mechanisms, the particle analyses presented provide clear support of ion exchange reactions between cationic organosilanes and CTAB.

3.3.3. Aminosilane modification and nitric oxide-release kinetics

As the structure of the precursor amine for *N*-diazeniumdiolate formation influences NO-release kinetics from both small molecules[11] and nonporous silica particles,[27] we sought to alter the NO-release kinetics from the MSNs using different organosilanes. The 30 nm particle system was systematically modified with several aminosilanes, including AHAP, DET, and MAP. The characterization of the precursor- and NO donor-modified MSNs is provided in Table 3.6. Both the geometric size (~35–43 nm) and PDI (<0.20) of the particles remained approximately constant ($p>0.5$), indicating that the small particle size and monodispersity were conserved during the chemical modification procedure regardless of aminosilane type. The measured hydrodynamic diameter (Z-average size) of each particle system (75–130 nm) was dependent on the composition of the aminosilane, but agreed well with the corresponding geometric sizes. Nitrogen content for each MSN system varied expectedly based on the elemental composition of the aminosilane reactant. Particles functionalized with the monoamine MAP incorporated the least amount of nitrogen (3.26%), while the nitrogen wt% was greatest for the triamine DET modification (5.60%). Intermediate nitrogen content was measured for MSNs with attached AHAP (4.18%) and AEAP (4.65%), which are diaminosilanes of differing carbon content.

The large degree of aminosilane incorporation translated to excellent particle NO storage, exceeding 1.00 μmol mg^{-1} for all particle systems tested except AEAP/NO. Lower total

Table 3.6. Physicochemical and nitric oxide-release characterization of 30 nm NO-releasing MSNs as a function of aminosilane modification.[a]

Aminosilane Modification	Particle Characterization				NO Release		
	Geometric Size (nm)[b]	Z-average Size (nm)[c]	PDI[c]	Nitrogen wt%[d]	$t_{1/2}$ (min)[e]	t_d (h)[f]	$[NO]_t$ (μmol mg^{-1})[g]
MAP	37.1±8.3	91.2±8.8	0.16±0.05	3.26±0.15	2.2±0.2	1.8±0.4	1.39±0.10
AHAP	42.3±8.1	131.8±9.4	0.17±0.04	4.18±0.05	4.7±2.3	5.9±0.2	1.20±0.10
AEAP	35.7±8.1	74.1±6.2	0.12±0.06	4.65±0.19	27.4±8.9	12.2±3.0	0.88±0.05
DET	34.5±7.6	83.0±7.6	0.17±0.04	5.60±0.31	47.0±11.9	33.2±4.7	1.37±0.19

[a]Error bars represent standard deviation for $n \geq 3$ separate syntheses. [b]Estimated using electron micrographs. [c]Measured via dynamic light scattering. [d]Nitrogen wt% measured via elemental analysis. [e]Half-life of NO release. [f]NO-release duration; time required for NO concentrations to reach $\leq$10 ppb mg^{-1}. [g]Total NO release.

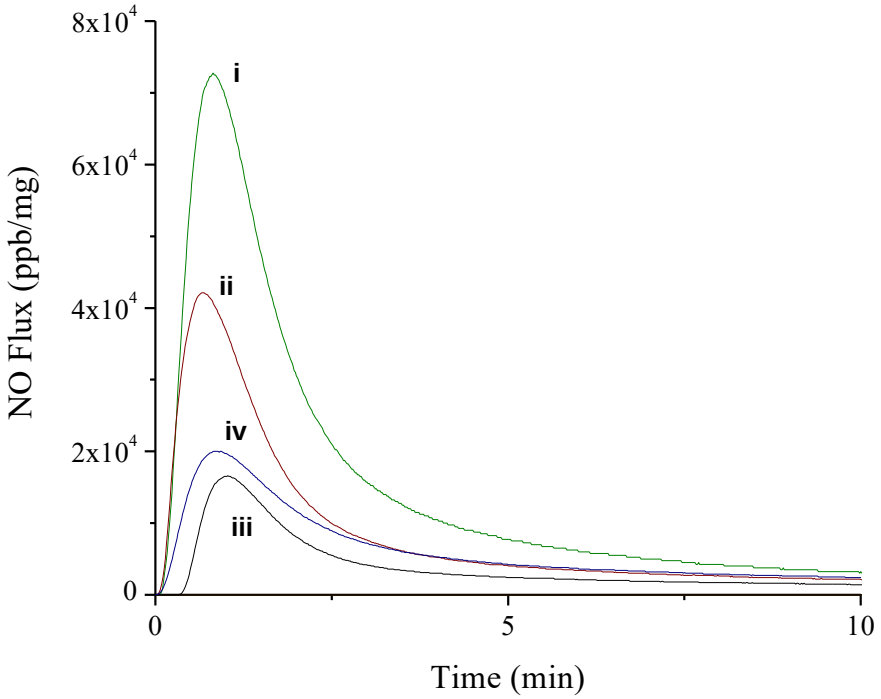

Figure 3.11. Real-time NO-release profiles for 30 nm (i) MAP/NO, (ii) AHAP/NO, (iii) AEAP/NO, and (iv) DET/NO particles after ~10 min in PBS (pH 7.4) at 37 ^{o}C.

NO storage for AEAP/NO was expected based on previous results, as intramolecular hydrogen bonding between the side chain amines hinders *N*-diazeniumdiolate formation.[11,65] While these interactions are also possible for DET, the presence of two secondary amines resulted in greater NO storage. As anticipated, the MSN NO-release kinetics were markedly different between the four particle systems ($p<0.01$). The MAP/NO and AHAP/NO particles were characterized with rapid initial NO release ($t_{1/2}$ of 2.2 and 4.7 min, respectively), while the NO release for the AEAP/NO and DET/NO particles was more sustained ($t_{1/2}$ of 27.4 and 47.0 min, respectively) as a result of *N*-diazeniumdiolate charge stabilization by neighboring protonated amines (Table 3.6; Figure 3.11).[11,65] The NO-release durations covered ~2–33 h, rendering these particles especially useful as NO-delivery vehicles where tuning NO-release kinetics is critical to efficacy.[9]

It should be noted that others have reported macromolecular NO donor scaffolds with total NO release values exceeding ~1.5 μmol mg^{-1}. For example, several porous metal organic frameworks (MOFs) have been developed which with NO storage approaching 1–7 μmol mg^{-1} through direct adsorption of NO gas.[66] However, NO release from MOFs is generally rapid, a feature that restricts their utility to applications in which the NO donor scaffold is in contact with humidified gas. Both dendrimers[67] and silica particles[24] modified with *S*-nitrosothiol (RSNO) NO donors also exhibit large NO payloads (2 and 4 μmol mg^{-1}, respectively) with NO-release durations exceeding two days in deoxygenated PBS buffer. Unfortunately, RSNOs are unstable NO donors, readily decomposing to yield NO under multiple triggers (e.g., light, heat, reaction with Cu^{+} ions or ascorbate).[68] In contrast, *N*-diazeniumdiolate NO donors alleviate the issue of uncontrolled decomposition, liberating NO at rates dependent on both the structure of the aminosilane and the solution pH. While poor NO storage and difficult synthetic procedures have traditionally excluded *N*-diazeniumdiolate-modified macromolecular NO donors from

therapeutic evaluation, the preparation of NO-releasing mesoporous silica particles was achieved in high yields via ion exchange reactions. Excellent NO storage and diverse NO-release kinetics from the MSNs were obtained by simply changing the aminosilane without further synthetic optimization, representing a significant improvement to *N*-diazeniumdiolate-based NO-delivery vehicles.

3.4. Conclusions

Nitric oxide-releasing mesoporous silica nanoparticles with a range of sizes (30, 150, 450, and 1100 nm) were successfully prepared using a straightforward aminosilane-CTAB ion exchange approach. The resulting MSNs were well-defined and exhibited a large degree of surface modification, which translated to competitive NO storage with other macromolecular NO donors (e.g., MOFs, RSNOs). Particle NO storage and release kinetics were dependent on both the structure of the pores and the identity of the precursor aminosilane. This report details the dependence of NO-release kinetics on the architectural properties of mesoporous silica. Further understanding of the intricate relationships between pore ordering and NO-release kinetics remains an exciting area of research, as controlled mesophase structure would also provide an additional degree of control in macromolecular NO donor design. Moreover, the ability to easily modify the MSNs with different aminosilanes enabled tuning of NO-release kinetics without sacrificing control over either total NO storage or particle size.

REFERENCES

(1) Cooke, J. P. "NO and angiogenesis." *Atherosclerosis Supplements* **2003,** *4*, 53-60.

(2) Ignarro, L. J.; Buga, G. M.; Wood, K. S.; Byrns, R. E.; Chaudhuri, G. "Endothelium-derived relaxing factor produced and released from artery and vein is nitric oxide." *Proceedings of the National Academy of Sciences of the United States of America* **1987,** *84*, 9265-9269.

(3) Luo, J. D.; Chen, A. F. "Nitric oxide: A newly discovered function on wound healing." *Acta Pharmacologica Sinica* **2005,** *26*, 259-264.

(4) Schwentker, A.; Vodovotz, Y.; Weller, R.; Billiar, T. R. "Nitric oxide and wound repair: Role of cytokines?" *Nitric Oxide* **2002,** *7*, 1-10.

(5) Bogdan, C. "Nitric oxide and the immune response." *Nature Immunology* **2001,** *2*, 907-916.

(6) MacMicking, J.; Xie, Q. W.; Nathan, C. "Nitric oxide and macrophage function." *Annual Review of Immunology* **1997,** *15*, 323-350.

(7) Kiss, J. P. "Role of nitric oxide in the regulation of monoaminergic neurotransmission." *Brain Research Bulletin* **2000,** *52*, 459-466.

(8) Hetrick, E. M.; Schoenfisch, M. H. "Analytical chemistry of nitric oxide." *Annual Review of Analytical Chemistry* **2009,** *2*, 409-433.

(9) Carpenter, A. W.; Schoenfisch, M. H. "Nitric oxide release part II. Therapeutic applications." *Chemical Society Reviews* **2012,** *41*, 3742-3752.

(10) Hetrick, E. M.; Shin, J. H.; Stasko, N. A.; Johnson, C. B.; Wespe, D. A.; Holmuhamedov, E.; Schoenfisch, M. H. "Bactericidal efficacy of nitric oxide-releasing silica nanoparticles." *ACS Nano* **2008,** *2*, 235-246.

(11) Keefer, L. K. "Fifty years of diazeniumdiolate research. From laboratory curiosity to broad-spectrum biomedical advances." *ACS Chemical Biology* **2011,** *6*, 1147-1155.

(12) Lu, Y.; Shah, A.; Hunter, R. A.; Soto, R. J.; Schoenfisch, M. H. "*S*-nitrosothiol-modified nitric oxide-releasing chitosan oligosaccharides as antibacterial agents." *Acta Biomaterialiaialia* **2015,** *12*, 62-69.

(13) Lu, Y.; Slomberg, D. L.; Shah, A.; Schoenfisch, M. H. "Nitric oxide-releasing amphiphilic poly(amidoamine) (pamam) dendrimers as antibacterial agents." *Biomacromolecules* **2013,** *14*, 3589-98.

(14) Lu, Y.; Sun, B.; Li, C.; Schoenfisch, M. H. "Structurally diverse nitric oxide-releasing poly(propylene imine) dendrimers." *Chemistry of Materials* **2011,** *23*, 4227-4233.

(15) Stasko, N. A.; Schoenfisch, M. H. "Dendrimers as a scaffold for nitric oxide release." *Journal of the American Chemical Society* **2006,** *128*, 8265-8271.

(16) Polizzi, M. A.; Stasko, N. A.; Schoenfisch, M. H. "Water-soluble nitric oxide-releasing gold nanoparticles." *Langmuir* **2007,** *23*, 4938-4943.

(17) Rothrock, A. R.; Donkers, R. L.; Schoenfisch, M. H. "Synthesis of nitric oxide-releasing gold nanoparticles." *Journal of the American Chemical Society* **2005,** *127*, 9362-9363.

(18) Backlund, C. J.; Sergesketter, A. R.; Offenbacher, S.; Schoenfisch, M. H. "Antibacterial efficacy of exogenous nitric oxide on periodontal pathogens." *Journal of Dental Research* **2014,** *93*, 1089-1094.

(19) Carpenter, A. W.; Slomberg, D. L.; Rao, K. S.; Schoenfisch, M. H. "Influence of scaffold size on bactericidal activity of nitric oxide-releasing silica nanoparticles." *ACS Nano* **2011,** *5*, 7235-7244.

(20) Carpenter, A. W.; Worley, B. V.; Slomberg, D. L.; Schoenfisch, M. H. "Dual action antimicrobials: Nitric oxide release from quaternary ammonium-functionalized silica nanoparticles." *Biomacromolecules* **2012,** *13*, 3334-3342.

(21) Slomberg, D. L.; Lu, Y.; Broadnax, A. D.; Hunter, R. A.; Carpenter, A. W.; Schoenfisch, M. H. "Role of size and shape on biofilm eradication for nitric oxide-releasing silica nanoparticles." *ACS Applied Materials & Interfaces* **2013,** *5*, 9322-9329.

(22) Frost, M. C.; Meyerhoff, M. E. "Synthesis, characterization, and controlled nitric oxide release from s-nitrosothiol-derivatized fumed silica polymer filler particles." *Journal of Biomedical Materials Research Part A* **2005,** *72*, 409-419.

(23) Kafshgari, M. H.; Cavallaro, A.; Delalat, B.; Harding, F. J.; McInnes, S. J. P.; Mäkilä, E.; Salonen, J.; Vasilev, K.; Voelcker, N. H. "Nitric oxide-releasing porous silicon nanoparticles." *Nanoscale Research Letters* **2014,** *9*, 333.

(24) Riccio, D. A.; Nugent, J. L.; Schoenfisch, M. H. "Stöber synthesis of nitric oxide-releasing *S*-nitrosothiol-modified silica particles." *Chemistry of Materials* **2011,** *23*, 1727-1735.

(25) Zhang, H.; Annich, G. M.; Miskulin, J.; Stankiewicz, K.; Osterholzer, K.; Merz, S. I.; Bartlett, R. H.; Meyerhoff, M. E. "Nitric oxide-releasing fumed silica particles: Synthesis, characterization, and biomedical application." *Journal of the American Chemical Society* **2003,** *125*, 5015-5024.

(26) Lu, Y.; Slomberg, D. L.; Sun, B.; Schoenfisch, M. H. "Shape- and nitric oxide flux-dependent bactericidal activity of nitric oxide-releasing silica nanorods." *Small* **2013,** *9*, 2189-2198.

(27) Backlund, C. J.; Worley, B. V.; Sergesketter, A. R.; Schoenfisch, M. H. "Kinetic-dependent killing of oral pathogens with nitric oxide." *Journal of Dental Research* **2015**.

(28) Koh, A.; Riccio, D. A.; Sun, B.; Carpenter, A. W.; Nichols, S. P.; Schoenfisch, M. H. "Fabrication of nitric oxide-releasing polyurethane glucose sensor membranes." *Biosensors and Bioelectronics* **2011,** *28*, 17-24.

(29) Soto, R. J.; Privett, B. J.; Schoenfisch, M. H. "In vivo analytical performance of nitric oxide-releasing glucose biosensors." *Analytical Chemistry* **2014,** *86*, 7141-7149.

(30) Beck, J. S.; Vartuli, J. C.; Roth, W. J.; Leonowicz, M. E.; Kresge, C. T.; Schmitt, K. D.; Chu, C. T. W.; Olson, D. H.; Sheppard, E. W. "A new family of mesoporous molecular sieves prepared with liquid crystal templates." *Journal of the American Chemical Society* **1992,** *114*, 10834-10843.

(31) Huo, Q.; Margolese, D. I.; Stucky, G. D. "Surfactant control of phases in the synthesis of mesoporous silica-based materials." *Chemistry of Materials* **1996,** *8*, 1147-1160.

(32) Huh, S.; Wiench, J. W.; Yoo, J.-C.; Pruski, M.; Lin, V. S. Y. "Organic functionalization and morphology control of mesoporous silicas via a co-condensation synthesis method." *Chemistry of Materials* **2003,** *15*, 4247-4256.

(33) Burleigh, M. C.; Markowitz, M. A.; Spector, M. S.; Gaber, B. P. "Direct synthesis of periodic mesoporous organosilicas: Functional incorporation by co-condensation with organosilanes." *The Journal of Physical Chemistry B* **2001,** *105*, 9935-9942.

(34) Trewyn, B. G.; Slowing, I. I.; Giri, S.; Chen, H.-T.; Lin, V. S. Y. "Synthesis and functionalization of a mesoporous silica nanoparticle based on the sol–gel process and applications in controlled release." *Accounts of Chemical Research* **2007,** *40*, 846-853.

(35) Chen, J.; Li, Q.; Xu, R.; Xiao, F. "Distinguishing the silanol groups in the mesoporous molecular sieve MCM-41." *Angewandte Chemie International Edition* **1996,** *34*, 2694-2696.

(36) Gartmann, N.; Brühwiler, D. "Controlling and imaging the functional-group distribution on mesoporous silica." *Angewandte Chemie International Edition* **2009,** *48*, 6354-6356.

(37) Sharma, K. K.; Anan, A.; Buckley, R. P.; Ouellette, W.; Asefa, T. "Toward efficient nanoporous catalysts: Controlling site-isolation and concentration of grafted catalytic sites on nanoporous materials with solvents and colorimetric elucidation of their site-isolation." *Journal of the American Chemical Society* **2008,** *130*, 218-228.

(38) Bruhwiler, D. "Postsynthetic functionalization of mesoporous silica." *Nanoscale* **2010,** *2*, 887-892.

(39) Lang, N.; Tuel, A. "A fast and efficient ion-exchange procedure to remove surfactant molecules from MCM-41 materials." *Chemistry of Materials* **2004,** *16*, 1961-1966.

(40) Kecht, J.; Bein, T. "Oxidative removal of template molecules and organic functionalities in mesoporous silica nanoparticles by peroxide treatment." *Microporous and Mesoporous Materials* **2008,** *116*, 123-130.

(41) Webb, P. A.; Orr, C. "Analytical methods in fine particle technology" Micromeritics Instrument Corporation: Norcross, GA, **1997**.

(42) Sing, K. S. W.; Everett, D. H.; Haul, R. A. W.; Moscou, L.; Pierotti, R. A.; Rouquerol, J.; Siemieniewska, T. "Reporting physisorption data for gas/solid systems with special reference to the determination of surface area and porosity." *Pure and Applied Chemistry* **1985,** *57*, 603–613.

(43) Nooney, R. I.; Thirunavukkarasu, D.; Chen, Y.; Josephs, R.; Ostafin, A. E. "Synthesis of nanoscale mesoporous silica spheres with controlled particle size." *Chemistry of Materials* **2002,** *14*, 4721-4728.

(44) Lee, C.H.; Lo, L.W.; Mou, C.Y.; Yang, C.S. "Synthesis and characterization of positive-charge functionalized mesoporous silica nanoparticles for oral drug delivery of an anti-inflammatory drug." *Advanced Functional Materials* **2008,** *18*, 3283-3292.

(45) Pauly, T. R.; Pinnavaia, T. J. "Pore size modification of mesoporous HMS molecular sieve silicas with wormhole framework structures." *Chemistry of Materials* **2001,** *13*, 987-993.

(46) Kruk, M.; Jaroniec, M. "Gas adsorption characterization of ordered organic−inorganic nanocomposite materials." *Chemistry of Materials* **2001,** *13*, 3169-3183.

(47) Albert, K.; Bayer, E. "Characterization of bonded phases by solid-state NMR spectroscopy." *Journal of Chromatography A* **1991,** *544*, 345-370.

(48) Kobler, J.; Möller, K.; Bein, T. "Colloidal suspensions of functionalized mesoporous silica nanoparticles." *ACS Nano* **2008,** *2*, 791-799.

(49) Smarsly, B.; Groenewolt, M.; Antonietti, M., "SAXS analysis of mesoporous model materials: A validation of data evaluation techniques to characterize pore size, shape, surface area, and curvature of the interface". In *Scattering methods and the properties of polymer materials*, Springer Berlin Heidelberg: **2005**; Vol. 130, 105-113.

(50) Kresge, C. T.; Leonowicz, M. E.; Roth, W. J.; Vartuli, J. C.; Beck, J. S. "Ordered mesoporous molecular sieves synthesized by a liquid-crystal template mechanism." *Nature* **1992,** *359*, 710-712.

(51) Huo, Q.; Margolese, D. I.; Ciesla, U.; Demuth, D. G.; Feng, P.; Gier, T. E.; Sieger, P.; Firouzi, A.; Chmelka, B. F. "Organization of organic molecules with inorganic molecular species into nanocomposite biphase arrays." *Chemistry of Materials* **1994,** *6*, 1176-1191.

(52) Beck, J. S.; Vartuli, J. C.; Kennedy, G. J.; Kresge, C. T.; Roth, W. J.; Schramm, S. E. "Molecular or supramolecular templating: Defining the role of surfactant chemistry in the formation of microporous and mesoporous molecular sieves." *Chemistry of Materials* **1994,** *6*, 1816-1821.

(53) Davies, K. M.; Wink, D. A.; Saavedra, J. E.; Keefer, L. K. "Chemistry of the diazeniumdiolates. 2. Kinetics and mechanism of dissociation to nitric oxide in aqueous solution." *Journal of the American Chemical Society* **2001,** *123*, 5473-5481.

(54) Coneski, P. N.; Schoenfisch, M. H. "Nitric oxide release part iii. Measurement and reporting." *Chemical Society Reviews* **2012,** *41*, 3753-3758.

(55) Andersson, J.; Rosenholm, J.; Areva, S.; Lindén, M. "Influences of material characteristics on ibuprofen drug loading and release profiles from ordered micro- and mesoporous silica matrices." *Chemistry of Materials* **2004,** *16*, 4160-4167.

(56) Lai, C.-Y.; Trewyn, B. G.; Jeftinija, D. M.; Jeftinija, K.; Xu, S.; Jeftinija, S.; Lin, V. S. Y. "A mesoporous silica nanosphere-based carrier system with chemically removable cds nanoparticle caps for stimuli-responsive controlled release of neurotransmitters and drug molecules." *Journal of the American Chemical Society* **2003,** *125*, 4451-4459.

(57) Winkler, H.; Birkner, A.; Hagen, V.; Wolf, I.; Schmechel, R.; Seggern, H. V.; Fischer, R. A. "Quantum-confined gallium nitride in MCM-41." *Advanced Materials* **1999,** *11*, 1444-1448.

(58) Cheng, K.; Landry, C. C. "Diffusion-based deprotection in mesoporous materials: A strategy for differential functionalization of porous silica particles." *Journal of the American Chemical Society* **2007,** *129*, 9674-9685.

(59) Kecht, J.; Schlossbauer, A.; Bein, T. "Selective functionalization of the outer and inner surfaces in mesoporous silica nanoparticles." *Chemistry of Materials* **2008,** *20*, 7207-7214.

(60) de Juan, F.; Ruiz-Hitzky, E. "Selective functionalization of mesoporous silica." *Advanced Materials* **2000,** *12*, 430-432.

(61) Dai, S.; Shin, Y.; Ju, Y.; Burleigh, M. C.; Lin, J. S.; Barnes, C. E.; Xue, Z. "A new methodology to functionalize surfaces of ordered mesoporous materials based on ion exchange reactions." *Advanced Materials* **1999,** *11*, 1226-1230.

(62) Bourlinos, A. B.; Karakostas, T.; Petridis, D. "“Side chain” modification of MCM-41 silica through the exchange of the surfactant template with charged functionalized organosiloxanes: An efficient route to valuable reconstructed MCM-41 derivatives." *The Journal of Physical Chemistry B* **2003,** *107*, 920-925.

(63) Dance, I. G. "The structural chemistry of metal thiolate complexes." *Polyhedron* **1986,** *5*, 1037-1104.

(64) Son, D.; Wolosiuk, A.; Braun, P. V. "Double direct templated hollow ZnS microspheres formed on chemically modified silica colloids." *Chemistry of Materials* **2009,** *21*, 628-634.

(65) Riccio, D. A.; Schoenfisch, M. H. "Nitric oxide release part I. Macromolecular scaffolds." *Chemical Society Reviews* **2012,** *41*, 3731-3741.

(66) Wheatley, P. S.; Butler, A. R.; Crane, M. S.; Fox, S.; Xiao, B.; Rossi, A. G.; Megson, I. L.; Morris, R. E. "NO-releasing zeolites and their antithrombotic properties." *Journal of the American Chemical Society* **2006,** *128*, 502-9.

(67) Stasko, N. A.; Fischer, T. H.; Schoenfisch, M. H. "*S*-nitrosothiol-modified dendrimers as nitric oxide delivery vehicles." *Biomacromolecules* **2008,** *9*, 834-841.

(68) Grossi, L.; Montevecchi, P. C. "A kinetic study of *S*-nitrosothiol decomposition." *Chemistry – A European Journal* **2002,** *8*, 380-387.

CHAPTER 4. DESIGN CONSIDERATIONS FOR SILICA PARTICLE-DOPED NITRIC OXIDE-RELEASING POLYURETHANE GLUCOSE BIOSENSOR MEMBRANES[4]

4.1. Introduction

Effective diabetes management relies on accurate blood glucose (BG) measurement to maintain target levels of glycemia.[1-3] Self-monitoring of capillary BG levels has traditionally been carried out using portable glucometers. Although glucometers are generally accurate and reliable, poor patient compliance and infrequent sampling lead to inconsistent BG control.[4] Severe hyperglycemia or brief and potentially life-threatening hypoglycemic events frequently go undetected as a result. Implantable electrochemical continuous glucose monitors (CGMs) that measure glucose in interstitial fluid have received significant focus with the goal of alleviating the sampling issues associated with discrete BG measurement.[5-6] Such devices facilitate identification of temporal BG fluctuations and, based on these trends, may be used to predict glycemia in the immediate future (i.e., as a hypoglycemic alarm).

Despite the availability of implantable glucose biosensors for human use, CGM devices have not been widely adopted due to performance issues and difficulty of use (e.g., frequent calibration, false hypoglycemic alarms).[4] Poor sensor accuracy is due in part to the foreign body response (FBR), a cascade of intense inflammatory/wound healing reactions that transpire at the surface of the implanted CGM.[4,7-10] Initial blood protein adhesion reduces sensor sensitivity by

[4]This chapter was adapted from an article that was submitted for publication. The original citation is as follows: Soto, R. J.; Schofield, J. B.; Walter, S. E.; Malone-Povolny, M. J.; Schoenfisch, M. H. "Design considerations for silica particle-doped nitric oxide-releasing polyurethane glucose biosensor membranes," *submitted*.

40–80% and this protein layer mediates later inflammatory cell attachment.[11] Influx of inflammatory cells occurs after tissue injury and has been identified as a contributing factor to erratic sensor response during the first several days of implantation.[8] Eventually, the sensor is sequestered from native tissue by fibroblast construction of a collagenous foreign body capsule that obstructs glucose transport to the device, resulting in sensor failure.

The performance of implanted glucose sensors is inherently linked with FBR severity.[12] A general belief is that in vivo sensors may benefit from reduced inflammation and increased neovascularization. A widely investigated approach for mitigating the FBR employ hydrophilic coatings (e.g., hydrogels,[13] zwitterionic polymers[14-16]) to reduce protein and concomitant cell adhesion. The release of bioactive molecules (e.g., Dexamethasone[17-19] and vascular endothelial growth factor[19]) from sensors have also been studied as methods for more directly influencing key inflammatory and wound healing events. Our laboratory has focused on the release of nitric oxide (NO), an endogenous radical gas with integral roles in angiogenesis and the wound healing.[20-22] Indeed, NO-releasing polymers have been shown to reduce FBR-related inflammation and collagen encapsulation.[23-25] In concert with tissue response studies, in vivo glucose biosensors coated with similar NO-releasing polymers have improved short-term (1–3 d) sensor accuracy.[26-27]

Due to NO's reactive nature, a significant body of literature has focused on suitable NO storage and release strategies. The most successful work to date (based on total NO storage and NO-release durations) has relied on incorporating NO-releasing molecules (NO donors) into polymeric sensor coatings (i.e., polyurethanes).[28-30] The NO-release properties (i.e., storage and kinetics) can be straightforwardly controlled by altering the identity/type of both the NO donor and polymer matrix. For example, NO-releasing silica nanoparticles (SNPs) have been used to

prepare NO-releasing polyurethane (PU) sensor membranes because of their large NO storage and controllable NO-release kinetics.[28,31-35] However, a key design challenge associated with many NO-releasing polymers is undesirable leaching of the entrapped NO donors.[27-30,36] Although silica is considered inert,[37] NO donor modifications to SNPs may alter their association with mammalian cells, thereby increasing cytotoxicity.[38] Leaching of constituent silica may also exacerbate local foreign body reactions, as the SNPs may be phagocytosed by macrophages and increase production of pro-inflammatory cytokines (e.g., tumor necrosis factor α, interleukin 1β).[39-40]

Herein, we report on the design of functional NO-releasing polyurethane glucose biosensor membranes with favorable partitioning of the NO donor-modified silica particles into the polymer matrix. The physicochemical properties of both the dopant SNPs (e.g., NO donor identity, extent of modification) and the PU matrix (water uptake) were examined for potential influence to particle leaching and NO-release properties of the membranes. The most promising membranes were employed to fabricate glucose biosensors with appropriate analytical performance and NO-release durations of up to 7 d.

4.2. Experimental section

4.2.1. Materials

Tetraethylorthosilicate (TEOS), tetramethylorthosilicate (TMOS), 3-mercaptopropyltrimethoxysilane (MPTMS), *N*-methylaminopropyltrimethoxysilane (MAP), *N*-(6-aminohexyl)-aminopropyltrimethoxysilane (AHAP), and 3-(trimethoxysilylpropyl)diethylenetriamine (DET) were purchased from Gelest (Morrisville, PA). Sodium methoxide (NaOMe; 5.4 M in methanol), anhydrous *N*,*N*-dimethylformamide (DMF), anhydrous methanol (MeOH), anhydrous tetrahydrofuran (THF), 200 proof ethanol (EtOH),

aqueous ammonium hydroxide (NH_4OH; 29.42 wt% ammonia), concentrated hydrochloric acid (HCl), toluene, cetyltrimethylammonium bromide (CTAB) and all salts were purchased from Fisher Scientific (Fair Lawn, NJ). Of note, toluene was dried/stored over molecular sieves. Methyltrimethoxysilane (MTMOS) and glucose oxidase (Type VII lyophilized powder, $\geq$ 100,000 U g^{-1}) from *Aspergillus niger* were purchased from Sigma (St. Louis, MO). Nitrogen (N_2), argon (Ar), and nitric oxide calibration (25.87 ppm in N_2) gases were purchased from Airgas National Welders (Raleigh, NC). Pure NO gas was purchased from Praxair (Danbury, CT). Silver wire (127 μm dia.) and PFA-coated 90:10 platinum:iridium (Pt:Ir) wire (127 μm bare dia.) were purchased from A-M Systems (Sequim, WA). Soft stainless steel wire (356 μm dia.) was purchased from McMaster-Carr (Atlanta, GA). Polyurethanes HP-93A-100, PC-3585A, SG-85A, and TT-2072D-B20 were received from Lubrizol (Cleveland, OH). Hydrothane polyurethane AL-25-80A was obtained from AdvanSource Biomaterials (Wilmington, MA). Water was purified to a resistivity of 18.2 MΩ cm and a total organic content of <6 ppb using a Millipore Reference water purification system.

4.2.2. Synthesis of N-diazeniumdiolate-modified silica nanoparticles

Secondary amine-modified nanoparticles were first synthesized by variants of the Stöber method. Ultimately, secondary amines introduced to the SNPs were converted to *N*-diazeniumdiolate NO donors by reaction with NO gas. Mesoporous silica nanoparticles of different sizes (~150, 450, and 800 nm) were synthesized via a previously published aminosilane-surfactant ion exchange approach.[32] Briefly, bare mesoporous silica was synthesized by addition of TEOS to a stirred solution of water, ethanol, ammonia, and CTAB (the template surfactant). After forming the SNPs (2 h following TEOS addition), the particles were reacted

Table 4.1. Reaction parameters for synthesis of amine-modified mesoporous SNPs.

Particle Size (nm)	Reagent/Solvent Volume (mL)				Aminosilane	
	H_2O	Aq. NH_4OH	EtOH	TEOS	Type	Volume (mL)
150 nm	107	2.6	41	0.554	DET3	0.520
450 nm	95	2.6	53	0.698	DET3	0.654
800 nm	162	11.8	175	1.395	DET3	1.310
800 nm	162	11.8	175	1.395	AHAP3	1.342
800 nm	162	11.8	175	1.395	MAP3	0.955

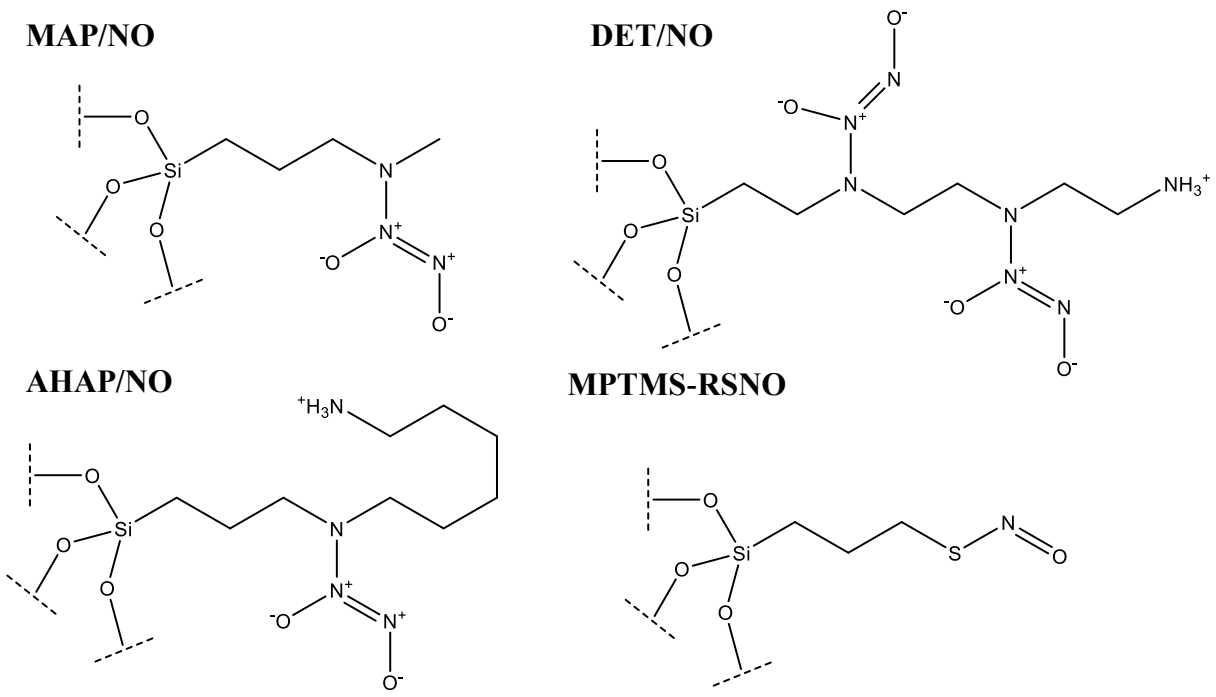

Figure 4.1. Proposed chemical structures of selected silanes modified with either *N*-diazeniumdiolate (MAP, AHAP, DET) or *S*-nitrosothiol (MPTMS) NO donors.

overnight (~16 h) with secondary amine-containing organosilanes (either MAP, AHAP, or DET) by dropwise addition of the silane to the TEOS precursor solution. Reactant concentrations and chemical structures of the aminosilanes are provided in Table 4.1 and Figure 4.1, respectively. Particles were recovered by centrifugation and purified as described previously.[32]

Bare (i.e., not functionalized with secondary amines) 150 nm mesoporous silica particles were synthesized according to the procedure above but were isolated/purified without further aminosilane ion exchange reaction. Nonporous ~150 nm silica particles were synthesized by adding 3.795 mL TEOS to a solution of EtOH (88.4 mL), water (1.10 mL), and aqueous NH_4OH (6.8 mL). The solution was stirred for 2 h to allow for particle nucleation and growth. The particle sol was centrifuged (6540*g*, 10 min, 4 ^{o}C) and the resulting pellet washed thrice with ethanol to remove residual ammonia/TEOS. The bare silica particles were recovered by drying the particle pellet under vacuum. For both bare particle systems (i.e., 150 nm mesoporous and nonporous particles), amine modification was carried out under identical conditions using a surface grafting approach. The bare SiO_2 particles (~200 mg) were exposed to ozone in a BioForce Tip Cleaner (Ames, IA) for 30 min to generate additional, modifiable surface silanols. Subsequently, the particles (100 mg) were reacted with DET3 (207 µL) and trimethylamine (50 µL) for 14 h at 90 ^{o}C in toluene. The reaction was carried out under nitrogen atmosphere and with an attached reflux condenser. Similarly to the procedures above, the particles were isolated via centrifugation, washed with EtOH to remove solvent and unreacted reagents, and dried under vacuum to yield the amine-based particles.

After amine functionalization, *N*-diazeniumdiolates were formed on the secondary amines by reaction with NO gas. The particles were dispersed via sonication at 5 mg mL^{-1} in a 9:1 mixture of DMF:MeOH and 25 µL 5.4 M methanolic NaOMe added to catalyze *N*-

diazeniumdiolate formation. Glass vials containing the particle dispersions were transferred to a stainless steel Parr bottle and connected to an in-house NO reactor. The Parr bottle was flushed with 8 bar Ar gas six times (three brief, three 10 min) to remove atmospheric oxygen and minimize formation of NO byproducts. The reaction vessel was then pressurized with 10 bar 99.99% NO gas (purified over solid potassium hydroxide for at least 4 h) and the particle solutions stirred for 3 d. Subsequently, the NO gas was vented from the Parr bottle and the vessel was again flushed with Ar gas (6×). The *N*-diazeniumdiolate-modified particles were collected via centrifugation, washed three times with EtOH, and dried under vacuum. The resulting NO-releasing particles were stored in a vacuum-sealed Mylar bag at -20 ^{o}C.

4.2.3. Synthesis of S-nitrosothiol-modified silica nanoparticles

Thiol-modified SNPs were synthesized by co-condensation of MPTMS with either TEOS or TMOS (tetraalkoxy backbone silanes).[34] The particles were formed by dropwise addition (0.5 mL min^{-1} using a syringe pump) of a silane mixture (MPTMS and the backbone silane) to stirred solutions of water, ethanol, and ammonia and allowed to react for 2 h. The MPTMS (i.e., alkanethiol) content of the product SNPs was controlled by altering the molar ratio of MPTMS to TEOS or TMOS in the silane precursor solution. Reactant and solvent amounts for each particle type are provided in Table 4.2. After particle formation, the particles were collected by centrifugation (6540*g*, 10 min, 4 ^{o}C), washed thrice with EtOH, and dried in vacuo.

S-nitrosothiol (RSNO) formation was carried out under identical conditions for all thiol-modified particle systems. Initially, 200 mg MPTMS-based particles were suspended in 4.00 mL MeOH via sonication and stirred. The mixture was acidified with the addition of excess HCl (2.00 mL 5 M HCl) and cooled on ice. Sodium nitrite (2.3 M in water; 2.00 mL) was added dropwise to the MPTMS particle solution and stirred on ice for 1 h in the dark. Of note, the

Table 4.2. Reaction parameters for synthesis of thiol-modified silica nanoparticles.

Mol % MPTMS	Reagent/Solvent Volume (mL)				Tetraalkoxysilane	
	H_2O	Aq. NH_4OH	EtOH	MPTMS	Type	Volume (mL)
25%	1.40	11.0	16.2	0.170	TMOS	0.404
40%	1.40	11.0	16.2	0.271	TMOS	0.324
75%	1.40	11.0	16.2	0.424	TEOS	0.169
85%	8.9	11.0	8.8	0.476	TMOS	0.066
85%	8.9	11.0	8.8	0.476	TEOS	0.099

sodium nitrite solution was supplemented with 500 μM diethylenetriaminepentaacetic acid (DTPA) to chelate trace metal ions in solution and prevent copper-mediated RSNO decomposition during the *S*-nitrosation reaction. The resulting pink RSNO-modified particles were collected by centrifugation (6540*g*, 10 min, 4 ^{o}C), washed thrice with cold MeOH, and dried under vacuum for 1 h. All experiments involving RSNO particles were carried out immediately following the *S*-nitrosation reaction.

4.2.4. Preparation and evaluation of nitric oxide-releasing mock sensors

Polyurethane (PU) solutions were prepared by adding 240 mg of the appropriate PU to 2.25 mL THF. The PU was dissolved by sonicating at 60 ^{o}C. A separate dispersion of the NO-releasing SNPs was prepared by sonication in THF. Aliquots of the particle dispersion were added to the PU solution after cooling to room temperature. Unless otherwise indicated, the PU concentration was 80 mg mL^{-1} and SNPs were incorporated at 20 wt% (20 mg mL^{-1}) relative to the polymer for all experiments.

Stainless steel wire (357 μm dia.) was selected as a coating substrate to mimic the size and geometry of functional, needle-type glucose sensors. Wires were first cleaned by sonication in EtOH, and then coated with the NO-releasing membranes by dip-coating into the PU/SNP solution. Each deposited layer was allowed to dry for ~20 s before additional coating. The number of coats was varied for each PU solution to provide uniform ~40–50 μm thick coatings, as determined by measurement with calipers and from the electron micrographs. Leaching of the SNPs was monitored over time via inductively coupled plasma optical emission spectrometry (ICP-OES) using a Prodigy high-dispersion ICP (Teledyne-Leeman Laboratiories; Hudson, NH). Coated substrates were immersed in PBS and incubated at 37 ^{o}C for 2 h–28 d. At pre-determined time points, the substrates were removed from solution and analyzed for silicon content. The

instrument was initially calibrated using sodium silicate standards (0.1–25 ppm in PBS; 251.611 nm Si emission line) to verify linear response over anticipated particle concentrations. Individual standards for each particle system were prepared and used to determine particle leaching from corresponding membranes (Figure 4.2). Of importance, all buffers/solutions that were used for leaching measurements were prepared in polypropylene tubes because silicic acid leaches from glass storage vials. It was verified that neither the wire substrates nor the polypropylene incubation vessels contributed to detectable Si signal.

4.2.5. Nitric oxide-release measurements

Nitric oxide release was evaluated in real-time (1 Hz sampling frequency) using a Sievers 280i chemiluminescent NO analyzer (NOA; Boulder, CO). The NOA was calibrated via a two-point linear calibration, with 25.87 ppm NO (in N_2) serving as the first calibration standard and air passed through an NO zero filter as the blank value. The NO-releasing material (either 1 mg of particles or a coated mock sensor) was added to deoxygenated phosphate buffered saline (PBS; 10 mM, pH 7.4) at 37 ^{o}C. In the case of RSNO-based materials, NO release was restricted to thermal mechanisms by addition of 500 μM DTPA to the PBS and by shielding the entire sample flask from light using aluminum foil. A stream of N_2 gas was bubbled into solution at 80 mL min^{-1} to carry the liberated NO to the NOA reaction cell. Supplemental N_2 gas was provided to the reaction flask in order to match the instrument collection rate of 200 mL min^{-1}. Nitric oxide was detected indirectly by reaction with ozone, which yields a chemiluminescent excited-state nitrogen dioxide species. Measurements were terminated when NO release from the silica particles decreased below 10 ppb mg^{-1}. For mock sensors coated with NO-releasing PU materials, NO release measurements were terminated when NO fluxes were below 0.8 pmol cm^{-2}

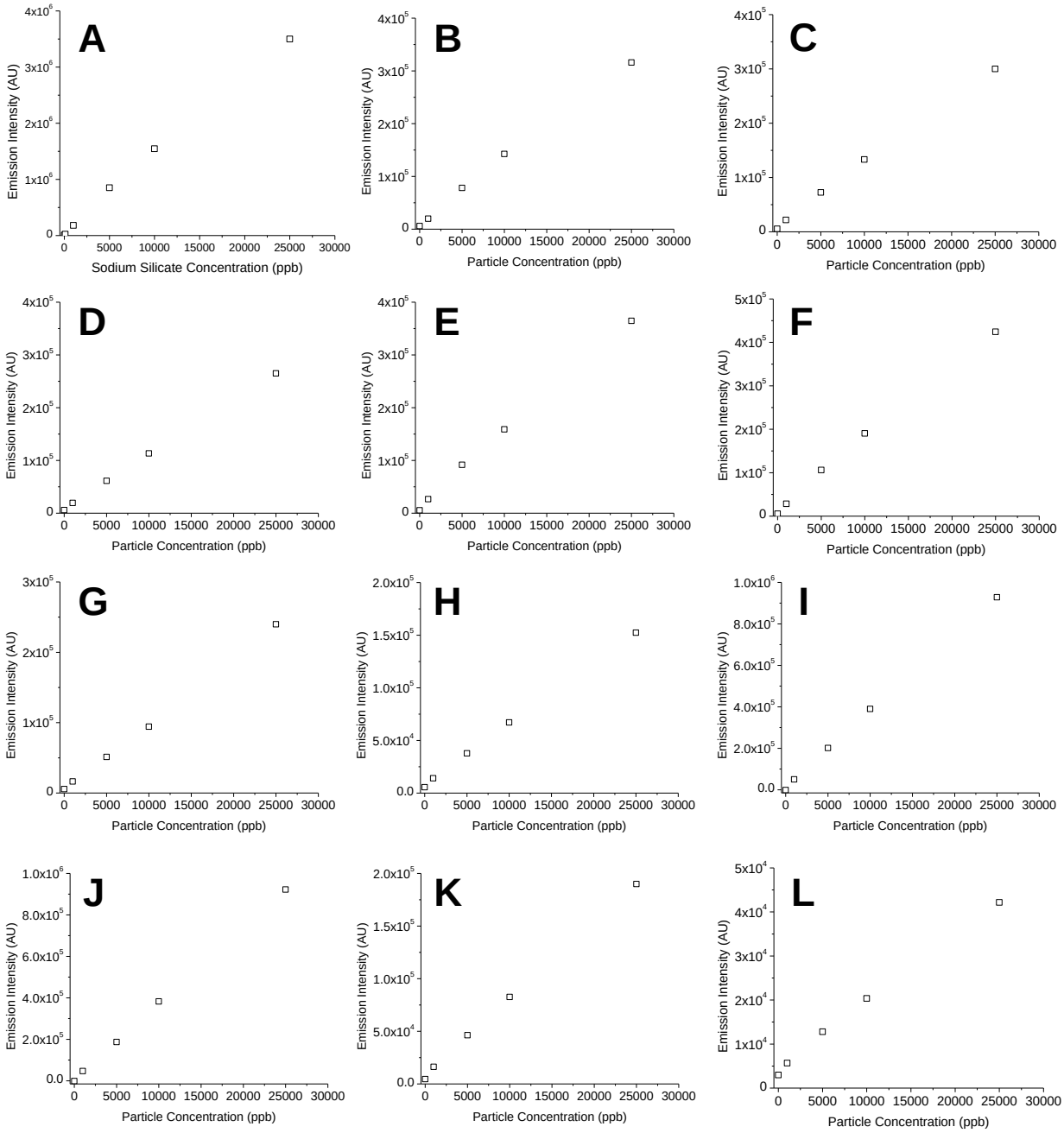

Figure 4.2. Inductively coupled plasma optical emission spectrometer instrumental response to sodium silicate standard solutions (A) and silica particle standard solutions (B–L) prepared in pH 7.4 PBS. The graphs in B–L represent calibration curves for 800 nm AHAP (B), 800 nm DET (C), 800 nm MAP (D), 450 nm DET (E), 150 nm DET (F), nonporous 150 nm DET (G), 150 nm DET functionalized via surface grafting (H), 25% MPTMS/TMOS (I), 40% MPTMS/TMOS (J), 75% MPTMS/TEOS (K), and 85% MPTMS/TEOS (L).

Table 4.3. Nitric oxide-release properties for selected NO donor-modified silica particles.

Particle Size (nm)	NO Donor Modification	Porosity	Synthesis Strategy	$t_{1/2}$ (min)	$[NO]_{total}$ (μmol mg^{-1})	t_d (h)
800	DET/NO	Mesoporous	Ion Exchange	35.6±7.5	1.61±0.17	38.6±4.2
800	AHAP/NO	Mesoporous	Ion Exchange	2.7±1.0	1.30±0.11	7.8±2.0
800	MAP/NO	Mesoporous	Ion Exchange	1.5±0.4	2.20±0.20	2.5±0.2
150	DET/NO	Mesoporous	Ion Exchange	38.8±7.9	1.88±0.05	34.2±3.1
450	DET/NO	Mesoporous	Ion Exchange	23.9	2.41	46.2
200	DET/NO	Mesoporous	Surface Grafting	169.5	1.13	42.8
200	DET/NO	Nonporous	Surface Grafting	91.2	0.22	11.0
620	75% MPTMS	Nonporous	Co-condensation	193.4±23.6	4.29±0.59	51.4±7.2

s^{-1} (instrument LOD at S/N ratio 6–10). Of note, NO-release properties for the NO donor-modified SNPs are provided in Table 4.3.

In cases where NO release from the PU membranes was below the NOA limit of detection, the Griess Assay was used to measure NO indirectly via its oxidative conversion to nitrite as previously described.[33] Briefly, samples for NO measurement in PBS (50 µL) were mixed with 50 µL each of 0.1% w/v aq. *N*-(1-napthyl)ethylene diamine and 1% w/v sulfanilamide in 5% v/v aqueous phosphoric acid and incubated for 10 min to form an azo dye. Sample absorbance measurements were collected at 540 nm on a Labsystem MultiskanRC microplate spectrophotometer (Helsinki, Finland) and compared to a calibration curve generated from nitrite standards (2–100 µM) for quantitative NO determination.

4.2.6. Design and analytical performance evaluation of miniaturized nitric oxide-releasing glucose biosensors

First generation (i.e., peroxide-detecting) needle-type electrochemical glucose biosensors were fabricated and used for evaluation of the NO-releasing membranes.[41-42] The bare sensors were constructed by winding a 127 µm silver/silver chloride (Ag|AgCl) reference electrode around a PFA-insulated 90:10 Pt:Ir wire (127 µm bare dia.). A ~2 mm length of Pt:Ir wire was exposed by removal of the PFA coating and served as the working electrode. Of note, all potentials defined hereafter are with respect to the integrated Ag|AgCl pseudo-reference electrode.

The bare sensors were initially cleaned via cyclic voltammetry in 0.5 M sulfuric acid (-0.25 to +1.20 V vs Ag|AgCl, 30 cycles, 0.1 V s^{-1}) and then functionalized for glucose detection and NO release via a multilayer deposition approach. A polymerized *m*-phenylenediamine (*m*-PD) membrane was first electrodeposited on the bare electrode surface as a size exclusion

membrane to improve selectivity for H_2O_2 oxidation.[43] The electropolymerization process was carried out via cyclic voltammetry (0 to +1.0 V, 20 cycles, 0.1 V s^{-1}) in a 100 mM *m*-PD solution prepared in deoxygenated PBS (pH 7.41). Next, GOx was immobilized on the working electrode by entrapment in a silica solution-gel (sol-gel).[44] The GOx sol-gel precursor solution was prepared by mixing a solution of GOx in water (50 µL; 120 mg mL^{-1}) with a mixture of EtOH (100 µL) and MTMOS (25 µL). The resulting solution was aged on a shaker for 10 min. The sensors were coated with the GOx/silica gel by dipcoating 15 times (5 s still time, 10 s intermittent dry periods) into the gel precursor solution. Last, the sensors were coated with either bare PU or the NO-releasing PU/SNP composites via a loop-casting protocol, which provided uniform coverage of the working and reference electrodes. A 6.5 µL droplet of the PU solution was deposited on a stainless steel wire loop (2 mm dia.) and the loop was passed over the working and reference electrodes. In the case of the NO-releasing membranes, subsequent layers were coated onto electrodes after brief (~5 min) dry times for a total of 7 PU/SNP depositions. The PU concentration used for the loop-casting procedure was varied for the unmodified PUs (20–80 mg mL^{-1}) and was 50 mg mL^{-1} (in 3:1 THF:DMF) for the NO-releasing membranes. The particle concentration was varied in the PU solution at 6.3–50.0 mg mL^{-1}. A PC-3585A outer layer ("topcoat") was applied via loopcasting using a 30 mg mL^{-1} PU solution prepared in 3:1 THF:DMF and allowed to dry for >1 h.

In vitro sensor analytical performance was assessed in PBS (pH 7.4) or porcine serum under stirred conditions using a CH Instruments model 1030C multi-channel potentiostat (Austin, TX). Sensors were pre-conditioned by polarizing sensors in PBS (37 ^{o}C; +0.600 V vs. Ag|AgCl) until a stable background current was measured. Glucose was detected indirectly by amperometric oxidation of H_2O_2 at +0.60 V vs. Ag|AgCl. Sensor glucose response was

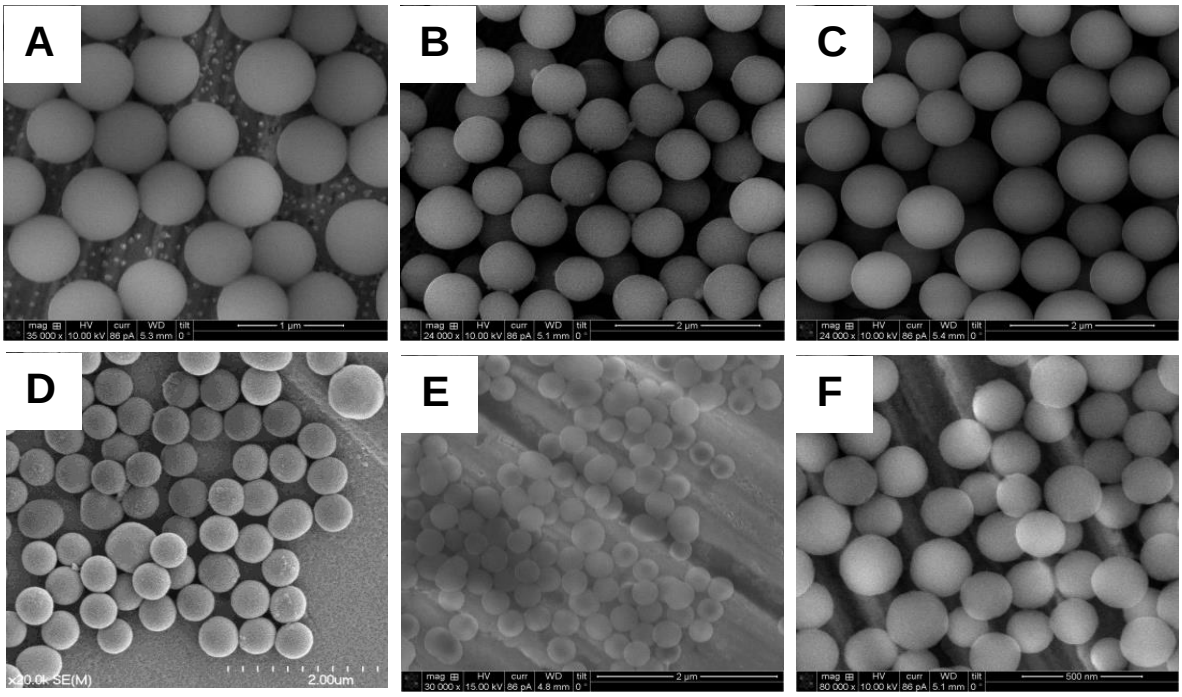

Figure 4.3. Scanning electron micrographs of 800 nm (A) DET, (B) AHAP, and (C) MAP mesoporous SNPs. (D) and (E) are SEM micrographs for smaller DET-modified mesoporous particles (450 and 150 nm, respectively), and (F) are non-porous DET-modified SNPs.

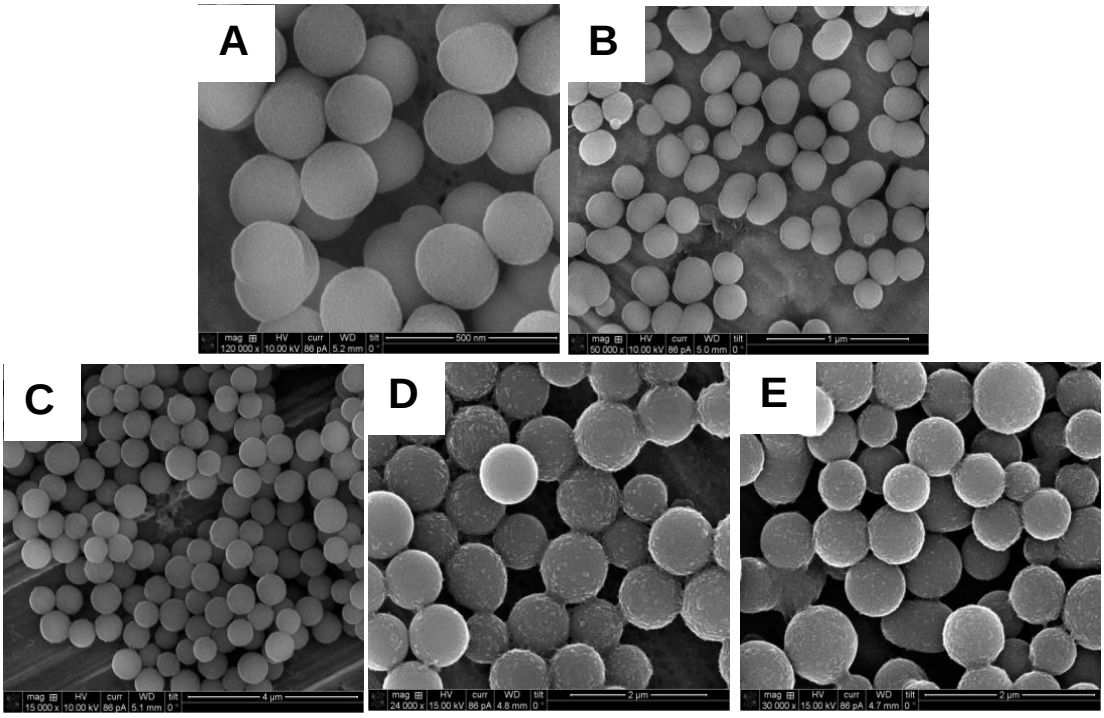

Figure 4.4. Scanning electron micrographs of (A) 25% MPTMS/TMOS, (B) 40% MPTMS/TMOS, (C) 75% MPTMS/TEOS, (D) 85% MPTMS/TEOS, and (E) 85% MPTMS/TMOS particles.

calibrated by incrementally increasing the buffer glucose concentration from 1–30 mM. The sensor linear dynamic range (LDR) was determined as the maximum glucose concentration achieved with no saturation in glucose response ($R^2 \geq 0.99$). Glucose sensitivities are reported as the slope of the linear trend line correlating the measured anodic current to glucose concentration over the linear response range ($R^2 > 0.99$). Amperometric selectivity coefficients for glucose over common electroactive interfering species were calculated according to published methods.[33,42]

4.2.7. Membrane and particle characterization

Morphology of the nanoparticles was evaluated using a FEI Helios 600 Nanolab scanning electron microscope (SEM; Hillsboro, OR). Scanning electron micrographs of the *N*-diazeniumdiolate- and *S*-nitrosothiol-modified particles are provided in Figures 4.3 and 4.4, respectively. Sensor membranes were imaged using a FEI Quanta 200 environmental scanning electron microscope (Hillsboro, OR). Nitrogen sorption isotherms were used to evaluate SNP porosity and were collected on a Micromeritics Tristar II 3020 surface area and porosity analyzer (Norcross, GA). Samples were dried at 110 ^{o}C under N_2 gas for 18 h and degassed for 2 h prior to analysis. Brunauer-Emmett-Teller (BET) analysis of the monolayer adsorption isotherm region ($0.05 < p/p^0 < 0.20$) was used for determination of specific surface area.

4.3. Results and discussion

Polyurethane (PU) materials have been utilized as glucose sensor membranes because they generally elicit only a mild FBR and, depending on their composition, have appropriate glucose/oxygen permeabilities necessary for fabricating glucose sensors.[45-46] Unfortunately, the literature is not clear as to how glucose sensor analytical performance depends on PU composition and water uptake—important parameters that may also impact NO release and NO donor leaching. Initial experiments thus focused on identifying PUs that could be used to

fabricate functional electrochemical glucose sensors prior to modification with NO-releasing scaffolds.

Glucose biosensors were systematically modified with glucose diffusion-limiting PU coatings via a loopcasting method. The analytical performance of the sensors was evaluated as a function of PU water uptake and the concentration of the PU loop-casting solution using four commercially-available PUs: HP-93A-100, AL-25-80A, SG-85A, and PC-3585A. Regardless of PU type, sensors that were prepared using low concentration PU solutions (20 and 35 mg mL^{-1}) did not yield stable glucose response (data not shown), whereas 50 mg mL^{-1} PU solutions lead to more predictable sensor performance. The glucose sensitivities and linear ranges of the sensors were dependent on the PU water uptake (Table 4.4). For instance, sensors that were modified with the high-water uptake PU HP-93A-100 had large glucose sensitivity (38.2 nA mM^{-1} mm^{-2}) but insufficient linear dynamic range (1–3 mM), indicating that the membrane did not serve as a substantial barrier to glucose diffusion. In contrast, more hydrophobic SG-85A and PC-3585A PUs (water uptake <0.2 mg per mg of PU) improved the linear glucose range of the sensors (1–15 mM).

The sensitivity of the glucose sensors steadily decreased during incubation in PBS, eventually stabilizing after ~7 d. The decrease in sensitivity was observed regardless of PU type and was consistent with sensors that were coated using 80 mg mL^{-1} PU solutions (Table 4.5). Although undesirable, slowly changing glucose sensitivity is a common occurrence noted in the literature for sensors coated with PU[41,43] or poly(vinyl alcohol).[47] Electrochemical glucose sensors generally require a 5–7 d pre-conditioning period for response stabilization as the polymer membranes undergo hydration and swelling.[41,43] The four PU types that were utilized in this study were the deemed satisfactory for further development of NO-releasing membranes.

Table 4.4. Analytical performance merits of glucose biosensors coated with different PUs (50 mg mL^{-1} PU solutions).[a,b]

PU Type	PU Water uptake (mg mg^{-1})[d]	Linear Dynamic Range[e]	Sensitivity (nA mM^{-1} mm^{-2})[f]	Sensitivity Retention (%)[g]			
				3 d	5 d	7 d	14 d
HP-93A-100	2.6±0.3[c]	1–3 mM	38.2±15.0	54.3±29.6	57.2±7.3	44.3±8.9	42.3±7.3
AL-25-80A	0.6±0.3[c]	1–6 mM	44.7±15.2	80.2±10.7	82.9±28.8	58.5±10.2	58.3±11.0
SG-85A	0.2±0.2[c]	1–15 mM	29.5±15.3	86.1±10.1	85.5±18.3	64.9±6.1	67.2±8.1
PC-3585A	0.0±0.0	1–15 mM	20.1±4.2	80.5±13.6	77.0±7.2	55.2±2.5	56.2±2.4

[a]Error bars represent standard deviation for $n \geq 3$ separate experiments. [b]PU concentration in the loop-casting solution was 50 mg mL^{-1}. [c]Water uptake measurements described in Koh et al., *Biosensors and Bioelectronics* **2011**, *28*, 17–24. [d]Water uptake expressed as mg_{water} per mg_{PU}. [e]Linear dynamic range determined from glucose sensor calibration curves as the concentration range over which the associated linear trendline had an R^2 value >0.99. [f]Determined as the slope of the trendline fit to the sensor current-glucose response over the linear dynamic range on the first day of testing. [g]Glucose sensitivity after soaking sensors in PBS at 37 ^{o}C (relative to the sensitivity on the first day of testing).

Table 4.5. Analytical performance merits of glucose biosensors coated with different PUs (80 mg mL^{-1} PU solutions).[a,b]

PU Type	PU Water uptake (mg mg^{-1})[d]	Linear Dynamic Range[e]	Sensitivity (nA mM^{-1} mm^{-2})[f]	Sensitivity Retention (%)[g]		
				3 d	5 d	14 d
AL-25-80A	0.6±0.3[c]	1–6 mM	85.6±13.4	71.0±12.8	56.0±4.3	42.9±3.9
SG-85A	0.2±0.2[c]	1–15 mM	12.4±1.6	92.9±11.2	91.3±16.5	53.5±6.9
PC-3585A	0.0±0.0	1–15 mM	9.6±4.2	99.7±4.7	86.8±3.2	57.1±2.4

[a]Error bars represent standard deviation for $n \geq 3$ separate experiments. [b]PU concentration in the loop-casting solution was 80 mg mL^{-1}. [c]Water uptake measurements described in Koh et al., *Biosensors and Bioelectronics* **2011**, *28*, 17–24. [d]Water uptake expressed as mg_{water} per mg_{PU}. [e]Linear dynamic range determined from glucose sensor calibration curves as the concentration range over which the associated linear trendline had an R^2 value >0.99. [f]Determined as the slope of the trendline fit to the sensor current-glucose response over the linear dynamic range on the first day of testing. [g]Glucose sensitivity after soaking sensors in PBS at 37 ^{o}C (relative to the sensitivity on the first day of testing).

4.3.1. Polyurethane membranes incorporating N-diazeniumdiolate-modified silica particles

Mesoporous SNPs were selected for developing NO-releasing PU membranes due to their favorable NO storage properties. The SNPs were synthesized using an approach that also allowed for the chemical structure of the amine modification and the size of the particles to be tuned independent of one another.[32] In a subsequent chemical step, the secondary amines were easily reacted with NO gas to form *N*-diazeniumdiolate NO donors. Particles ~800 nm in diameter and modified with DET/NO (see Figure 4.1 for silane structures) were selected for initial because a preliminary study suggested that large (~1 μm) particles may be less prone to leaching than <300 nm SNPs.[28]

Nitric oxide release from DET particle-doped PU membranes was measured in physiological buffer (pH 7.4 PBS at 37 ^{o}C) as a function of PU composition. Expectedly, PU membranes with moderate-to-high water uptake properties (HP-93A-100, AL-25-80A, and 1:1 mixture of AL-25-80A :SG-85A) released large initial NO fluxes (124.0–311.5 pmol cm^{-2} s^{-1}) due to more rapid *N*-diazeniumdiolate decomposition relative to membranes consisting of either SG-85A or PC-3585A (<20 pmol cm^{-2} s^{-1}; Figure 4.5A). For instance, DET/NO embedded in HP-93A-100 PU (a hydrogel PU formulation with water uptake at ~150 wt% PU mass) released the largest NO fluxes (311.5 pmol cm^{-2} s^{-1}, t_{max}=37.0 min) and maintained NO fluxes above 0.8 pmol cm^{-2} s^{-1} (the detection limit of the NOA for this experiment) for only ~60 h. In contrast, composites that were prepared using the more hydrophobic PC-3585A PU (<2 wt% water uptake) released low, detectable NO fluxes (1–14 pmol cm^{-2} s^{-1}) for 7 d.

Leaching of the DET/NO particles from the PU composites was assessed by monitoring the silicon emission intensity via ICP-OES from membrane soak solutions (PBS at 37 ^{o}C) over 7 d. All DET/NO-based membrane compositions exhibited detectable levels of leaching (8–42%

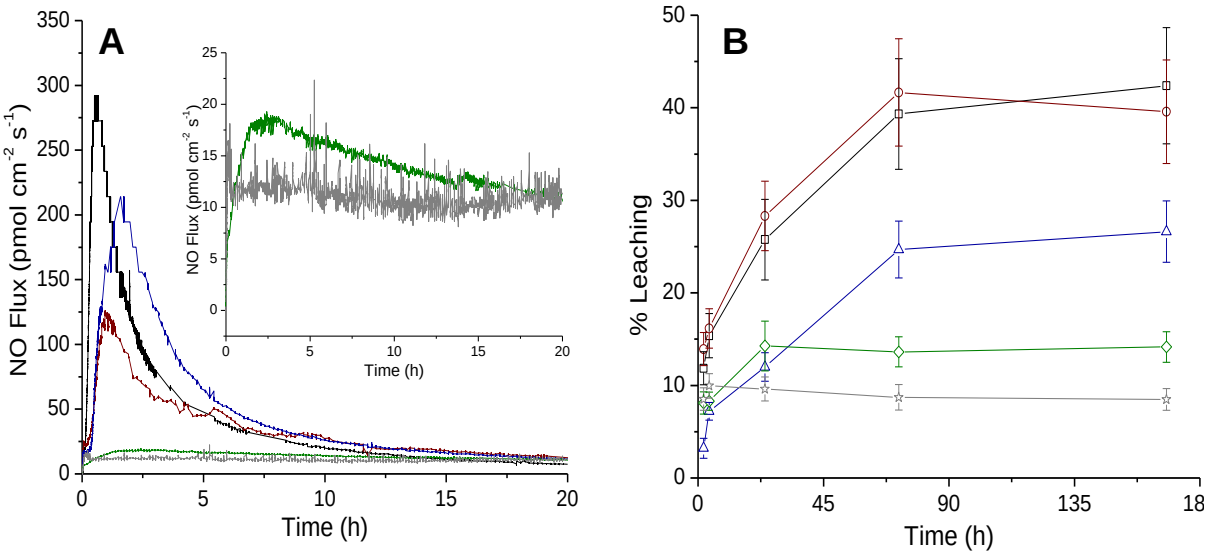

Figure 4.5. (A) Initial (20 h) NO release and (B) 1 wk particle leaching measurements for HP-93A-100 (black, square), AL-25-80A (red, circle), SG-85A (green, diamond), and PC-3585A (gray, star) polyurethane materials. The blue (triangle) trace in both figures is a 1:1 mixture of AL-25-80A:SG-85A. Inset in (A) shows low NO fluxes released from SG-85A and PC-3585A composites. All materials are doped with 20 wt% 800 nm DET/NO SNPs.

total mass of incorporated particles) over 1–3 d incubation in PBS, with no additional leaching beyond 3 d (Figure 4.5B). The degree of leaching correlated strongly with PU water uptake. The more hydrophobic polyurethanes PC-3585A and SG-85A (water uptake <0.2 mg/mg for both PUs) leached 14.2 and 8.5% the total encapsulated DET/NO SNPs (321 and 181 μg cm^{-2}, respectively) over the 7 d soak period. Significantly greater particle leaching (39.6 and 42.4%) was measured for high water uptake HP-93A-100 and AL-25-80A PUs, respectively, corresponding to ~900 μg SNPs cm^{-2}.

Membranes prepared using similarly-sized (800 nm) particles with either MAP/NO or AHAP/NO *N*-diazeniumdiolate modifications (monoamine- and diamine-based NO donors, respectively) were used to elucidate the influence of aminosilane structure on particle leaching. Comparable 7 d leaching values were measured for AHAP/NO and DET/NO particles (43.8 and 42.4%, respectively), whereas MAP/NO particles leached from the membranes completely (100.7%; Figure 4.6). Although the chemical structure of the aminosilane surface modifications likely impacted interactions between the particle surface and the encompassing PU matrix, it was noted that a greater degree of *N*-diazeniumdiolate modification (2.22 vs 1.30–1.61 μmol NO mg^{-1}) was a hallmark of the particle system (MAP/NO) with the greatest leaching propensity.

To further understand the particle leaching process, we evaluated DET/NO particle leaching over a range of particle sizes (150, 450, and 800 nm). The DET/NO system was selected because this modification led to lower values for leaching in all of the PUs that were tested (data not shown). Experiments were carried out in a moderately hydrophobic PU mixture (1:1) of AL-25-80A:SG-85A, as more hydrophilic PUs (e.g., HP-93A-100) yielded elevated leaching (~100%) for most of the particle types tested. In contrast with previous suggestions that larger particles are less prone to leaching,[28] no clear relationship between particle size and the

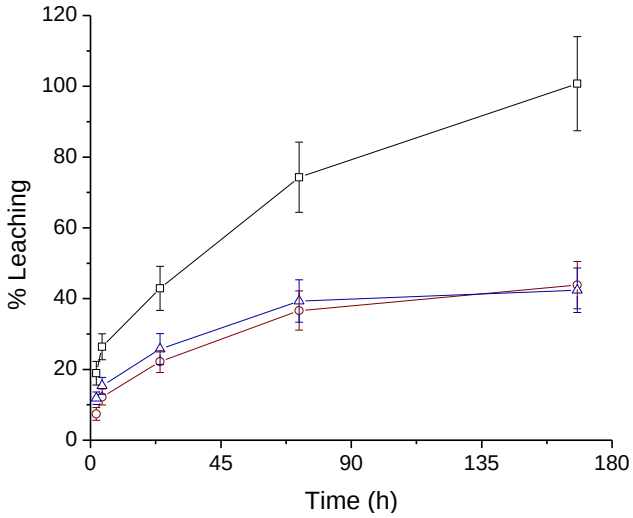

Figure 4.6. Leaching measurements over 1 wk incubation in PBS at 37 ^{o}C for 800 nm particles modified with MAP/NO (black, square), AHAP/NO (red, circle), and DET/NO (blue, triangle). Particles were incorporated at 20 wt% (relative to PU mass) in AL-25-80A PU.

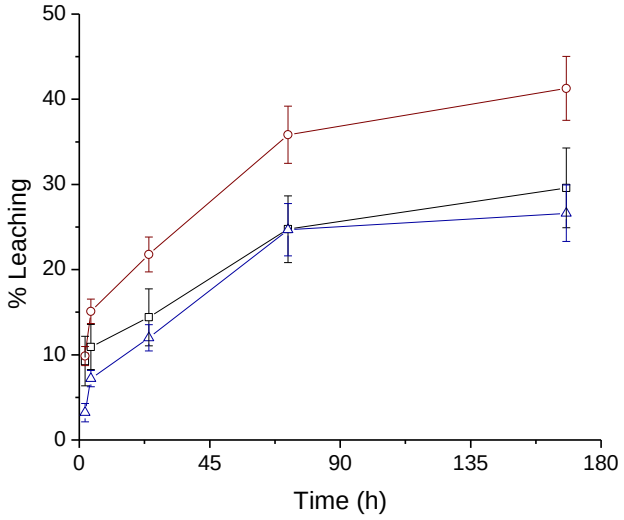

Figure 4.7. Leaching measurements over 1 wk incubation in PBS at 37 ^{o}C for 150 (black, square), 450 (red, circle), and 800 nm (blue, triangle) DET/NO-modified SNPs. Particles were incorporated at 20 wt% (relative to PU mass) in a 1:1 mixture of AL-25-80A:SG-85A PUs.

extent leaching was observed (Figure 4.7). Similar leaching values were measured after 7 d immersion in PBS for 150 nm (26.4%) and 800 nm (23.7%) DET/NO SNPs. The 450 nm particles were associated with the greatest particle leaching (40.0%) despite having the same DET/NO modification as the other two SNP systems. Of importance, the 450 nm particles had larger NO storage (2.41 μmol NO mg^{-1}) relative to the 150 nm and 800 nm particle sizes (1.87 and 1.61 μmol mg^{-1}, respectively), again implicating the *N*-diazeniumdiolate modification as a potential factor in the leaching process.

The relationship between *N*-diazeniumdiolate modification and particle leaching was more directly interrogated in two additional experiments using the same PU compositions (1:1 AL-25-80A:SG-85A). First, non-NO-releasing 800 nm DET particles (i.e., DET particles that did not undergo the NO donor formation reaction) were doped into PU membranes and compared with analogous NO-releasing membranes. Leaching of the total incorporated silica was reduced to 13.4% at 1 wk compared with 26.6% for the NO-releasing membrane. Second, the role of *N*-diazeniumdiolate density (i.e., total NO storage) on membrane stability was examined using two similarly-sized DET-modified SNPs with different NO storage capacity. Two separate bare SiO_2 particle types were synthesized with a nominal size of ~150 nm but distinct porosity (i.e., mesoporous or nonporous). After NO donor modification, the mesoporous and nonporous DET/NO particles stored 1.33 and 0.22 μmol NO mg^{-1}, with comparable specific surface areas (21 and 19 m^2 g^{-1}, respectively). As anticipated, increased levels of particle leaching (17.6±0.2%) were measured for the NO-releasing SNPs that stored more NO versus 6.4±1.1% for the nonporous particles.

Greater particle NO storage consistently correlated with increased leaching regardless of particle size, the chemical structure of the aminosilane precursor, or the water uptake of the

polyurethane matrix. These leaching data pointed to the high surface charge density of the particles being a key contributing factor to particle stability in the membranes. We rationalized that greater leaching may be due to favorable interactions of the SNPs with water. This assertion was confirmed by the obvious correlation between leaching and PU water uptake. However, *N*-diazeniumdiolate modification was not the sole factor for particle leaching, as even amine-modified (non-NO-releasing) particles leached from the PU. In total, it was concluded that ionic silanoates, ammonium groups, and *N*-diazeniumdiolates all contribute to the overall particle surface charge and associated leaching. In preliminary experiments, additional hydrophobic PU layers (e.g., PC-3585A, SG-85A) without NO-releasing particles were deposited on top of the NO-releasing PU coating to serve as a barrier to particle leaching. Although additional PU "topcoats" generally reduced the magnitude of particle leaching, they did not prevent leaching from any of the formulations tested. For example, leaching was reduced from 14.2 to 6.6% for PC-3585A membranes incorporating 800nm DET/NO SNPs upon modification with an SG-85A topcoat (i.e., by dipcoating into a 60 mg mL^{-1} PU solution). Leaching of *N*-diazeniumdiolate-based SNPs was minimized in low-water uptake polyurethanes. When embedded in hydrophobic TT-2072D-B20 PU membranes, only ~4.7% of the incorporated 800 nm DET/NO particles were detected after one month soak periods. Unfortunately, these formulations were incompatible as functional sensor membranes due to poor glucose permeability. Even sensors with thin (<5 μm) coatings did not respond to physiological glucose concentrations (data not shown).

4.3.2. Polyurethane membranes incorporating S-nitrosothiol-modified silica particles

S-nitrosothiols (RSNOs) are neutral NO donors formed on thiols and, in this manner, are structurally distinct from zwitterionic *N*-diazeniumdiolates. We hypothesized that the neutral RSNO modification might reduce the tendency of the SNPs to leach from PU membranes by

eliminating charge contributions characteristic of cationic amines and zwitterionic *N*-diazeniumdolates. Thiol-functionalized silica-based particles were prepared using a variant of the Stöber method by co-condensation of MPTMS (a mercaptosilane) with a backbone tetraalkoxysilane.[34] *S*-nitrosothiol NO donors were subsequently formed on the primary thiols by reaction of the SNPs with acidified nitrite. Leaching measurements were initially carried out for a single SNP composition (75 mol% MPTMS balance TEOS) as a function of PU type, analogous to the study of the *N*-diazeniumdiolate-modified particles. The measured Si emission intensity after a 7 d membrane soak period (PBS at 37 ^{o}C) was below the ICP-OES method limit of detection for all PU compositions tested, corresponding to <0.6% (16.5 μg SNPs cm^{-2}) of the total mass of SNPs incorporated in the membranes.

To assess the role of MPTMS modification on particle leaching, SNPs of varying alkanethiol content (25, 40, 75, and 85% MPTMS; SEMs provided in Figure 4.4) were incorporated into HP-93A-100 films (for comparison to the 75% MPTMS system) and soaked in physiological buffer for 7 d (Table 4.6). Unexpectedly, the data revealed a clear dichotomy in leaching measurements for RSNO-modified SNPs. Particles with low alkanethiol content (i.e., 25 and 40% MPTMS, with reported thiol content <3.0 % sulfur by mass)[34] leached entirely from the HP-93A-100 membranes over 7 d (2.90 and 2.89 mg cm^{2}, respectively), while reduced leaching (<0.024 mg cm^{-2}, below ICP-OES LOD) was observed for membranes containing SNPs with greater MPTMS character (75 and 85% MPTMS; 15.2–20.6 wt% sulfur).[34] The RSNO-modified particles retain moderate, anionic zeta-potentials (due to acidic silanol groups) that did not vary appreciably with MPTMS content (-29.9, -30.8, and -31.2 mV for the 25, 40, and 75% MPTMS particles). Despite similar surface charges, only SNPs with >75% MPTMS content did

Table 4.6. Particle leaching measurements for HP-93A-100 membranes doped with RSNO-modified silica particles of varying MPTMS content.[a,b]

mol% MPTMS	Backbone Silane	Size[c] (nm)	Leaching[d]	
			mg cm^{-2}	%
25	TMOS	234±37	2.90±0.35	99.7±6.6
40	TMOS	248±41	2.89±0.19	100.3±12.0
75	TEOS	622±53	<0.016	<0.6
85	TMOS	660±86	<0.024	<0.8
85	TEOS	864±94	<0.024	<0.8

[a]Error bars represent standard deviation for $n \geq 3$ separate samples. [b]MPTMS-modified particles were doped into polyurethanes at concentrations of 20 wt%. [c]Geometric size estimated from scanning electron micrographs of particles (n>100 individual particles). [d]Determined by ICP-OES measurement [Si] in membrane soak solutions after 7 d incubation in PBS.

not leach appreciably from the HP-93A-100 PU, reinforcing the concept that the large degree of hydrophobic alkanethiol modification counteracts particle leaching.

The leaching experiments above were carried out using membranes in which the total particle composition was 20 wt%. For *N*-diazeniumdiolate-doped materials, increasing the SNP mass contribution to >20 wt% generally resulted in a larger degree of particle leaching. For example, 800 nm DET/NO particles doped into SG-85A PU at 33.3 and 50.0 wt% leached 38.7 and 76.8% of the encapsulated silica over a 1 wk period. In contrast, membranes that were prepared using 75% MPTMS/TEOS particles at the same concentrations (33.3 and 50.0 wt%) leached minimal amounts of silica when immersed in aqueous buffer. Even at the highest concentration tested (50.0 wt%), particle leaching was measured just above the instrument limit of detection at 28.1 μg cm^{-2}, corresponding to <1 % of the silica doped into the PU membrane.

4.3.3. Nitric oxide release from S-nitrosothiol-based polyurethane/silica membranes

S-nitrosothiols decompose to yield NO through multiple mechanisms. Both light (330–350 and 550–600 nm for primary RSNOs) and thermal irradiation cause homolytic scission of the S–N bond to yield NO and thiyl radicals. Subsequent reaction of the thiyl radical with a second RSNO can also trigger release, generating a disulfide and an additional mole of NO. *S*-nitrosothiol NO donors may also undergo irreversible catalytic redox reactions with several transition metal ions (Cu^{2+}, Ag^{+}, and Hg^{2+}).[48] Although these RSNO decomposition pathways are well-known, in vivo NO release is triggered thermally or through thiyl-mediated mechanisms only, due to the absence of light and presence of only trace amounts of transition metal ions in physiologic fluids. As such, all NO release evaluations were carried out in a light-shielded sample flask and in PBS supplemented with DTPA (a metal chelator) to most accurately recapitulate physiologic conditions.

Table 4.7. Particle leaching and nitric oxide release measurements for PU membranes doped with 75 mol% MPTMS/TEOS particles.[a,b]

PU Type	$[NO]_{max}$[c] (pmol cm^{-2} s^{-1})	$[NO]_t$[d] (μmol cm^{-2})	$t_{1/2}$[e] (h)	t_d[f] (h)	Leaching[g] (%)
HP-93A-100	277±21	0.70±0.04	3.13±0.17	38.0±4.5	<0.6
AL-25-80A	432±12	0.43±0.02	0.38±0.02	21.2±1.2	<0.6
PC-3585A	301±16	0.48±0.09	0.30±0.03	8.3±1.1	<0.6

[a]Error bars represent standard deviation for $n \geq 3$ separate samples. [b]75% MPTMS/TEOS particles were doped into polyurethanes at concentrations of 20 wt%. [c]Maximum initial NO surface flux. [d]Total NO storage determined by integration of the NO-release profile measured via chemiluminescence. [e]Half-life of NO release. [f]Duration of NO release above 1 pmol cm^{-2} s^{-1}. [g]Determined by ICP-OES measurement [Si] in membrane soak solutions after 7 d incubation in PBS.

The NO release from 75% MPTMS-doped membranes varied considerably between the different PU compositions (Table 4.7). For example, membranes that were prepared using either AL-25-80A or PC-3585A released large initial NO fluxes (432 and 301 pmol cm^{-2} s^{-1}, respectively) and exhausted their NO supply rapidly (half-life of NO release <0.5 h). The release of NO from both films was limited to 24 h. In contrast, 75% MPTMS-doped HP-93A-100 membranes released NO more slowly ($t_{1/2}$ 3.13 h) for 38 h. The differences in NO-release kinetics was attributed to a cage effect that the polymer matrix imposes on immobilized RSNOs.[49] The microenvironment surrounding the RSNO species dictates the rates of reversible RSNO decomposition (homolytic cleavage of the S–N bond) and recombination between the resulting thiyl radicals and NO.[49-50] In aqueous solutions, NO readily escapes the surrounding solvent cage upon RSNO decomposition, thus mitigating recombination between the thiyl radicals and NO. Slower RSNO decomposition rates have been previously reported in polymer matrices (e.g., polyethylene glycol, Pluronic F127) that are capable of facilitating enhanced geminate recombination (related to a more viscous polymer microenvironment) relative to analogous recombination rates in solution.[51-52] Following this rationale, NO was detected for extended periods of time for the most hydrophilic (i.e., greatest water uptake) HP-93A-100 membrane, with successive decreases in NO-release half-lives/durations in PUs with lower water uptake (AL-25-80A and PC-3585A). The total NO storage (0.43–0.70 μmol NO cm^{-2}) was roughly an order of magnitude lower than expected, indicating that the majority of the stored NO is either not released from the films or is being released at fluxes below the detection limit of the NO analyzer. Indeed, the membranes retain a characteristic pink hue upon removal from the NO analysis flask, confirming the presence of unreacted primary RSNOs.

4.3.4. Analytical performance of nitric oxide-releasing electrochemical glucose biosensors

Of the polyurethanes tested, HP-93A-100 was unique in that the RSNO particle-doped membranes had the longest NO-release durations and adequate water uptake (2.6 mg H_2O per mg PU) to facilitate glucose partitioning into the PU. Functional glucose sensors were fabricated using HP-93A-100 doped with 75% MPTMS particles. The analytical performance of the sensors was not appreciably altered by the mass percentage of the particles in the final coating (11.1–50.0 wt% SNPs). Indeed, the sensitivity to glucose was in the range of 53–71 nA mM^{-1} mm^{-2} regardless of the MPTMS particle content in the membrane. Particles were thus doped in the HP-93A-100 membranes at 33.3 wt% for further experiments to facilitate large NO storage (2.85±0.06 μmol cm^{-2}). For all membrane formulations tested (11.1–50.0 wt% MPTMS), the linear glucose response range of the sensors proved inadequate (6 mM upper limit; Figure 4.8) and similar to sensors coated solely with HP-93A-100 (i.e., without particles). An inverse relationship between sensitivity and dynamic range is often noted upon enzyme saturation by glucose and insufficient oxygen (GOx co-substrate) concentrations. In order to extend the dynamic range of the sensors to capture physiological concentrations (1–15 mM),[41] an additional external PC-3585A coat was applied to the sensor electrodes. This PC-3585A "topcoat" served to obstruct glucose diffusion to the immobilized enzyme, balancing the effective glucose and oxygen concentrations in the enzyme layer. As expected, the additional PU coat extended the glucose linear dynamic range to 30 mM but still allowed for a usable glucose sensitivity (2.89±1.65 nA mM^{-1} mm^{-2}).

The NO-releasing glucose sensors (33.3 wt% MPTMS balance HP-93A-100 with the PC-3585A topcoat) released NO for at least 3 d, as determined via chemiluminescence (Figure 4.9). Release of low NO fluxes (0.8 pmol cm^{-2} s^{-1}, below the NOA LOD) for an additional four days

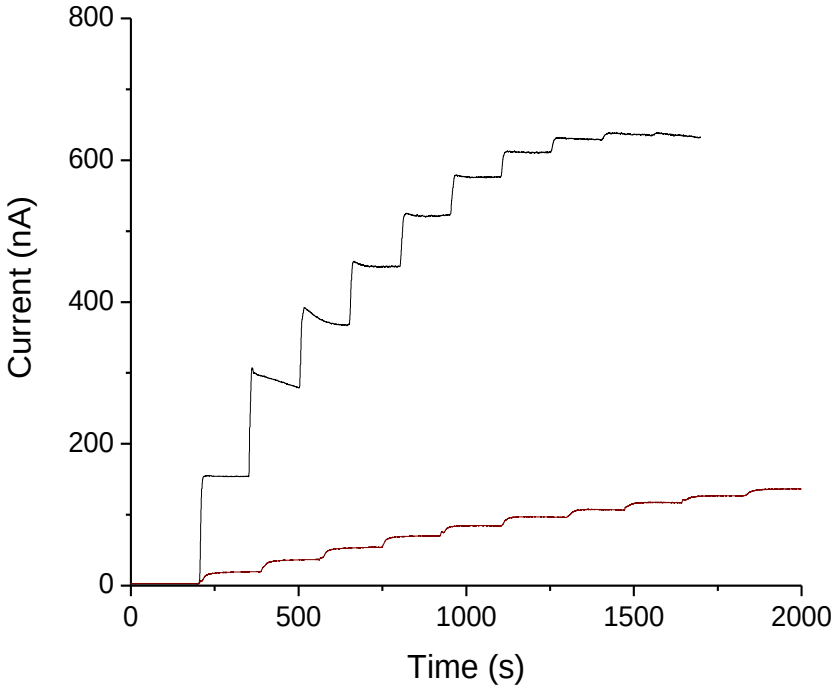

Figure 4.8. Amperometric glucose response for sensors coated with 75% MPTMS/TEOS-doped HP-93A-100 at 33.3 wt% SNP without (black trace) and with (red trace) an additional PC-3585A topcoat.

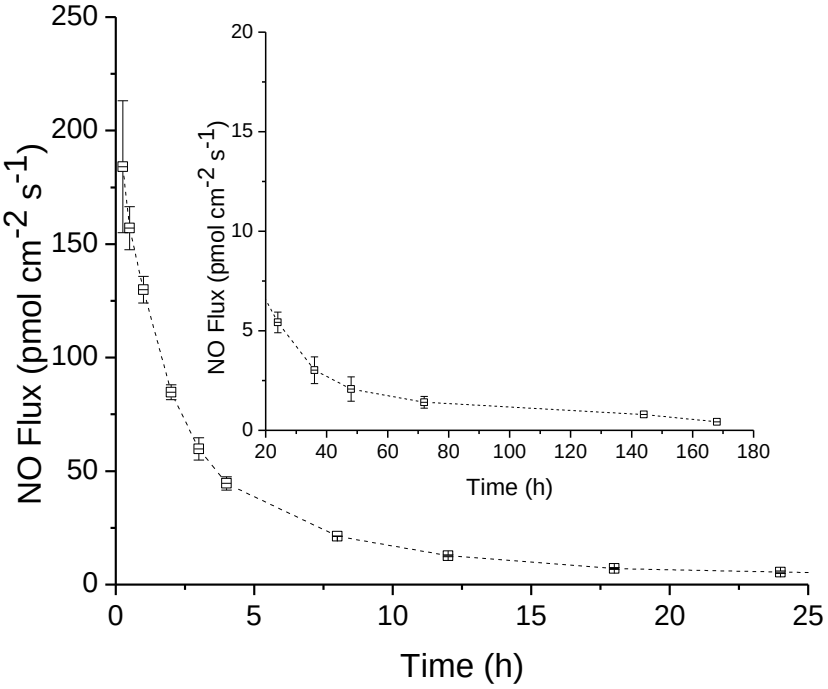

Figure 4.9. Nitric oxide release from HP-93A-100 membranes doped with 75 mol% MPTMS/TEOS particles (33.3 wt%) with an additional PC-3585A topcoat. Inset shows the low NO fluxes released from sensor membranes at durations beyond 24 h.

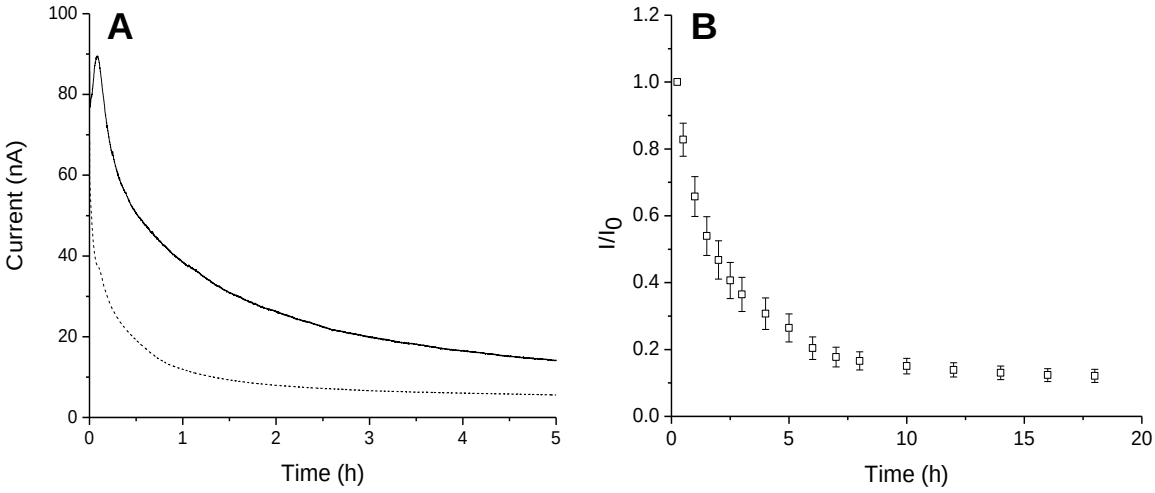

Figure 4.10. Amperometric response for sensors modified with both the 75% MPTMS/TEOS-doped HP-93A-100 (33.3 wt% SNP) NO-releasing layer and the PC-3585A topcoat. (A) background current response for control (dashed line) and NO-releasing sensors (solid line) upon immersion in PBS at 37 ^{o}C. (B) Electrooxidation of NO at the working electrode surface contributes to the sensor current response during the first ~6 h, achieving a stable background current after 8 h polarization at +0.600 V vs Ag|AgCl.

was measured by the Griess assay,[53] an indirect method for measuring NO that has been aerobically oxidized to nitrite. Sensors coated with the 33.3 wt% MPTMS/HP-93A-100 membrane release NO for 7 d, a three-fold greater duration those used previously for an in vivo study of sensor performance (NO release at fluxes >0.8 pmol cm^{-2} s^{-1} for <48 h).[26,32] As such, the NO-release properties (fluxes) of the sensors are in line with those expected to improve long-term in vivo sensor function.[54]

A pre-conditioning period in the sensing medium (e.g., PBS) was necessary for all sensors to initiate membrane hydration and for stabilization of the electrical double-layer charging current. For control sensors (i.e., sensors coated with non-NO-releasing particles), a minimum electrode polarization period of 4–5 h in PBS (37 ^{o}C) was sufficient, as evidenced by the low baseline current drift (<0.5 nA h^{-1}; Figure 4.10B). For the NO-releasing sensors, an anodic current peak was observed in the background sensor response due to NO oxidation; a feature that was absent in the control sensor experiments (Figure 4.10A). The slight response of the sensor to NO was mitigated at the working potential of +0.600 V, as NO oxidation occurs more readily at higher electrode potentials (~+0.9 V versus +0.7 V for H_2O_2 on platinum surfaces).[33,55] Indeed, stable current backgrounds (<0.4 nA h^{-1} I_0) were achieved for the NO-releasing sensors after 6–8 h.

Although the glucose sensitivity of the biosensors coated solely with PU gradually decreased during 7 d incubation in PBS (Tables 4.4 and 4.5), the sensitivity of the NO-releasing sensors increased during the same time frame (7 d), remaining constant thereafter (Figure 4.11A). The selectivity coefficients of the NO-releasing sensor against acetaminophen, ascorbate, and nitrite on the first day of testing were 1.64±0.19, -0.29±0.23, and 0.56±0.18, respectively. This performance did not vary discernably throughout the incubation period (data

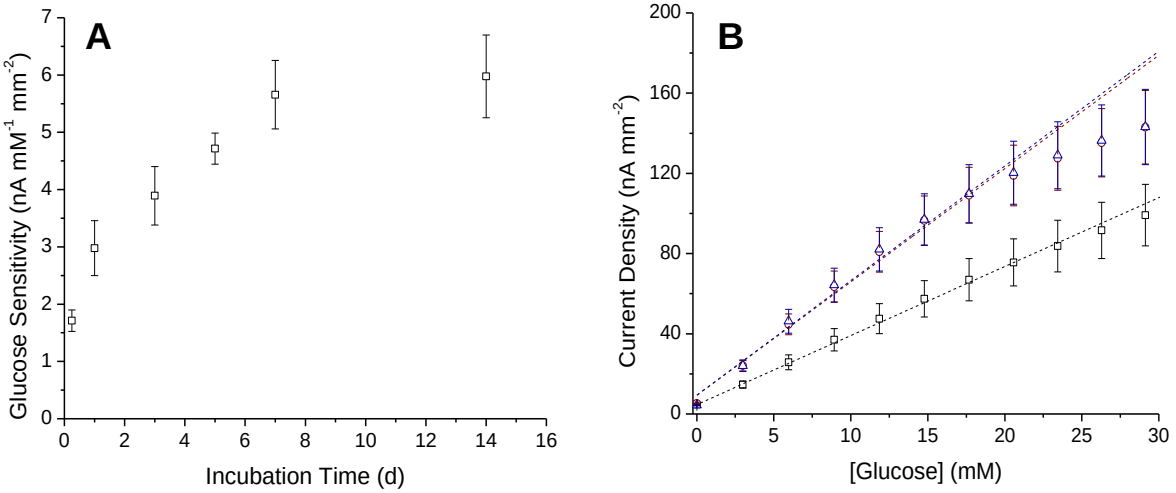

Figure 4.11. Amperometric glucose response of sensors coated with both the 75% MPTMS/TEOS-doped HP-93A-100 (33.3 wt% SNP) NO-releasing layer and the PC-3585A topcoat. (A) glucose sensitivity over 2 wk incubation in PBS at 37 ^{o}C. (B) glucose response calibration for NO-releasing sensors after 1 (black, square), 7 (red, circle), and 14 d (blue, triangle) PBS immersion periods. The glucose response is linear over 1–30 mM initially (1 d), with decreased upper limit (21 mM) after 1 wk.

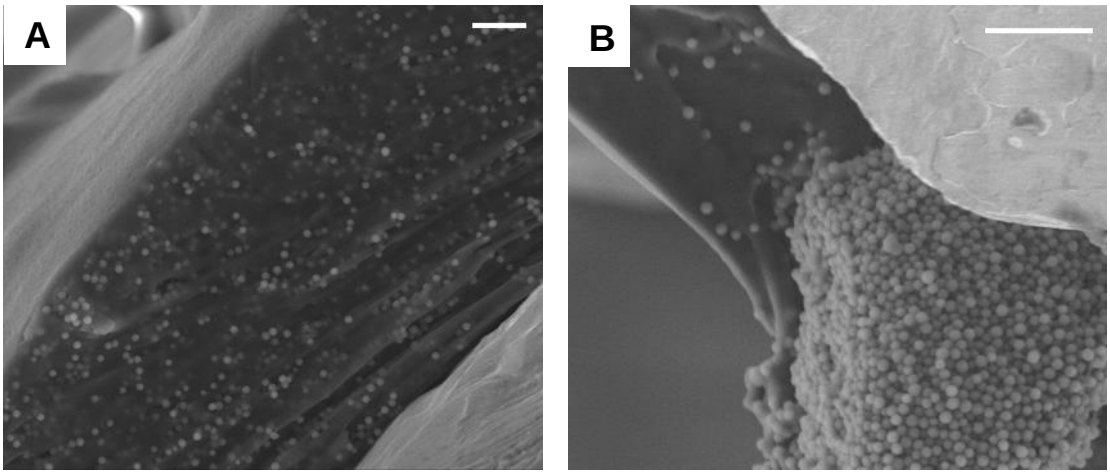

Figure 4.12. Scanning electron micrographs of glucose biosensors coated with both the 75% MPTMS (33.3 wt%) HP-93A-100 NO-releasing layer and the PC-3585A topcoat. Cross-sections of the sensors (A) as prepared and (B) after 2 wk immersion in PBS revealed the particles aggregate over time. The scale bar in the electron micrographs represents 5 μm.

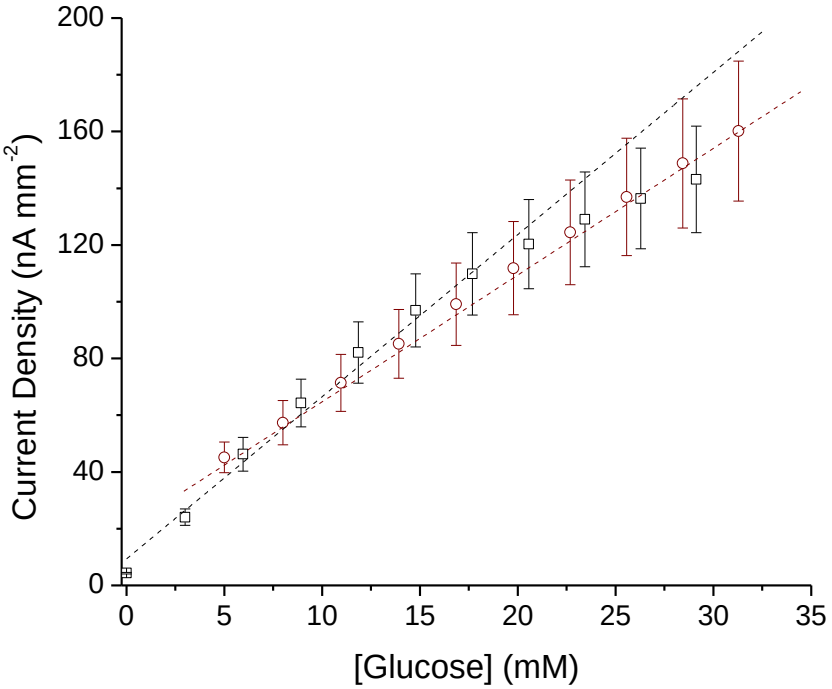

Figure 4.13. Calibrated glucose response of sensors coated with both the 75% MPTMS/TEOS-doped HP-93A-100 (33.3 wt% SNP) NO-releasing layer and the PC-3585A topcoat in PBS (black, square) and serum (red, circle) at 37 ^{o}C.

not shown), indicating that the relative permeabilities of both glucose and the interfering species remained constant. The gradual change in amperometric glucose response was also accompanied by enzyme saturation and reduced linear dynamic range (1–21 mM; Figure 4.11B), although the glucose response range still covered relevant physiological concentrations (1–18 mM). The rising glucose sensitivity is most likely associated with physical changes (e.g., swelling) to the permselective PU membrane. Electron microscopy revealed that, while the particles were homogeneously dispersed in the PU originally (Figure 4.12A), they sequestered into large aggregates after 2 wk incubation in buffer (Figure 4.12B). The induced particle aggregation may have been responsible for the increased glucose sensitivity.

The glucose biosensors experienced a perceptible decrease in glucose sensitivity upon testing in porcine serum relative to PBS (3.82±2.22 and 5.62±2.73 nA mM^{-1} mm^{-2}, respectively) due to impeded glucose permeability (Figure 4.13). This decreased sensitivity was accompanied by an extended upper limit of glucose quantification (>32 mM). The measured sensitivity values are comparable to other in vivo glucose sensors (2.5–7.5 nA mM^{-1} mm^{-2})[26-27] with no further change in response through 6 h operation in serum (3.78±2.49 nA mM^{-1} mm^{-2}).

4.4. Conclusions

Nitric oxide release is a demonstrated strategy to improve both the biocompatibility and in vivo performance of glucose biosensors.[24-27] Despite promising pre-clinical results, NO donor leaching and limited NO-release capacities may hinder implementation. The results presented herein indicate that the leaching of entrapped NO donors must be evaluated with due caution. Silica particles functionalized with *N*-diazeniumdiolate NO donors leach indiscriminately from many biomedical-grade polyurethanes barring the most hydrophobic materials. Unfortunately, such membranes were not compatible with electrochemical glucose biosensors due to

insufficient glucose permeability. The underpinnings of the leaching process involve the total particle surface electrical charge and surface hydrophobicity. Silica particles modified with neutral RSNO donors are more stable (i.e., minimal or no leaching) in a wide selection of polyurethanes, provided that the degree of organic modification is substantial (>75% MPTMS). Polyurethane membranes doped with MPTMS particles yielded glucose biosensors with attractive analytical performance merits and NO-release durations. The extended NO-releasing sensors developed here hold promise for mitigating the FBR and improving in vivo sensor functional lifetimes. Studies evaluating in vivo sensor performance using these sensors are currently underway.

REFERENCES

(1) National diabetes statistics report “Estimates of diabetes and its burden in the united states, 2014.” Centers for Disease Control and Prevention: Atlanta, GA: U.S. Department of Health and Human Services; **2014**.

(2) National Diabetes Data Group “Classification and diagnosis of diabetes mellitus and other categories of glucose intolerance.” *Diabetes*, 1979; Diabetes 1039-1057.

(3) Diabetes Control and Complications Trial Group “The effect of intensive treatment of diabetes on the development and progression of long-term complications in insulin-dependent diabetes mellitus” *New England Journal of Medicine* **1993**; 329, 977-986.

(4) Nichols, S. P.; Koh, A.; Storm, W. L.; Shin, J. H.; Schoenfisch, M. H. "Biocompatible materials for continuous glucose monitoring devices." *Chemical Reviews* **2013,** *113,* 2528-2549.

(5) Benhamou, P. Y.; Catargi, B.; Delenne, B.; Guerci, B.; Hanaire, H.; Jeandidier, N.; Leroy, R.; Meyer, L.; Penfornis, A.; Radermecker, R. P.; Renard, E.; Baillot-Rudoni, S.; Riveline, J. P.; Schaepelynck, P.; Sola-Gazagnes, A.; Sulmont, V.; Tubiana-Rufi, N.; Durain, D.; Mantovani, I.; Sola-Gazagnes, A.; Riveline, J. P. "Real-time continuous glucose monitoring (cgm) integrated into the treatment of type 1 diabetes: Consensus of experts from sfd, evadiac and sfe." *Diabetes & Metabolism* **2012,** *38,* S67-S83.

(6) Radermecker, R. P.; Saint Remy, A.; Scheen, A. J.; Bringer, J.; Renard, E. "Continuous glucose monitoring reduces both hypoglycaemia and HbA1c in hypoglycaemia-prone type 1 diabetic patients treated with a portable pump." *Diabetes & Metabolism* **2010,** *36,* 409-413.

(7) Anderson, J. M. "Biological responses to materials." *Annual Review of Materials Research* **2001,** *31,* 81-110.

(8) Anderson, J. M.; Rodriguez, A.; Chang, D. T. "Foreign body reaction to biomaterials." *Seminars in Immunology* **2008,** *20,* 86-100.

(9) Kenneth Ward, W. "A review of the foreign-body response to subcutaneously-implanted devices: The role of macrophages and cytokines in biofouling and fibrosis." *Journal of Diabetes Science and Technology* **2008,** *2,* 768-77.

(10) Koh, A.; Nichols, S. P.; Schoenfisch, M. H. "Glucose sensor membranes for mitigating the foreign body response." *Journal of Diabetes Science and Technology* **2011,** *5,* 1052-9.

(11) Thomé-Duret, V.; Gangnerau, M. N.; Zhang, Y.; Wilson, G. S.; Reach, G. "Modification of the sensitivity of glucose sensor implanted into subcutaneous tissue." *Diabetes & Metabolism* **1996,** *22*, 174-178.

(12) Williams, D. F. "On the mechanisms of biocompatibility." *Biomaterials* **2008,** *29*, 2941-2953.

(13) Sussman, E. M.; Halpin, M. C.; Muster, J.; Moon, R. T.; Ratner, B. D. "Porous implants modulate healing and induce shifts in local macrophage polarization in the foreign body reaction." *Annals of Biomedical Engineering* **2014,** *42*, 1508-16.

(14) Jiang, S.; Cao, Z. "Ultralow-fouling, functionalizable, and hydrolyzable zwitterionic materials and their derivatives for biological applications." *Advanced Materials* **2010,** *22*, 920-32.

(15) Yang, W.; Xue, H.; Carr, L. R.; Wang, J.; Jiang, S. "Zwitterionic poly(carboxybetaine) hydrogels for glucose biosensors in complex media." *Biosensors and Bioelectronics* **2011,** *26*, 2454-2459.

(16) Zhang, L.; Cao, Z.; Bai, T.; Carr, L.; Ella-Menye, J. R.; Irvin, C.; Ratner, B. D.; Jiang, S. "Zwitterionic hydrogels implanted in mice resist the foreign-body reaction." *Nature Biotechnology* **2013,** *31*, 553-556.

(17) Vallejo-Heligon, S. G.; Brown, N. L.; Reichert, W. M.; Klitzman, B. "Porous, dexamethasone-loaded polyurethane coatings extend performance window of implantable glucose sensors in vivo." *Acta Biomaterialia* **2016,** *30*, 106-15.

(18) Vacanti, N. M.; Cheng, H.; Hill, P. S.; Guerreiro, J. D. T.; Dang, T. T.; Ma, M.; Watson, S.; Hwang, N. S.; Langer, R.; Anderson, D. G. "Localized delivery of dexamethasone from electrospun fibers reduces the foreign body response." *Biomacromolecules* **2012,** *13*, 3031-3038.

(19) Norton, L. W.; Koschwanez, H. E.; Wisniewski, N. A.; Klitzman, B.; Reichert, W. M. "Vascular endothelial growth factor and dexamethasone release from nonfouling sensor coatings affect the foreign body response." *Journal of Biomedical Materials Research Part A* **2007,** *81*, 858-69.

(20) MacMicking, J.; Xie, Q. W.; Nathan, C. "Nitric oxide and macrophage function." *Annual Reviews of Immunology* **1997,** *15*, 323-50.

(21) Witte, M. B.; Barbul, A. "Role of nitric oxide in wound repair." *American Journal of Surgery* **2002,** *183*, 406-12.

(22) Cooke, J. P.; Losordo, D. W. "Nitric oxide and angiogenesis." *Circulation* **2002,** *105*, 2133-2135.

(23) Carpenter, A. W.; Schoenfisch, M. H. "Nitric oxide release: Part II. Therapeutic applications." *Chemical Society Reviews* **2012,** *41*, 3742-3752.

(24) Hetrick, E. M.; Prichard, H. L.; Klitzman, B.; Schoenfisch, M. H. "Reduced foreign body response at nitric oxide-releasing subcutaneous implants." *Biomaterials* **2007,** *28*, 4571-4580.

(25) Nichols, S. P.; Le, N. N.; Klitzman, B.; Schoenfisch, M. H. "Increased in vivo glucose recovery via nitric oxide release." *Analytical Chemistry* **2011,** *83*, 1180-1184.

(26) Gifford, R.; Batchelor, M. M.; Lee, Y.; Gokulrangan, G.; Meyerhoff, M. E.; Wilson, G. S. "Mediation ofin vivo glucose sensor inflammatory response via nitric oxide release." *Journal of Biomedical Materials Research Part A* **2005,** *75*, 755-766.

(27) Soto, R. J.; Privett, B. J.; Schoenfisch, M. H. "In vivo analytical performance of nitric oxide-releasing glucose biosensors." *Analytical Chemistry* **2014,** *86*, 7141-7149.

(28) Koh, A.; Carpenter, A. W.; Slomberg, D. L.; Schoenfisch, M. H. "Nitric oxide-releasing silica nanoparticle-doped polyurethane electrospun fibers." *ACS Applied Materials and Interfaces* **2013,** *5*, 7956-7964.

(29) Wo, Y.; Li, Z.; Brisbois, E. J.; Colletta, A.; Wu, J.; Major, T. C.; Xi, C.; Bartlett, R. H.; Matzger, A. J.; Meyerhoff, M. E. "Origin of long-term storage stability and nitric oxide release behavior of carbosil polymer doped with s-nitroso-n-acetyl-d-penicillamine." *ACS Applied Materials and Interfaces* **2015,** *7*, 22218-27.

(30) Worley, B. V.; Soto, R. J.; Kinsley, P. C.; Schoenfisch, M. H. "Active release of nitric oxide-releasing dendrimers from electrospun polyurethane fibers." *ACS Biomaterials Science and Engineering* **2016,** *2*, 426-437.

(31) Backlund, C. J.; Worley, B. V.; Sergesketter, A. R.; Schoenfisch, M. H. "Kinetic-dependent killing of oral pathogens with nitric oxide." *Journal of Dental Research* **2015,** *94*, 1092-1098.

(32) Soto, R. J.; Yang, L.; Schoenfisch, M. H. "Functionalized mesoporous silica via an aminosilane surfactant ion exchange reaction: Controlled scaffold design and nitric oxide release." *ACS Applied Materials and Interfaces* **2016,** *8*, 2220-2231.

(33) Koh, A.; Riccio, D. A.; Sun, B.; Carpenter, A. W.; Nichols, S. P.; Schoenfisch, M. H. "Fabrication of nitric oxide-releasing polyurethane glucose sensor membranes." *Biosensors and Bioelectronics* **2011,** *28*, 17-24.

(34) Riccio, D. A.; Nugent, J. L.; Schoenfisch, M. H. "Stöber synthesis of nitric oxide-releasing s-nitrosothiol-modified silica particles." *Chemistry of Materials* **2011,** *23*, 1727-1735.

(35) Carpenter, A. W.; Johnson, J. A.; Schoenfisch, M. H. "Nitric oxide-releasing silica nanoparticles with varied surface hydrophobicity." *Colloids and Surfaces A: Physicochemical and Engineering Aspects* **2014,** *454*, 144-151.

(36) Frost, M. C.; Reynolds, M. M.; Meyerhoff, M. E. "Polymers incorporating nitric oxide releasing/generating substances for improved biocompatibility of blood-contacting medical devices." *Biomaterials* **2005,** *26*, 1685-93.

(37) Chen, G.; Roy, I.; Yang, C.; Prasad, P. N. "Nanochemistry and nanomedicine for nanoparticle-based diagnostics and therapy." *Chemical Reviews* **2016,** *116*, 2826-2885.

(38) Backlund, C. J.; Worley, B. V.; Sergesketter, A. R.; Schoenfisch, M. H. "Kinetic-dependent killing of oral pathogens with nitric oxide." *Journal of Dental Research* **2015,** *94*, 1092-1098.

(39) Kusaka, T.; Nakayama, M.; Nakamura, K.; Ishimiya, M.; Furusawa, E.; Ogasawara, K. "Effect of silica particle size on macrophage inflammatory responses." *PLoS ONE* **2014,** *9*, e92634.

(40) Waters, K. M.; Masiello, L. M.; Zangar, R. C.; Tarasevich, B. J.; Karin, N. J.; Quesenberry, R. D.; Bandyopadhyay, S.; Teeguarden, J. G.; Pounds, J. G.; Thrall, B. D. "Macrophage responses to silica nanoparticles are highly conserved across particle sizes." *Toxicological Sciences* **2009,** *107*, 553-569.

(41) Bindra, D. S.; Zhang, Y.; Wilson, G. S.; Sternberg, R.; Thevenot, D. R.; Moatti, D.; Reach, G. "Design and in vitro studies of a needle-type glucose sensor for subcutaneous monitoring." *Analytical Chemistry* **1991,** *63*, 1692-1696.

(42) Koh, A.; Lu, Y.; Schoenfisch, M. H. "Fabrication of nitric oxide-releasing porous polyurethane membranes-coated needle-type implantable glucose biosensors." *Analytical Chemistry* **2013,** *85,* 10488-10494.

(43) Chen, X.; Matsumoto, N.; Hu, Y.; Wilson, G. S. "Electrochemically mediated electrodeposition/electropolymerization to yield a glucose microbiosensor with improved characteristics." *Analytical Chemistry* **2002,** *74*, 368-372.

(44) Shin, J. H.; Marxer, S. M.; Schoenfisch, M. H. "Nitric oxide-releasing sol-gel particle/polyurethane glucose biosensors." *Analytical Chemistry* **2004,** *76*, 4543-9.

(45) Ward, W. K.; Jansen, L. B.; Anderson, E.; Reach, G.; Klein, J. C.; Wilson, G. S. "A new amperometric glucose microsensor: In vitro and short-term in vivo evaluation." *Biosensors and Bioelectronics* **2002,** *17,* 181-189.

(46) Zdrahala, R. J.; Zdrahala, I. J. "Biomedical applications of polyurethanes: A review of past promises, present realities, and a vibrant future." *Journal of Biomaterials Applications* **1999,** *14*, 67-90.

(47) Vaddiraju, S.; Wang, Y.; Qiang, L.; Burgess, D. J.; Papadimitrakopoulos, F. "Microsphere erosion in outer hydrogel membranes creating macroscopic porosity to counter biofouling-induced sensor degradation." *Analytical Chemistry* **2012,** *84*, 8837-8845.

(48) McCarthy, C. W.; Guillory, R. J.; Goldman, J.; Frost, M. C. "Transition metal mediated release of nitric oxide (NO) from *S*-nitroso-*N*-acetylpenicillamine (SNAP): Potential applications for endogenous release of NO on the surface of stents via corrosion products." *ACS Applied Materials and Interfaces* **2016,** *8*, 10128–10135.

(49) de Oliveira, M. G.; Shishido, S. M.; Seabra, A. B.; Morgon, N. H. "Thermal stability of primary *S*-nitrosothiols: Roles of autocatalysis and structural effects on the rate of nitric oxide release." *The Journal of Physical Chemistry A* **2002,** *106,* 8963-8970.

(50) Adachi, H.; Sonoki, H.; Hoshino, M.; Wakasa, M.; Hayashi, H.; Miyazaki, Y. "Photodissociation of nitric oxide from nitrosyl metalloporphyrins in micellar solutions." *The Journal of Physical Chemistry A* **2001,** *105,* 392-398.

(51) Shishido, S. M.; de Oliveira, M. G. "Polyethylene glycol matrix reduces the rates of photochemical and thermal release of nitric oxide from *S*-nitroso-N-acetylcysteine." *Photochemistry and Photobiology* **2000,** *71,* 273-80.

(52) Shishido, S. M.; Seabra, A. B.; Loh, W.; Ganzarolli de Oliveira, M. "Thermal and photochemical nitric oxide release from *S*-nitrosothiols incorporated in pluronic F127 gel: Potential uses for local and controlled nitric oxide release." *Biomaterials* **2003,** *24*, 3543-53.

(53) Tsikas, D. "Analysis of nitrite and nitrate in biological fluids by assays based on the griess reaction: Appraisal of the griess reaction in the L-arginine/nitric oxide area of research." *Journal of Chromatography B* **2007,** *851*, 51-70.

(54) Nichols, S. P.; Koh, A.; Brown, N. L.; Rose, M. B.; Sun, B.; Slomberg, D. L.; Riccio, D. A.; Klitzman, B.; Schoenfisch, M. H. "The effect of nitric oxide surface flux on the foreign body response to subcutaneous implants." *Biomaterials* **2012,** *33*, 6305-6312.

(55) Privett, B. J.; Shin, J. H.; Schoenfisch, M. H. "Electrochemical nitric oxide sensors for physiological measurements." *Chemical Society Reviews* **2010,** *39*, 1925-1935.

CHAPTER 5. FOREIGN BODY RESPONSE TO NITRIC OXIDE-RELEASING SUBCUTANEOUS IMPLANTS IN A STREPTOZOTOCIN-INDUCED SWINE MODEL OF DIABETES

5.1. Introduction

In vivo glucose biosensors have been developed as a technology for continuous glucose monitoring by patients afflicted with diabetes mellitus.[1] Unfortunately, the in vivo analytical performance of such devices in subcutaneous tissue is compromised due to the foreign body response (FBR).[1-3] Sensor insertion damages vascularized tissue, resulting in local bleeding and accumulation of proteins and protein fragments on the surface of the sensor.[4] The adsorbed protein layer is responsible for an immediate decrease (40–80%)[5] in glucose sensitivity and serves as an anchor for cell adhesion. Infiltration of the implant site by inflammatory cells (e.g., neutrophils, macrophages)[3] during the ensuing inflammatory response further impacts in vivo sensor performance.[6-9] For instance, pro-inflammatory macrophages have abnormally large metabolic demands and create glucose depletion zones in the sensor microenvironment.[7,9] Failure to digest the sensor incites frustrated phagocytosis and macrophage fusion to form foreign body giant cells.[3] Stress-cracking or delamination of sensor coatings by these polynuclear cells is a frequent cause of in vivo sensor failure.[10] Even for materials that are relatively insusceptible to oxidative damage (e.g., polycarbonate urethanes),[11] phagocytic activity by macrophages and giant cells may decrease the pH in the tissue surrounding the sensor (extreme pH values 3.6)[12] with the potential to interfere with the enzyme-based sensor response. Conclusion of the FBR is marked by the deposition of a dense, avascular collagen capsule around the implanted sensor. Capsule formation obstructs interstitial glucose transport and causes a pronounced temporal lag

in the sensor signal, thereby preventing the sensor from accurately tracking glucose concentrations.[8,13-14]

The analytical performance of in vivo glucose sensors is inherently linked with FBR severity.[15] The FBR has classically been studied as a function of material surface chemistry,[16] but proper selection of coating materials alone has proven insufficient to improve glucose sensor function. The most promising biocompatibility strategies have instead aimed to reduce inflammation and simultaneously guide wound healing at the sensor tissue interface. Topographical cues (i.e., porosity),[17] active release of anti-inflammatory agents (e.g., Dexamethasone),[18-19] and delivery of angiogenic stimulators (vascular endothelial growth factor, platelet-derived growth factor)[20] have all been investigated as approaches to reduce the FBR. Our laboratory has proposed the release of nitric oxide (NO) as a way to mitigate the FBR.[21-24] Nitric oxide functions as an angiogenic agent by upregulating vascular endothelial growth factor (VEGF) production.[25-28] Although the mechanisms of NO's involvement in inflammation are still being investigated, NO is known to influence inflammatory cell recruitment and phenotypes by regulating key cytokines/chemokines involved in the FBR (e.g., tumor necrosis factor-α, macrophage chemoattractant protein-1, interleukin-1β).[29-32]

Prior research in our laboratory has shown that NO-releasing surfaces reduce the FBR and improve attributes of glucose sensor performance.[21-24,33] Hetrick et al. first demonstrated the use of NO-releasing silica xerogels to mitigate FBR-related inflammation and collagen deposition in mouse subcutaneous tissue. Subsequent work by Nichols et al. revealed a dependence of the FBR on NO-release kinetics.[22] Subcutaneous implants capable of extended NO release ($\geq$3 d) reduced inflammation and collagen deposition, whereas rapid release ($\leq$24 h) lead to increased collagen capsule formation. Two separate studies have confirmed the benefits

of NO release and a reduced FBR to in vivo glucose sensor accuracy.[24,33]

Despite promising tissue histology and preclinical sensor performance data,[21-24,33] these initial studies utilized healthy animal models that do not account for several known pathological deficiencies associated with diabetes. Diabetic wounds are generally characterized with inadequate wound repair,[34] delayed inflammatory cell infiltration and cytokine production,[35] and disrupted blood flow.[36] Reduced angiogenesis and cytokine production is at least partially due to inhibited NO production.[37-38] Although these disparities have been well-characterized in the context of wound healing, the effects of a foreign body (i.e., an implanted glucose sensor) on inflammation and tissue reconstruction have not been studied in great detail. As diabetes leads to impaired NO production in subcutaneous wounds, administration of exogenous NO (i.e., from NO-releasing polymers) represents a promising approach to counteracting the delayed wound healing and inflammation associated with diabetes.

Herein, the tissue responses to control and NO-releasing polyurethane materials are evaluated in both healthy and diabetic porcine models to generate new information on how diabetes impacts FBR-related inflammation and collagen deposition. Polymers capable of tunable NO release were employed to assess the role of NO on the FBR in diabetic tissue.

5.2. Experimental Section

5.2.1. Materials

Tetraethylorthosilicate (TEOS), *N*-(3-trimethoxypropyl)diethylenetriamine (DET) and 3-mercaptopropyltrimethoxysilane (MPTMS) were purchased from Gelest (Morrisville, PA) and stored under nitrogen. Aqueous ammonium hydroxide (NH_4OH; 29.41 wt% ammonia), sodium methoxide (NaOMe; 5.4 M in methanol) ethanol (EtOH; 200 proof), hydrochloric acid (HCl), all salts, and anhydrous solvents *N*,*N*-dimethylformamide (DMF), tetrahydrofuran (THF), and

methanol (MeOH) were purchased from Fisher Scientific (Fair Lawn, NJ). Cetyltrimethylammonium bromide (CTAB) was purchased from Sigma (St Louis, MO). Nitrogen (N_2), argon (Ar), and nitric oxide calibration (25.87 ppm in nitrogen) gases were purchased from Airgas National Welders (Raleigh, NC). Pure NO gas was purchased from Praxair (Danbury, CT). Soft stainless steel wire (356 μm dia.) was purchased from McMaster-Carr (Atlanta, GA). Tecoflex SG-85A (TPU) and Tecothane TT-2072D-B20 (TT) polyurethanes (PUs) were received from Lubrizol (Cleveland, OH). Streptozotocin was purchased as a sterile powder from Teva and reconstituted in sterile saline at 100 mg mL^{-1}. Water was purified to a resistivity of 18 MΩ cm and a total organic content of <6 ppb using a Millipore Reference water purification system.

5.2.2. Synthesis of N-diazeniumdiolate-modified mesoporous silica nanoparticles

Mesoporous silica nanoparticles (MSNs) functionalized with *N*-diazeniumdiolate NO donors were prepared using a variant of the Stöber method, as reported previously.[39] Bare mesoporous silica particles were first prepared by adding TEOS (1.395 mL) to a solution of water (162 mL), EtOH (175 mL), NH_4OH (11.8 mL), and CTAB (280 mg). The silicate solution was allowed to stir for 2 h until MSN formation was complete, after which DET (1.31 mL) was added dropwise over 1 min to initiate cation exchange between CTAB and the aminosilanes. The reaction was stirred overnight (~18 h). Secondary amine-modified particles were subsequently collected via centrifugation (6540*g*, 4 ^{o}C, 5 min). Residual CTAB in the MSN mesopores was removed via ion exchange with H^+ ions by agitating the particles in an ethanolic HCl solution (9:1 v/v EtOH:HCl; 3×20 min). The amine-modified MSNs were then washed with EtOH (2×) and dried under reduced pressure.

Secondary amines on the MSNs were converted to *N*-diazeniumdiolate NO donors by

reaction with gaseous NO. The DET particles were initially dispersed in 9:1 (v/v) DMF:MeOH at 5 mg mL^{-1} prior to adding 5.4 M methanolic NaOMe (5 μL per 3 mg MSN) as a catalyst for NO donor formation. Glass vials containing the particle solutions were equipped with stir bars, placed in a stainless-steel Parr hydrogenation vessel, and connected to an in-house NO reactor. The Parr bottle was flushed with Ar (3×short, 3×10 min) to remove oxygen from the reaction solution prior to pressurizing the vessel with pure (>99.5%) NO gas (10 bar) for 3 d. Of note, the NO gas was scrubbed over solid potassium hydroxide for at least 4 h prior to the *N*-diazeniumdiolate formation reaction. After 3 d the NO gas was vented and the vessel again flushed with Ar. The NO donor-modified particles were collected via centrifugation, washed with EtOH (3×), and dried under reduced pressure. The resulting NO-releasing particles were stored in a vacuum-sealed Mylar bag at -20 ^{o}C until further use. Control (i.e., non-NO-releasing) DET MSNs were treated similarly with NaOMe but without the *N*-diazeniumdiolate formation process.

5.2.3. Synthesis of S-nitrosothiol-modified mesoporous silica nanoparticles

Thiol-based MSNs were synthesized using a mercaptosilane/alkoxysilane co-condensation method adapted from reported procedures for nonporous, thiol-modified particles.[40] A silane precursor solution was initially prepared by mixing MPTMS (1.32 mL) and TEOS (1.19 mL) in a glass vial. The silane mixture (2.28 mL) was added to a stirring solution of water (210 mL), EtOH (84 mL), NH_4OH (9.6 mL), and CTAB (240 mg). The reaction was allowed to proceed for 2 h. The thiol-modified particles were collected and purified using the same washing and CTAB removal steps described above for the DET MSNs. *S*-nitrosothiol (RSNO) NO donors were formed on the thiol groups in a subsequent nitrosation step. The MPTMS MSNs (200 mg) were dispersed in a mixture of MeOH (4.00 mL) and 5 M HCl (2.00

mL) and stirred on ice. A solution (2.00 mL) of sodium nitrite (2.27 M) and diethylenetriaminepentaacetic acid (DTPA; 500 μM) in water was added dropwise to particle dispersion and stirred on ice for 1 h. The MSNs were collected via centrifugation, washed with cold MeOH (3×), and dried under reduced pressure. The RSNO-modified particles were used immediately thereafter.

5.2.4. Preparation of nitric oxide-releasing polyurethane membrane-coated implants

Nitric oxide-releasing polymeric membranes were fabricated by doping control or NO donor-modified MSNs into a biomedical-grade polyurethane, TT-2072D-B20 (TT). Polymer solutions were initially prepared by dissolving 360 mg polyurethane (PU) in THF (3.38 mL). The silica particles were dispersed in THF in a separate container, added to the PU solution, and vortexed. The final PU concentration was 80 mg mL^{-1} for all solutions. The final concentration of particles in the PU solution was 20 mg mL^{-1}. In cases of dual RSNO and DET/NO particle incorporation, two separate particle dispersions were prepared and added to the PU.

Stainless steel wire served as the substrate for depositing the NO-releasing PU composites due to similar geometry and size compared to needle-type glucose sensors (~350 μm). The wire was initially cut into 7 cm pieces and sterilized in a steam autoclave. All subsequent coating procedures were carried out in a sterile biological safety cabinet. The wires were modified with the NO-releasing membranes via dipcoating into the PU/MSN solution and drying for 1 h. The total number of coats was 16. A TPU topcoat (60 mg mL^{-1} in THF) was applied to all membranes to minimize leaching of the MSNs from the membranes. The external PU coat also served to ensure consistent surface chemistry across the different implants, as surface chemistry could represent a convoluting variable with respect to FBR severity. The coated portion of the wire was cut to a final length of 15 mm prior to coating the exposed ends

with the TPU topcoat solution. After drying (~1 h), the implants were housed individually in sterile microcentrifuge tubes and stored in a sterile vacuum-sealed Mylar bag at -80 ^{o}C until use. Control (i.e., non-NO-releasing) materials were prepared in an identical manner except that the particles were not functionalized to release NO. Of note, the control particles were washed 3× with sodium methoxide following the H^{+} ion exchange step of the MSN purification process in to remove ionically bound protons.

5.2.5. Membrane characterization

Nitric oxide release from the PU membranes was measured using a Sievers 280i chemiluminescence NO analyzer (NOA; Boulder, CO). The NOA was calibrated immediately before all measurements using air passed through an NO–zero filter as the blank value and 25.87 ppm NO (in nitrogen gas) as the second calibration standard. The NO-releasing membranes were immersed in phosphate buffered saline (PBS; 10 mM, pH 7.41) at 37 ^{o}C. For membranes that contained RSNO-modified particles, the NOA sample flask was shielded from light. In addition, 500 μM DTPA was added to the PBS to chelate trace copper ions, thus restricting NO release to thermal mechanisms. The NO that was released from the materials was carried to the instrument by stream of nitrogen gas (80 mL min^{-1}) bubbled through the PBS solution. Supplemental nitrogen gas flow was provided to the NOA to match the 200 mL min^{-1} gas flow input. Nitric oxide was detected indirectly by reaction with ozone, forming an excited-state nitrogen dioxide species. Chemiluminescence data was collected at a sampling frequency of 1 Hz, providing near real-time measurements of NO release from the PU membranes. Measurements were terminated when NO concentrations fell below the detection limit of the NOA (~6 ppb or 0.8 pmol cm^{-2} s^{-1}).

Particle leaching from the membranes was assessed by soaking membranes in PBS for a pre-determined period of time (1–28 d) and measuring the silicon content of soak solutions via

inductively coupled plasma optical emission spectrometry (ICP-OES; Teledyne-Leeman Labs Prodigy high-dispersion ICP; Hudson, NH). The instrument was initially calibrated using sodium silicate standards in PBS (0.1–25 ppm; 251.611 nm Si emission line) to ensure linear response over the anticipated range of particle concentrations. Calibration curves were subsequently generated for each type of silica particle and compared to Si emission values from the membrane soak solutions for leaching determination.

5.2.6. In vivo protocol

All procedures and protocols were in accordance with institutional guidelines and approved by the Institutional Animal Care and Use Committee at the University of North Carolina in Chapel Hill. Twelve mixed gender Yorkshire-type piglets weighing approximately 12–17 kg were used for this study. Diabetes was induced in half of the piglets (three males and three females) by repeated intravascular administration of streptozotocin (25–50 mg kg^{-1}, 4 doses over 4–6 d) until elevated post-prandial blood glucose values (171±50 mg dL^{-1}, mean ± standard deviation) were consistently observed via ear prick glucose measurements. Pooled blood glucose values for controls (i.e., without STZ treatment) were 61±18 mg dL^{-1}. The pigs were maintained for 2–6 days prior to implanting the mock sensors. On the day of implantation, the pigs were sedated with telazol. Anesthesia was maintained with isoflurane using an endotracheal tube. The mock sensors were implanted using aseptic technique by cannulation into the subcutaneous tissue using a 18 G catheter inserter and the entry wound marked with tattoo ink. The implants were organized into 6 groups of 4 implants (24 implants per animal) on either side of the spine to control for variability due to implant location. After a pre-determined period of time (3, 10, or 25 d), the pigs were euthanized and the implants located using a portable X-ray imager. Tissue surrounding the mock sensors explanted en bloc for histopathological evaluation of the FBR.

After first removing the implants from the tissue samples, the tissues were fixed in 10 vol% buffered formalin. Thin sections (~5 μm) were stained with hematoxylin and eosin (H&E) or Masson's Trichrome for visualization of inflammatory cells or collagen, respectively. Immunohistochemical analysis for cluster of differentiation marker 31 (CD31; an endothelial cell surface marker) was carried out after an antigen retrieval step using pig-reactive anti-CD31 antibodies from Abcam (ab28364; 1:500 dilution).

The severity of the inflammatory response was assessed from photomicrographs of hematoxylin and eosin-stained tissue slices. The number of inflammatory cells (e.g., neutrophils, macrophages) within ~200 μm of the implant surface was counted by a blinded observer. Average numbers of inflammatory cells (ICs), normalized to the tissue area (i.e., IC densities), served as indicators of inflammatory response severity. Collagen deposition was quantified within 200 μm of the implant surface similarly to previous reports[21-22,41] using Masson's Trichrome-stained tissue sections. Portions of the photomicrographs that stained blue, originating from collagen fibers, were isolated using a color filter in photoshop and then inverted so that white pixels corresponded to collagen fibers. Regions 200×50 μm in size were then cropped from the image and saved as text images. A custom MATLAB script was used to determine a percent collagen density by comparing the number of white pixels to the total number of pixels in the image. Immunohistochemical staining for CD31 was employed to quantitatively evaluate angiogenesis by counting the total number of blood vessels, identified as open tubular brown structures, within 400 μm of the implant surface.

5.2.7. Statistical analysis

Inflammatory cell densities and collagen deposition data were tested for normality using a Shapiro-Wilk test. In all cases, the data were determined to be distributed normally at >99% confidence. Thus, the data were analyzed using a two-tailed student's t-test with p-values <0.05 considered statistically significant. For multiple comparisons, one-way Analysis of Variance was used followed by individual comparisons using a student's t-test with an applied Bonferroni correction.

5.3. Results and discussion

5.3.1. Characterization of nitric oxide-releasing polyurethanes

Polyurethane materials with diverse NO-release properties were fabricated by doping Tecothane (TT) PU membranes with a range of NO-releasing MSNs (Figure 5.1). The NO-releasing polymers were coated onto steel wire substrates that mimicked the size and geometry of needle-type electrochemical glucose biosensors. The mock sensors were further modified with a TPU topcoat that normalized the surface chemistry of all implants. The NO-release kinetics from the membranes were manipulated intentionally by careful selection of the NO donor-modified silica particle dopants. For example, the *N*-diazeniumdiolate NO donor moiety undergoes proton-initiated decomposition and releases NO at rates dependent on pH, temperature, and the chemical structure of the precursor amine.[42] Incorporation of *N*-diazeniumdiolate-modified DET particle into a hydrophobic aromatic Tecothane PU resulted in membranes (DET/NO) that released low NO fluxes (1–12 pmol cm^{-2} s^{-1}) for ~13 d (Table 5.1).

To study the influence of initial NO flux on the FBR, RSNO-modified MSNs were co-incorporated with DET/NO particles in Tecothane PU. *S*-nitrosothiols undergo thermally-initiated S–N bond cleavage in vivo. Membranes prepared exclusively with RSNO particles

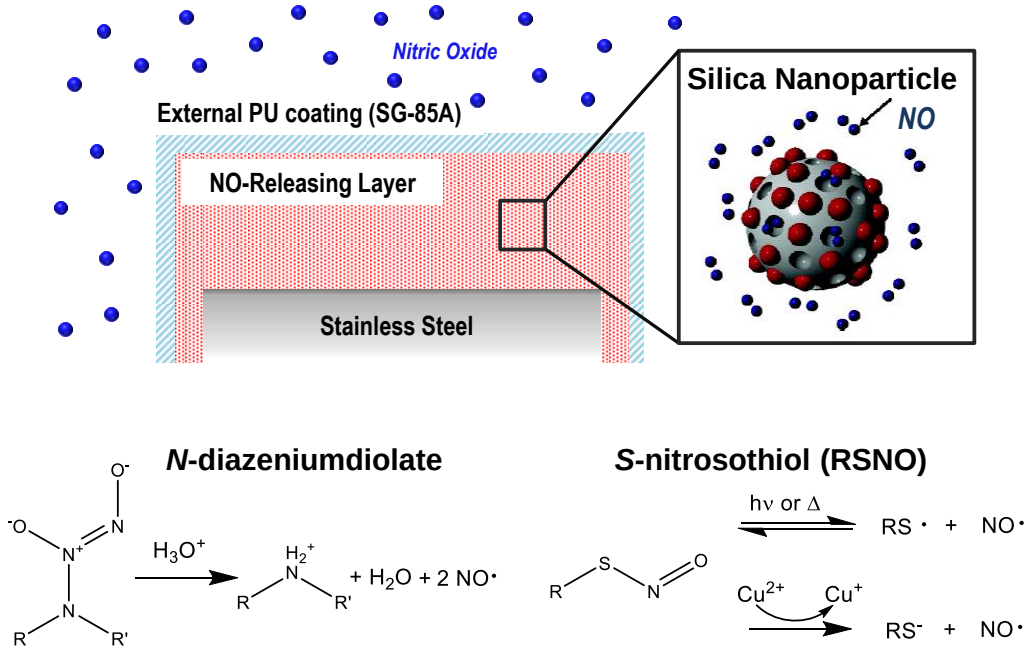

Figure 5.1. Schematic of NO-releasing subcutaneous implants. The NO-releasing silica nanoparticles were doped into TT polyurethane membranes. An external SG-85A PU coating was applied to limit particle leaching and ensure consistent surface chemistry for all implant types. The implants released NO upon decomposition of the NO donors in vivo by either reaction with protons (*N*-diazeniumdiolates) or through a thermal mechanism (*S*-nitrosothiols).

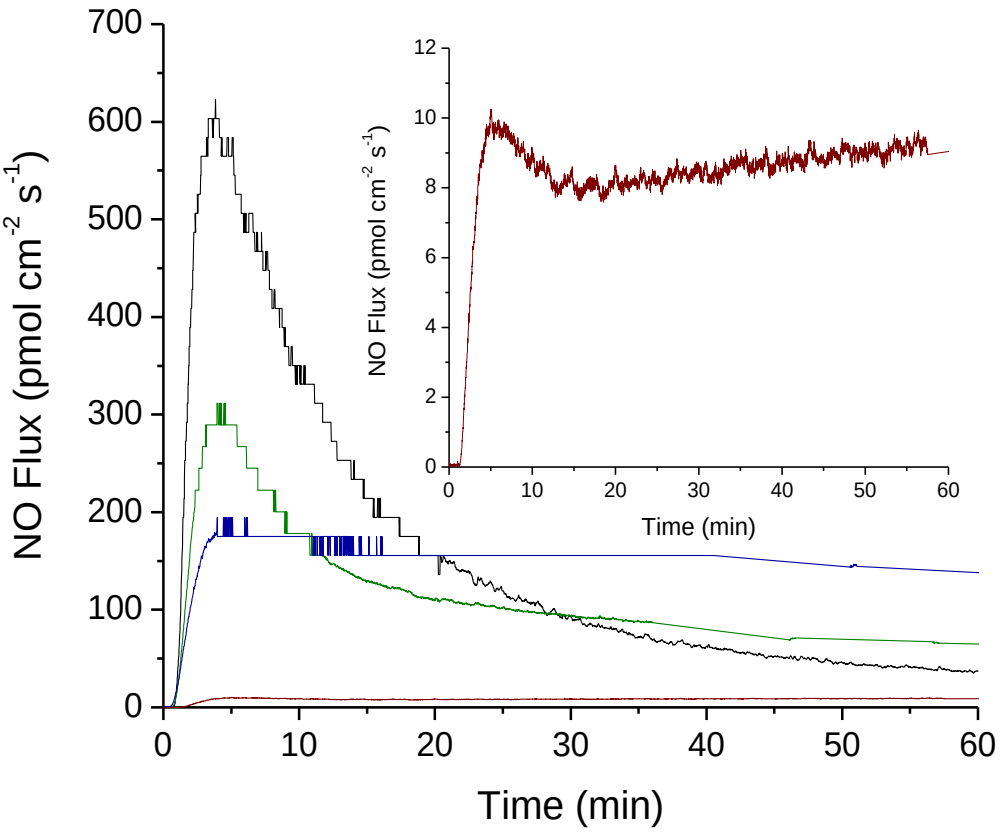

Figure 5.2. Initial (1 h) NO release from PUs in PBS (37 ^{o}C, pH 7.41) for (black) RSNO, (green) 3:1 RSNO:DET, (blue) 1:1 RSNO:DET, and (red) DET/NO systems. The inset displays a magnified view of the initial NO-release profile for the DET/NO sample.

Table 5.1. Nitric oxide release from polyurethane membranes doped with different NO donor-modified silica nanoparticles.[a]

NO-Release System	[NO] (pmol cm^{-2} s^{-1})[b]							
	4 h	**12 h**	**24 h**	**48 h**	**72 h**	**96 h**	**144 h**	**240 h**
RSNO	18.1±8.9	6.1±2.1	3.2±0.8	0.9±0.1	---	---	---	---
3:1 RSNO:DET	23.5±2.9	5.3±1.9	3.8±0.4	1.8±0.7	0.8±0.3	---	---	---
1:1 RSNO:DET	54.7±8.5	18.5±2.2	9.7±0.8	8.4±3.6	5.5±1.6	3.3±1.0	2.1±0.5	---
DET/NO	8.4±0.7	5.7±0.5	4.1±0.6	3.5±0.4	2.9±0.4	3.2±0.6	2.6±0.5	1.4±0.2

[a]Results are expressed as average values ± standard deviation of $n \geq 3$ separate experiments. [b]Instantaneous NO flux measured from mock sensor surfaces via chemiluminescence NO analysis.

released large, maximum NO fluxes (630 pmol cm^{-2} s^{-1}) and exhausted their NO supply within 48 h (Table 5.1; Figure 5.2). Materials incorporating both types of NO donor-modified MSNs (at 3:1 and 1:1 RSNO:DET mass ratios) released more intermediate NO fluxes initially (285 and 200 pmol cm^{-2} s^{-1}, respectively) and maintained NO release above >0.8 pmol cm^{-2} s^{-1} for longer durations (3 and 7 d, respectively) than the RSNO system alone. The four NO-releasing membranes that were chosen for evaluation (i.e., DET/NO, 3:1 RSNO:DET, 1:1 RSNO:DET, and RSNO) exhibit NO-release durations that align with the anticipated timelines of the acute and chronic inflammatory responses (~1–2 and 3–14 d, respectively).[3,43-44]

Although silica is generally tolerable in vivo,[45] leaching of the silica particles from the PU membranes may exacerbate the FBR. For example, nano-sized silica particles may be phagocytosed by macrophages, increasing production of pro-inflammatory cytokines (e.g., interleukin-1β, tumor necrosis factor-α).[46-47] Given the potential of silica to counteract NO's ability to reduce the FBR, we assessed particle leaching from the MSN-doped membranes. Quantitative analysis of silicon concentrations in membrane soak solutions was carried out using ICP-OES. Even after incubation in PBS at 37 ^{o}C for 28 d, silica particle leaching from NO-releasing and control membranes (i.e., particle-doped membranes that were not functionalized to release NO) was minimal (<5%). The materials were thus deemed suitable for further evaluation of the FBR.

5.3.2. Inflammatory response

A porcine model was selected for FBR evaluation due to similarities in subcutaneous tissue composition (i.e., proportion of adipose tissue and collagen content) between pigs and humans.[48-51] Chemical induction of diabetes was carried out by administrating multiple doses of the pancreatic β-cell cytotoxin, streptozotocin (STZ), over a 10 d period preceding implantation

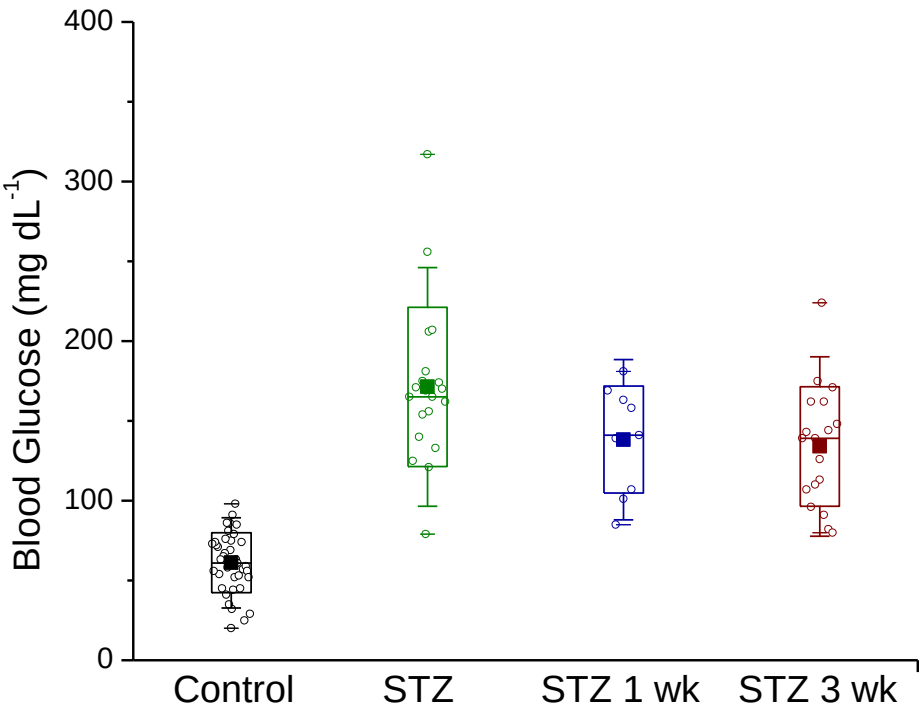

Figure 5.3. Box-and-whisker plot of post-prandial blood glucose values determined by a Freestyle Lite glucometer before and after STZ administration.

of the materials. Diabetes induction in the pigs was confirmed by greater post-prandial blood glucose values relative to untreated pigs (171±50 and 61±18 mg dL^{-1}, respectively; Figure 5.3). Hyperglycemia was maintained for the entire study duration (i.e., 1 mo) using this protocol.

Inflammatory cells (e.g., macrophages) are known to negatively impact glucose sensor performance, due in part to their large, localized glucose/oxygen consumption and ability to damage sensor components via respiratory bursts (i.e., release of reactive oxygen and nitrogen species).[7-8,10,12] Elevated inflammatory cell presence is linked to poor sensor performance.[7-9] As such, photomicrographs of hematoxylin and eosin-stained tissues were used to quantitatively assess the inflammatory response. The severity of the inflammatory response was determined at three different implantation periods (3, 10, and 25 d) and considered with respect to both NO and animal model disease state. The 3 d tissue response was localized to ~100 μm from the surface of the implants and consisted primarily of macrophages (based on nuclear morphologies observed in the hematoxylin and eosin stains; Figure 5.4). This initial time point represented onset of the chronic inflammatory response.[3] Inflammatory cell densities adjacent to control (non-NO-releasing) implants at 3 d were similar between the healthy and diabetic pigs (~$3.3–3.9\times10^3$ cells mm^{-2}). The release of NO during this initial period in the FBR elicited a modest reduction in the inflammatory response (10–30%; Figure 5.5A). No differences in IC densities were observed between the NO-releasing implants (ANOVA p-value 0.457), indicating that the initial NO flux had no effect on the 3 d inflammatory response. Inflammation was mitigated to a greater degree by NO in the STZ-treated pigs, with 35–50% reductions in the number of ICs at NO-releasing implants relative to controls (Figure 5.5B). As was the case in the healthy swine model, NO-release kinetics did not impact inflammation in the diabetic pigs at 3 d (ANOVA p-value 0.621).

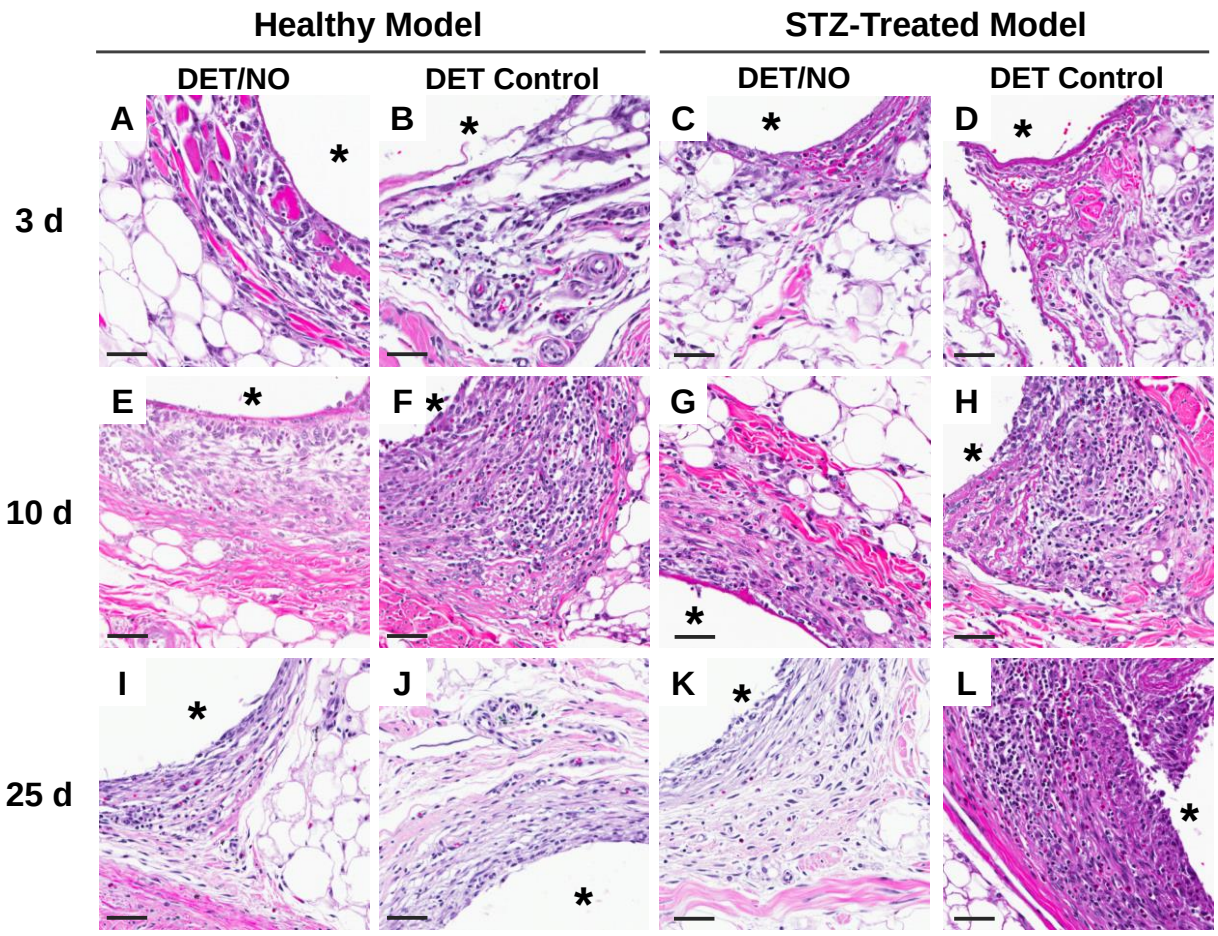

Figure 5.4. Photomicrographs of hematoxylin and eosin-stained tissues adjacent to implanted PU materials at (A–D) 3; (E–H) 10; and (I–L) 25 d post-implantation. The number of dark purple inflammatory cell nuclei were quantitated as a measure of inflammation severity. The asterisk (*) in each image indicates the location of the implant. The scale bar at the bottom of the image represents a distance of 50 μm.

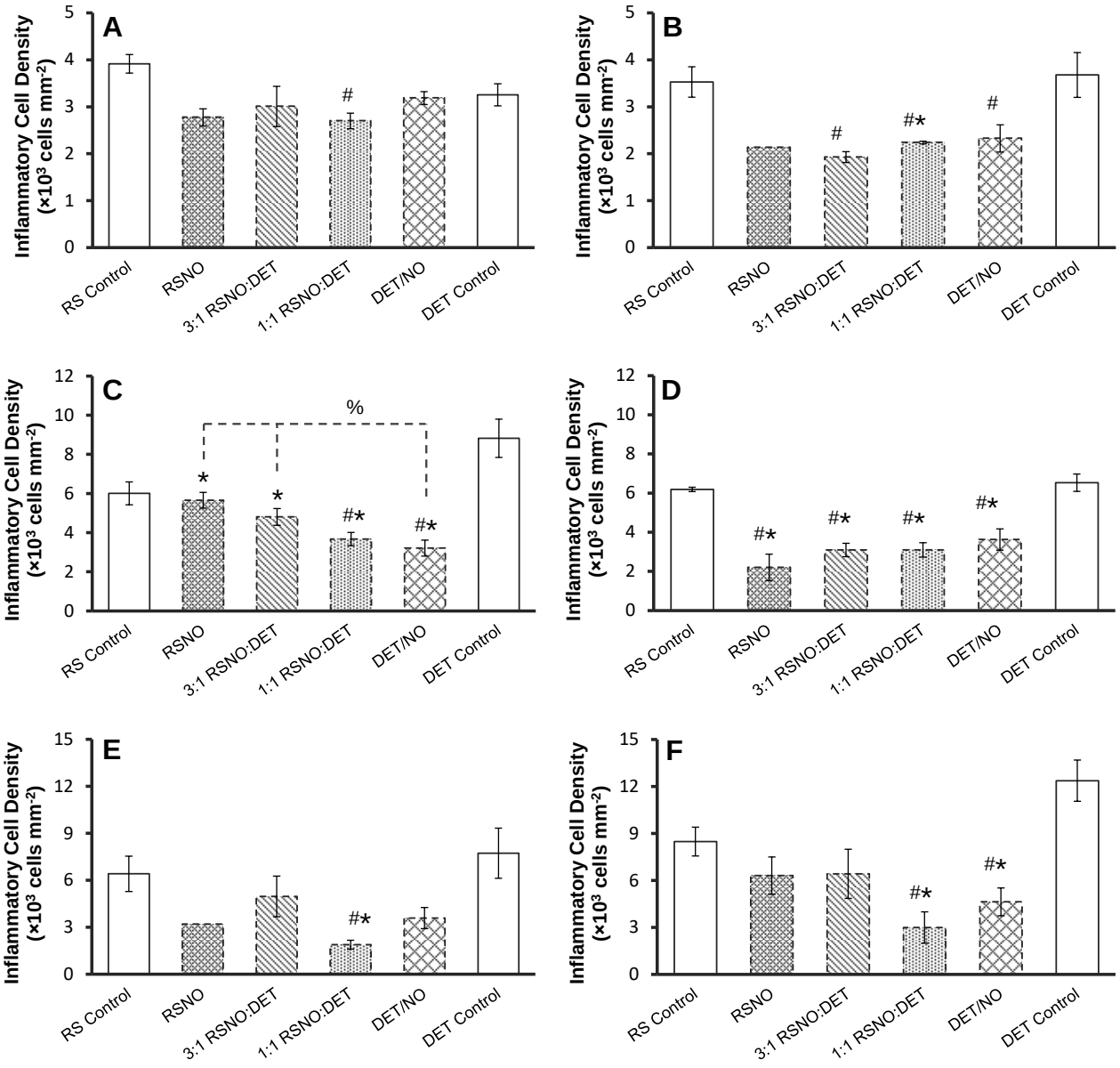

Figure 5.5. Inflammatory cell densities in the vicinity of subcutaneously-implanted mock sensors at (A, B) 3; (C, D) 10; and (E, F) 25 d post-implantation in (A, C, E) healthy and (B, D, F) STZ-treated pigs. Inflammatory cell counts are expressed as average densities (±standard error of the mean) within 200×100 µm areas of tissue immediately adjacent to the implants. Symbols above individual bars denote statistical significance between NO-releasing and either DET (*) or RSNO (#) control samples at $p<0.05$. Where appropriate, differences between individual NO-release systems are marked with a % symbol. Statistical testing was not carried out for the RSNO sample in graphs (B) and (E) due to insufficient sample size.

A more severe inflammatory response was observed at RSNO and DET control implants after 10 d relative to the initial (3 d) time point (Figures 5.4E–H) regardless of disease state. For example, IC densities for the RSNO control materials in the healthy and STZ-treated animals were 6.0×10^{3} and 6.2×10^{-3} cells mm^{-2}, respectively. A reduced inflammatory response was evident at all NO-releasing implants in both the healthy and STZ-treated pigs (Figures 5.5C and 5.5D). Longer NO release from the DET/NO materials (i.e., 13 d NO-release duration) mitigated inflammation to a greater degree in the healthy swine model relative to the 2–3 d NO-release systems (ANOVA $p=0.0037$).[22] However, there were no discernable differences arising from varying NO-release kinetics in the STZ-treated pig model (ANOVA $p=0.364$).

Additional recruitment of ICs to the implant site ceased after 10 d in the healthy swine model, indicating resolution of the inflammatory response. Indeed, IC densities at 10 and 25 d post-implantation were similar for both sets of controls. In contrast, a more severe 25 d inflammatory response was observed in the STZ-treated pigs. Inflammatory cell densities at the DET controls nearly doubled after 25 d in comparison to the 10 d values (12.4×10^{3} and 6.4×10^{3} cells mm^{-2}, respectively; $p=0.006$). The inflammatory response for RSNO controls was similarly elevated (8.5×10^{3} and 6.2×10^{3} cells mm^{-2}; $p=0.031$). This data disagrees with a previous study by Wang et al. that evaluated the FBR in STZ-induced diabetic rats to silicon substrates coated with poly(vinyl alcohol). The authors indicated that STZ treatment did not alter the degree of inflammation after a similar implant duration (28 d).[52] This discrepancy most likely relates to the use of different animal models (i.e., porcine and rodent models). This difference notwithstanding, the persistent inflammation observed in the diabetic pigs was not surprising, as a delayed inflammatory response has been identified as at least partially responsible for the deficient wound healing associated with diabetes.[38]

The short-term NO-release systems (NO-release durations <2–3 d) were incapable of maintaining the low levels of inflammation observed at 10 d, eliciting a similar inflammatory response to controls at 25 d post-implantation (Figures 5.5E,F). In contrast, the more extended NO-release systems (i.e., DET/NO and 1:1 RSNO:DET) maintained low IC densities ($2–5\times10^3$ cells mm^{-2}) throughout implantation, highlighting an unequivocal benefit of 7–13 d NO release (relative to 2–3 d durations). However, the mechanisms through which the long-term NO release mitigates the chronic inflammatory response (i.e., at 25 d) remain unclear. A reduced 10 d inflammatory response was also evident for the 2–3 d NO-release systems. These observations are consistent with prior work by Hetrick et al.[21] and Nichols et al.[22] Nitric oxide mediates the production of several key chemokines/cytokines involved in the FBR, including tumor necrosis factor-α, macrophage chemoattractant-1, and interleukin-1β.[29-32] In this regard, NO may delay the inflammatory response by interfering with inflammatory cell recruitment to the implant site.

5.3.3. Collagen deposition

The most often observed outcome in the FBR to indwelling glucose biosensors is the formation of a dense, collagenous tissue layer that segregates the sensor from the surrounding extracellular matrix.[8,13-14] The collagen capsule is populated by metabolically active ICs and lacks the extensive vascular network of uninjured subcutaneous tissue. Collectively, the characteristic density and avascularity of the collagenous tissue renders the capsule remarkably impermeable to glucose transport. Consequences of poor glucose transport include attenuation of the glucose sensor signal and a pronounced temporal lag (20–30 min relative to blood), ultimately resulting in sensor failure.[8]

To visualize and assess collagen deposition, tissue slices harvested from the regions surrounding the mock sensors were stained with Masson's Trichrome. Photomicrographs of the

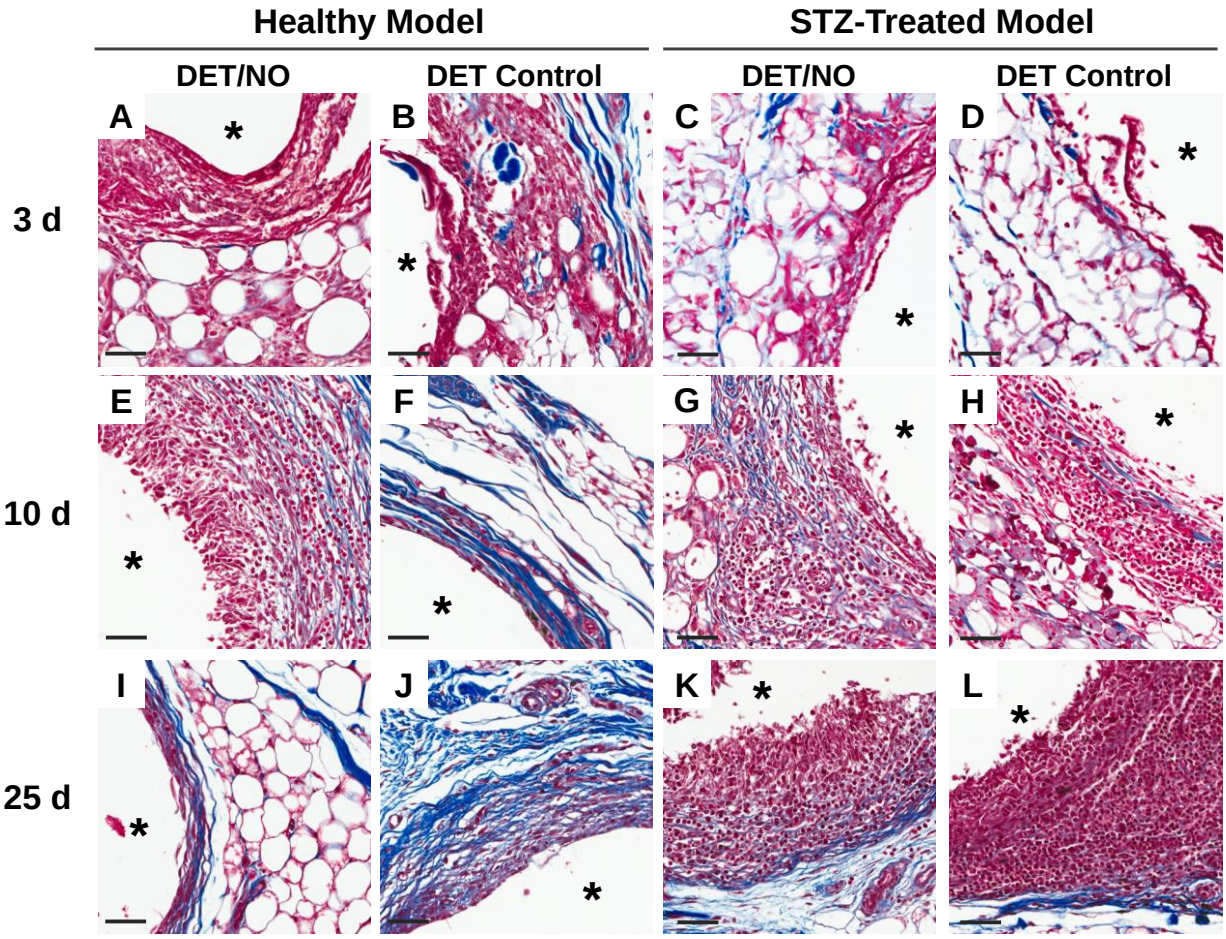

Figure 5.6. Photomicrographs of Masson's Trichrome-stained tissues adjacent to implanted PU materials at (A–D) 3; (E–H) 10; and (I–L) 25 d post-implantation. Collagen density was analyzed in 200×50 µm areas immediately proximal to the implant surface and expressed as the % area occupied by blue collagen pixels. The asterisk (*) in each image indicates the location of the implant. The scale bar at the bottom of the image represents a distance of 50 µm.

stained tissues were used to quantify collagen deposition proximal to the implant surface (within 200 μm) as a percentage (density) of the total image area occupied by blue collagen pixels (Figure 5.6). Of note, collagen analysis was not carried out at 3 d as the collagen in the tissue samples was sparse (Figures 5.6A–D). By 10 d, a dense capsular layer (collagen densities ~20–30%) had formed around most of the control and NO-releasing implants in the healthy pigs (Figures 5.6E–H and 5.7A). After 25 d, typical collagen densities had increased to ~30–50% (Figures 5.6E–L and 5.7B). The sustained NO-release system (DET/NO; 13 d NO release) mitigated capsule formation in healthy swine at both 10 and 25 d. Investigations by Hetrick et al.[21] and Nichols et al.[22] also demonstrated reduced collagen deposition at NO-releasing implants. However, the mechanisms through which NO is involved in capsule formation remain unclear. The apparent inhibition of collagen deposition may be due to NO's involvement in the production of transforming growth factor β (TGF-β),[26] a known stimulator of collagen production by fibroblasts.[53]

Reduced collagen deposition was consistently observed for tissue samples in the STZ-treated pigs relative to control swine. Typical % collagen values were in the range of 5.8–11.5% after 10 d for all samples in the STZ-treated model compared to 9.2–29.8% in the healthy pigs. Similar disparities in collagen deposition were also observed at 25 d (11.8–17.4% vs. 29.7–50.0% for the STZ and control pigs, respectively). Prior research has also identified inhibited collagen deposition as a hallmark of the diabetic FBR,[54-55] in agreement with our results. No discernable difference was noted in the % collagen values between any of the implants (control or NO-releasing) in the diabetic pigs at either 10 or 25 d (ANOVA p-values 0.80 and 0.87, respectively). Socarrás et al. observed lower levels of TGF-β as a result of diabetes in rat tissue surrounding implanted polyetherurethane sponges,[54] which may account for the lack of an

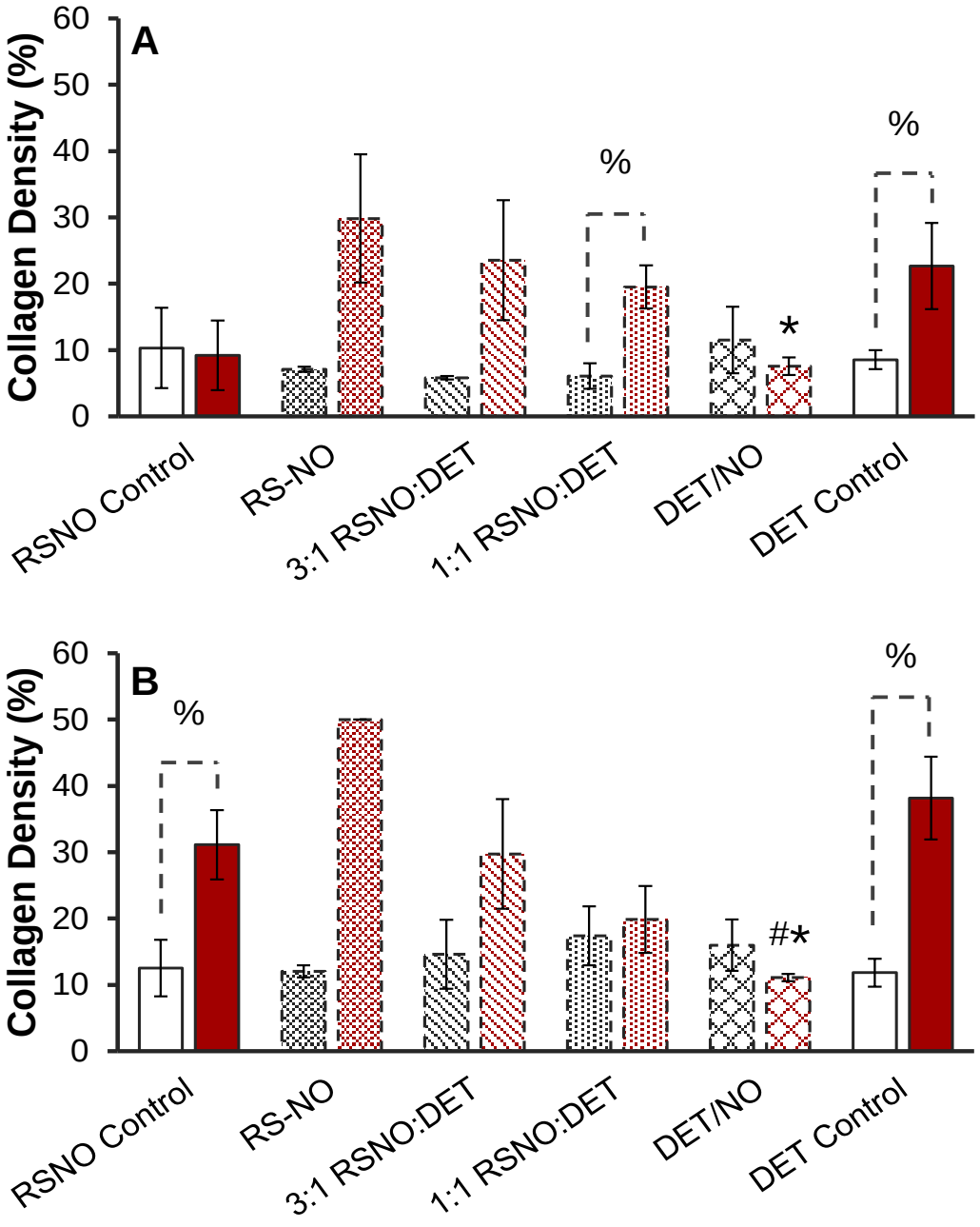

Figure 5.7. Collagen densities in the tissue surrounding mock sensors at (A) 10 and (B) 25 d post-implantation for healthy (red) and diabetic swine (black). Collagen densities are expressed as average values (±standard error of the mean). Symbols above individual bars denote statistical significance between NO-releasing and either DET (*) or RSNO (#) control samples at $p<0.05$. Where appropriate, differences between identical samples implanted in healthy or STZ-treated pigs are denoted with a % symbol. Statistical testing was not carried out for the RSNO sample in (B) due to insufficient sample size.

observable effect of NO release on collagen deposition in the diabetic pig model.

5.3.4. Angiogenesis

Glucose sensor implantation disrupts native tissue and destroys vascular structures in the immediate vicinity of the device. The sensor-tissue interface remains devoid of local vasculature as the sensor becomes progressively more isolated by inflammatory cells and collagen during the FBR. The lack of blood vessels at the implant site prevents consistent glucose transport to the sensor, reducing glucose concentrations at the implant surface and thereby contributing to erratic sensor response.[8,14,56-57] Adequate vascularization has thus been suggested as a key requirement for ensuring consistent glucose sensor function.[8,14,56]

The DET/NO and its analogous control (DET control) were selected for evaluation of blood vessel formation after 10 d of implantation due to the favorable reductions in collagen deposition and inflammation afforded by extended (13 d) NO release. Vessels in the vicinity of the implants were visualized by immunohistochemical tissue staining for the endothelial cell surface marker CD31. Representative photomicrographs of the tissue samples (counterstained with hematoxylin) are provided in Figure 5.8. Impaired angiogenesis is a known manifestation of diabetes in humans[58] that has been recreated intentionally in STZ-induced diabetic rat models.[54] Blood vessel counts at control implants were compared between the healthy and diabetic pigs, revealing a potential difference that approached statistical significance ($p=0.095$). The tissue surrounding the DET/NO implants was consistently more vascularized relative to control materials (Figure 5.9), with 47.1 and 70.4% more blood capillaries adjacent to implants in the healthy and diabetic pigs, respectively. This result was somewhat expected, as NO derived from endothelial nitric oxide synthase is an essential component of angiogenesis during tissue remodeling.[28] Several pro-angiogenic growth factors (e.g., VEGF) elicit NO production.[26,59] In

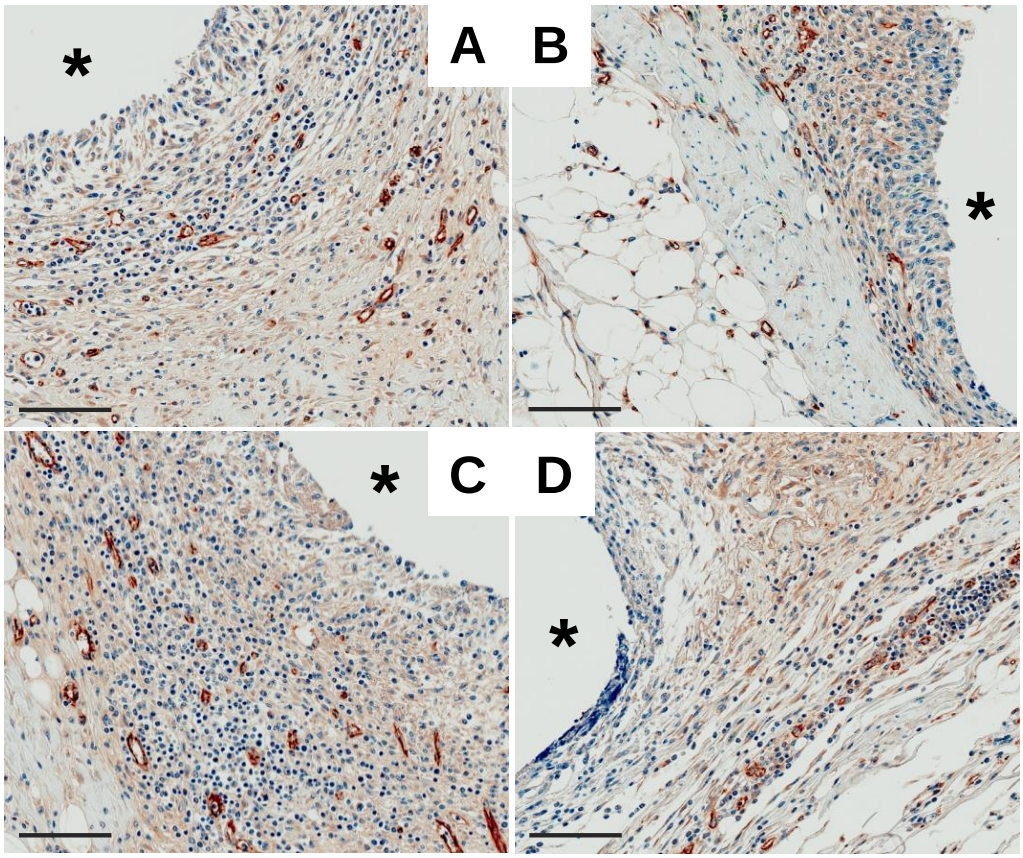

Figure 5.8. Photomicrographs of anti-CD31 and hematoxylin stained tissues adjacent to (A, C) DET/NO and (B, D) DET control implants after 10 d in the (A, B) healthy and (C, D) diabetic pigs. Blood vessels were identified as open tubular brown structures. The asterisk (*) marks the implant location and the scale bar at the bottom left of each image represents 100 µm.

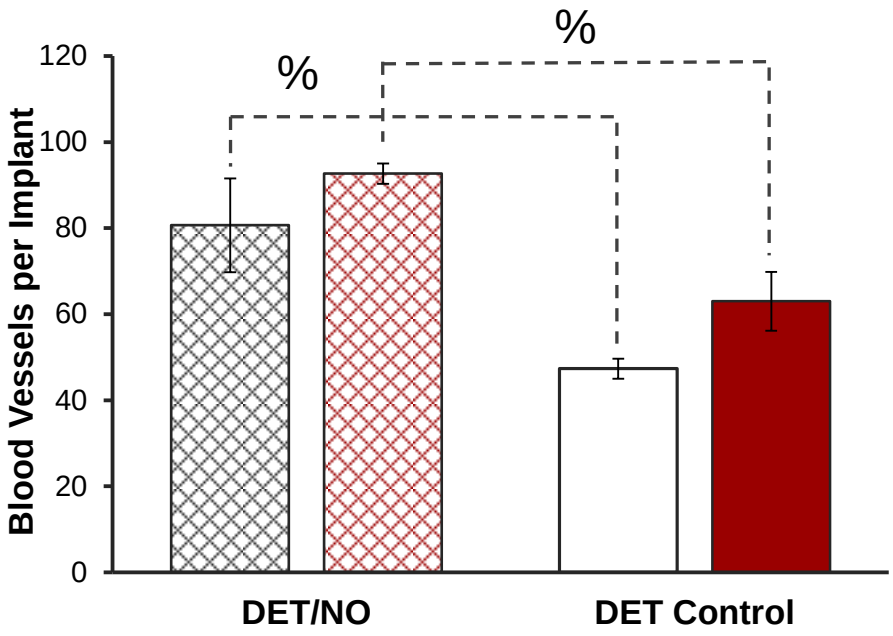

Figure 5.9. Blood vessels within 400 μm of the surface of DET/NO and DET control implants 10 d post-implantation in healthy (red) and diabetic (black) swine. The % symbol denotes a significant difference between two implants at $p<0.05$.

addition, NO has also been shown to stimulate VEGF expression.[25] Hetrick et al. also reported increased blood vessel formation in healthy rats at materials that released a range of NO fluxes (1–110 pmol cm^{-2} s^{-1}) for 3 d.[21] This data indicates that lower NO fluxes (~1–12 pmol cm^{-2} s^{-1}) are primarily responsible for enhanced angiogenesis.

5.4. Conclusions

Prior research has established the utility of polymeric NO release for reducing FBR-related inflammation and collagen deposition.[21-23] In turn, the analytical performance of in vivo glucose biosensors has been shown to be positively influenced.[24,33] However, insufficient literature regarding the impact of diabetes on the FBR brings into question the relevance of this data. The research described herein represents a first step to understanding differences in the porcine FBR to subcutaneously-implanted polyurethane biomaterials arising from STZ-induced diabetes. In particular, a delayed—but more severe—inflammatory response was a unique feature in diabetic pigs. Nitric oxide release from the polyurethane materials mitigated the early inflammatory response (i.e., at 3 and 10 d) in both models, highlighting a key anti-inflammatory benefit associated with this strategy. However, only long-term NO-releasing implants (with 7 and 13 d NO-release durations) maintained low degrees of inflammation at extended periods (25 d), counteracting the severe inflammation observed in the diabetic swine. Sustained NO release stimulated angiogenesis at the implant-tissue interface in both the healthy and diabetic swine models. These data confirm that the anti-inflammatory and angiogenic properties of NO are preserved regardless of disease state. The sustained (13 d) NO-release system also mitigated collagen deposition in healthy pigs, confirming the benefits of extended NO-release kinetics. A key distinction of the FBR in the diabetic swine model was the lack of capsular tissue. As such, deposition was unaffected by NO. This apparent inhibition of collagen deposition in the diabetic

pigs serves to caution against extrapolating histological outcomes in healthy animal models to anticipated results in diabetic tissue.

REFERENCES

(1) Nichols, S. P.; Koh, A.; Storm, W. L.; Shin, J. H.; Schoenfisch, M. H. "Biocompatible materials for continuous glucose monitoring devices." *Chemical Reviews* **2013,** *113*, 2528-2549.

(2) Wilson, G. S.; Zhang, Y. In *In vivo glucose sensing* Cunningham, D. D.; Stenken, J. A., Eds. John Wiley & Sons: Hoboken, **2009**; 1–27.

(3) Anderson, J. M.; Rodriguez, A.; Chang, D. T. "Foreign body reaction to biomaterials." *Seminars in Immunology* **2008,** *20*, 86-100.

(4) Gifford, R.; Kehoe, J. J.; Barnes, S. L.; Kornilayev, B. A.; Alterman, M. A.; Wilson, G. S. "Protein interactions with subcutaneously implanted biosensors." *Biomaterials* **2006,** *27*, 2587-2598.

(5) Thévenot, D. R.; Toth, K.; Durst, R. A.; Wilson, G. S. "Electrochemical biosensors: Recommended definitions and classification1." *Biosensors and Bioelectronics* **2001,** *16*, 121-131.

(6) Avula, M. N.; Rao, A. N.; McGill, L. D.; Grainger, D. W.; Solzbacher, F. "Foreign body response to subcutaneous biomaterial implants in a mast cell-deficient KIT(W-SH) murine model." *Acta Biomaterialia* **2014,** *10*, 1856-1863.

(7) Klueh, U.; Qiao, Y.; Frailey, J. T.; Kreutzer, D. L. "Impact of macrophage deficiency and depletion on continuous glucose monitoring in vivo." *Biomaterials* **2014,** *35*, 1789-1796.

(8) Novak, M. T.; Yuan, F.; Reichert, W. M. "Modeling the relative impact of capsular tissue effects on implanted glucose sensor time lag and signal attenuation." *Analytical and Bioanalytical Chemistry* **2010,** *398*, 1695-1705.

(9) Novak, M. T.; Yuan, F.; Reichert, W. M. "Macrophage embedded fibrin gels: An in vitro platform for assessing inflammation effects on implantable glucose sensors." *Biomaterials* **2014,** *35*, 9563-9572.

(10) Zhao, Q.; Topham, N.; Anderson, J. M.; Hiltner, A.; Lodoen, G.; Payet, C. R. "Foreign-body giant cells and polyurethane biostability: In vivo correlation of cell adhesion and surface cracking." *Journal of Biomedical Materials Research* **1991,** *25*, 177-183.

(11) Christenson, E. M.; Anderson, J. M.; Hiltner, A. "Oxidative mechanisms of poly(carbonate urethane) and poly(ether urethane) biodegradation: In vivo and in vitro correlations." *Journal of Biomedical Materials Research Part A* **2004,** *70A*, 245-255.

(12) Wilson, G. S.; Johnson, M. A. "In-vivo electrochemistry: What can we learn about living systems?" *Chemical Reviews* **2008,** *108*, 2462-2481.

(13) Sharkawy, A. A.; Klitzman, B.; Truskey, G. A.; Reichert, W. M. "Engineering the tissue which encapsulates subcutaneous implants. I. Diffusion properties." *Journal of Biomedical Materials Research Part A* **1997,** *37*, 401-412.

(14) Sharkawy, A. A.; Klitzman, B.; Truskey, G. A.; Reichert, W. M. "Engineering the tissue which encapsulates subcutaneous implants. II. Plasma-tissue exchange properties." *Journal of Biomedical Materials Research Part A* **1998,** *40*, 586-597.

(15) Williams, D. F. "On the mechanisms of biocompatibility." *Biomaterials* **2008,** *29*, 2941-2953.

(16) Brodbeck, W. G.; Shive, M. S.; Colton, E.; Nakayama, Y.; Matsuda, T.; Anderson, J. M. "Influence of biomaterial surface chemistry on the apoptosis of adherent cells." *Journal of Biomedical Materials Research* **2001,** *55*, 661-668.

(17) Brown, B. N.; Ratner, B. D.; Goodman, S. B.; Amar, S.; Badylak, S. F. "Macrophage polarization: An opportunity for improved outcomes in biomaterials and regenerative medicine." *Biomaterials* **2012,** *33*, 3792-3802.

(18) Vallejo-Heligon, S. G.; Brown, N. L.; Reichert, W. M.; Klitzman, B. "Porous, dexamethasone-loaded polyurethane coatings extend performance window of implantable glucose sensors in vivo." *Acta Biomaterialia* **2016,** *30*, 106-115.

(19) Vallejo-Heligon, S. G.; Klitzman, B.; Reichert, W. M. "Characterization of porous, dexamethasone-releasing polyurethane coatings for glucose sensors." *Acta Biomaterialia* **2014,** *10*, 4629-38.

(20) Kastellorizios, M.; Papadimitrakopoulos, F.; Burgess, D. J. "Multiple tissue response modifiers to promote angiogenesis and prevent the foreign body reaction around subcutaneous implants." *Journal of Controlled Release* **2015,** *214*, 103-111.

(21) Hetrick, E. M.; Prichard, H. L.; Klitzman, B.; Schoenfisch, M. H. "Reduced foreign body response at nitric oxide-releasing subcutaneous implants." *Biomaterials* **2007,** *28*, 4571-4580.

(22) Nichols, S. P.; Koh, A.; Brown, N. L.; Rose, M. B.; Sun, B.; Slomberg, D. L.; Riccio, D. A.; Klitzman, B.; Schoenfisch, M. H. "The effect of nitric oxide surface flux on the foreign body response to subcutaneous implants." *Biomaterials* **2012,** *33*, 6305-6312.

(23) Nichols, S. P.; Le, N. N.; Klitzman, B.; Schoenfisch, M. H. "Increased in vivo glucose recovery via nitric oxide release." *Analytical Chemistry* **2011,** *83*, 1180-1184.

(24) Soto, R. J.; Privett, B. J.; Schoenfisch, M. H. "In vivo analytical performance of nitric oxide-releasing glucose biosensors." *Analytical Chemistry* **2014,** *86*, 7141-7149.

(25) Dulak, J.; Jozkowicz, A.; Dembinska-Kiec, A.; Guevara, I.; Zdzienicka, A.; Zmudzinska-Grochot, D.; Florek, I.; Wojtowicz, A.; Szuba, A.; Cooke, J. P. "Nitric oxide induces the synthesis of vascular endothelial growth factor by rat vascular smooth muscle cells." *Arteriosclerosis, Thrombosis, and Vascular Biology* **2000,** *20*, 659-666.

(26) Inoue, N.; Venema, R. C.; Sayegh, H. S.; Ohara, Y.; Murphy, T. J.; Harrison, D. G. "Molecular regulation of the bovine endothelial cell nitric oxide synthase by transforming growth factor-β 1." *Arteriosclerosis, Thrombosis, and Vascular Biology* **1995,** *15*, 1255-1261.

(27) Cooke, J. P. "NO and angiogenesis." *Atherosclerosis Supplements* **2003,** *4*, 53-60.

(28) Cooke, J. P.; Losordo, D. W. "Nitric oxide and angiogenesis." *Circulation* **2002,** *105*, 2133-2135.

(29) Deakin, A. M.; Payne, A. N.; Whittle, B. J.; Moncada, S. "The modulation of IL-6 and TNF-α release by nitric oxide following stimulation of J774 cells with LPS and IFN-γ." *Cytokine* **1995,** *7*, 408-416.

(30) Wetzler, C.; Kampfer, H.; Pfeilschifter, J.; Frank, S. "Keratinocyte-derived chemotactic cytokines: Expressional modulation by nitric oxide in vitro and during cutaneous wound repair in vivo." *Biochemical and Biophysical Research Communications* **2000,** *274*, 689-696.

(31) Bogdan, C. "Nitric oxide and the immune response." *Nature Immunology* **2001,** *2*, 907-916.

(32) MacMicking, J.; Xie, Q. W.; Nathan, C. "Nitric oxide and macrophage function." *Annual Review of Immunology* **1997,** *15*, 323-350.

(33) Gifford, R.; Batchelor, M. M.; Lee, Y.; Gokulrangan, G.; Meyerhoff, M. E.; Wilson, G. S. "Mediation of in vivo glucose sensor inflammatory response via nitric oxide release." *Journal of Biomedical Materials Research Part A* **2005,** *75*, 755-66.

(34) Schaper, N. C.; Apelqvist, J.; Bakker, K. "Reducing lower leg amputations in diabetes: A challenge for patients, healthcare providers and the healthcare system." *Diabetologia* **2012,** *55*, 1869-1872.

(35) Fahey, T. J.; Sadaty, A.; Jones, W. G.; Barber, A.; Smoller, B.; Shires, G. T. "Diabetes impairs the late inflammatory response to wound healing." *Journal of Surgical Research* **1991,** *50*, 308-313.

(36) Vinik, A. I.; Maser, R. E.; Mitchell, B. D.; Freeman, R. "Diabetic autonomic neuropathy." *Diabetes Care* **2003,** *26*, 1553-1579.

(37) Witte, M. B.; Kiyama, T.; Barbul, A. "Nitric oxide enhances experimental wound healing in diabetes." *The British Journal of Surgery* **2002,** *89*, 1594-1601.

(38) Le, N. N.; Rose, M. B.; Levinson, H.; Klitzman, B. "Implant healing in experimental animal models of diabetes." *Journal of Diabetes Science and Technology* **2011,** *5*, 605-618.

(39) Soto, R. J.; Yang, L.; Schoenfisch, M. H. "Functionalized mesoporous silica via an aminosilane surfactant ion exchange reaction: Controlled scaffold design and nitric oxide release." *ACS Applied Materials and Interfaces* **2016,** *8*, 2220-2231.

(40) Riccio, D. A.; Nugent, J. L.; Schoenfisch, M. H. "Stöber synthesis of nitric oxide-releasing *S*-nitrosothiol-modified silica particles." *Chemistry of Materials* **2011,** *23*, 1727-1735.

(41) Koschwanez, H. E.; Yap, F. Y.; Klitzman, B.; Reichert, W. M. "In vitro and in vivo characterization of porous poly-L-lactic acid coatings for subcutaneously implanted glucose sensors." *Journal of Biomedical Materials Research Part A* **2008,** *87*, 792-807.

(42) Keefer, L. K. "Fifty years of diazeniumdiolate research. From laboratory curiosity to broad-spectrum biomedical advances." *ACS Chemical Biology* **2011,** *6*, 1147-1155.

(43) Wilson, G. S.; Ammam, M. "In vivo biosensors." *FEBS Journal* **2007,** *274*, 5452-5461.

(44) Wilson, G. S.; Gifford, R. "Biosensors for real-time in vivo measurements." *Biosensors and Bioelectronics* **2005,** *20*, 2388-2403.

(45) Chen, G.; Roy, I.; Yang, C.; Prasad, P. N. "Nanochemistry and nanomedicine for nanoparticle-based diagnostics and therapy." *Chemical Reviews* **2016,** *116*, 2826-2885.

(46) Kusaka, T.; Nakayama, M.; Nakamura, K.; Ishimiya, M.; Furusawa, E.; Ogasawara, K. "Effect of silica particle size on macrophage inflammatory responses." *PLoS One* **2014,** *9*, e92634.

(47) Waters, K. M.; Masiello, L. M.; Zangar, R. C.; Tarasevich, B. J.; Karin, N. J.; Quesenberry, R. D.; Bandyopadhyay, S.; Teeguarden, J. G.; Pounds, J. G.; Thrall, B. D. "Macrophage responses to silica nanoparticles are highly conserved across particle sizes." *Toxicological Sciences* **2009,** *107*, 553-569.

(48) Koschwanez, H. E.; Reichert, W. M. "In vitro, in vivo, and post-explantation testing of glucose-detecting biosensors: Current methods and recommendations." *Biomaterials* **2007,** *28*, 3687–3703.

(49) Larsen, M. O.; Rolin, B. "Use of the Göttingen minipig as a model of diabetes, with special focus on type 1 diabetes research." *ILAR Journal* **2004,** *45*, 303–313.

(50) Swindle, M. M.; Makin, A.; Herron, A. J.; Clubb, F. J.; Frazier, K. S. "Swine as models in biomedical research and toxicology testing." *Veterinary Pathology* **2012,** *49*, 344–356.

(51) Bellinger, D. A.; Merricks, E. P.; Nichols, T. C. "Swine models of type 2 diabetes mellitus: Insulin resistance, glucose tolerance, and cardiovascular complications." *ILAR Journal* **2006,** *47*, 243-58.

(52) Wang, Y.; Papadimitrakopoulos, F.; Burgess, D. J. "Polymeric "smart" coatings to prevent foreign body response to implantable biosensors." *Journal of Controlled Release* **2013,** *169*, 341-347.

(53) Chu, A. J.; Prasad, J. K. "Up-regulation by human recombinant transforming growth factor β-1 of collagen production in cultured dermal fibroblasts is mediated by the inhibition of nitric oxide signaling." *Journal of the American College of Surgeons* **1999,** *188*, 271-280.

(54) Socarras, T. O.; Vasconcelos, A. C.; Campos, P. P.; Pereira, N. B.; Souza, J. P.; Andrade, S. P. "Foreign body response to subcutaneous implants in diabetic rats." *PLoS One* **2014,** *9,* e110945.

(55) Thomson, S. E.; McLennan, S. V.; Hennessy, A.; Boughton, P.; Bonner, J.; Zoellner, H.; Yue, D. K.; Twigg, S. M. "A novel primate model of delayed wound healing in diabetes: Dysregulation of connective tissue growth factor." *Diabetologia* **2010,** *53,* 572-83.

(56) Sharkawy, A. A.; Klitzman, B.; Truskey, G. A.; Reichert, W. M. "Engineering the tissue which encapsulates subcutaneous implants. III. Effective tissue response times." *Journal of Biomedical Materials Research Part A* **1998,** *40,* 598-605.

(57) Paul, D. W.; Stenken, J. A. "A review of flux considerations for in vivo neurochemical measurements." *Analyst* **2015,** *140,* 3709-3730.

(58) Brem, H.; Tomic-Canic, M. "Cellular and molecular basis of wound healing in diabetes." *The Journal of Clinical Investigation* **2007,** *117,* 1219-1222.

(59) van der Zee, R.; Murohara, T.; Luo, Z.; Zollmann, F.; Passeri, J.; Lekutat, C.; Isner, J. M. "Vascular endothelial growth factor/vascular permeability factor augments nitric oxide release from quiescent rabbit and human vascular endothelium." *Circulation* **1997,** *95,* 1030-1037.

CHAPTER 6. SUMMARY AND FUTURE DIRECTIONS

6.1. Summary of dissertation research

Nitric oxide-releasing materials have been shown to mitigate FBR-associated inflammation and collagen deposition,[1-2] both of which are key parameters that negatively impact the in vivo function of glucose biosensors.[3-6] My research has focused broadly on how NO release might alter the analytical performance of such biosensors. In Chapter 2, the first 10-day in vivo sensor performance studies are described. Two separate NO-releasing glucose sensors were shown to have improved accuracy and greater glucose sensitivity compared to analogous controls during an initial 3 d implantation period. An especially important outcome of this study was that sensors with short-term NO-release properties (~16 h NO-release durations) were unable to maintain acceptable accuracy after longer (>3 d) durations in vivo. In contrast, sensors that released NO for 3.1 d exhibited consistent MARD and lag times during the entire 10 d implantation period, emphasizing the potential importance of long-term NO release. Collectively, this research validated that the reduced FBR to NO-releasing polymer coatings translates to perceptible improvements to in vivo glucose sensor analytical performance.

Despite promising initial in vivo sensor data, many aspects of the NO-releasing glucose sensors demanded improvements, particularly with respect to the NO-releasing membrane technology. Critical shortcomings associated with the *N*-diazeniumdiolate-modified silica filler particles, including low NO storage (<0.6 μmol mg^{-1}) and NO-release durations (<12 h),[7-11] ultimately limited NO release from glucose sensor membranes to a timeframe (~2–3 d)

insufficient for mitigating the long-term FBR. In Chapter 3, an interfacial ion exchange reaction between cationic aminosilanes and the quaternary-ammonium surfactant cetrimonium bromide was exploited to functionalize mesoporous silica with secondary amines for subsequent conversion to *N*-diazeniumdiolate NO donors. The resulting materials stored 2–5× more NO than previous silica particles.[7-11] The ion exchange reaction approach was compatible with a diverse selection of particle sizes and aminosilane precursors, permitting exact control over physical morphology and NO-release kinetics. Particle systems based on the DET/NO modification were capable of ~40 h of continuous NO release and proved indispensable for the tissue biocompatibility studies described in Chapter 5.

The approach developed in Chapter 3 for the synthesis of NO-releasing silica particles was adapted to the systematic study of particle leaching from PU membranes in Chapter 4. The use of low-water uptake PU membranes resulted in negligible particle leaching. However, the hydrophobic membranes were incompatible as glucose sensor membranes due to poor glucose permeability. Polyurethanes with greater water uptake facilitated improved glucose partitioning into the membranes, yet leached considerable levels of NO donor-modified silica. Careful study of more hydrophilic PU membranes revealed that the zwitterionic *N*-diazeniumdiolate moiety was largely responsible for particle leaching from glucose sensor coatings. The dependence of particle leaching on the extent of NO donor modification and PU water uptake indicated that the leaching process was mediated by membrane hydration. This assertion was further confirmed in subsequent leaching experiments using NO-releasing particles with electrically neutral *S*-nitrosothiol NO donors. Particles with a substantial degree of alkanethiol modification ($\geq$75% relative to the backbone silane) did not leach from the membranes, regardless of polyurethane water uptake. These membranes were thus adapted to serve as the NO-releasing glucose

diffusion-limiting coating for subsequent, next-generation electrochemical glucose biosensors. The optimized sensors were capable of releasing NO for 7 d (i.e., 2–3× greater NO-release durations than previous systems) and retained suitable analytical performance merits required for in vivo glucose sensing.

The *N*-diazeniumdiolate and *S*-nitrosothiol particles that were employed in Chapters 3 and 4 were utilized to study the FBR in a streptozotocin-induced diabetic swine model. This work was described in Chapter 5. Induction of diabetes produced several key pathological differences in the FBR, including a more severe chronic inflammatory response, inhibited angiogenesis, and arrested collagen deposition. Materials capable of 7–13 d NO release reduced inflammation and increased blood vessel densities in the surrounding tissue, largely counteracting the FBR and wound-healing deficiencies associated with chemically-induced diabetes.

6.2. Future directions

6.2.1. Hydrophobic surface modification of N-diazeniumdiolate-based silica particles

The utility of the the *N*-diazeniumdiolate-based particles (Chapter 3) as membrane dopants is restricted to low-water uptake polyurethanes (e.g., TT-2072D-B20, PC-3585A; water uptake <0.01 mg per mg of polyurethane), as the particles leached from more hydrophilic polymers. Based on the hydrogen bonding and coulombic interactions between the particle and water molecules promoting leaching, hydrophobic modifications to the particle may lessen this effect by interfering with the surface hydration layer. In a preliminary study, Carpenter et al. grafted alkyl chains to the surface of pre-formed silica particles modified with the aminosilane *N*-(6-aminohexyl)aminopropyltrimethoxysilane (AHAP).[12] Following the alkyl chain modification step, the particles were reacted with NO to form *N*-diazeniumdiolate NO donors.

Ethyl and isobutyl chain-modified AHAP/NO particles leached up to 75% less from Tecoplast (TP-470) polyurethane materials than the corresponding particles without alkyl chains. Unfortunately, the already limited NO storage of the AHAP/NO particles (0.28 μmol mg^{-1}) was further reduced by the alkyl chain modification process to values insufficient for use as sensor membrane dopants ($\leq$0.1 μmol mg^{-1}). The NO-releasing particles developed in Chapter 3 store 3–8× more NO than the those described by Carpenter et al.,[12] regardless of the aminosilane modification. Thus, these scaffolds are more likely to retain suitable NO storage after hydrophobic modification.

The strategy employed by Carpenter et al.[12] relied on reacting alkylsilanes with residual silanol groups on the surface of the AHAP-modified silica particles. However, the alkyl chain grafting procedure was not optimized. Reactant (i.e., silane) concentration, solvent system, and reaction temperature are all important parameters that should be studied for their impact to modification efficiency, NO-release kinetics, and leaching. The selection of hydrophobic silane modifications should also be expanded to include fluorosilanes of varying alkyl chain lengths and fluorine content. Ideally, these studies should be carried out using particles with a range of amine modifications (e.g., MAP, AHAP, DET, AEAP) as the extent of hydrophobic modification may depend on aminosilane identity.

Surface analysis (i.e., X-ray photoelectron spectroscopy) and bulk chemical methods (e.g., elemental analysis, solid-state $^{13}C/^{19}F/^{29}Si$ cross- or direct-polarization magic angle spinning nuclear magnetic resonance spectroscopy) should be utilized to confirm successful modification as a function of the silane identity and reaction conditions (e.g., solvent system). After verifying incorporation of the hydrophobic modifications, NO-release measurements and leaching assays should be carried out in a similar manner to the experiments outlined in Chapters

3 and 4. Special care should be taken to evaluate particle leaching with respect to PU identity and the mass of the particles incorporated into the membranes, as leaching is especially sensitive to both parameters.

6.2.2. Improving the handling and storage stability of S-nitrosothiol-based particles

The RSNO-based silica particles described in Chapter 4 (75% MPTMS/TEOS) were unique in that they did not leach from any of the polyurethane materials tested. Unfortunately, the primary *S*-nitrosothiol-based materials (i.e., *S*-nitrosothiols with an unsubstituted α-carbon) are susceptible to numerous degradation triggers during synthesis, necessitating careful handling. For example, special precaution was taken to avoid Cu^{+}-mediated RSNO degradation by supplementing synthesis solvents with metal chelators.[13] Similarly, RSNOs readily degrade upon exposure to visible/ultraviolet light or even during room temperature handling steps (thermal pathway), although decomposition was minimized by performing wash steps in the dark and at low temperatures (e.g., using -20 ^{o}C MeOH).[14] However, even small amounts of NO generated during synthesis/handling (regardless of the mechanism) may react with atmospheric oxygen to form nitrogen trioxide, a RSNO-reactive chemical species that initiates rapid autocatalytic decomposition. *S*-nitrosothiol-based membranes/sensors must thus be stored cold ($\leq$-20 ^{o}C) and devoid of molecular oxygen.

Future research efforts should thus strive to improve upon the handling/storage stability of RSNO-modified particles, while simultaneously maintaining suitable NO storage and low particle leaching. One potential strategy to produce more stable primary RSNO-based particles is to alter the particle porosity (i.e., mesoporous rather than nonporous) or the method of MPTMS (thiol) incorporation. Either of these methods could potentially alter transnitrosation reaction rates and RSNO "cage effects," in turn affecting RSNO decomposition kinetics.[15-17] Use of a

mesoporous silica scaffold may provide more versatility in terms of introducing thiol functionalities through either surface grafting or co-condensation strategies to achieve sufficient NO storage (>0.6 μmol mg^{-1}). Thiol incorporation, as measured by an elemental analyzer, should be evaluated as a function of solvent choice, reaction temperature, and reagent concentrations. Furthermore, these parameters are likely to influence the spatial orientation of individual thiols over the silica scaffold (i.e., clustered groups versus homogeneously distributed), thereby affecting storage stability and NO-release kinetics of the particles.

The chemical structure of the RSNO readily impacts storage and NO-release kinetics.[18] Primary RSNOs (e.g., the nitrosated form of MPTMS) degrade rapidly at room temperature or upon exposure to light.[18-19] Both RSNO decomposition triggers provide sufficient energy for homolytic cleavage of the S–N bond, yielding NO and a thiyl radical. It is generally believed that dimerization between two thiyl radicals, forming a disulfide, is required to prevent recombination with NO.[18-21] Tertiary RSNOs, characterized by a disubstituted α-carbon, are more stable than their primary RSNO counterparts. Bulky alkyl substitutions to the α-carbon increase the steric hindrance surrounding the sulfur atom, decreasing the likelihood of dimerization between thiyl radicals and thus promoting recombination with NO.[18,20-21] Bainbrigge et al.[20] suggested that electron-donating groups at the α-carbon also decrease the lability of the S–N bond. The authors demonstrated that temperatures in excess of 148 ^{o}C were required to initiate breakdown of the tertiary RSNO *S*-nitroso-*N*-acetylpenicillamine (SNAP). Goudie et al. developed SNAP-doped polyurethane membranes that retained >90% NO after 6 months storage at room temperature, confirming the stability of the tertiary RSNO.[22]

Based on prior work,[18,20-23] modification of silica particles with tertiary RSNOs represents an attractive option to improve the storage stability of these materials. Unfortunately,

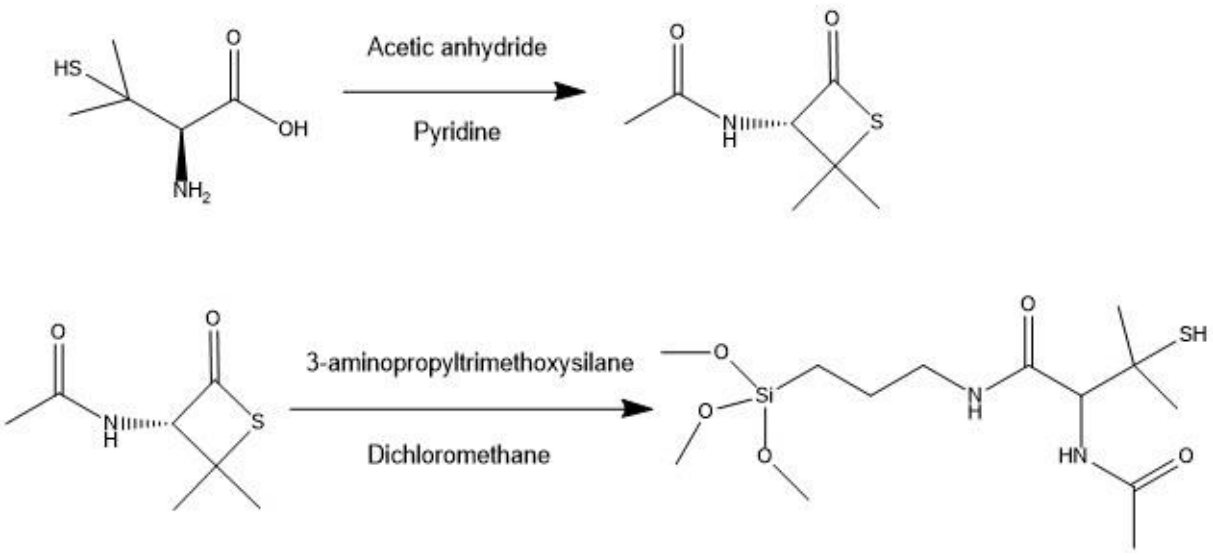

Figure 6.1. Synthesis of *N*-acetylpenicillamine**propyltrimethoxysilane** from penicillamine and 3-aminopropyltrimethoxysilane.

few mercaptosilanes are commercially available, necessitating the synthesis of new silanes intended for use as NO donors. Riccio and coworkers reported on the design of a tertiary thiol-based mercaptosilane (*N*-acetylpenicillaminepropyltrimethoxysilane; NAPTMS) based on the reaction between *N*-acetyl penicillamine and 3-aminopropyltrimethoxysilane (Figure 6.1).[23] This silane may be grafted to the surface of bare mesoporous silica or incorporated into the particle backbone via a co-condensation approach. However, a potential difficulty noted by Riccio et al.[23] is the relatively slow hydrolysis/co-condensation reactions between NAPTMS and typical backbone silanes (e.g., tetraethoxysilane, tetramethoxysilane, methyltrimethoxysilane). Particle synthesis strategies relying co-condensation will therefore likely fail to form monodisperse particles and/or result in low NAPTMS incorporation. Surface grafting of NAPTMS to bare mesoporous silica represents a more promising initial approach, but will require careful optimization of grafting conditions (e.g., solvent, base catalyst amounts, temperature) for reproducible modification.

6.2.3. Molecular and cellular basis for the anti-inflammatory capacities of NO

The NO-releasing materials evaluated in Chapter 5 proved useful for reducing FBR-related inflammation in both healthy and diabetic swine. Although NO's involvement in angiogenesis is well-understood, less is known about its anti-inflammatory properties. Nitric oxide has been implicated as a mediator of chemokine/cytokine production (e.g., tumor necrosis factor-α, macrophage chemoattractant protein-1, interleukin-1β).[24-25] This evidence notwithstanding, the physiological basis for the reduced inflammation to NO-releasing materials remains inconclusive. Therefore, research that seeks to elucidate the molecular and cellular mechanisms behind NO's anti-inflammatory capacities represents an important and exciting route of future study.

As outlined in Chapter 1, the phenotypes of inflammatory cells (e.g., mast cells, macrophages) appear to be strong determinants of FBR severity. Studies by Avula et al.[26-28] and Klueh et al.[29] highlighted the critical roles of tissue mast cells during the acute inflammatory response (1–3 d) in orchestrating infiltration of the implant by neutrophils/macrophages and, ultimately, collagen capsule formation. Macrophage functional polarization has also been identified as a key parameter in the chronic inflammatory response ($\geq$5 d) to in vivo glucose sensors.[30-39] For example, pro-inflammatory macrophages consume large amounts of glucose and oxygen at the sensor surface, contributing to erratic glucose sensor response.[38] Products of macrophage phagocytic activity may also reduce the local pH[40] and damage sensor coatings.[41] Based on the reduced inflammatory response to NO-releasing polymers (described in Chapter 5), NO may influence mast cell and macrophage activity during the FBR. This hypothesis is in agreement with previous studies that implicated NO as a mediator of inflammatory cell chemotaxis.[24-25]

Future work should use in vitro and in vivo models to evaluate inflammatory cell phenotypes after treatment with exogenous NO. Novak et al. designed an in vitro platform to examine macrophage glucose consumption in a glucose sensor FBR model.[38] The authors immobilized RAW 264.7 murine macrophages in an extracellular matrix gel surrounding electrochemical glucose biosensors. Macrophages in the gel were polarized toward a pro-inflammatory phenotype (by exposure to lipopolysaccharide) to increase glucose metabolism, eliciting a concomitant decrease in glucose concentrations detected by the sensor. The authors also showed that anti-inflammatory macrophages (stimulated with genistein) only produced a slight decrease in the sensor signal due to less overall glucose consumption. Although the assay relies on glucose metabolism as an indirect indicator of macrophage phenotype, such an

approach may be a useful starting point for determining if NO alters macrophage polarization. Macrophages self-regulate pro-inflammatory activity (e.g., expression of major histocompatibility complex class II, phagocytic activity) via generation of NO,[42-44] suggesting that glucose metabolism may also be affected. The proposed studies should be carried out similarly to those described by Novak et al.[38] using the NO-releasing sensor that was developed in Chapter 4. Alternatively, non-NO-releasing glucose sensors may be used for these studies, instead exposing macrophages to NO donors (e.g., SNAP, *N*-diazeniumdiolate-modified spermine) prior to or during the assay. Treatment with free NO donors (rather than using the NO-releasing glucose sensors) allows for NO concentrations and NO-release kinetics to be straightforwardly controlled and evaluated as parameters in relation to macrophage polarization. Additionally, experiments involving macrophages that are "pre-polarized" to pro-inflammatory or anti-inflammatory states (i.e., with interferon-γ/lipopolysaccharide or interleukin-10, respectively) should be carried out to determine if NO may induce phenotypic switching.

Although in vitro studies may reveal mechanisms through which NO exerts its anti-inflammatory effects, these experiments are limited to single-cell cultures and do not accurately recapitulate the inherent complexities of the FBR (e.g., multiple infiltrating cell types, cellular communication mechanisms). As such, positive or negative results that are obtained in benchtop studies will need to be validated in an appropriate animal model (i.e., diabetic swine). Similar to the work described in Chapter 5, immunohistochemical staining may be used to identify key cell surface markers and cytokines (e.g., tumor necrosis factor-α, interferon-γ, macrophage chemoattractant protein-1, and interleukin-10) at NO-releasing subcutaneous implants, although quantification via this approach will not be possible. Future studies should utilize implanted microdialysis probes for cytokine quantitation. Microdialysis probes are percutaneous implants

with diameters of approximately 200–300 μm and thus elicit a similar FBR to needle-type glucose sensors. Moreover, microdialysis allows for direct recovery of cytokines in the probe perfusate solution for offline quantification (e.g., via enzyme-linked immunosorbent assay). Microdialysis has been used successfully for monitoring cytokine production during the acute (1–3 d) inflammatory response and would be a useful tool to study potential cytokine regulation by NO. Nichols et al.[45] demonstrated the ability to release near constant NO fluxes (~162 pmol cm^{-2} s^{-1}) from microdialysis probes by using NO-saturated buffer as the perfusate solution. A similar design could be employed for cytokine recovery experiments. Nitric oxide fluxes from the microdialysis probes could be tuned by altering the NO concentration in the perfusate solution, thereby permitting the study cytokine levels in relation to NO levels generated from the probes. A caveat to this approach, however, is that cytokine quantitation via microdialysis cannot be relied upon after ~3 d, as inflammation and collagen deposition may alter cytokine diffusion in the immediate vicinity of the probe. A reduced FBR at the NO-releasing probes would thus confound any potential differences in cytokine production. Nevertheless, the proposed study would aid in identifying key mechanisms behind NO's anti-FBR capabilities.

6.2.4. In vivo glucose sensor analytical performance evaluation in diabetic swine

Although NO release reduced inflammation and improved angiogenesis in diabetic swine (Chapter 5), collagen deposition appeared to be unaffected. As such, it is unclear if the in vivo glucose sensor performance benefits associated with NO release will be preserved in a diabetic animal model. These studies should be carried out similarly to the research described in Chapter 2, instead utilizing streptozotocin-treated pigs as the diabetic animal model. The optimized glucose sensor membranes developed in Chapter 4 will ultimately prove useful for carrying out this research.

A critical experimental parameter that must be carefully considered prior to in vivo sensor testing is the method for blood glucose administration. Bolus glucose administration (0.7 g kg^{-1}), although reproducible and effective for achieving severe hyperglycemia, can be overly demanding as the sensor is challenged greater than normal glucose excursion rates (typical values 0–2 mg dL^{-1} min^{-1}).[46] Although the in vitro sensor response time may be sufficient for tracking rapid changes in glucose concentrations, the literature suggests the existence of a physiological glucose lag arising from passive transport from the vascular to the sensor site.[40] A similar sensor lag (~3–11 min) was determined for the sensor systems that were studied in Chapter 2. As such, rapid glucose administration risks inflated sensor error calculation and masking of potential beneficial effects of NO (Figure 6.2). Intraperitoneal glucose injections are routinely used to manipulate BG levels in smaller animals (i.e., rats and mice) to circumvent difficulties in intravenous administration. Although larger glucose doses must be administered (≥1.5 g kg^{-1}) to achieve hyperglycemia, the slower rate of glucose absorption may better approximate normal, gradual BG fluctuations in diabetic patients, thereby increasing the relevance of sensor accuracy data at the cost of reproducibility. Another potential route to gradual glucose administration is to deliver dilute glucose solutions via constant rate infusion using an intravascular catheter. Regardless of the glucose delivery method, the glucose dose must be determined carefully so that adequate amounts of data are obtained in both the euglycemic and hyperglycemic regime for proper sensor evaluation. Excursions into the hypoglycemic BG range via insulin administration would also provide valuable sensor performance data.

A limitation of the research presented in Chapter 2 is that the tissues surrounding the percutaneous sensors were not examined using standard tissue histology. The previous

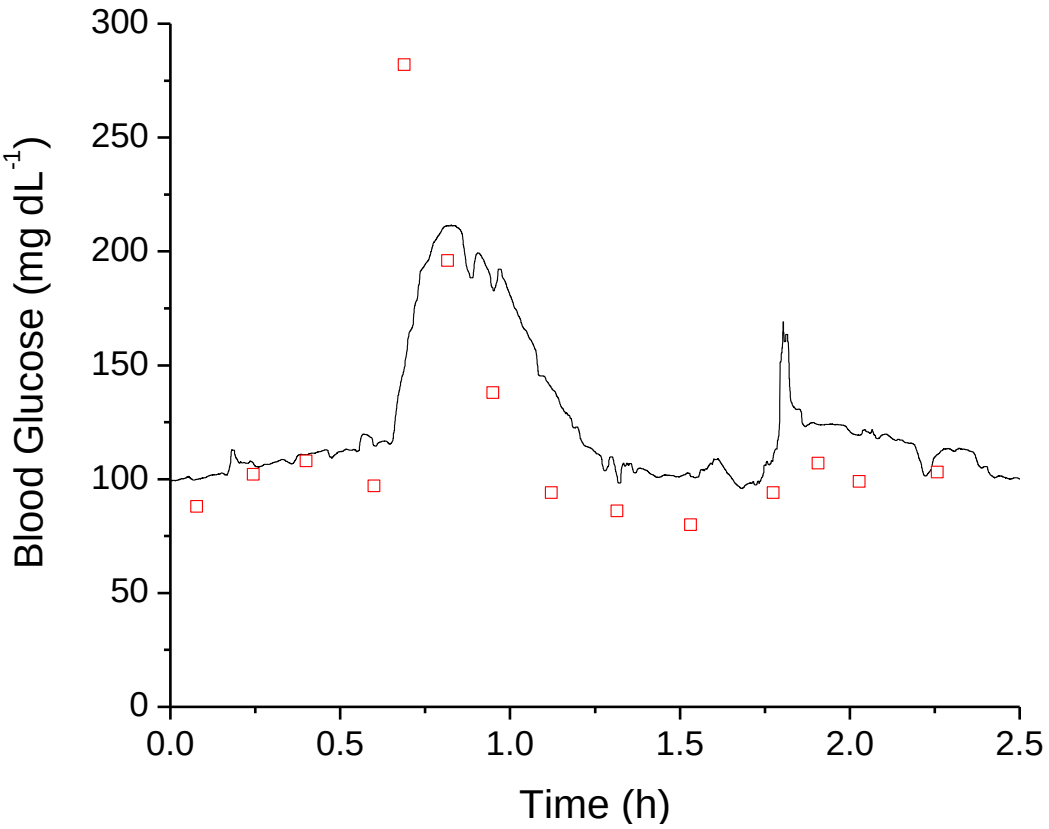

Figure 6.2. Graph depicting paired reference glucose measurements (red, squares) and corresponding implanted CGM trace (black line) after IV glucose administration in a swine model. While the direct measurement of glucose using a handheld glucometer indicated an increase in BG, the sensor was unable to accurately track rapid fluctuations in BG. The BG maximum detected by the continuous sensor was thus both delayed in time and attenuated in magnitude.

investigations by Hetrick et al.,[1] Nichols et al.,[2] and this dissertation research all utilized subcutaneous implants not subject to the tethering forces associated with percutaneous sensors. As such, it is possible that the tissue biocompatibility benefits of NO in the diabetic swine model may be counteracted by shear interactions related to sensor micromotion. Future in vivo sensor assessments should perform tissue histology at discrete timepoints and consider trends in sensor performance alongside quantitative collagen deposition and inflammation data.

Finally, the few quantitative sensor evaluations described to date are limited in duration ($\leq$10 d).[47-48] By comparison, the NO-releasing materials that were evaluated in Chapter 5 exhibited low grades of inflammation and collagen deposition even after 25 d, suggesting potential benefit to in vivo sensor performance at implant periods beyond 10 d. Accordingly, future research should extend in vivo sensor evaluation to similar durations. Sensor data should be analyzed with respect to failure rates (i.e., survival analysis), in addition to standard numerical accuracy metrics (i.e., mean absolute relative deviation).

6.3. Conclusions

The FBR is the primary obstacle to reliable subcutaneous glucose sensing. The research described in this dissertation carried the concept of the NO-releasing glucose sensor from a laboratory curiosity to a formidable potential CGM technology. Initial evidence of a reduced FBR associated with NO-releasing polymers was shown to translate to greater in vivo glucose sensor accuracy. Membranes with suitable NO-release properties for mitigating the FBR and minimal particle leaching were adapted to prepare functional glucose biosensors. However, it was unclear if the same optimal NO-release kinetics would maintain desirable FBR qualities (i.e., low inflammation and collagen deposition) in diabetic tissue. Deficient wound healing and delayed inflammation are known qualities of diabetic wounds that also manifest in the presence

of an implantable glucose sensor, ultimately coalescing in an unfavorable in vivo sensing environment. Nitric oxide-releasing polymer membranes proved capable of counteracting the exacerbated FBR associated with diabetes and thus hold great promise as materials for in vivo glucose sensing.

REFERENCES

(1) Hetrick, E. M.; Prichard, H. L.; Klitzman, B.; Schoenfisch, M. H. "Reduced foreign body response at nitric oxide-releasing subcutaneous implants." *Biomaterials* **2007,** *28*, 4571-4580.

(2) Nichols, S. P.; Koh, A.; Brown, N. L.; Rose, M. B.; Sun, B.; Slomberg, D. L.; Riccio, D. A.; Klitzman, B.; Schoenfisch, M. H. "The effect of nitric oxide surface flux on the foreign body response to subcutaneous implants." *Biomaterials* **2012,** *33*, 6305-6312.

(3) Novak, M. T.; Yuan, F.; Reichert, W. M. "Modeling the relative impact of capsular tissue effects on implanted glucose sensor time lag and signal attenuation." *Analytical and Bioanalytical Chemistry* **2010,** *398*, 1695-1705.

(4) Sharkawy, A. A.; Klitzman, B.; Truskey, G. A.; Reichert, W. M. "Engineering the tissue which encapsulates subcutaneous implants. I. Diffusion properties." *Journal of Biomedical Materials Research Part A* **1997,** *37*, 401-412.

(5) Sharkawy, A. A.; Klitzman, B.; Truskey, G. A.; Reichert, W. M. "Engineering the tissue which encapsulates subcutaneous implants. III. Effective tissue response times." *Journal of Biomedical Materials Research Part A* **1998,** *40*, 598-605.

(6) Sharkawy, A. A.; Klitzman, B.; Truskey, G. A.; Reichert, W. M. "Engineering the tissue which encapsulates subcutaneous implants. II. Plasma-tissue exchange properties." *Journal of Biomedical Materials Research Part A* **1998,** *40*, 586-597.

(7) Backlund, C. J.; Sergesketter, A. R.; Offenbacher, S.; Schoenfisch, M. H. "Antibacterial efficacy of exogenous nitric oxide on periodontal pathogens." *Journal of Dental Research* **2014,** *93*, 1089-1094.

(8) Carpenter, A. W.; Slomberg, D. L.; Rao, K. S.; Schoenfisch, M. H. "Influence of scaffold size on bactericidal activity of nitric oxide-releasing silica nanoparticles." *ACS Nano* **2011,** *5*, 7235-7244.

(9) Carpenter, A. W.; Worley, B. V.; Slomberg, D. L.; Schoenfisch, M. H. "Dual action antimicrobials: Nitric oxide release from quaternary ammonium-functionalized silica nanoparticles." *Biomacromolecules* **2012,** *13*, 3334-3342.

(10) Lu, Y.; Slomberg, D. L.; Sun, B.; Schoenfisch, M. H. "Shape- and nitric oxide flux-dependent bactericidal activity of nitric oxide-releasing silica nanorods." *Small* **2013,** *9*, 2189-2198.

(11) Slomberg, D. L.; Lu, Y.; Broadnax, A. D.; Hunter, R. A.; Carpenter, A. W.; Schoenfisch, M. H. "Role of size and shape on biofilm eradication for nitric oxide-releasing silica nanoparticles." *ACS Applied Materials and Interfaces* **2013,** *5*, 9322-9329.

(12) Carpenter, A. W.; Johnson, J. A.; Schoenfisch, M. H. "Nitric oxide-releasing silica nanoparticles with varied surface hydrophobicity." *Colloids and Surfaces A: Physicochemical and Engineering Aspects* **2014,** *454*, 144-151.

(13) McCarthy, C. W.; Guillory, R. J.; Goldman, J.; Frost, M. C. "Transition metal mediated release of nitric oxide (NO) from *S*-nitroso-*N*-acetylpenicillamine (SNAP): Potential applications for endogenous release of NO on the surface of stents via corrosion products." *ACS Applied Materials and Interfaces* **2016,** *8*, 10128–10135.

(14) Riccio, D. A.; Nugent, J. L.; Schoenfisch, M. H. "Stöber synthesis of nitric oxide-releasing *S*-nitrosothiol-modified silica particles." *Chemistry of Materials* **2011,** *23*, 1727-1735.

(15) Adachi, H.; Sonoki, H.; Hoshino, M.; Wakasa, M.; Hayashi, H.; Miyazaki, Y. "Photodissociation of nitric oxide from nitrosyl metalloporphyrins in micellar solutions." *The Journal of Physical Chemistry A* **2001,** *105*, 392-398.

(16) de Oliveira, M. G.; Shishido, S. M.; Seabra, A. B.; Morgon, N. H. "Thermal stability of primary s-nitrosothiols: Roles of autocatalysis and structural effects on the rate of nitric oxide release." *The Journal of Physical Chemistry A* **2002,** *106*, 8963-8970.

(17) Shishido, S. M.; Seabra, A. B.; Loh, W.; Ganzarolli de Oliveira, M. "Thermal and photochemical nitric oxide release from *S*-nitrosothiols incorporated in pluronic F127 gel: Potential uses for local and controlled nitric oxide release." *Biomaterials* **2003,** *24*, 3543-3553.

(18) Wang, P. G.; Xian, M.; Tang, X.; Wu, X.; Wen, Z.; Cai, T.; Janczuk, A. J. "Nitric oxide donors: Chemical activities and biological applications." *Chemical Reviews* **2002,** *102*, 1091-1134.

(19) Grossi, L.; Montevecchi, P. C. "A kinetic study of *S*-nitrosothiol decomposition." *Chemistry* **2002,** *8*, 380-387.

(20) Bainbrigge, N.; R. Butler, A.; Gorbitz, C. "The thermal stability of *S*-nitrosothiols: Experimental studies and ab initio calculations on model compounds." *Journal of the Chemical Society, Perkin Transactions* **1997,** *2*, 351-354.

(21) Lin, C.-E.; Richardson, S. K.; Wang, W.; Wang, T.; Garvey, D. S. "Preparation of functionalized tertiary thiols and nitrosothiols." *Tetrahedron* **2006,** *62*, 8410-8418.

(22) Goudie, M. J.; Brisbois, E. J.; Pant, J.; Thompson, A.; Potkay, J. A.; Handa, H. "Characterization of an *S*-nitroso-*N*-acetylpenicillamine-based nitric oxide releasing polymer from a translational perspective." *International Journal of Polymeric Materials* **2016,** *65*, 769-778.

(23) Riccio, D. A.; Coneski, P. N.; Nichols, S. P.; Broadnax, A. D.; Schoenfisch, M. H. "Photoinitiated nitric oxide-releasing tertiary *S*-nitrosothiol-modified xerogels." *ACS Applied Materials and Interfaces* **2012,** *4*, 796-804.

(24) Deakin, A. M.; Payne, A. N.; Whittle, B. J.; Moncada, S. "The modulation of IL-6 and TNF-α release by nitric oxide following stimulation of J774 cells with LPS and IFNγ." *Cytokine* **1995,** *7*, 408-416.

(25) Wetzler, C.; Kampfer, H.; Pfeilschifter, J.; Frank, S. "Keratinocyte-derived chemotactic cytokines: Expressional modulation by nitric oxide in vitro and during cutaneous wound repair in vivo." *Biochemical and Biophysical Research Communications* **2000,** *274*, 689-696.

(26) Avula, M.; Jones, D.; Rao, A. N.; McClain, D.; McGill, L. D.; Grainger, D. W.; Solzbacher, F. "Local release of masitinib alters in vivo implantable continuous glucose sensor performance." *Biosensors and Bioelectronics* **2016,** *77*, 149-156.

(27) Avula, M. N.; Rao, A. N.; McGill, L. D.; Grainger, D. W.; Solzbacher, F. "Modulation of the foreign body response to implanted sensor models through device-based delivery of the tyrosine kinase inhibitor, masitinib." *Biomaterials* **2013,** *34*, 9737-9746.

(28) Avula, M. N.; Rao, A. N.; McGill, L. D.; Grainger, D. W.; Solzbacher, F. "Foreign body response to subcutaneous biomaterial implants in a mast cell-deficient KIT(W-SH) murine model." *Acta Biomaterialia* **2014,** *10*, 1856-1863.

(29) Klueh, U.; Kaur, M.; Qiao, Y.; Kreutzer, D. L. "Critical role of tissue mast cells in controlling long-term glucose sensor function in vivo." *Biomaterials* **2010,** *31*, 4540-4551.

(30) Keeler, G. D.; Durdik, J. M.; Stenken, J. A. "Effects of delayed delivery of dexamethasone-21-phosphate via subcutaneous microdialysis implants on macrophage activation in rats." *Acta Biomaterialia* **2015,** *23*, 27-37.

(31) Sussman, E. M.; Halpin, M. C.; Muster, J.; Moon, R. T.; Ratner, B. D. "Porous implants modulate healing and induce shifts in local macrophage polarization in the foreign body reaction." *Annals of Biomedical Engineering* **2014,** *42*, 1508-1516.

(32) Zhang, L.; Cao, Z.; Bai, T.; Carr, L.; Ella-Menye, J. R.; Irvin, C.; Ratner, B. D.; Jiang, S. "Zwitterionic hydrogels implanted in mice resist the foreign-body reaction." *Nature Biotechnology* **2013,** *31*, 553-556.

(33) Garg, K.; Pullen, N. A.; Oskeritzian, C. A.; Ryan, J. J.; Bowlin, G. L. "Macrophage functional polarization (M1/M2) in response to varying fiber and pore dimensions of electrospun scaffolds." *Biomaterials* **2013,** *34*, 4439-4451.

(34) Gratchev, A.; Guillot, P.; Hakiy, N.; Politz, O.; Orfanos, C. E.; Schledzewski, K.; Goerdt, S. "Alternatively activated macrophages differentially express fibronectin and its splice variants and the extracellular matrix protein betaIg-H3." *Scandinavian Journal of Immunology* **2001,** *53*, 386-392.

(35) Mantovani, A.; Biswas, S. K.; Galdiero, M. R.; Sica, A.; Locati, M. "Macrophage plasticity and polarization in tissue repair and remodelling." *The Journal of Pathology* **2013,** *229*, 176-185.

(36) Mosser, D. M.; Edwards, J. P. "Exploring the full spectrum of macrophage activation." *Nature Review of Immunology* **2008,** *8*, 958-969.

(37) Murray, Peter J.; Allen, Judith E.; Biswas, Subhra K.; Fisher, Edward A.; Gilroy, Derek W.; Goerdt, S.; Gordon, S.; Hamilton, John A.; Ivashkiv, Lionel B.; Lawrence, T.; Locati, M.; Mantovani, A.; Martinez, Fernando O.; Mege, J.-L.; Mosser, David M.; Natoli, G.; Saeij, Jeroen P.; Schultze, Joachim L.; Shirey, Kari A.; Sica, A.; Suttles, J.; Udalova, I.; van Ginderachter, Jo A.; Vogel, Stefanie N.; Wynn, Thomas A. "Macrophage activation and polarization: Nomenclature and experimental guidelines." *Immunity* **2014,** *41*, 14-20.

(38) Novak, M. T.; Yuan, F.; Reichert, W. M. "Macrophage embedded fibrin gels: An in vitro platform for assessing inflammation effects on implantable glucose sensors." *Biomaterials* **2014,** *35*, 9563-9572.

(39) Zhu, L.; Zhao, Q.; Yang, T.; Ding, W.; Zhao, Y. "Cellular metabolism and macrophage functional polarization." *International Reviews of Immunology* **2015,** *34*, 82-100.

(40) Wilson, G. S.; Johnson, M. A. "In-vivo electrochemistry: What can we learn about living systems?" *Chemical Reviews* **2008,** *108*, 2462-2481.

(41) Zhao, Q.; Topham, N.; Anderson, J. M.; Hiltner, A.; Lodoen, G.; Payet, C. R. "Foreign-body giant cells and polyurethane biostability: In vivo correlation of cell adhesion and surface cracking." *Journal of Biomedical Materials Research* **1991,** *25*, 177-183.

(42) Swallow, C. J.; Grinstein, S.; Sudsbury, R. A.; Rotstein, O. D. "Nitric oxide derived from L-arginine impairs cytoplasmic ph regulation by vacuolar-type H+ ATPases in peritoneal macrophages." *The Journal of Experimental Medicine* **1991,** *174*, 1009-21.

(43) Sicher, S. C.; Vazquez, M. A.; Lu, C. Y. "Inhibition of macrophage Ia expression by nitric oxide." *Journal of Immunology* **1994,** *153*, 1293-1300.

(44) MacMicking, J.; Xie, Q. W.; Nathan, C. "Nitric oxide and macrophage function." *Annual Review of Immunology* **1997,** *15*, 323-350.

(45) Nichols, S. P.; Le, N. N.; Klitzman, B.; Schoenfisch, M. H. "Increased in vivo glucose recovery via nitric oxide release." *Analytical Chemistry* **2011,** *83*, 1180-1184.

(46) Kamath, A.; Mahalingam, A.; Brauker, J. "Analysis of time lags and other sources of error of the dexcom seven continuous glucose monitor." *Diabetes Technology and Therapeutics* **2009,** *11*, 689-695.

(47) Gifford, R.; Batchelor, M. M.; Lee, Y.; Gokulrangan, G.; Meyerhoff, M. E.; Wilson, G. S. "Mediation of in vivo glucose sensor inflammatory response via nitric oxide release." *Journal of Biomedical Materials Research* **2005,** *75*, 755-766.

(48) Soto, R. J.; Privett, B. J.; Schoenfisch, M. H. "In vivo analytical performance of nitric oxide-releasing glucose biosensors." *Analytical Chemistry* **2014,** *86*, 7141-7149.